Chang'E Lunar Microwave Radiometer Data Analysis and Lunar Subsurface Temperature Profile Modelling

Weijia Zhang

St Hugh's College

Atmospheric, Oceanic and Planetary Physics

University of Oxford

Trinity Term 2016

Thesis submitted for the degree of Doctor of Philosophy

Abstract

The subsurface temperature distribution of airless bodies across the Solar System can provide important clues to their formation and evolution. This thesis investigates the lunar soil temperature profile using data from the recent Chinese lunar orbiting spacecrafts Chang'E 1 and 2 to explore variations in the subsurface temperature of the Moon. These variations include heat flow information of the subsurface and the interior of the Moon. Before the launch of Chang'E-1 (CE-1), the temperatures of the deep layers of the Moon have only been measured at the landing sites of Apollo 15 and 17 by in situ temperature probes. The CE-1/2 lunar orbiters were both equipped with a 4-frequency microwave radiometer (MRM) to detect the lunar surface brightness temperature (TB) and to retrieve data on lunar regolith thickness, temperature, dielectric constant, and other related properties. The MRM can penetrate to a nominal depth of 5 metres in the subsurface with the 3 GHz channel. This research aims to develop a radiative transfer forward model for an airless body and then utilize MRM data to study an observed anomaly of elevated 2 m deep TBs measurements in the Oceanus Procellarum region on the lunar subsurface.

After initial validation of the MRM data and modelling of the lunar regolith parameters, a multi-layer radiative transfer forward model has been derived using the fluctuation dissipation theorem. The forward model calculates the radiometric contribution from several depths on the TB that would be observed by the MRM instrument around the Moon (at different frequencies), as a basis for an inverse method. Sensitivity analysis indicates that, as expected, mineralogy and density information are very important to the inverse calculation. Therefore new FeO/TiO_2 distributions derived from the Moon Mineralogy Mapper (M^3) were incorporated into the calculation. The derived FeO/TiO_2 distributions were also used to derive the bulk density of the lunar surface which was also incorporated into the calculation.

The forward model was then used to invert the MRM measured TB data to generate 2 m depth subsurface temperature profiles. The provisional results show that, as expected, the 2 m subsurface temperature is potentially correlated to the distribution of radioactive elements such as uranium and thorium in the lunar crust. The 2 m subsurface temperature map was then converted to a lunar heat flow map, which was validated by the Apollo 15 and 17 measurements. Inspecting this heat flow map, abnormal high heat flow in the Oceanus Procellarum KREEP Terrain (PKT) region was noticed. The PKT is enriched with a high abundance of radioactive elements such as uranium and thorium. Hence a heat flow model based on radioactive elements as well as internal cooling was built up to investigate such a finding.

In this thesis, a radiative transfer model for the analysis of MRM was developed and proven to be a useful tool for studying the lunar heat flow, as well as subsurface temperature. Rough surface scattering effects on the MRM measured TB values were also analyzed for future calibration. Possible improvements to the MRM instrument design are discussed in the future work as well as the possible application of the MRM instrument on the Martian surface.

Acknowledgements

I would like to express my gratitude to my dear supervisor Prof. Neil Bowles. I would also like to thank Dr Tristram Warren, Professor Patrick Irwin, Professor Simon Calcutt, Dr Jessica Arnold, Mrs Sarah Harrington, Professor Ouyang Ziyuan, Professor Liu Xiaohan, Dr Hangjie Yu and Dr. Yang Lei for their kind help. I would also like to thank my reviewers for their careful review and helpful comments.

I appreciate contributors of China's Lunar Exploration Program and Diviner Lunar Radiometer Experiment. It's their contribution that makes available the observation data of CE-1, CE-2 and Diviner.

Commonly Used Abbreviations

Below is a list of abbreviations seen in the text; some with a small description. All are defined throughout the thesis, but are also listed here for quick reference.

AOPP, Atmospheric, Oceanic and Planetary Physics. A sub-department of the Department of Physics at Oxford University.
CE, Chang'E
FWHM, Full Width at Half Maximum
KREEP, an acronym built from the letters K (the atomic symbol for potassium), REE (Rare Earth Elements) and P (for phosphorus), which is a geochemical component of some lunar impact breccia and basaltic rocks.
LRO, Lunar Reconnaissance Orbiter
MRM, Microwave Radiometer
M^3, Moon Mineralogy Mapper
PKT, Procellarum KREEP Terrain
TB, Brightness Temperature

Contents

Chapter 1 Introduction

1.1. Importance of Studying Lunar Subsurface Temperature and Heat Flow

Missions exploring the lunar surface have greatly improved our understanding of the Moon's composition, origin and evolution. Over geologic time, the lunar surface has been shaped by impacts, solar irradiation and cosmic rays. After the Apollo and Luna landings in the 1970s, subsequent lunar exploration mainly used visible and infrared remote sensing to study the topography, composition, and near-surface thermal properties of the Moon.

However, information about the properties of the lunar subsurface, deep structural features, and thermal environment are hard to determine, except for measurements obtained at the Apollo and Luna landing sites and from returned lunar samples (*Lunar Source Book, 1991*). Geochemical surveys of returned lunar samples cannot provide direct information on the global composition and physical properties of the subsurface. As a result, knowledge of the Moon's basic geophysical properties, including its internal structure, which can help in constraining theories about its formation and evolution, remain lacking, and our understanding of the lunar origin and evolution is still limited (*Hartmann, 1986*).

Due to these limitations, the lunar subsurface, deep structural features, and thermal environment are still not fully understood. For example, the Moon, once thought to be cold and dead, may have experienced recent volcanic eruptions in the last tens of millions of years (*Braden et al., 2014*) and hence some parts of the Moon may be warmer than previously thought (*Braden et al., 2014*).

The thermal evolution and current thermal state of the Moon is therefore a very important active area of research. By measuring the internal heat flow and the deep subsurface temperature profile (1-5 metres) of the Moon, this work can trace back and determine the lunar core's thermal flow. The results are important for developing theories about the Moon's crust and any residual activity in its core. Specifically:

a) **Modelling the heat flow of the Moon as part of diagnostic tests for thermal evolution models.** Heterogeneities affect in situ measurements of heat flow, so it is not possible to draw conclusions about the whole Moon without global coverage.

b) **Using the distribution of radioactive elements to constrain the evolution of the lunar crust and its connection to differentiation processes during the Moon's formation.** This can help us understand the quantity and distribution of radioactive elements between the crust and mantle, part of its differentiation story**.** The heat flow of the Moon greatly depends on the concentration of a large number of radioactive isotopes, especially uranium, thorium and potassium. However, the distribution of these isotopes below the

surface of the Moon remains unknown. Measurements by e.g. the Lunar Prospector spacecraft (*Lawrence et al., 2002*), only observe the abundance and distribution of radioactive isotopes in the shallow surface (approximately 20 cm) of the Moon. Also, according to heat flow measurements made by the Apollo 15 and 17 missions, the concentration of uranium on the Moon varies between an Earth-like 20/21 ppb (*Warren and Rasmussen, 1987*) and 46 ppb (*Langseth et al., 1976*). However, the current range of uncertainties in the concentrations of radioactive isotopes observed in the lunar crust is too large to test the widely believed lunar formation hypothesis that the Moon was formed by a giant impact between proto-Earth and a Mars sized body called Theia (*Halliday, 2000; Young et al., 2016*). The study presented in this thesis can generate a highly rigorous global estimate of the mean endogenic heat flow of the Moon, which, in turn, will lead to a more accurate estimate of the abundance of radioactive materials on the Moon, thereby providing better tests for formation hypotheses.

c) **To understand the nature of the Procellarum KREEP Terrane (PKT).**[1]

Geochemical surveys have shown *(Haskin, 1998*) that KREEP mainly occurs in the northwest quadrant of the Moon (Figure 1.1) (*Haskin, 1998*). The thermal modelling by Wieczorek and Phillips (*2000*) showed that the high radioactivity of PKT could contribute as much as 20 mW/m^2 of heat flow at the centre of PKT, so is it is a significant energy source that needs to be

[1] KREEP is an acronym built from the letters K (potassium), REE (Rare Earth Elements) and P (phosphorus).

[2]Dielectric loss angle tangent: Dielectric loss measures a dielectric material's inherent dissipation of

quantified. By comparing the heat flow at the centre of the PKT with the average heat flow of the Moon the overall abundance of radioactive materials can be estimated. The Apollo measurements were made at only two locations (Figure 1.2) so the available samples may not reasonably represent the concentration of radioactive elements in KREEP (*Korotev, 1998*).

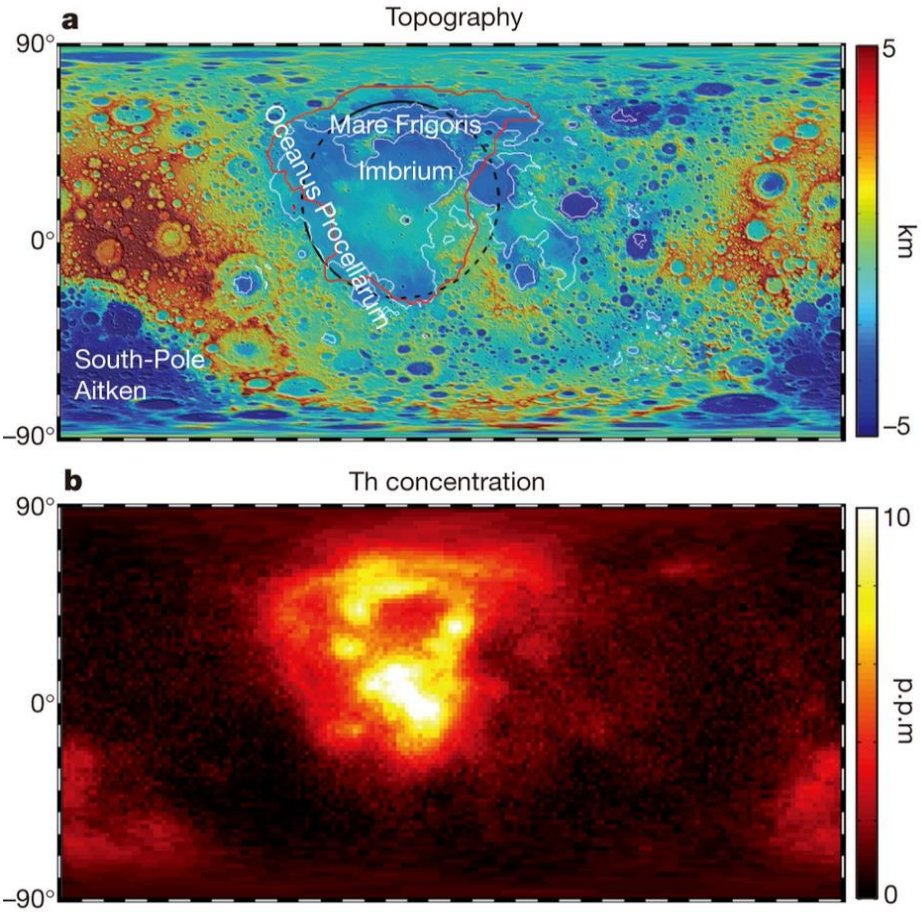

Figure 1.1. Global maps of the Moon showing: a, Topography; b, Th concentration (*Andrews-Hanna et al., 2014*). The red line on the topographic map shows the extent of the PKT region. The PKT region is also clearly visible in the mapped Th concentration (b) (*Lawrence et al. 1998)*. The circular rim of the Oceanus Procellarum region is shown by a black dashed line in a (*Whitaker 1981)*. The outline of the Maria is also shown by white lines, (*Hiesinger et al. 2010)*.

d) **Understanding the lunar subsurface temperature distribution is also critical in studying the timing and evolution of lunar volcanism (*Andrews-Hanna et al., 2014*).** The detection of any anomalous hotspots not correlated with KREEP terrain needs to be investigated.

1.2. The Advantages of Microwave Remote Sensing Measurements for Determining Lunar Heat Flow.

Clearly, global measurements of lunar heat flow are required for understanding the Moon. Subsurface heat flow can generally be estimated in two ways; in situ measurements and by remote sensing. In situ measurements involve drilling a hole in the lunar surface and determining the temperature at specific depths. At the time of writing, the Apollo 15 and 17 missions were the only experimental sites that probed the lunar temperature below the surface (Figure 1.2).

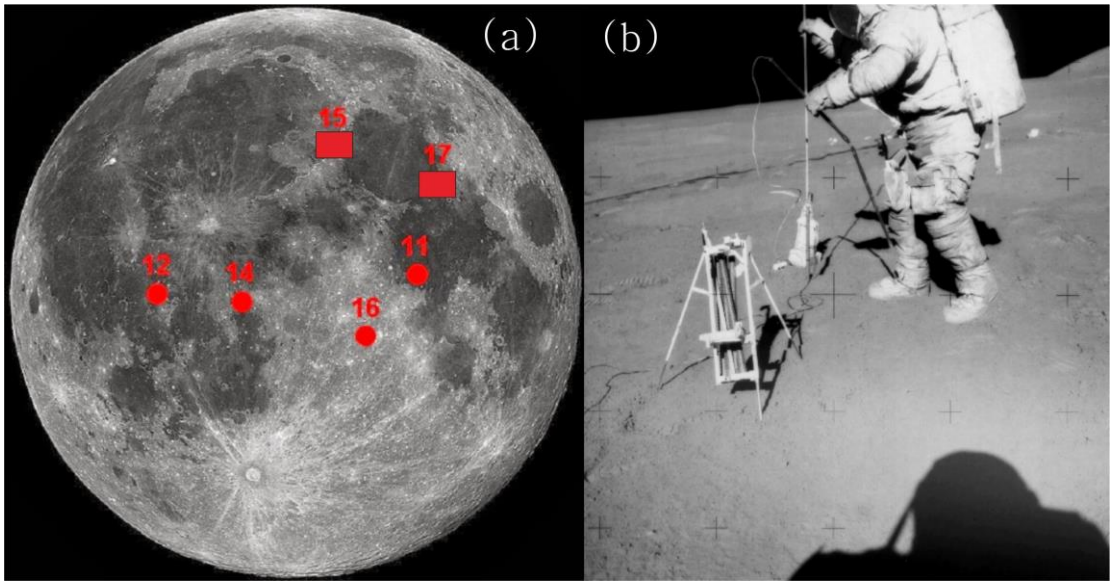

Figure 1.2. (a) Location of Apollo landing sites, where Apollo 15 and 17 landing sites are represented by red boxes, while other Apollo landing sites are represented by red dots; (b) Astronaut David Scott inserts the Heat Flow Experiment probe into the regolith

Measurements during the Apollo era at the Apollo 15 and 17 sites are complicated to interpret because of experimental difficulties, including making sure the regolith was not compacted prior to inserting the heat probe (*Lunar Source Book, 1991*). In addition, both the Apollo 15 and 17 heat measurement sites were in Maria regions near the lunar equator (Figure 1.2.a) and thus cannot be easily compared with other areas, such as the lunar highlands that are known to be compositionally different. More importantly, the Apollo 15 and 17 sites are in or nearby KREEP rich terrain. Therefore, they cannot represent the lunar crust as whole (Hagermann and Tanaka, 2006).

The second way to measure temperature profiles is by remote sensing. Since September 2009, the Diviner Lunar Radiometer Experiment (Diviner) on the Lunar Reconnaissance Orbiter (LRO) (*Paige et al., 2010*) has been acquiring an extensive set of thermal emission measurements from the lunar surface at infrared wavelengths generating global bolometric maps of the top 2 mm surface temperatures. Remote sensing techniques such as Diviner that use thermal infrared or visible wavelengths, can only provide compositional and temperature information to a depth of a few millimeters. As a result, data on the global, deep (50 cm or more) lunar subsurface

temperature structure, mineralogy, and heat flow are limited.

Longer electromagnetic wavelengths in microwave region of the spectrum (> 1 mm) have much greater penetration depths and so can potentially probe at greater depths than infrared techniques alone, thereby revealing the lunar regolith's deeper (> 50 cm) temperature structure. In addition to regolith temperature, microwave remote sensing measurements can also potentially give information about other properties such as dielectric constant and density etc.

Microwave remote sensing aims to look into the shape and structure of an object by detecting radiation reflected or emitted at wavelengths that are typically > 1 mm. Microwave remote sensing techniques developed for Earth measurements in the late 20th century can also be applied to other planets and extraterrestrial bodies, including the Moon. Using these longer wavelengths, temperatures at depths of several metres can then be estimated. Therefore, microwave remote sounding can compensate for the shortcomings of other remote sensing techniques (which can only penetrate < 2 cm), providing additional data. However, the modelling of microwave remote sensing is challenging because there is a dependence on many parameters including mineralogy, density, heat capacity and dielectric constant etc.

Depending on the working principle, microwave remote sensing devices can be divided into two categories:

1. Active, which proactively transmits microwave signals and then receives the reflected or scattered signal off of a target in a similar way to radar.
2. Passive, which works in a similar way to an infrared radiometer such as Diviner by using a highly sensitive microwave receiver to obtain the faint radiation signals of the target.

Since the 1960s, passive microwave propagation from the surface of Earth has been the subject of numerous studies. However, water absorption prevents measurements at appreciable depths (~5 cm) (*Burke and Schmugge, 1979; Tsang et al., 1975; Njokuand Kong, 1977*). Therefore, microwave transmission on Earth does not typically contain information on soil thickness and underlying rocks, but can be used to measure soil humidity. Fortunately, this problem does not exist in the desiccated environment of the Moon.

Furthermore, recent Chinese remote sensing satellites have carried microwave radiometers, which can measure the deep subsurface. The original goal of these instruments was to map He^3 composition (*Wang et al. 2008*). CE-1, China's first lunar probe, was successfully launched on October 24, 2007 in Xichang and on March 1, 2009, and a controlled landing of CE-1 on the lunar surface was accomplished (*Li et al., 2010*). After the successful launch of CE-1, the Chang'E-2 (CE-2) probe was launched on October 1, 2010. Compared with CE-1, CE-2 has a better spatial resolution and observed the lunar surface for a wider range of local times. Details will

be described in Chapter 2.

Both CE-1 and CE-2 lunar orbiters were equipped with a passive microwave radiometer (MRM) to measure the brightness temperature of the lunar surface (*Li et al., 2010*). The measured lunar brightness temperature (TB) can then be used to determine the lunar subsurface temperature after taking into account certain lunar regolith properties (e.g. density, heat capacity, mineralogy, dielectric constants, etc.). Data in the microwave region of the electromagnetic spectrum measured by instruments, such as the MRM on CE-1 and CE-2, can penetrate deeper (up to 5 m) into the lunar subsurface than visible or thermal infrared instruments (~2 mm). This opens a window into the deep lunar subsurface temperature and heat flow, presenting a "microwave moon."

This window into the deep lunar subsurface shows an interesting phenomenon in the Oceanus Procellarum region. The PKT region described earlier is found inside Oceanus Procellarum (Figure 1.1.). From the MRM data, the Oceanus Procellarum region exhibits a higher subsurface temperature at depths between 1-5 metres than surrounding regions of the Moon, which indicates a significant compositional difference (Figure 1.3).

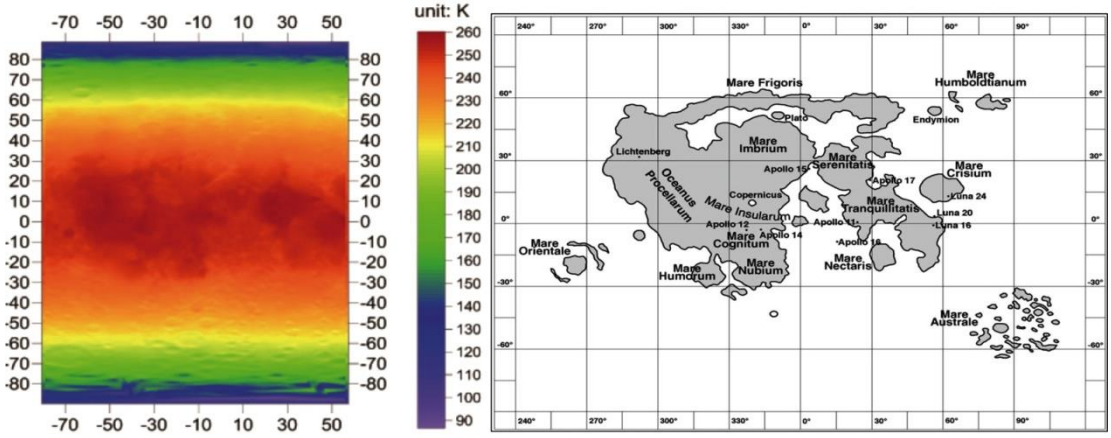

Figure 1.3 Enlarged lunar deep TB map (left) shows clearly the shape and position of Oceanus Procellarum. The right-hand map of the lunar surface shows the location of basins inside the PKT region. The Apollo and Luna landing sites shown on the right-hand map are cited from Hiesinger et al. (*2003*). Labels of the right map are in longitudes (x) and latitudes (y).

The Procellarum basin has a large concentration of radioactive elements such as thorium and uranium that produce heat *(Hiesinger et al., 2003; Lawrence, 2007).* Thus, this area may have undergone periods of reprocessing, such as partial re-melting, and the residual higher concentrations of radioactive elements may have led to higher subsurface temperatures. Based on crater counts, Oceanus Procellarum is the location of the youngest basalts on the lunar nearside, where the youngest volcanic flows are found (*Hiesinger et al., 2003*).

However, a more detailed model is required to extract the maximum information from measurements made in the microwave spectrum. The next chapters describe how this initial (Figure 1.3.) analysis can be improved to provide a quantitative study of lunar subsurface composition and heat flow. I will also investigate the phenomenon shown

in Figure 1.3 and then find the mechanism that causes it in chapter 6 and chapter 7.

1.3. Outline of this Thesis

The main problem addressed by this thesis is determining the appropriate technique to interpret the microwave data on an airless body such as the Moon. To answer this question, this thesis focuses on the establishment of a microwave-sounding model for airless bodies, with the Moon as an example, including the quantification of lunar subsurface parameters, the transmission analysis of microwave radiation in the lunar regolith, and the retrieval.

Temperature profiles at metre depth around the equator region can then be derived from the one dimensional thermal diffusion equation using the surface temperatures provided by Diviner's infrared observations as a boundary condition. Based on a microwave radiative transfer model and using the fluctuation dissipation theorem, the 2 m subsurface temperatures and heat flow of the Moon are inverted from the CE-1 and CE-2 multichannel microwave brightness temperatures. A comparison of the heat flow from CE-1 and CE-2 MRM and the simulated heat flow based on radioactive isotopes are also discussed. A flow chart of this research is shown in Figure 1.4.

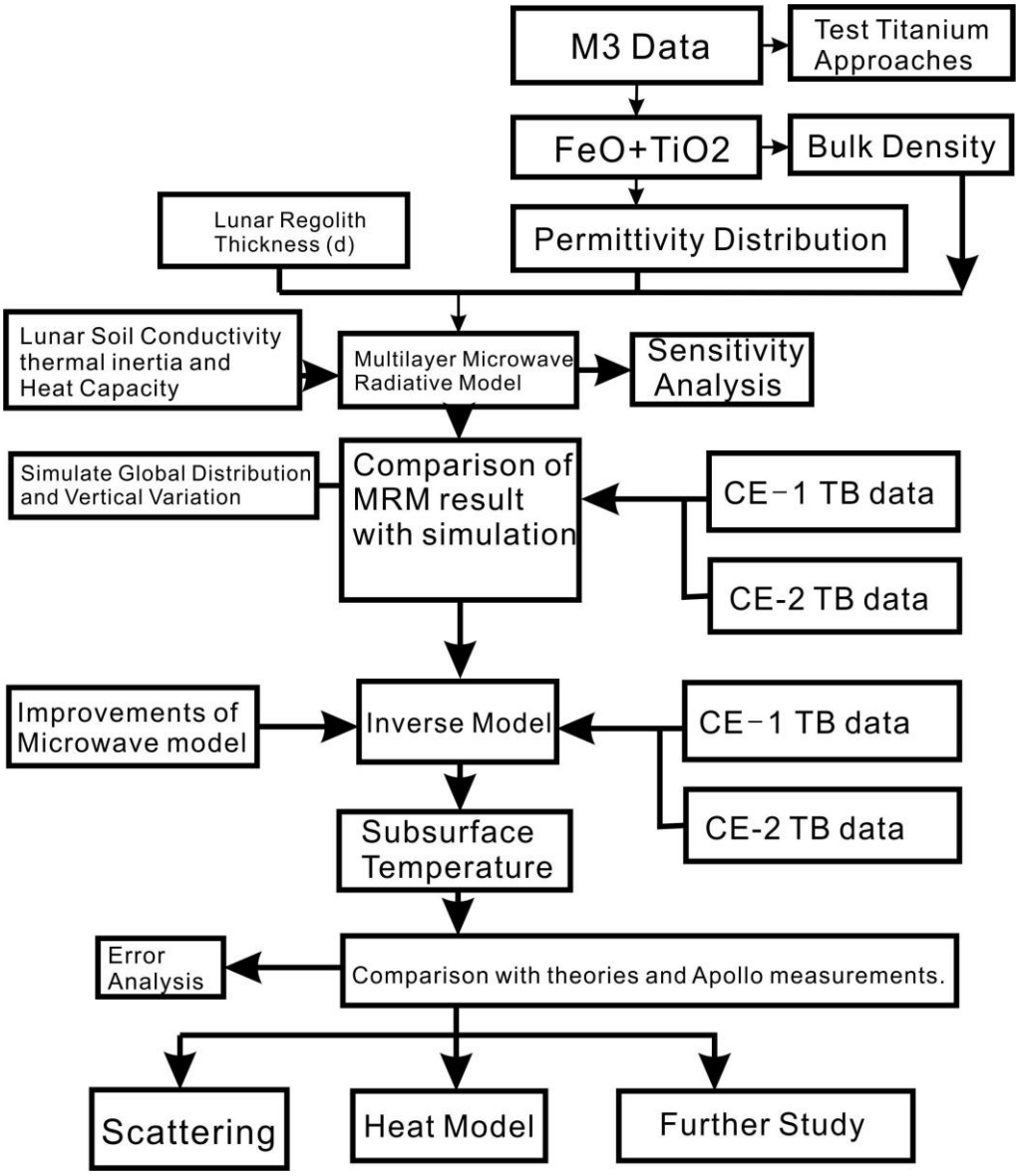

Figure 1.4.Flow diagram of this thesis. CE MRM data will be validated in the first two chapters. Then a microwave radiative transfer model will be built in chapter 3/4, and be improved in chapter 5. The subsurface temperature will be inverted in chapter 6. Finally the subsurface heat flow will be mapped in chapter 7, with theoretical explanations.

To summarize the work flow of this thesis the first step was extracting and plotting the brightness temperatures derived from the CE missions. Then the MRM data was validated in chapter 2 by comparing it to the Diviner data.

After validating the MRM data, the parameters needed to develop an inversion model

of the MRM data were investigated in chapter 3. These parameters included: lunar regolith density, specific heat capacity, dielectric constant and conductivity. The number of layers required in the inversion model was also investigated.

In chapter 3, a one dimensional thermal vertical model was developed and several thermal latitude models were discussed. The MRM data was further validated by comparing the measurements with the theoretical thermal depth simulations of the one dimensional thermal vertical model. The modeled temperature profile of the lunar regolith varied mainly within the top 20 cm. Below 20 cm the temperature was stable with depth (diurnal variation $< \pm 5$ K).

A microwave radiative transfer model for the CE-1 and CE-2 MRM data was developed in chapter 4, which was used as a forward model in the later inverse scheme. The forward model calculated the contribution of each depth to the TB (at different frequencies), thereby determining the depth that each MRM channel sounds to. The inverse temperature vertical profile can then be compared with the Apollo 15 and 17 site measurements. The MRM measured temperature profile beneath the lunar surface matches well with the calculations provided by the theoretical model simulation and with the Apollo in situ measurements. Chapter 4 also explored the error analysis by using both standard error propagation and Monte Carlo analysis. The main error sources were found to be Maria mineralogy and the density of the lower bedrock, whereas the TB error from the instrument or the highland mineralogy

displayed a much smaller influence.

In chapter 5 lunar mineralogy and density data sources were added to improve the model. Mineralogy (especially FeO and TiO_2) and density are particularly important in the radiative transfer modelling, as the dielectric constant (which is dependent on mineralogy and density) changes the penetration depth of the microwave signal. In the current study, new global maps of FeO and TiO_2 were derived from measurements made by the Moon Mineralogy Mapper (M^3) onboard Chandrayaan-1 (*Green et al., 2011*). After including the mineralogy information, the lunar bottom soil and bedrock density was studied and modelled. The regolith density profile has a correlation with the local minerology (*Huang and Wieczorek 2012)* and hence the mapped mineralogy was used to calculate an improved density profile of the lunar regolith. The density profile measured at the Apollo (11, 12, 14, 15, 16 and 17) landing sites was shown to compare well with the derived density profile, validating this technique.

In chapter 6, a priori information was added to the model and the lunar subsurface temperature distribution from the newly developed MRM inversion model was plotted. The inverse model was used in mapping the nearside subsurface temperature at a depth of 2 m and compared with previous solar radiation heating models (e.g., *Keihm et al. 1973*). Interestingly, aside from the previously identified KREEP region the mapped subsurface temperature fitted the previous solar radiation heating models well.

In chapter 7, the inverse model was then used to calculate the lunar subsurface heat flow. It was found that the 2 m deep lunar subsurface heat flow ranges from 2 mW/m^2 to 68 mW/m^2, which is consistent with earlier ground-based remote sensing measurements (*Little et al., 2003*) and estimates calculated based on heating from radioactive elements. Spatial distribution of the lunar heat flow at a depth of 2 m was also in good agreement with both the ground based remote sensing measurements and the model of radioactive heating.

Comparison between this inverse model result with Apollo 15 and 17 measurements also shows consistency. Thus, I attempted to confirm that source of the anomalous heat flow in Figure 1.3 was local concentrations of radioactive isotopes.

A heat flow model based on radiogenic heating and lunar mantle cooling was also built in chapter 7. The modeled heat flow due to radioactive isotopes ranges from 1.2 to 59.0 mW/m^2, providing an average flow of 10.0 (9.98) mW/m^2. This is in accordance with the MRM inversion result, and also the Apollo 15 and 17 measurements. The areas with the highest modeled heat flow are concentrated in the Oceanus Procellarum, which again supported the MRM inversion result. All these findings suggest that the Moon's heat flow is influenced by nuclear decay (uranium, thorium and potassium). Radiogenic heat formed the subsurface hot area, including the Oceanus Procellarum, and it also shaped the KREEP region.

In the Appendix, the influence of scattering on the radiance received by the MRM was studied. The results show that large (km) scale lunar surface roughness affects the input solar radiation depending on the topography, as expected. The small-scale (cms) roughness may increase TB due to scattering effects in the higher frequency channels. However, the small-scale roughness of the lunar surface only minimally affects long wavelength channels, such as the 3 GHz channel.

Finally, in chapter 8, future applications of MRMs on Mars and other airless bodies are discussed. In addition, possible improvements for the MRM instrument are also suggested.

Chapter 2. MRM Details and Validation

2.1. Chang'E-1 and Chang'E-2

As described in the introduction, on an airless body such as the Moon, microwave remote sensing can provide information on subsurface heat flow and composition to depths of several metres (pp. 14~15). This section will describe the most comprehensive set of Lunar microwave data currently available from the MRM instrument on the Chang'E 1 and 2 spacecraft (*Wang et al., 2010*). Figure 2.1 provides photographs of CE-1.

2.2. MRM Instrument Details

2.2.1. Instrument Description

Both CE-1 and CE-2 MRMs (Table 2.1 and Figure 2.1-2.2) have been used to detect the brightness temperature (TB) of the lunar surface and retrieve lunar regolith thickness, temperature, dielectric constant, and other related properties (Figure 2.1) (*Wang et al., 2008*). Details of the instrument and ground calibrations are described by Wang et al. (*2010*).

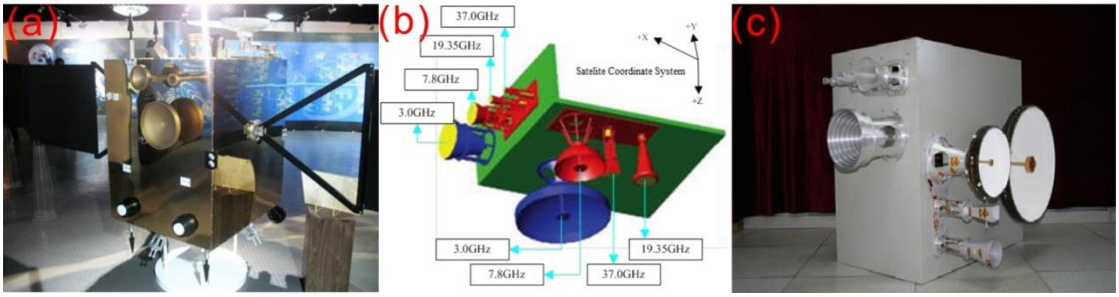

Figure 2.1 (a) Chang'E-1 (CE-1) spacecraft. (b) CAD model of MRM on CE-1. (c) MRM instrument. The size of CE-1 is 200 cm × 172 cm × 220 cm, and the size of the MRM instrument itself is 120 cm × 172 cm × 90 cm.

Table 2.1.Basic performance information of the MRMs carried by CE-1 and CE-2 (*Wang et al., 2010*)

Operation Details:

Flight control period	Operating time (h)	Effective access time(h)	Coverage
2007.11.27~2008.01.27（first flying period）	1380.7	1160.3	84%
2008.01.30~2008.02.04 （ first side-flying period）	120.9	100.4	83%
2008.05.15~2008.07.29 （ second flying period）	1624.6	1396.6	86%
2008.11.12~2009.01.14（life Extension）	858.2	705.8	82%
Total	3984.4	3363.1	84.4%

Instrument Details:

Name	CE-1 index
Frequency (GHz)	3.0(±1%), 7.8(±1%), 19.35(±1%), 37(±1%)
Integral time (ms)	100(±15%), 200(±15%), 500(±15%), 500(±15%)
Temperature resolution (K)	≤0.5
Orbits number	1690 orbits
Orbit Height	200 km
Spatial resolution	35 km
Orbital inclination	31.0 degree

Name	CE-2 index
Frequency (GHz)	3.0(±1%), 7.8(±1%), 19.35(±1%), 37(±1%)
Integral time (ms)	100(±15%), 200(±15%), 500(±15%), 500(±15%)
Temperature resolution (K)	≤0.5
Orbits number	2401 orbits
Orbit Height	100 km
Spatial resolution	17.5 km
Orbital inclination	31.0 degree

Each frequency channel has three input sources, namely, the lunar observing antenna, the cold-air calibration antenna, and the hot load antenna. The three antennas share one receiver, so the MRM works with two in-orbit calibrations. High and low temperature calibrations were used to determine the microwave radiometer calibration equation Eq. 2.1. This calibration equation can be used to accurately calibrate the lunar regolith microwave TB captured by the observing antenna. In addition, the receiver is equipped with a temperature measurement circuit and can perform

real-time temperature monitoring of the 28 key points in the antennae and receiver easily affected by temperature (*Cui et al., 2009*).

No large internal temperature variations (e.g. temperature variation >25 K) were observed during the operation and the status of the instrument remained stable during the whole detection period for the MRM. The temperature variations in all operational orbits were between 12 K and 23 K, with no more than 5 K temperature variation for each detected orbit period receiver (*Wang et al., 2010*). According to the following Eq. 2.1, the performance is then acceptable to meet the radiometric accuracy requirement of < 0.5 K.

According to the antenna calibration equation, the antenna temperature can be calculated as follows:

$$T_A = [\frac{V_A - V_C}{V_H - V_C} T_h + \frac{V_H - V_A}{V_H - V_C}(c_1 T_c + c_2 T_{w\text{-}c} + c_3 T_h) - a_2 T_w - a_3 T_h] / a_1 \qquad \text{(Eq. 2.1)}$$

where T_A is the antenna temperature, T_w is the physical temperature of the wave guide, T_c is the temperature of the calibration antenna which is dependent on the size of the calibration antenna. The value of T_c in the absence of contamination is ~2.7 K. The corresponding equivalent TB for the cold-air calibration input branch is T_{w-c}. The equivalent TB of the load for the hot branch is T_h. V_A, V_H, and V_C are the average output voltages of the observation, hot and cold-air branches through the receiver, respectively. $T_{w\text{-}c}$, T_w, and T_h can be obtained by the platinum thermistor in the hot

and cold branches, whereas the calibration coefficients of a_1, a_2, a_3, c_1, c_2, and c_3 are captured by the ground calibration test before launch. These values are provided by the CE Load Research and Development unit (CE Space Center).

The standard error as applied to the transmission formula, that is, the error of the antenna temperature calibration equation ΔT_A, can be expressed as a function of the RMS error of each variable from Eq 2.1 which is given by:

$$\Delta T_A^2 = \Delta T^2 + \Delta V^2 \left[\left(\frac{\partial T_A}{\partial V_A} \right)^2 + \left(\frac{\partial T_A}{\partial V_H} \right)^2 + \left(\frac{\partial T_A}{\partial V_C} \right)^2 \right] + \Delta T_n^2 \left[\left(\frac{\partial T_A}{\partial T_h} \right)^2 + \left(\frac{\partial T_A}{\partial T_w} \right)^2 + \left(\frac{\partial T_A}{\partial T_{w-c}} \right)^2 \right] + \Delta T_c^2 \left(\frac{\partial T_A}{\partial T_c} \right)^2 \quad \text{(Eq. 2.2)}$$

Eq. 2.2 demonstrates that the following instrumental parameters are important:

1) ΔT represents the sensitivity of the receiver and has a value < 0.5 K;
2) ΔV is the digitization error of the voltage value, and ΔV =0.1525 mV;
3) ΔT_n is the measurement error of the platinum thermistor and based on the CE MRM ground calibration (*Cui et al., 2009*). $\Delta T_n \leq 0.08$ K;
4) ΔT_c is the uncertainty error of the cold space background calibration antenna temperature. Around the equator ΔT_c is 2.7 K (*Cui et al. 2009*).

Considering the above error terms in the calculation, the calibration error of the antenna temperature (ΔT_A) is mainly affected by the sensitivity of the radiometer (ΔT), and $\Delta T_A \leq 0.5$ K. The internal structure of the MRM is shown in Figure 2.2.

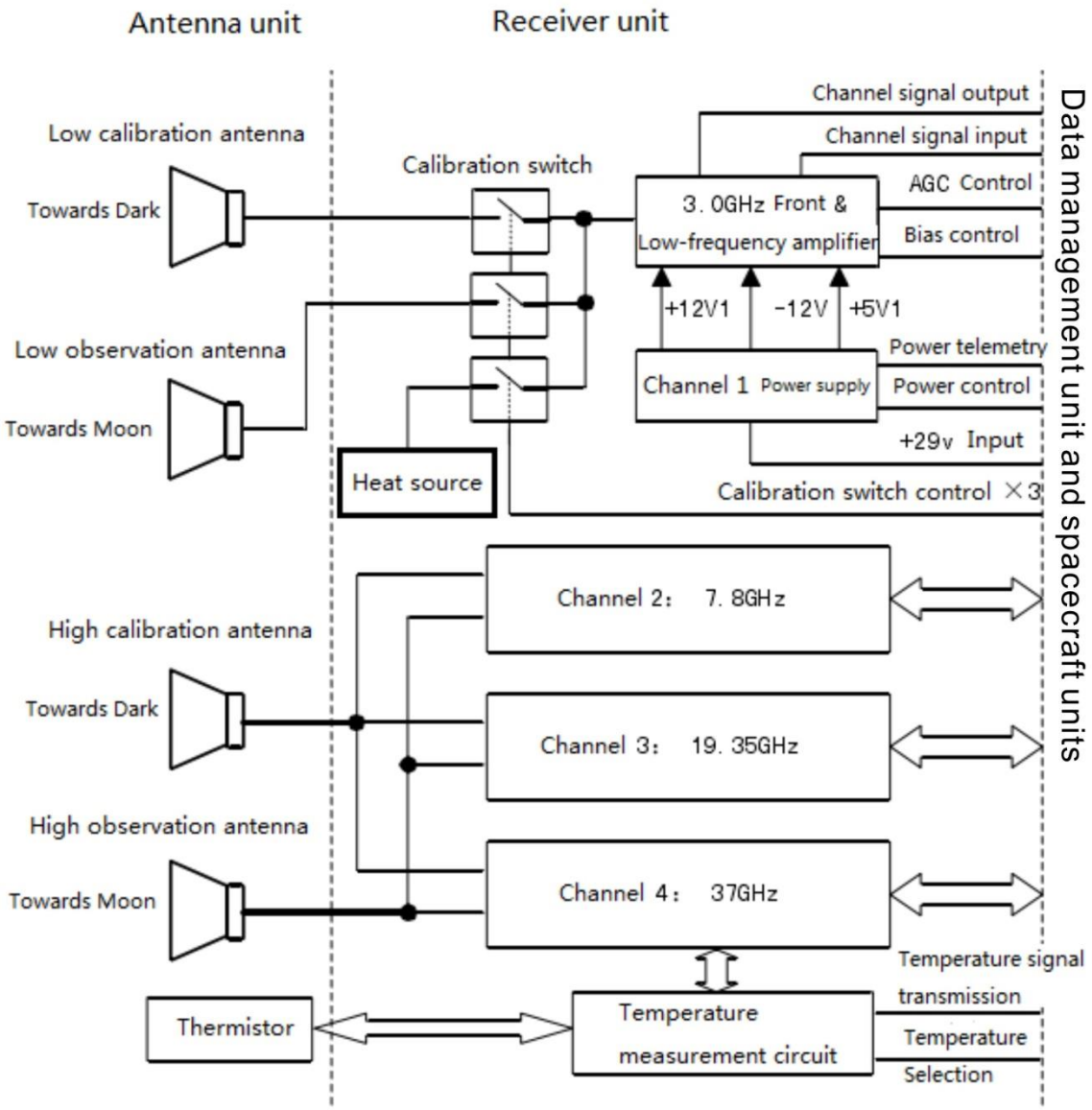

Figure 2.2 Internal structure of CE MRM device *(Li et al, 2010*). The observation antenna receives the microwave radiation from lunar surface, while as the calibration antenna observes the cold sky during every 11.6 s measuring period. The real-time calibration used two reference sources. The heat source was an internal source of 300 K, and the cold reference was the 2.7 K space background.

2.2.2. MRM Sounding Depth

The sounding depth for each channel on the MRM decreases with increasing frequency. Assuming a nominal lunar regolith mineral content of S=10% (S is defined as S=Ti%+Fe%), density of 1.9 g/cm^3, the predicted penetrating depths are <0.5, <1.0, <2.0, ≥5 m at 37.0, 19.35, 7.8 and 3 GHz, respectively (*Wang et al., 2008; Li et al., 2010*).

2.3. Data Acquisition and Lunar Surface Coverage

The CE-1 spacecraft was placed into lunar polar orbit, and ground track coverage was repeated twice a month, that is, during lunar day and night. Measurements were taken by the MRM from November 27, 2007 at 23:23 until January 14, 2009 at 19:11. The accumulated data covered the entire lunar surface. The altitude of satellite orbit was approximately 200 km in the early stage of satellite operation. However, the height of the satellite orbit was reduced to approximately 100 km in the extended mission period after December 10, 2008, generating an additional 210 circular orbit tracks of data at higher spatial resolution (from 35 km to 18.2 km).

Figures 2.3 and 2.4 show the measured MRM data on a homolographic grid (each grid in the equatorial region is $2° \times 2°$ and has an area of approximately 3,678 km^2) for the entire detection (observational) phase. During the lunar day, the lunar nearside

(70 ° W to 40 ° E) and farside (160 ° E to 130 ° W) (Figure 1.1) were frequently observed by the MRM instrument. The lunar nearside and farside were mapped more than five times, and a maximum of nine separate observations (nine different local times) were conducted from 20 ° W to 60 ° W. The coverage of lunar night was the same as that of lunar day.

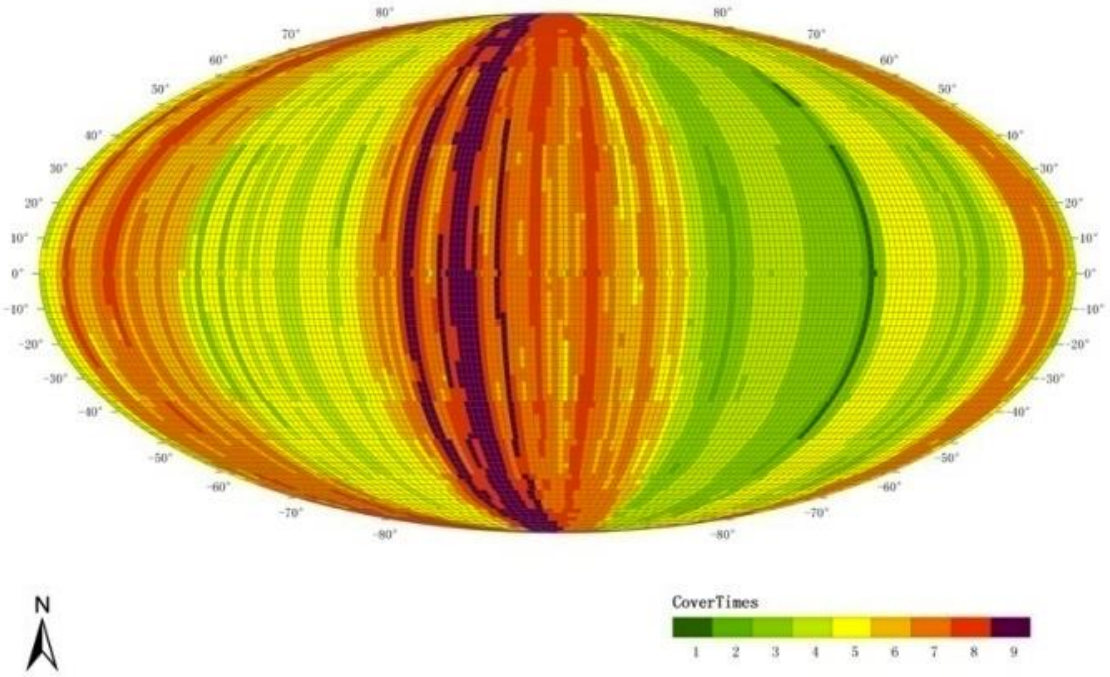

Figure 2.3 MRM data coverage on lunar day during the CE-1 detection period. The lunar surface is divided into 11,306 homolographic boxes. The colours of the boxes represent the number of observations.

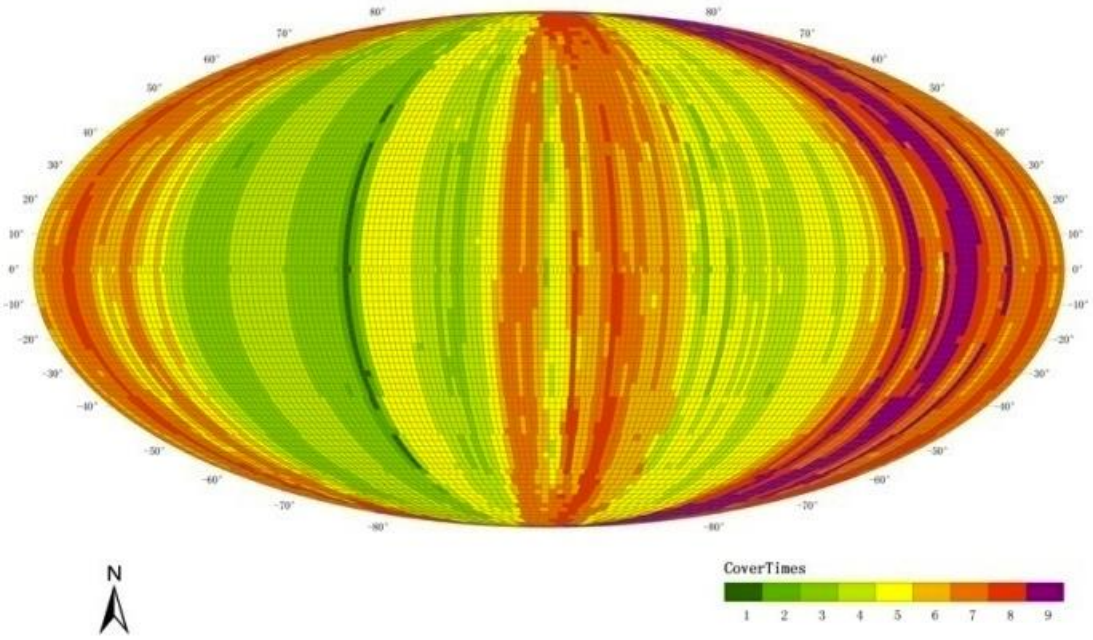

Figure 2.4 MRM data cover on lunar night–day during the CE-1 detection period.

CE-2 was very similar to CE-1. The only difference of note was that CE-2 had a much smaller antenna footprint size (17.5 km compared to 35 km) due to its 100 km orbital altitude. Interpolated maps of the TB distribution on the lunar surface obtained by one month of CE-2 MRM data during the lunar day are plotted in Figure 2.5. (Note: the plotted TB is not the real temperature of the lunar soil but the TB derived from the MRM data. The TB is defined as the temperature of the surface assuming all radiation received by the MRM instrument was emitted by the lunar surface modelled as a perfect blackbody. This thesis also uses MRM TB as important input data, to derive real temperatures in chapter 6).

In Figure 2.5(c-d) an apparent discontinuity can be noticed at longitude −100°. Such a

discontinuity is caused by the conjunction of the first and last tracks of data. Although the detection areas of the first and last tracks are similar, the solar elevation angles of the two tracks can be quite different (in Figure 2.5 they differ by one month), resulting in significant differences in the derived TB from the high frequency channels (c is 19.35 GHz TB, while d is 37 GHz TB). For low frequency channels such as the 3 GHz channel, solar elevation angle is not as important due to the increased sounding depth.

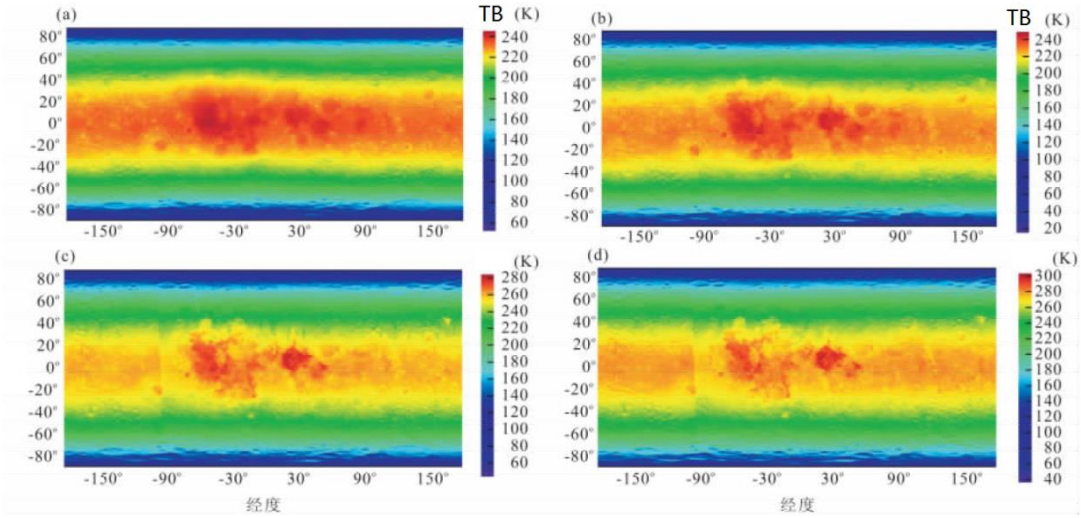

Figure 2.5 Interpolated maps of the TB distribution on the lunar surface obtained by CE-2 MRM during the lunar day. a. 3 GHz, b. 7.8 GHz, c. 19.35 GHz, and d. 37 GHz (*Feng et al., 2003*).

2.4. Data Availability and Product Generation

CE-1 data were received and processed by the Chinese National Observatory Ground Application System. Relevant data is free to download from the following website: http://moon.bao.ac.cn/ceweb/datasrv/dmsce1.jsp. CE-2 MRM data is also free to

download from: http://moon.bao.ac.cn/ceweb/datasrv/dmsce2.jsp and http://159.226.88.30:8080/CE2release/cesMain.jsp. Users must first create a free login account before browsing the data.

The TB values of the lunar surface used in this thesis are the CE-MRM level 2C data, which is derived from the raw data format after a three-step data process, namely: an antenna temperature calculation, geometric positioning, and TB calculation. The TB product can then be plotted using standard latitude and longitude coordinate systems in Figures 2.6 and 2.7.

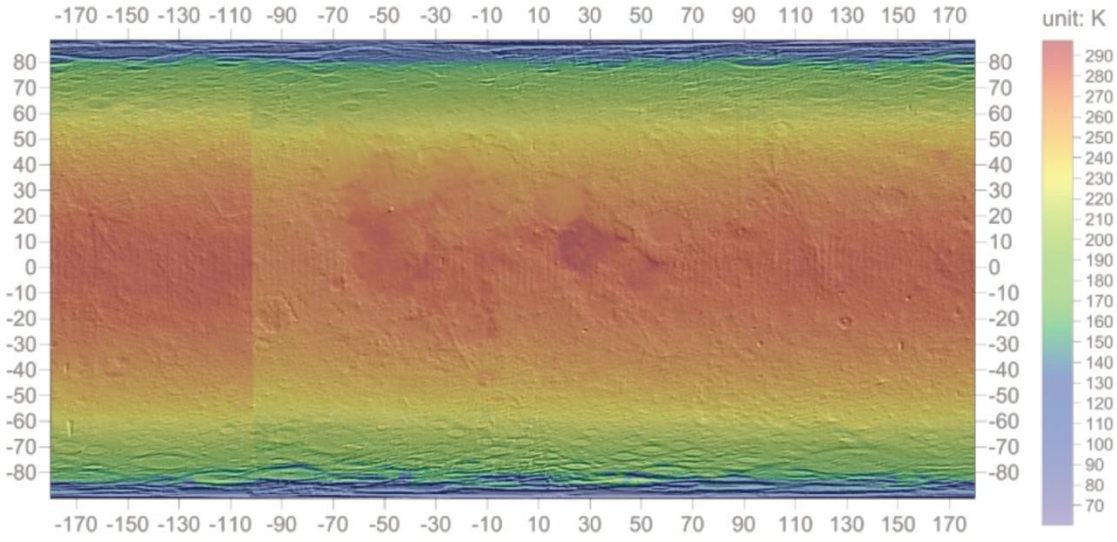

Figure 2.6 Interpolated image of 37 GHz TB distribution on the lunar surface during lunar day obtained by the radiometer during the first month of MRM operation (overlapped on the Clementine lunar basemap). Simple cylindrical projection and Kriging interpolation method are used in the images. Interpolation involved 520,000 data points, and spatial resolution is 18.2 km.

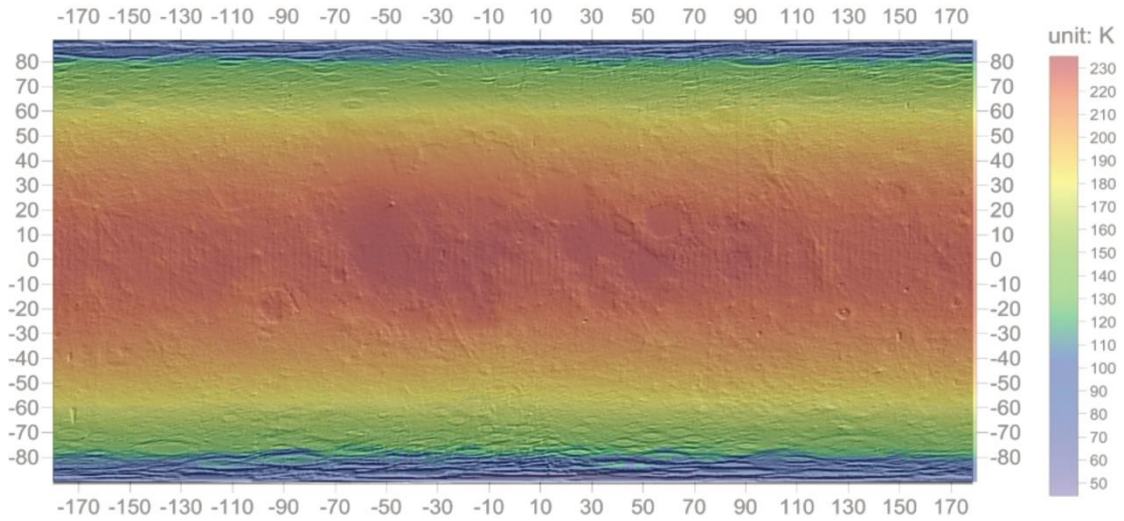

Figure 2.7 Interpolated image of 3 GHz TB distribution on the lunar surface during the lunar day obtained by the radiometer during the first month (overlapped on the Clementine lunar basemap).

For highland regions, microwaves penetrate deeper because of the low dielectric constant (low FeO and TiO_2 mineralogy content, Eq. 3.4 < 8% total), while for Maria regions, microwave signals received by MRM are emitted closer to the surface. This difference in composition can be seen in Figure 2.6 and 2.7 as the measurements during the daytime show increased TB values in the Maria regions compared to the highland regions. The observed difference in the TB values between the Maria and the highland regions is also due to variations in albedo. The 3 GHz TB mainly comes from deep layers (> 50 cm), where the temperature is no longer affected by daily fluctuations (*Spencer et al., 1989*; Figure 3.6). Even in this deep layer the compositional and albedo differences between Maria and highland can be observed. This is explored further in chapter 3.

2.5. Data Validation

The 3.0 GHz channel of the MRM can sense temperatures from depths of approximately 5 m below the lunar surface. Therefore, comparing data obtained from MRM with those gathered from instruments, such as the Diviner radiometer (which can sense temperatures to depths of 2 mm) of the LRO, is of great interest (*Paige et al., 2010*).

The Diviner Lunar Radiometer Experiment is a multi-channel solar reflectance and infrared radiometer with 7 spectral channels, of which 3 spectral filters are near 8 μm wavelengths, and four filters cover approximately 13–23, 25–41, 50–100, and 100–400 μm wavelengths (*Paige et al., 2010*). Data is collected in a push-broom configuration across the surface of the Moon. The radiometer charts the temperature of the entire lunar surface at approximately 500 m horizontal scales. To identify potential ice deposits, Diviner has been mapping the global thermal state of the Moon since July 2009.

Overlaps between CE-1 and Diviner data at specific local times were checked to verify the validity of both the Diviner and CE-1 MRM data, as an independent inter-comparison of both datasets. CE-1 data was checked against the Diviner results when sampled on a similar spatial grid (Figure 2.8). The effects of topography and local time were minimized by extracting Diviner data with local times (hour angle),

and latitude/longitude coordinates within the region with the most CE-1 flyby times, e.g. 0 °–5 °N and 40 °–35 °W for midday (11 a.m.–1 p.m. local time) and 0 °–5 °N and 140 °–145 °E for midnight (11 p.m.–1 a.m.). A narrow range of local times was chosen to minimize the effect of local topography in the equatorial regions and provide a straightforward baseline for initial cross-checks. Fifty random points were used to compare the two datasets. The data of the two spacecraft are consistent, because their TBs matched within expected variation (±5 K) (Figure 2.8-2.9). There was an expected variation due to the different sounding depths of the two instruments and the temperature spatial variations on the lunar surface within a field of view.

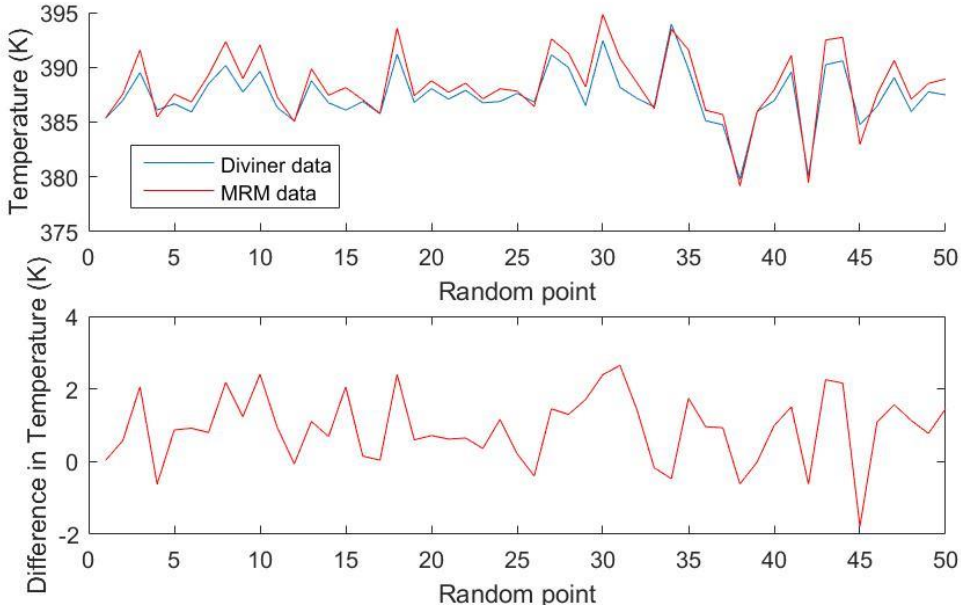

Figure 2.8. A comparison graph which takes 50 random equatorial lat/lon points and compares the maximum Diviner measured temperature to the MRM data.

Ran et al (*2014*) compared Diviner TB with the CE MRM 37 GHz channel in Copernicus crater region during midday and showed general agreement (Figure 2.9).

Based on the analyses of CE-1/2 MRM and the Diviner TB measurements, Ran et al (*2014*) suggested that the data from these two instruments have a high correlation coefficient.

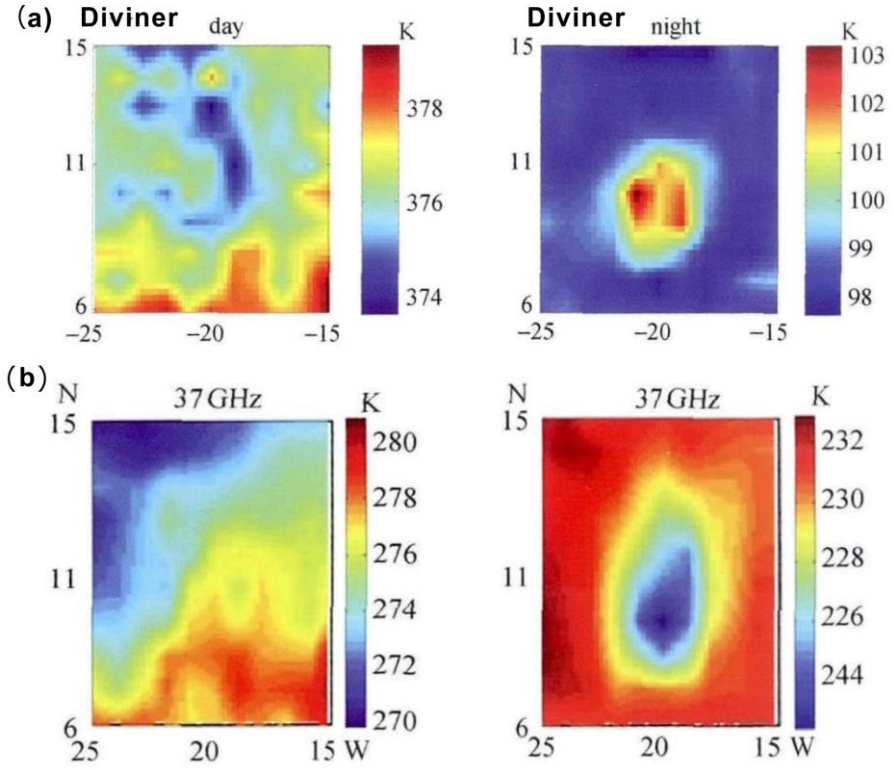

Figure 2.9 Comparison between lunar surface 37 GHz TB from MRM (10-20 cm depth) and infrared temperatures from Diviner (~2 mm depth) in Copernicus crater region during lunar day and night (*Ran et al., 2014*).

Chapter summary:

This chapter discussed a detailed description of the MRM. The main characteristics and uses of the MRM were presented in detail. The initial MRM results were described and analyzed.

Chapter 3. Numerical Model of Lunar Regolith and Lunar Soil: Thermal Environment Simulations

3.1. Chapter Introduction

Chapter 2 provided an overview of the MRM instrument. Modelling is required to understand the physics of the MRM data set, to extract information of the lunar heat flow, and to answer the Oceanus Procellarum question in chapter 1.

Given that, to a first order at least, the MRM instruments are measuring the thermal-physical properties of the lunar regolith it is important to define the controlling physical parameters such as density, permittivity and specific heat capacity as well as the sources of input energy. By combining these sources of information it is then possible to start modelling the expected lunar sub-surface temperature structure using thermal transfer models appropriate for the analysis of microwave remote sensing data.

3.2. Bulk Density

The depth profile of the lunar surface and subsurface can be divided into three parts (*Lunar Sourcebook, 1991*) (Figure 3.1):

1. A 2 cm dust layer on the surface;

2. A 5 to 10 m soil layer just below the dust layer;
3. A thick lunar bedrock layer below the soil layer (*Fa et al., 2009*);

The top two parts of the lunar regolith are referred to as the upper lunar regolith.

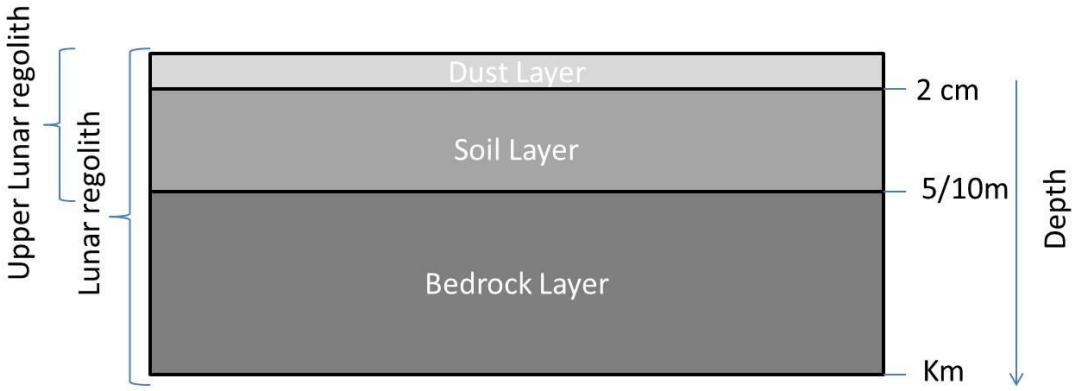

Figure 3.1. Depth profile of the lunar surface and subsurface.

Due to the lack of atmosphere and erosion processes on the lunar surface, individual grains that make up the upper lunar regolith layers have a 'pointy' structure. This combined with the low gravity of the Moon (1/6 that of Earth's) results in the upper lunar regolith layers being highly porous with large spaces between individual grains. The bulk densities of the upper lunar regolith layers are defined as the mass per unit volume of the lunar regolith including these spaces.

Vasavada et al. *(1999)* assumed that the bulk density of the top 2 cm lunar dust layer is 1.3 g/cm^3, and of lunar soil layer is 1.6-2.1 g/cm^3 *(Lunar Source Book, 1991)*. The relationship of the lunar soil layer bulk density profile with depth can be described as follows *(Lunar Sourcebook, 1991)*:

$$\rho = 1.92 \frac{z + 12.2}{z + 18} \qquad \text{(Eq. 3.1)}$$

where z is the lunar regolith depth, in centimetres.

Measurements of the Apollo core samples show that the average density of the upper lunar regolith layer increases with depth, as shown in Figure 3.2 *(Cartier et al., 1973)*. Knowledge of the density profile allows the study of another important factor, the dielectric permittivity.

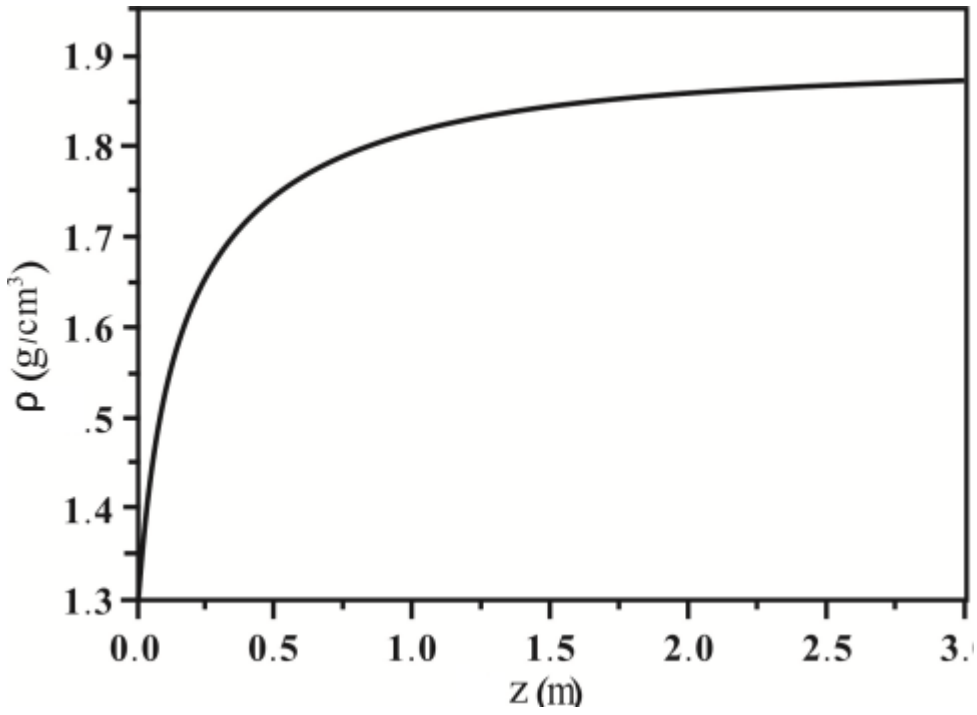

Figure 3.2. Density variation against depth (z) based on measured Apollo core samples.

3.3. Dielectric Permittivity

The dielectric permittivity constant is important for modelling the MRM data because it determines from what depth the received radiance was emitted (see Figure 2.6 and

2.7 in chapter 2,). The results of measurements on lunar samples from the Apollo and Luna missions *(Lunar Sourcebook, 1991)* show that when the frequency is greater than 1 MHz, the real part of the permittivity (dielectric constant) of the lunar regolith is dependent on the density of the lunar regolith assuming a nominal chemical composition *(Lunar Sourcebook, 1991).* Hence the permittivity $\varepsilon_r^{'}$ can be estimated using an empirical relationship:

$$\varepsilon_r^{'} = 1.919^{\rho} \qquad \text{(Eq. 3.2)}$$

The imaginary part $\varepsilon_r^{''}$ of permittivity of the lunar soil is the product of the real part of the permittivity and the loss angle tangent[2] of lunar soil (*Lunar Sourcebook, 1991; Olhoeft and Strangway, 1975*) ,

$$\varepsilon_r^{''} = \varepsilon_r^{'} \times \tan\delta \qquad \text{(Eq. 3.3)}$$

Where tanδ is the dielectric loss angle tangent of the lunar soil.

The current well-accepted theory *(Olhoeft and Strangway, 1975)* is that the loss tangent is not only a function of the density of the lunar soil, but also related to the TiO_2 and FeO abundance (expressed by S). This can be modelled using a three-dimensional regression equation, which was derived from the lunar soil samples *(Olhoeft and Strangway, 1975)*

$$\tan\delta = 10^{0.038\cdot(\%TiO2+\%FeO)+0.312\rho-3.260} \qquad \text{(Eq. 3.4)}$$

Where $\%TiO_2$ and %FeO are the TiO_2 and FeO abundances in the lunar soil, respectively.

[2]Dielectric loss angle tangent: Dielectric loss measures a dielectric material's inherent dissipation of electromagnetic energy into heat, usually parameterized in loss angle tangent tanδ.

We define S as the sum of TiO_2 and FeO content present in the minerals found in the lunar soil. Figure 3.3 below shows the relationship between S, lunar regolith depth, and the imaginary part of the dielectric constant.

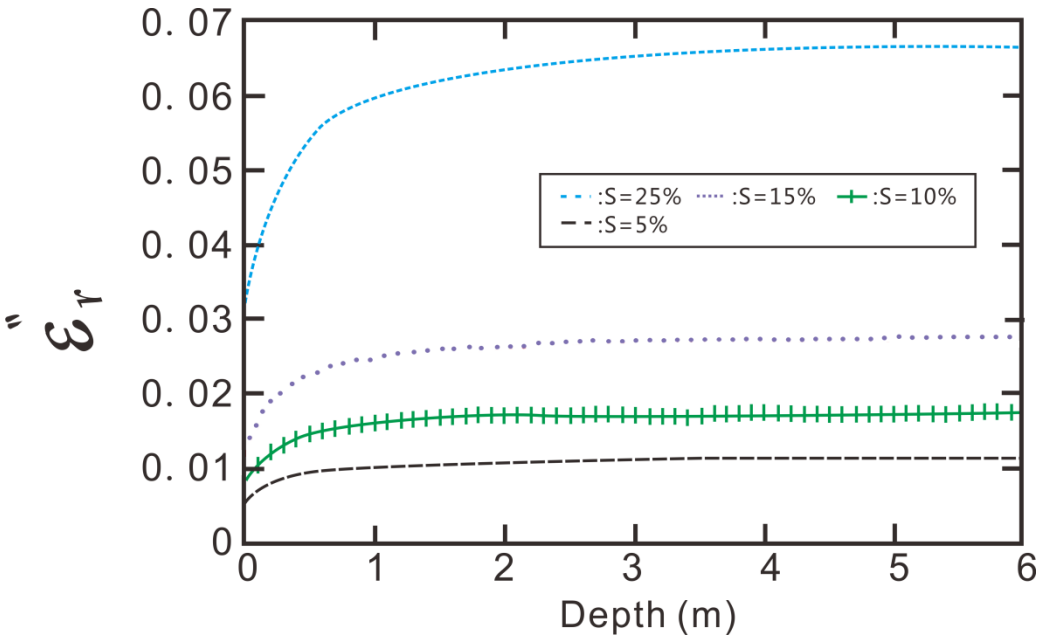

Figure 3.3. The imaginary part of the dielectric constant increases with lunar soil depth. The imaginary part of the dielectric constant also increases with increasing S value.

3.4. Thermal Conductivity

According to *the Lunar Source Book (1991)*, the upper 2 cm layer of lunar regolith (dust layer) has an extremely low thermal conductivity (1.5×10^{-5} W/cm^2 measured at the Apollo 15 Landing Site). Below the dust layer the soil layer has a much larger thermal conductivity (7.5×10^{-5} W/cm^2~10.5×10^{-5} W/cm^2). This is because thermal

conductivity is dependent on density and the lunar dust layer has a much lower density of 1.3 g/cm^3, compared to the soil layer density of 2.1 g/cm^3. The variation with depth of thermal conductivity of the lunar soil can be expressed as (*Mitchell and de Pater, 1994*),

$$k = k_c[1+\chi(\frac{T}{T_{350}})^3] \qquad \text{(Eq. 3.5)}$$

Where k_c is the phonon conductivity, χ is the ratio of "radiative conductivity" to phonon conductivity at 350 K, T is subsurface temperature in kelvin, T_{350} is 350 K. Vasavada et al. *(1999)* gave the coefficients of k_c and χ for lunar dust and soil layers as: k_c=9.22×10^{-4} W m^{-1} K^{-1}, χ=1.48 for the dust layer, and k_c=9.3×10^{-3} W m^{-1} K^{-1}, χ=0.073 for the soil layers.

3.5. Specific Heat Capacity

After parametrising the thermal conductivity, a parametrisation for the specific heat capacity was explored. Horai et al. *(1971)* found that the specific heat (C) of the lunar regolith varies with temperature. Later Jones et al. *(1975)* provided an empirical third-degree polynomial formula (determined by the least-squares technique based upon Apollo 11 regolith sample data) that determined its dependence on temperature (70-400 K):

$$C(T) = c_1T^3 + c_2T^2 + c_3T + c_4 \qquad \text{(Eq. 3.6)}$$

Where C is in units of J·g^{-1}K^{-1}. Urquhart et al. *(Urquhart and Jacksky, 1997)* found that c_1=5.19×10^{-9} J·g^{-1}K^{-4}, c_2=−8.20×10^{-6} J·g^{-1}K^{-3}, c_3=4.98×10^{-3} J·g^{-1}K^{-2},

c_4=−15.48×10^{-2} J·g^{-1}K^{-1}. A plot showing variation of specific heat capacity with temperature is shown in Figure 3.4.

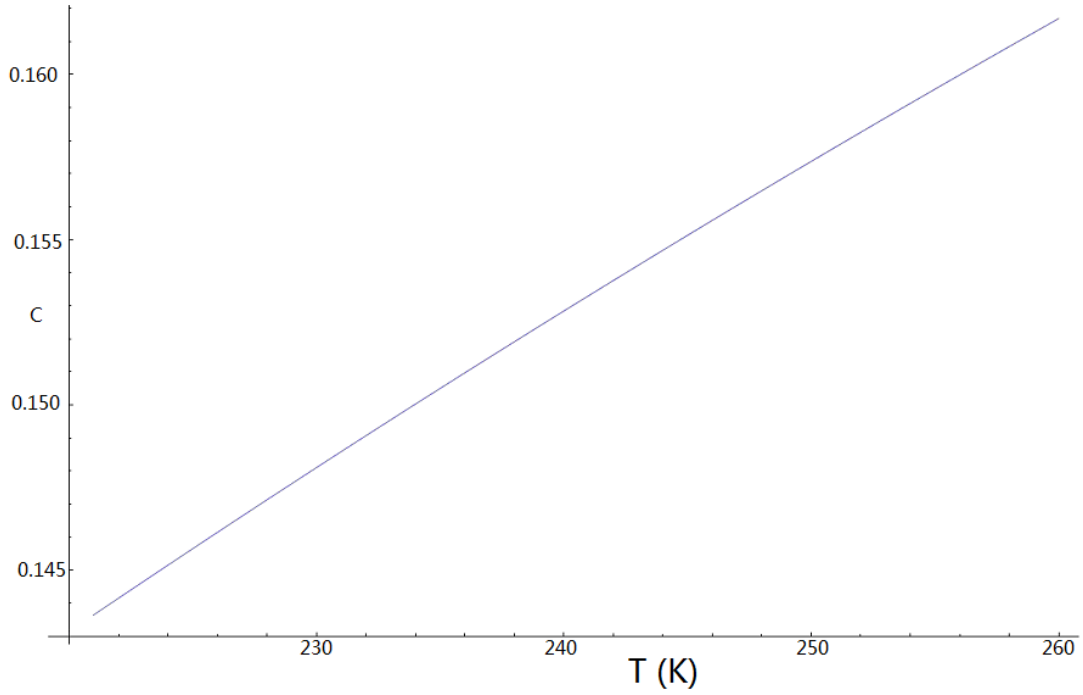

Figure 3.4. Variation of specific heat capacity with temperature.

3.6. Lunar Subsurface Temperature Latitudinal Distribution

The previous sections outlined the parameters that are keys to the modelling of energy transfer through the lunar regolith by thermal radiation and thermal conduction. Of similar importance is an estimate of the subsurface temperature variation with latitude, due to variations in solar insolation.

There have been several attempts to provide a semi-empirical model of the latitudinal

temperature profile but there is not a conclusive model that is in good agreement with remotely sensed data yet (*Li et al, 2009*). Therefore this thesis will list such models and construct a new thermal model which is then used to compare with MRM results later in chapter 6. The models described in this section are *(Keihm et al, 1973)* and *(Li et al, 2009).*

A theoretical model was built by Keihm *(Keihm et al, 1973; Keihm and Langseth, 1973, 1976)* to the simulate lunar subsurface temperature at different latitudes, which can be fitted as:

$$T(z)=\begin{cases} T_0 - g\cdot z, & z < 2\ cm \\ ([T(d_{dust})-T_2]e^{-\beta z}+T_2), & 2\ cm < z < 50\ cm \\ T_2, & z > 50\ cm \end{cases} \qquad \text{(Eq. 3.7)}$$

where T_0 is the surface temperature; g is the temperature gradient; T_2 is the temperature at regolith depth below 50 cm; β = 0.1; d_{dust} is the thickness of the dust layer. In *Keihm et al, (1973), Keihm and Langseth, (1973, 1976), g*=50, T_2 has been calculated by Li et al *(Li et al, 2009)*, and T_0 can be obtained by the heat conduction equation:

$$\frac{\partial}{\partial z}[k(z,T)\frac{\partial T}{\partial z}]+Q(z,T)=\rho(z,T)c(z,T)\frac{\partial T}{\partial t} \qquad \text{(Eq. 3.8)}$$

where $\rho(z,T)$, $c(z,T)$, $k(z,T)$ are bulk density, specific heat, and heat conductivity at temperature T and depth z, respectively. $Q(z,T)$ is the constant flux originating from internal heat sources, which *Keihm* states is negligible for radioactive heat flow. This models prediction of yearly mean surface and subsurface temperatures at different

latitudes is shown in Figure 3.5.

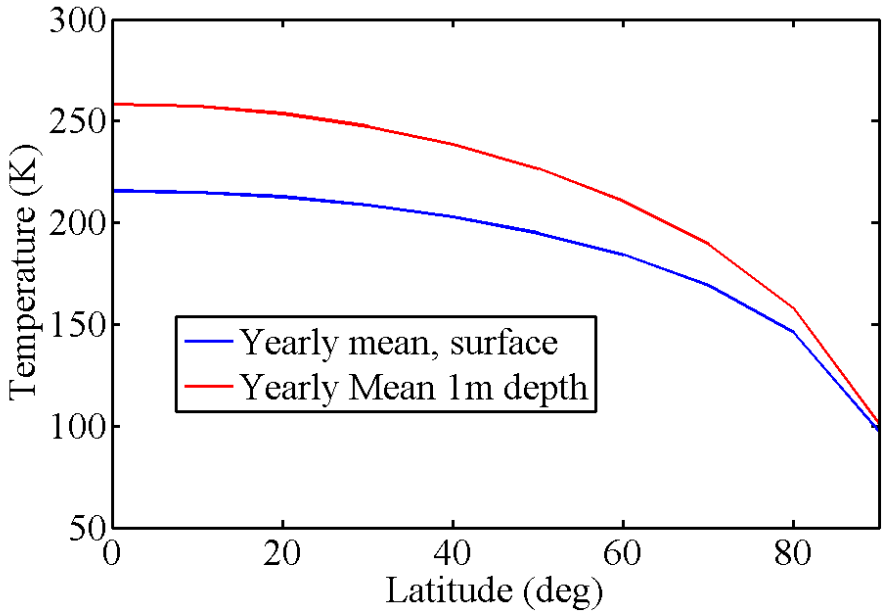

Figure 3.5.Predicted yearly mean surface and 1 m subsurface temperatures from Keihm's model.

The second model considered in this section is Li et al *(2009)*. Li et al *(2009)* ignores the lunar sub-surface heat flow's contribution, and suggests that the lunar soil's bedrock temperature (defined in this model as 2-6 m deep) is determined by solar radiation as a function of latitude using the expression below (Figure 3.6).

$$T_{bottom} = -5.48e^{-8}\varphi^5 + 8.52e^{-6}\varphi^4 - 5.17e^{-4}\varphi^3 + 0.0029\varphi^2 - 0.128\varphi + 240$$

(Eq. 3.9)

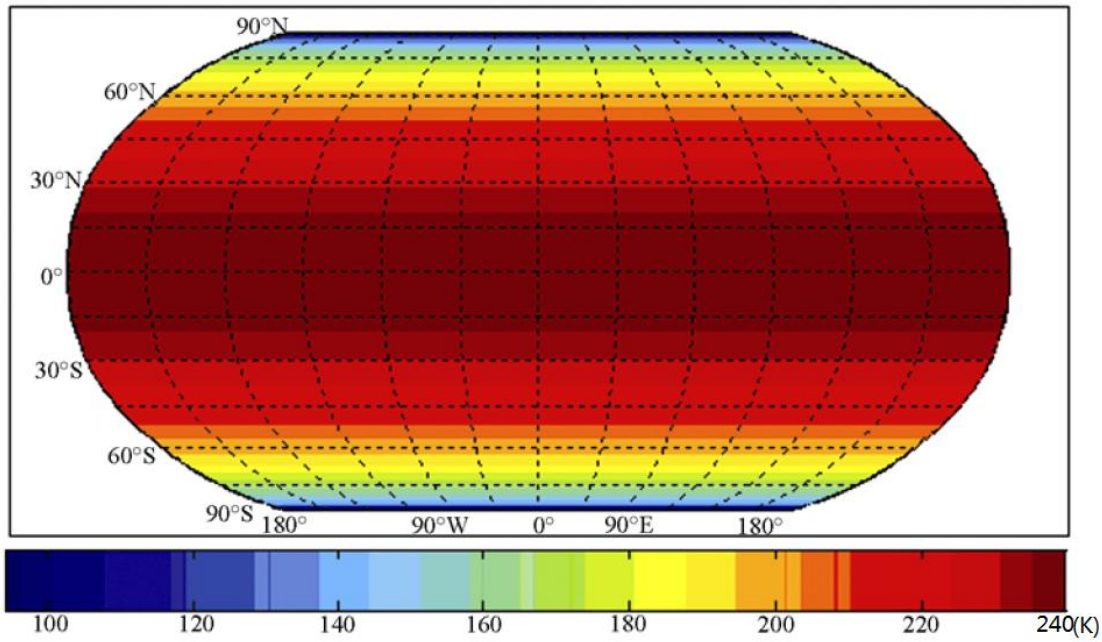

Figure 3.6. The 2-6 m depth temperature distribution simulation results from *Li et al (2009)* model.

Although semi-empirical, both models above provide a baseline for comparison with later results derived from the Chang'E MRM datasets.

3.7. Vertical Distribution of Lunar Subsurface Temperature as the First Estimate

3.7.1 Previous Thermal Diffusion Modelling Work

There is currently no conclusive data on the Moon's vertical temperature distribution. The sub-surface heat flow has been measured at only two landing sites (Apollo 15 and Apollo 17) and these results show that the temperature fluctuations due to the diurnal wave decrease with depth until at about ~0.8 m below the lunar surface where

they become negligible (*Lunar sourcebook, 1991; Horai et al., 1971*). For example, Figure 3.7 shows the simulated regolith temperature profile at the Apollo 15 landing site at different local times of day using the thermal diffusion model from *Vasavada et al. (1999)*.

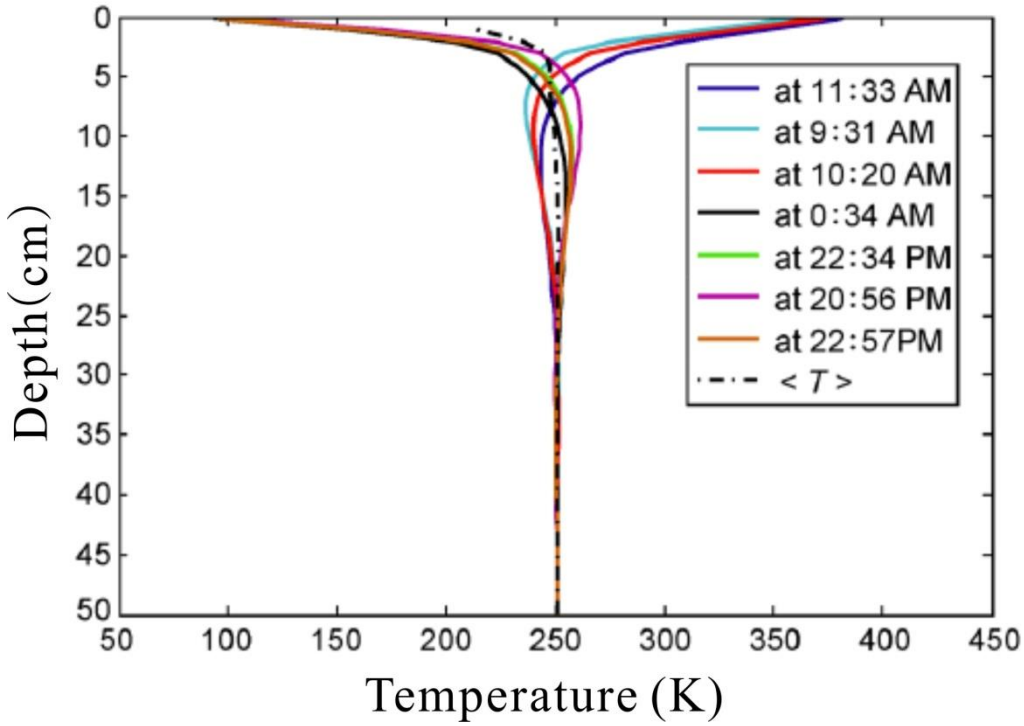

Figure 3.7. Regolith temperature profile of Apollo 15 area at different lunar local time (*Vasavada et al., 1999*). After 20 cm depth, the subsurface temperatures no longer have significant diurnal changes.

One dimensional thermal diffusion models such as *Vasavada et al., (1999*) predict the surface and subsurface profile of the lunar soil. The predicted surface and subsurface temperature structure can then be used in a microwave radiative transfer forward model to predict the TB observed by the MRM instrument (Figure 3.8).

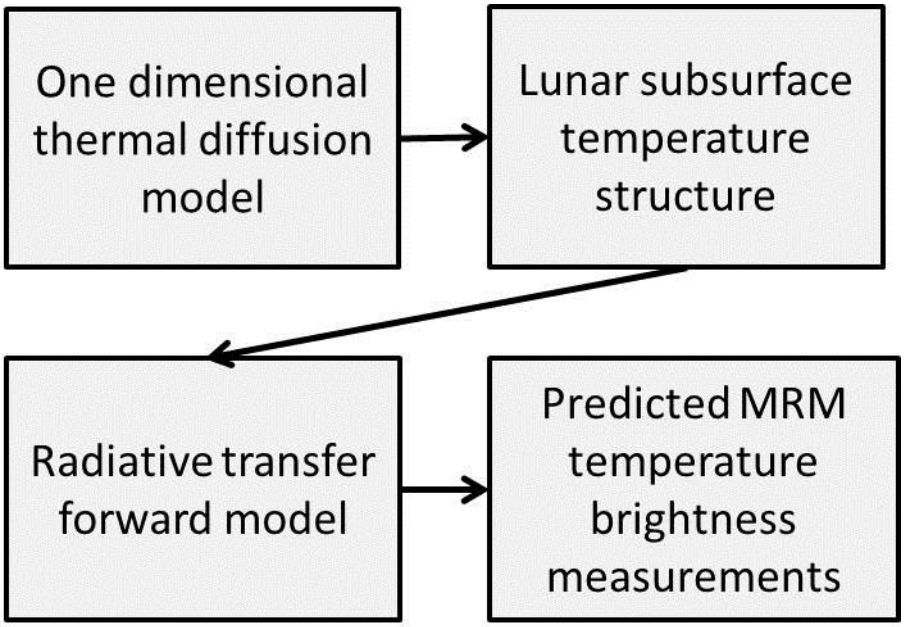

Figure 3.8. Model flow and clarification: a thermal diffusion model is used to describe subsurface temperature structure. This is then used in a radiative transfer model to predict brightness temperatures.

Microwave radiative transfer in lunar surface layers can generally be modelled with the use of multilayer models (*Fung et al., 2006*). Fa and Jin (*2006*) proposed a two-layer model composed of a lunar regolith layer and an underlying bedrock layer. Fa and Jin (*2007*) also developed a three-layer model, which includes a top dust layer, a soil layer, and an underlying bedrock layer. In both models it is assumed that the vertical temperature distribution in the same layer is homogeneous and the dielectric permittivity is constant. Both models then use the strong fluctuation random medium theory to calculate the subsurface TB of each layer. Lan and Zhang (*2004*), Meng (*2008*), and Vasavada et al. (*1999*) also used two-layer models and combined them with ground-based radar data of the lunar poles to derive the upper lunar regolith thickness.

The two-layer and three-layer models are simple stratifications of important parameters (e.g. density, permittivity, and conductivity) that affect the TB. However, such simplified stratification can also cause problems. For example, the Vasavada et al *(1999)* two layer model predicts larger temperature values during the daytime for areas with a large lunar regolith thickness (e.g. 2 m or more) than the temperature values measured by the Diviner radiometer, whereas the model simulated temperatures at night-time is predicted to be smaller than the actual temperatures measured by Diviner *(Bandfield et al, 2011)*. There is trade off with the number of layers in the model and the accuracy of the model. The larger the number of the layers, the longer the computational time of the model, but the greater the potential accuracy.

For a thermal microwave emission model the dielectric profile of the upper lunar regolith is very important as it changes the amount of microwave radiation adsorbed. The dielectric constant is dependent on the density of the lunar soil which changes rapidly in the lunar soil layer with depth (see section 3.3). It is therefore important to have enough layers in a thermal microwave emission model to capture this change in the dielectric constant. In the two-layer models (*Fa and Jin, 2006; Lan and Zhang, 2004; Meng, 2008; Vasavada et al., 1999*), the dielectric properties of the lunar regolith were simplified, with an approximate average dielectric constant, instead of the dielectric profile of the lunar regolith layer. The simulated TB from these two layer models will therefore produce errors due to this over simplification. Therefore,

the dielectric constant should be modeled to a greater accuracy than the reported two- and three-layer models.

Although the three-layer model (*Fa and Jin, 2007*) is an improvement compared with the two-layer model, by considering the density and thermal property differences between top 2 cm dust layer and lunar soil beneath it, the three-layer model is still too simple to simulate the parameters affecting TB as shown in Figure 3.9.

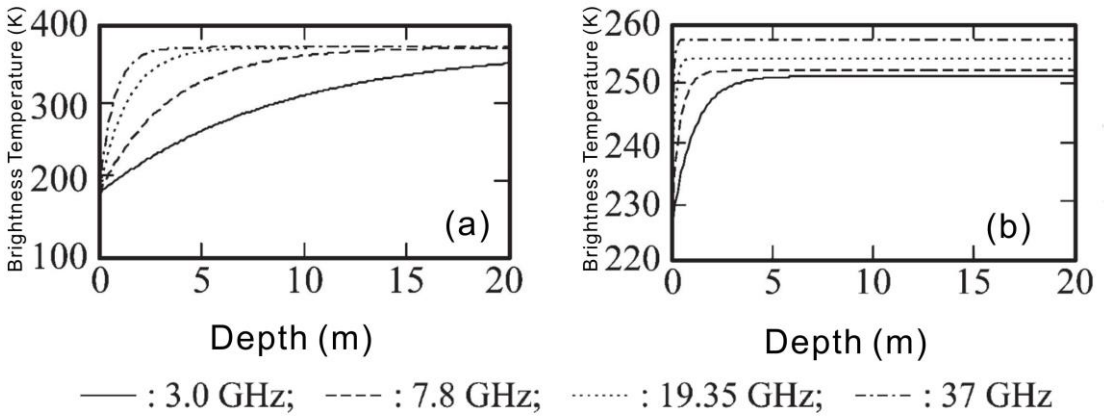

Figure 3.9 The midday TB at the equatorial regions (Note: as previously defined, TB is not the real surface temperature), as simulated on the basis of the (a) two-layer (*Vasavada et al., 1999*) and (b) three-layer (*Fa and Jin, 2006*) models, respectively. Curves are derived on the basis of layers setup in Vasavada et al. (*1999*) and Fa and Jin (*2006*), as Vasavada et al. (*1999*) itself is a thermal diffusion model which did not predict TB. Both models are theoretical calculations, which do not involve real MRM data.

Figure 3.9 shows that the TB simulated by the three-layer and the two-layer models are remarkably different, in the two-layer model TB changes do not change rapidly

enough in the top 50 cm of the lunar surface when compared to data from the Apollo heat flow experiments. Even after a depth of 20 metres the TB is still changing which is not supported by lunar soil lab simulation experiments (*Zhang et al., 2009*).

Theoretical and simulation results show that the 3-layer model error (deviation with in situ measurements and observations) is smaller than that of the simple 2-layer model, and therefore has better stability (e.g., smaller differences between simulated 1 m depth temperature at day and night). Clearly with a larger number of layers the model has better accuracy, however, at a cost of greater computational time and more unconstrained parameters.

A detailed multi-layer model can more accurately reflect the change in the parameters with depth (e.g., density, permittivity, conductivity) and obtain good results. However, the computing complexity will increase proportional to the number of layers, which will complicate the inversion of lunar subsurface temperature. Therefore, we should consider the instrument details and number of available microwave channels to make a compromise before the construction of a model.

3.7.2. Six-layer Thermal Diffusion Simulation Model

In this work, a one-dimensional (1-D) thermophysical six-layer model was used based on both lunar soil properties (section 3.2–3.6) and the measurements of the MRM

instruments. All four MRM channels should be included to invert the MRM data effectively, and therefore this model should be a multilayer model (assuming that each channel has a different maximum penetration depth). However, a trade off exists with complexity. Hence, a total of six layers are considered in the model, as follows: the top 2 cm lunar dust layer, followed by four layers between 2 cm -5 m (with a greater number of layers in the top 20 cm where the temperature changes most rapidly) and a deepest layer at 5 m (bedrock layer). The depth of the four layers between 2 cm -5 m was set by taking into account the predicted penetration depth of each of the four MRM channels using a nominal lunar soil composition. Hence the following stratification was used:

$$Zarr = \begin{cases} 2, \ lunar\ dust\ d_1 \\ 3, \ lunar\ soil\ d_2 \\ 5, \ lunar\ soil\ d_3 \\ 10, \ lunar\ soil\ d_4 \\ 480, \ lunar\ soil\ d_5 \\ Infinity, \ lunar\ regolith\ d_6 \end{cases} \quad \text{(Eq. 3.10)}$$

In the model, *Zarr* is the array of depths from the surface to the base of each layer (not layer thicknesses) in centimetres, and *z* is the symbol representing depth in this work. An illustration is plotted in Figure 3.10.

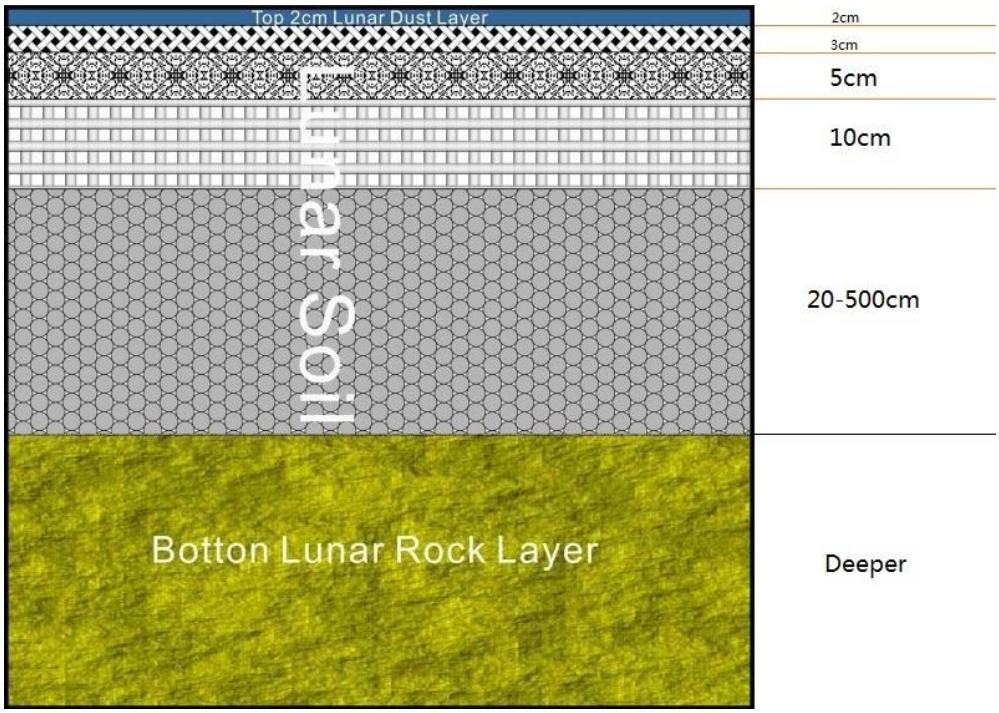

Figure 3.10 Lunar soil layers for the thermal simulation model (which will also be used in the microwave radiative transfer model, section 4.3).

Prior to constructing the forward model, a calculation of the vertical temperature distribution was made to test this six layer stratification. The calculation, which is mainly based on the code described by Spencer et al. (*1989*), is a 1-D numerical thermal model written in IDL. The code calculates the surface and subsurface temperatures on a rotating body as a function of local time. Documentation of the basic model can be found in Spencer et al. (*1989*) and is subsequently referred to as the 'Spencer' code in this work.

The Spencer code is based on an equilibrium model (EQM). Spencer et al. (*1989*) suggested the following:

1. A set of standard thermal model equations

$$\begin{cases} \eta\varepsilon\sigma T_{SS}^4 = (1-A)S_1 / R^2 \\ T = T_{SS}\cos^{1/4}\varphi, \quad \varphi \le \pi/2 \\ T = 0, \qquad\quad \varphi \le \pi/2 \end{cases} \qquad \text{(Eq. 3.11)}$$

where T is the temperature, φ is the latitude, ε is the bolometric emissivity, σ is the Boltzmann's constant, η is an empirical beaming factor, A is the bolometric albedo, S is the solar constant at 1 AU, and R is the heliocentric distance in AU.

2. The model obtains the temperature T as a function of depth below the surface z and time t by numerically solving the 1-D thermal conductive heat flow equation, as follows:

$$\rho c \frac{\partial T(z,t)}{\partial t} = \frac{\partial}{\partial z}\left[k \frac{\partial T(z,t)}{\partial t} \right] \qquad \text{(Eq. 3.12)}$$

where ρ is the density, c is specific heat capacity, and k is the thermal conductivity.

Spencers original use for the model was rapidly rotating asteroids, so for this calculation the parameters were adapted for the Moon. The equation is evaluated over the z interval from 0, at the surface, to some depth d. Setting: the albedo to a lunar value of 0.14 (*Spencer et al., 1989*), the emissivity to a lunar value of 0.94 (*Spencer et al., 1989*), the time increments to ~ 250 s, the number of runs for energy balance to 50 (after 50 runs the results are almost identical - <1% difference), and the distance to the sun to 1 AU, the following temperature profile was obtained (Figure 3.11).

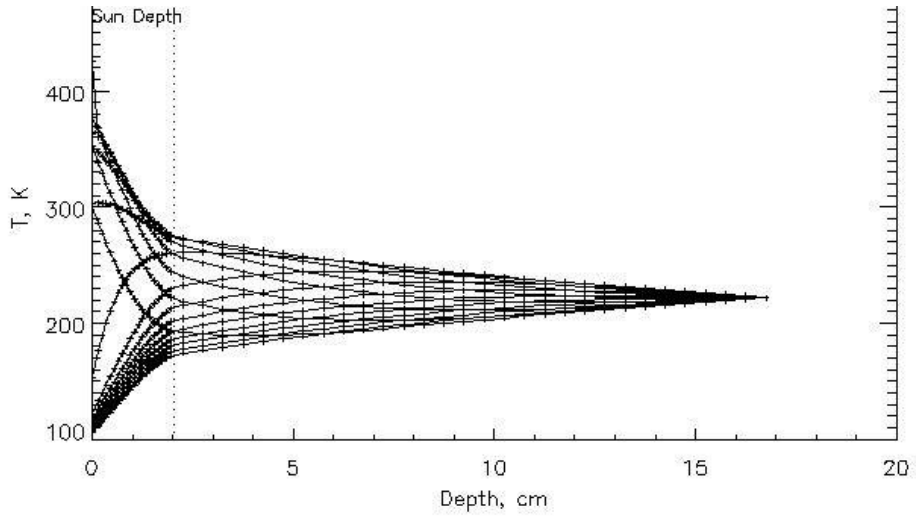

Figure 3.11 Calculated depth profile of mean temperature at various local times (from midday to midnight). Heat conductivity k values from section 3.4 were used.

Figure 3.11 shows that the lunar surface temperature around the equator varies significantly in the upper 17 cm. At the surface the hottest temperature can reach up to 380 K during lunar daytime, while the coldest can be 100 K during lunar nights. This compares well with the Diviner observations of lunar surface *(Paige et al, 2010)*. Diviner measures the maximum temperature at equatorial regions as 380 K and the minimum temperature was found to be 100 K. This calculation did not involve lunar interior heat and solar radiation was considered as the only heat source, which shall be challenged in chapters 7–9. This simplified simulation will also be compared with the later MRM inversion result in chapter 6.

Chapter Summary:

This chapter is divided into two parts.

The first part (section 3.1-3.6) mainly presented models for parameters that affect MRM TB measurements. These parameters included density, dielectric permittivity constants, thermal conductivity, specific heat, temperature latitudinal distribution, and vertical distribution.

The second part (section 3.7) describes different multilayer one dimensional thermal diffusion models of the lunar subsurface. The trade-off between the number of required layers and the accuracy of the model is discussed. A six layer thermal diffusion model was developed which will be used later in the radiative transfer forward model and the inverse scheme. The choice of a six-layer stratification was explained. To test the accuracy of the stratification a subsurface thermal diffusion model from the Spencer code was developed and compared to Diviner measurements. Such six-layer stratification will also be used in the microwave radiative transfer model in the next chapter.

Chapter 4. Subsurface Microwave Radiative Transfer Forward Model

4.1. Chapter Introduction

Although some preliminary results were derived in chapter 2, these only represent a qualitative first order analysis of the Chang'E MRM data, for lunar subsurface temperature sounding. To exploit fully the measurements made by the MRM instrument and future microwave radiometers, the establishment of a lunar regolith microwave radiative transfer forward model is required. This will allow quantitative insights into the subsurface temperature and compositional structure to be included when interpreting the MRM data. In turn, this is the key to exploiting the information on subsurface heat flow and its possible connection to the large-scale evolution of the lunar curst.

By considering the main factors affecting the measured brightness temperature with depth within the lunar regolith, I have developed a non-uniform multi-layer lunar soil radiative transfer model. This new model is entirely different to the models of Spencer et al. *(Spencer et al., 1989)* or Vasavada et al. *(Vasavada et al., 1999)*, because it is not an energy balance (thermal diffusion) model, but a microwave radiative transfer model using input data from the MRM measurements, effectively modelling the global subsurface radiative transfer for the time of the remote sensing

observation. According to microwave radiative transfer theory *(Jin et al 1998; Ulaby, 1981)*, the Chang'E MRM measurements of the lunar regolith contain TB contributions from different layers within a certain depth of the subsurface. Physical properties of different depths of lunar soil, such as different temperature, dielectric constant, density, thermal conductivity and specific heat parameters, will be reflected in the microwave radiation transport model and thus the TB measured by the instrument.

The radiative transfer forward model is used to calculate contributions from different depths to the TB measured by the MRM radiometer's four channels. This can then be compared with other models and methods such as *Keihm's model (1973)* or *Spencer (1989)*, assuming a known vertical temperature distribution. Furthermore, to try and understand if there is correlation with the Fe/Ti content and the effective emission depth for the different MRM channels a sequence of more complex models investigating radiative and conductive heating measured by each of the MRM channels has been developed.

4.2. Radiative Transfer Forward Model Derivation

The first step in developing the thermal transfer model is determining the contributions from each layer to the subsurface microwave propagation that is then

received by the instrument. In this initial analysis a six layer model has been used for the reasons outlined in section 3.7.

The rationale for using a total of six layers is described in chapter 3, but to a first order is due to the number of available channels (4) of MRM data, assuming each channel is sounding to a different depth (section 2.2.2). The number of required layers is equal to the number of channels plus a top layer and a bottom layer. The top layer is constrained by the surface temperature data from the Diviner instrument on the Lunar Reconnaissance Orbiter *(Paige et al., 2010)* (i.e. layer 1), the four MRM channels potentially provide measurements at four different depths (i.e. layers 2-5) and the bedrock temperature can be considered as a constant (i.e. layer 6). This allows the number of unknowns to equal the number of equations, making the problem pseudo-exact due to the presence of measurement and modelling error.

Existing microwave propagation models developed for the Earth's subsurface are not appropriate. The microwave propagation in the Earth's subsurface is heavily attenuated by the presence of moisture *(Jin et al., 1998; Zhang et al., 2008)* so existing terrestrial models are not applicable for the analysis of data from desiccated airless bodies such as the Moon. Therefore I have constructed my own model using underlying principles of microwave radiative transfer theory. This approach will be

summarised below, with references to the individual model components cited as required unless it is an original derivation.

4.2.1 Attenuation of Microwaves through Particulate Media: Quantitative Derivation and Analysis

Any substance with a temperature above absolute zero has a large number of charged particles that constantly collide with one another, causing the charged particles to be in a state of motion. Such changes in motion (i.e. acceleration) generate electromagnetic radiation, and different frequencies of non-correlated wave components constitute emission of electromagnetic wave radiation. In electromagnetic terminology, the frequency range from 1000 MHz to 300 GHz is called microwave radiation (this will be Planck radiation modified by the material if it is not transparent to its own radiation).

A microwave radiometer is a high-sensitivity receiver designed to receive and record low emission random microwave noise[3] radiation from a material. Objects in thermodynamic equilibrium have an emission power (in radio frequency microwave language this is referred to as the transmission power) P, which is a function of their

[3] 'Noise' in this case implies that the radiation is not coherent, in contrast, for example, to a microwave receiver as used in communications or similar.

physical temperature *T*. In the microwave range, *P* is proportional to *T* (the long-wave limit of the Planck function) *(Ulaby et al., 1981)*. This is expressed as

$$P = \sigma e T \Delta \nu \qquad \text{(Eq.4.1)}$$

Where σ is the Boltzmann constant, *T* is the thermodynamic temperature of the object, *e* is the emissivity of the material, and $\Delta\nu$ is the radiometer bandwidth. This relationship between power and temperature defines the brightness temperature (T_B), which is characterised by the power received in a real scene:

$$T_B = eT = \frac{P}{\sigma \Delta \nu} \qquad \text{(Eq.4.2)}$$

Since *e* (the emissivity of the material) is dependent on the dielectric constant, it also is dependent on density and elemental composition etc. The observed microwave TB is thus dependent on these characteristics (e.g. density, elemental composition etc), therefore we could, in principle, derive these lunar subsurface parameters, based on the MRM remote measurements of the lunar surface brightness temperature using this Eq. 4.2.

Figure 4.1 is a schematic diagram of the microwave radiation from a typical three-layer lunar regolith and bedrock structure (after *Li et al., 2009*). In addition to the microwaves being attenuated by the medium during their propagation through the lunar surface, they will also be affected by changes in the medium. For example, if the lunar regolith comprises three layers with different dielectric properties and

temperatures (T0, T1, T2, T3), then the emitted microwave radiation from each layer will be affected by reflection and transmission at every interface.

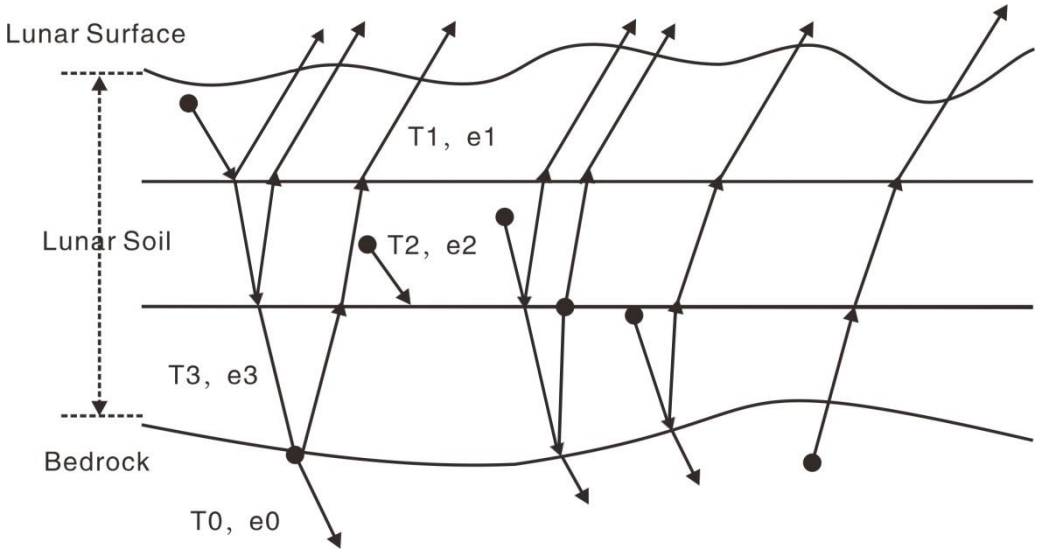

Figure 4.1. Schematic diagram of microwave radiation emitted from a three-layer lunar regolith and bedrock structure. The T_B received by the MRM contains direct emission from each layer, as well as reflected beams at layer interfaces, although multiple reflections will not be considered in this model.

The total amount of radiation received by the microwave detector from the lunar surface is expressed by (*Ulaby et al., 1981*) as Eq. 4.3

$$T_B = T_S e_s = T_s(1-r_s) \qquad \text{(Eq.4.3)}$$

Where *Ts* is the thermodynamic temperature of the surface, e_s is the emissivity of the surface, and r_s is the surface reflectivity. r_s can be calculated according to Fresnel's Law of reflection,

$$r_s = \left| \frac{\varepsilon_{rs}\cos\theta - \sqrt{\varepsilon_{rs} - \sin^2\theta}}{\varepsilon_{rs}\cos\theta + \sqrt{\varepsilon_{rs} - \sin^2\theta}} \right|^2 \qquad \text{(Eq.4.4)}$$

where ε_{rs} is the relative permittivity of the surface.

In the case of normal incidence, the reflectivity then becomes

$$r_s = \left| \frac{1 - \sqrt{\varepsilon_{rs}}}{1 + \sqrt{\varepsilon_{rs}}} \right|^2 \qquad \text{(Eq. 4.5)}$$

The subsurface temperature profile is given by $T(z)$, the absorption coefficient profile is $\alpha(z)$ and permittivity profile is $\varepsilon(z)$, all are functions of the depth z. The depth profile of the layer dielectric constant $\varepsilon(z)$ is given by *Tsang et al. (1975)* and the absorption coefficient profile of the electric field intensity $\alpha(z)$ is expressed as

$$\alpha(z) = \frac{2\pi}{\lambda}\left\{ \frac{\mu_r(z)\varepsilon_r'(z)}{2}\left[\sqrt{1 + \left(\frac{\varepsilon_r''(z)}{\varepsilon_r'(z)} \right)^2} - 1 \right] \right\}^{1/2} \qquad \text{(Eq. 4.6)}$$

Where λ is wavelength, ε_r' is the real part of the relative permittivity while ε_r'' is the imaginary part, μ_r is the real part of the magnetic permittivity. The power absorption coefficient $\kappa(z)$ is twice that of $\alpha(z)$, as expressed by

$$\kappa(z) = 2\alpha(z) \qquad \text{(Eq. 4.7)}$$

where the $\kappa(z)$ and $\alpha(z)$ units are both in nepers (Np) per metre (neper is defined as 1 Np/m=8.686dB/m). If the dielectric of each layer is the same and $\mu_r(z)$=1, then the absorption coefficient $k(z)$ can be expressed as

$$\kappa(z) = 2\,\mathrm{Im}\left\{ \frac{2\pi\sqrt{\varepsilon_r(z) - \sin^2\theta}}{\lambda} \right\} \qquad \text{(Eq. 4.8)}$$

We need to define a difference between real temperature, effective temperature and brightness temperature:

1. **Real temperature** is the thermodynamic temperature of the regolith. This is the temperature that would be measured by an in-situ temperature probe. In this model it is assumed that each layer is isothermal at one real temperature.
2. The lunar surface is composed of many different temperatures. i.e. across a horizontal 2 cm space on the lunar surface the temperature can vary by up to 100 K. As seen in section 3.7 the temperature in the subsurface of the moon can vary by 150 K to depths of 5 m. The MRM instrument can sound to depths of 5 m and its footprint is 18 km at its best resolution, so contains a scene composed of many different temperatures, both vertically and horizontally. The **effective temperature** can be thought of as the average temperature in such a scene.
3. **Brightness temperature** is the effective temperature multiplied by the effective emissivity of the lunar regolith as measured by a microwave radiometer.

The model calculates the real temperatures of each layer. The real temperature from each layer is then multiplied by a weighting which is the power coefficient and the exponential of the negative power coefficient (Eq. 4.9). The real temperature multiplied by the weighing coefficient for each layer is then added together to give the effective temperature (Eq. 4.9). This effective temperature is then multiplied by

the effective emissivity to give the TB that is measured by the MRM instrument. Then Eq. 4.2 transforms into Eq. 4.9,

$$T_B = eT = e_{eff} T_{eff} = e_{eff} \int_{-\infty}^{0} T(z)\kappa(z)e^{-\kappa(z)}dz \qquad \text{(Eq. 4.9)}$$

Where T_{eff} is the effective temperature, e_{eff} is the effective emissivity and represents the ratio of T_{eff} to the T_B measured by MRM. Here the $\kappa(z)e^{-\kappa(z)}$ weighting term comes from the derivative of $exp(-\kappa(z))$.

Microwave radiation in the media can be simulated using two methods. The first is the coherent method, based on Maxwell's equations and the fluctuation dissipation theorem (FDT). The coherent method considers the effects of reflection on both the amplitude and phase. The coherent method must be solved using Maxwell's equations to calculate the electromagnetic field vectors and obtain the radiation intensity. This approach requires that the medium is uniform as the scattering within each layer is ignored. The dielectric constant of each layer is also considered to be constant *(Jin et al., 1998).*

The second method is the incoherent approach based on the vector radiative transfer theory, which only considers the amplitude and not the phase. This approach requires a large amount of scattering bodies whose dimensions are comparable to the

wavelength of radiation (*Ulaby, 1981*). The random distribution of such scattering bodies generates random phase functions in wave transmission between two points, thus making the transmission an incoherent process.

Considering the nature of the lunar soil (e.g. the layers are almost level and uniform, and each layer has a constant dielectric constant) and the wavelengths measured by the MRM, the coherent method was chosen for this work. In coherent methods, the microwave radiation of the medium is caused by charged particles' fluctuating in the microscopic scale, that is, the fluctuant electromagnetic radiation. The expected relationship between the value of the electric current source (generated by the movement of charged particles) and TB is described by the fluctuation dissipation theorem (FDT). Details of this theorem are explained in *(Jin et al., 1998)* and are summarized below.

The fluctuation-dissipation theorem relies on the assumption that the response of a system in thermodynamic equilibrium to a small-applied force is the same as its response to a spontaneous fluctuation[4]. Therefore, the theorem connects the linear response relaxation of a system from a prepared non-equilibrium state to its statistical fluctuation properties in equilibrium. According to FDT,

[4] Another example is Einstein's model of Brownian motion, also a use of fluctuation/dissipation theorem and derivation of refractive index.

$$(\bar{J}_l(\bar{r},\omega) * \bar{J}_l(\bar{r}',\omega')) = \frac{4}{\pi}\omega\varepsilon_l''(z)\sigma T_l(z)\cdot\bar{I}\,\delta(\omega-\omega')\delta(r-r') \quad \text{(Eq.4.10)}$$

where $\bar{J}_l(\bar{r},\omega)$ is the heat source of layer l among all N layers, ω is the heat radiation's angular frequency, r is the displacement vector, σ is the Boltzmann constant, and $T_l(z)$ is the real temperature distribution of layer l, $\varepsilon_l''(z)$ is the imaginary part of the permittivity (dielectric constant), the term I in Eq.4.10 is defined as

$$\bar{I} = \hat{x}\hat{x} + \hat{y}\hat{y} + \hat{z}\hat{z} \quad \text{(Eq.4.11)}$$

Therefore, by the definition of TB and Eq.4.9 - 4.11, the polarized radiation TB can be written as Eq.4.12

$$T_B^P(\hat{k},\omega) = \frac{(2\pi)^3}{B}\left(\frac{c}{\omega}\right)\frac{1}{2}c\varepsilon_0\int_0^\infty d\omega'\int_0^\infty k^2 dk\int dk'\times\left\{\hat{p}\cdot\left(\bar{E}(k,\omega)\bar{E}'(k',\omega')\right)\cdot\hat{p}\exp[i(\bar{k}-\bar{k}')\cdot(r-i(\omega-\omega')t)]\right\}$$

(Eq.4.12)

Where $\hat{p}$ is the polarization sense, $\hat{p}=(\hat{v},\hat{h})$, $\hat{h}$ is the horizontal polarization vector, $\hat{v}$ is the vertical polarization vector, c is the light speed, ω is the frequency, r is the distance vector, and ε_0 is the vacuum relativity. Also, by using the parallel-layered media dyadic Green's function *(Jin et al., 1998)* the electric field intensity (E) can be written as:

$$\vec{E}\left(\vec{r},\omega\right) = \sum_{l=1}^{N+1}\int_{-\infty}^{\infty} d\bar{\rho}'\int_{-d_l}^{-d_{l-1}} dz'\bar{\bar{G}}_{0l}\left(\bar{r},\bar{r}'\right)\bullet J_l\left(\bar{r}'\right)\omega' \quad \text{(Eq. 4.13)}$$

In Eq. 4.13, J_l is the heat source, ρ is the x-y plane, $\bar{r} \in$ Region 0; $\acute{\bar{r}} \in$ the l th layer, $-d_l$represents the longitudinal coordinates of the l th layer; $d_{N+1\to\infty}$, dyadic Green function in the region l $\overline{\overline{G_{0l}}}(\bar{r},\acute{\bar{r}})$ can be written as

$$\overline{\overline{G_{0l}}}\left(\bar{r},\bar{r}'\right)=-\frac{\omega\mu}{8\pi^2}\int d\bar{k}\delta\left[k_z-\sqrt{\omega^2\mu\varepsilon_0-k_\rho^2}\right]\frac{1}{k_z}e^{i\bar{k}\bullet\bar{r}}\times$$
$$\left\{h\left(k_z\right)\left[A_l h\left(-k_{lz}\right)e^{-i\bar{k}\bullet\bar{r}}+B_l h\left(k_{lz}\right)e^{-i\bar{k}\bullet\bar{r}}\right]+\hat{v}\left(k_z\right)\left[C_l\hat{v}\left(-k_{lz}\right)e^{-i\bar{k}\bullet\bar{r}}+D_l\hat{v}\left(k_{lz}\right)e^{-i\bar{k}\bullet\bar{r}}\right]\right\}$$

(Eq. 4.14)

Where subscript $0l$ indicates that the observation point $\bar{r}$ is in area 0 and the microwave emission source is located in area l. k_ρ is the wavenumber on the x/y plane, k_x is the wavenumber projected into the x axis and k_y is the wavenumber projected into the y axis, $k_\rho^2=k_x^2+k_y^2$. μ is the vacuum magnetic permittivity; A_l, B_l, C_l, D_l, can be derived by tangential continuous boundary constraints at layer interfaces. For an N-layer unevenly paralleled dissipation medium, when the observation angel is θ, the zero-order p-polarization TB of layered lunar soil medium measured by MRM can be transformed into Eq. 4.15,

$$T_B^p(\theta)=\frac{k_0}{\cos\theta}\sum_{i=1}^{n}\left\{\frac{\varepsilon_{ri}''}{2k_{iz}''}\left|\beta_i^p\right|^2\cdot\left(1-e^{-2k_{iz}''d_i}\right)\cdot\left(1+\left|R_{i(i+1)}^p\right|^2e^{-2k_{iz}''d_i}\right)T_i\prod_{j=0}^{i=1}\left(\left|Q_{j(j+1)}^p\right|^2\cdot\left(e^{-2k_{jz}''d_j}\right)\right)\right\}+$$
$$\frac{k_0\varepsilon_{r(n+1)}''\left|\beta_{n+1}^p\right|^2}{\cos\theta\cdot 2k_{(n+1)z}''}\cdot\prod_{j=0}^{n}\left(\left|Q_{j(j+1)}^p\right|^2\cdot\left(e^{-2k_{jz}''d_j}\right)\right)T_r$$

(Eq.4.15)

Where k is the wavenumber, k_{iz} is the projection on z direction of the i layer's wavenumber. d_i is the thickness of the i layer; T_r is the temperature of the lunar

rock layer, the superscript '' means the imaginary part. The transmission coefficient (Q_{ij}) is

$$Q_{ij} = 1 + R_{ij} \qquad \text{(Eq.4.16)}$$

And the reflection coefficient is

$$R_{ij} = \frac{k_{iz} - k_{jz}}{k_{iz} + k_{jz}} \qquad \text{(Eq.4.17)}$$

Therefore, for a six layer non-uniform parallel layered dissipative media, when the observation angle is zero, as in the CE MRM data, based on Eq. 4.15, the layered medium polarized radiation brightness temperature measured by the microwave radiation detector can be deduced as

$$T_B = \frac{k_0 \varepsilon_1''}{2\varepsilon_0 k_1''} \left|Q_{01}\right|^2 (1 - e^{-2k_1'' d_1})(1 + \left|R_{12}\right|^2 e^{-2k_1'' d_1}) T_1$$

$$+ \frac{k_0 \varepsilon_2''}{2\varepsilon_0 k_2''} \left|Q_{01}Q_{12}\right|^2 (1 - e^{-2k_2'' d_2})(1 + \left|R_{23}\right|^2 e^{-2k_2'' d_2}) e^{-2k_1'' d_1} T_2$$

$$+ \frac{k_0 \varepsilon_3''}{2\varepsilon_0 k_3''} \left|Q_{01}Q_{12}Q_{23}\right|^2 (1 - e^{-2k_3'' d_3})(1 + \left|R_{34}\right|^2 e^{-2k_3'' d_3}) e^{-2k_1'' d_1} e^{-2k_2'' d_2} T_3$$

$$+ \frac{k_0 \varepsilon_4''}{2\varepsilon_0 k_4''} \left|Q_{01}Q_{12}Q_{23}Q_{34}\right|^2 (1 - e^{-2k_4'' d_4})(1 + \left|R_{45}\right|^2 e^{-2k_4'' d_4}) e^{-2k_1'' d_1} e^{-2k_2'' d_2} e^{-2k_3'' d_3} T_4$$

$$+ \frac{k_0 \varepsilon_5''}{2\varepsilon_0 k_5''} \left|Q_{01}Q_{12}Q_{23}Q_{34}Q_{45}\right|^2 (1 - e^{-2k_5'' d_5})(1 + \left|R_{56}\right|^2 e^{-2k_5'' d_5}) e^{-2k_1'' d_1} e^{-2k_2'' d_2} e^{-2k_3'' d_3} e^{-2k_4'' d_4} T_5$$

$$+ \frac{k_0 \varepsilon_6''}{2\varepsilon_0 k_6''} \left|Q_{01}Q_{12}Q_{23}Q_{34}Q_{45}Q_{56}\right|^2 e^{-2k_1'' d_1} e^{-2k_2'' d_2} e^{-2k_3'' d_3} e^{-2k_4'' d_4} e^{-2k_5'' d_5} T_6 \qquad \text{(Eq.4.18)}$$

This Eq.4.18 is the core of the model. Each term in this equation corresponds to a layer's contribution to the received TB (of specific wavelength), and is calculated based on Eq.4.15. The first term corresponds to the lunar dust layer's radiation, the last term corresponds to the lunar bedrock layer's radiation, while the other four terms correspond to each layer of the lunar soil. Except for the last term, all the other five terms contain both upwards radiation and downwards-reflected radiation. Eq. 4.18 calculates the zero-order radiation TB, e.g. the effect of scattering is not considered. Other assumptions include: T_6=250 K (bedrock temperature), the vacuum permittivity is unity and the bedrock layer permittivity is 8.0+0.5i *(Lunar Sourcebook, 1991)*. To determine the wavenumber *k*, we can write,

$$k = \frac{\omega}{c}(\beta + i\alpha) \qquad \text{(Eq. 4.19)}$$

Then according to *Burke et al. (1979)*, the dispersion relation gives:

$$\beta = \left\{ \frac{1}{2}(\varepsilon_{RJ} - \sin^2\theta_0)[1 + (1 + \frac{\varepsilon_{Ij}^{\ 2}}{(\varepsilon_{RJ} - \sin^2\theta_0)^2})^{1/2}] \right\}^{\frac{1}{2}} \qquad \text{(Eq. 4.20)}$$

$$\alpha = \frac{\varepsilon_I}{2\beta} \qquad \text{(Eq.4.21)}$$

Equations (4.16-4.17) are widely used in microwave remote sounding including moisture estimation of terrestrial soil (*Zhang et al., 2008*). Eq 4.19- 4.21 are also used in the inversion model developed in thesis to allow estimation of k.

4.3. Forward Model Calculation

So far all parameters (e.g. bulk density, dielectric permittivity, thermal conductivity, specific heat, wavenumber, mineralogy, etc) found in Chapter 3 have been included in the mathematical expressions of the model. In this thesis the sum of TiO_2 content (%) and FeO content (%) on the lunar surface is denoted as S (%). The MRM measured temperature depth profile of the lunar surface is dependent on the value of S and its variation with depth. The MRM observed TB (T_B) could be calculated from Eq. 4.18; each term in Eq. 4.18 corresponds to each layer's contribution; while T_1,T_2,.. T_6 represent the real temperature of each layer.

Here T_1 is provided from the Diviner mission data product *(Paige et al., 2010)*. T_6 is set as 250 K constrained by the Apollo measurements *(Lunar Sourcebook, 1991)*, hence only T_2-T_5 are unknowns.

4.3.1 Microwave radiative transfer model tests

The initial tests of the forward model behaviour used the theoretical values of T_2-T_5 derived from Figure 3.10 using the Spencer model to calculate the 'expected', synthetic MRM TB for all four channels, using each subsurface layer's 'approximate' energy contribution. Then in the inverse model steps, the measured TB values from the MRM data product will be used to estimate values for T_2-T_5. Both the model and

inverse algorithms have been coded in MATLAB/Fortran and example calculation runs are described below.

Using the expected values for the lunar subsurface temperatures from section 3.7, the forward model results are derived, see Figure 4.2-4.3. When S=10 (i.e. close to lunar average FeO and TiO_2), radiance comes mainly from the deepest layer, especially for the 3 GHz channel and under these circumstances most contributions are from the 5th layer (50 cm-500 cm).

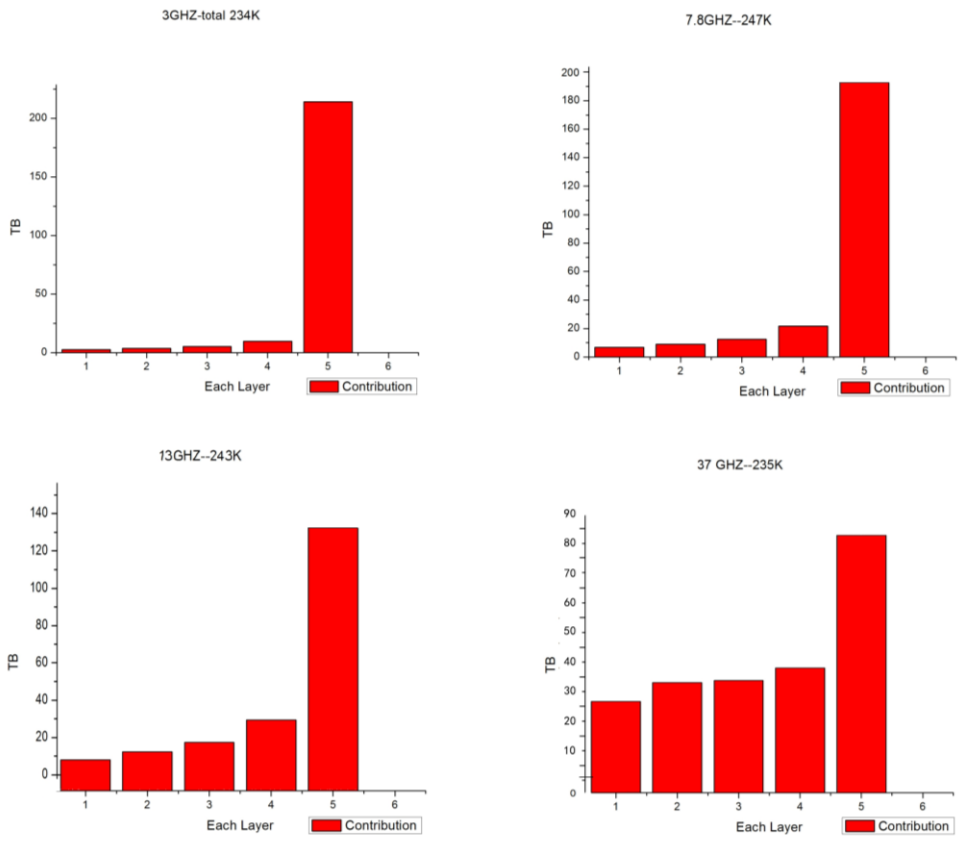

Figure 4.2**.** Each layer's weight (contribution) in the ChangE-1 and ChangE-2 MRM brightness temperature measurements (when S=10), with the measured MRM brightness temperature marked on the top. With the lunar average S value being close to 10, we can see that the MRM data is close to the forward model's prediction (234 K, 235 K), which validated this forward model.

As the lunar highlands typically have a low S value (1-5) *(Lunar Sourcebook, 1991)*, from Figure 4.2, one can use 3 GHz as the deep layer temperature (50 cm-5 m). Figure 4.3 shows the contribution from each layer when S is the largest value (25%) expected for the lunar surface (*Lunar Source Book 1991*).

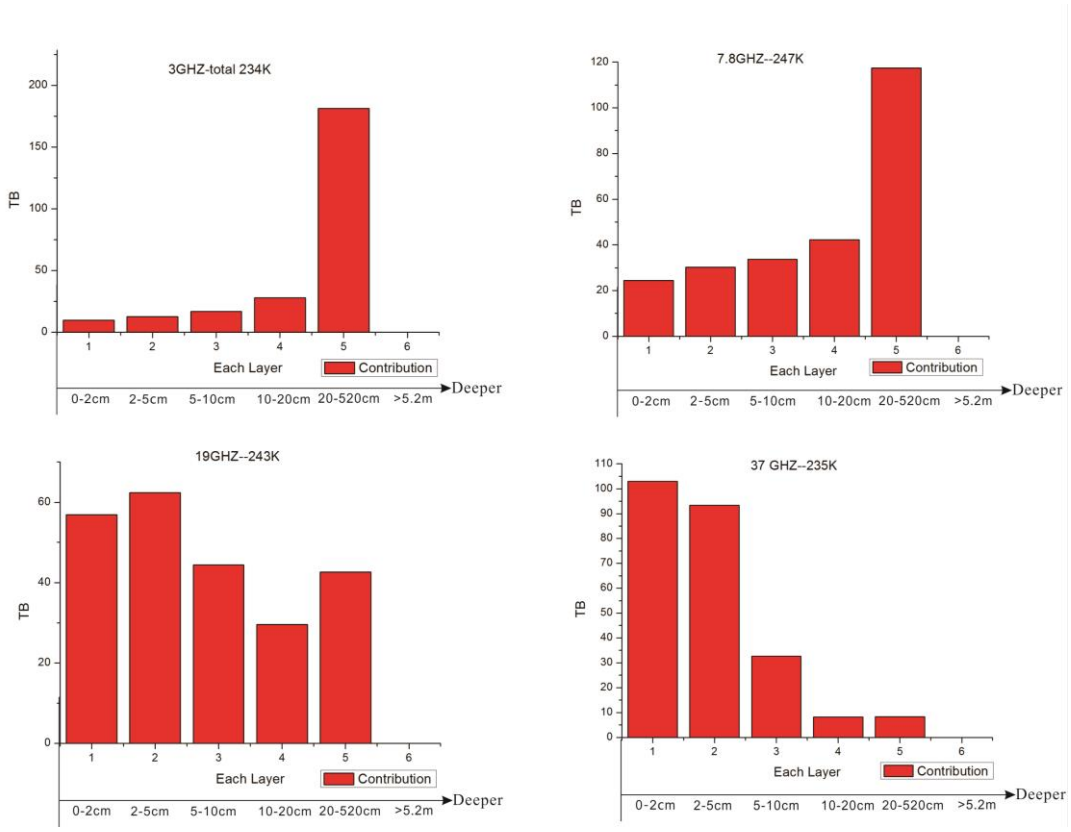

Figure 4.3**.** Each layer's weight (contribution) in the ChangE-1 and ChangE-2 MRM brightness temperature measurements (when S=25). In order to avoid the effect of contamination with depth between channels, which is a common problem in atmospheric retrievals, a priori information will be included in the inversion process; this is discussed later in chapter 6. This calculation here is only for demonstration purpose and no a priori information has been included.

As the Maria regions typically have a high S value (15-20) due to their more mafic composition, according to Figure 4.3, for Maria regions, one can use 37 GHz as the top 5 cm-10 cm layer temperature.

From Figure 4. and Figure 4.3 it is clear that the sub-surface composition (S) is significant in determining the subsurface depth sounded by microwave instruments such as the MRM. This result is also supported by a simplified analytical calculation. If S=0, the penetration depth of each channel is shown in Figure 4.4, while S increases, the penetration depth of each channel decreases, as shown in Figure 4.5,

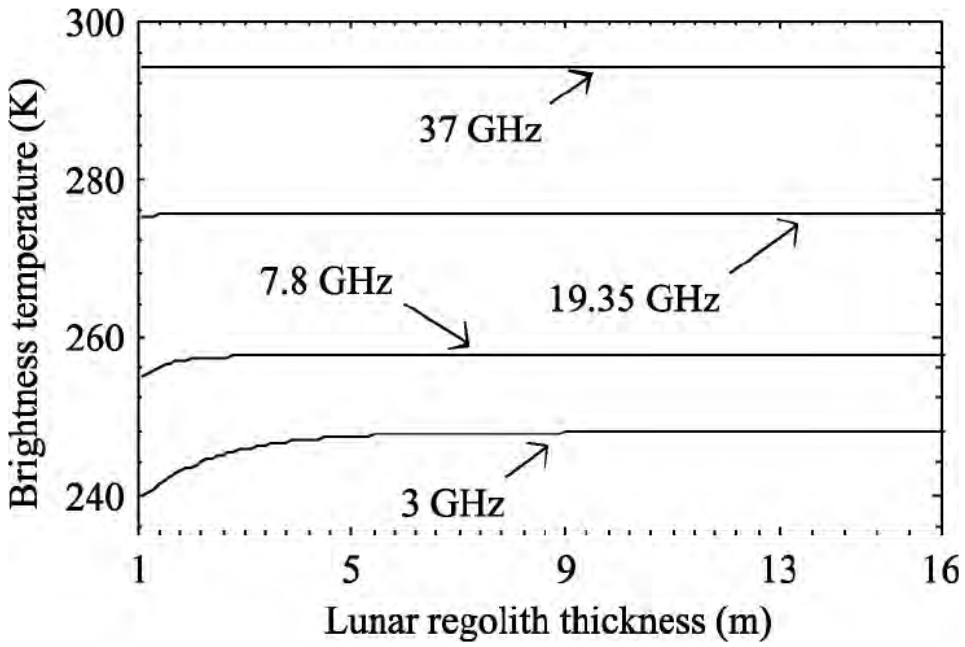

Figure 4.4. The deepest depth that each channel could sound to when S=0. After this depth, the brightness temperature of each channel no longer increases as there is no more contribution from deeper layers.

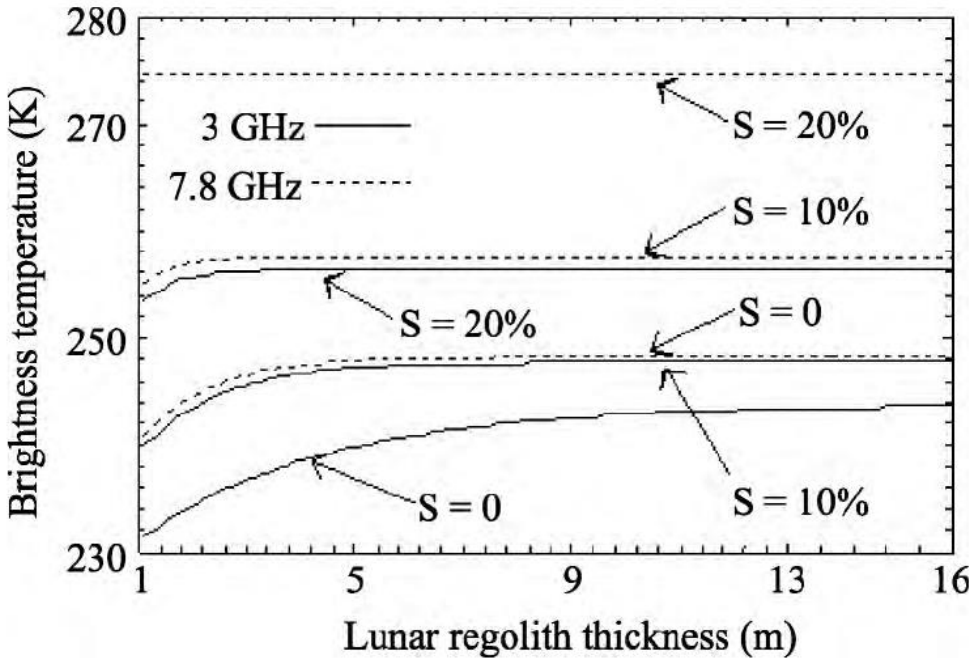

Figure 4.5. The deepest depth that each channel could sound to under different S values. After this depth, the brightness temperature of each channel no longer increases as there is no more contribution from deeper layers.

4.4. Inverting Vertical Subsurface Temperatures of the Equatorial Region from MRM data and using the Microwave Forward Model

The lunar subsurface is not isothermal, so the microwave radiation of the lunar surface is also affected by the actual temperature distribution of the subsurface of the Moon. By solving the radiation transmission equations (Eq. 4.1 – 4.21), this thesis will establish a lunar subsurface temperature inversion model, using the CE MRM measurements.

To study the typical vertical distribution of the lunar subsurface temperature, this work will use the analytical microwave radiative transfer model to attempt an inversion of the equatorial region subsurface temperatures at different depths, based on the MRM data (section 4.2).

What MRM 'measured' is then numerically studied: using the inverse method to retrieve the subsurface temperatures (T_2-T_5), defined as the unknown matrix x in the following discussion. To setup the basic equations for the inversion, the measurement vector should be the 4 MRM measured brightness temperatures in each channel, e.g. TB1 (3 GHz), TB2 (7.8 GHz), TB3 (19.35 GHz), TB4 (37 GHz), each with a measurement error of ±0.5 K, respectively. The unknown vector x should be made of the real sub-surface temperatures, T_2 (5 cm), T_3 (10 cm), T_4 (20 cm) and T_5 (2 m).

According to the inverse method (e.g. *Rodgers et al, 2000*), the measurement vector (y) is equal to the vector of unknowns (x) multiplied by the weighting function matrix (K) plus the error matrix (y=K*x+error). The matrix of unknowns is defined by x=[T_2, T_3, T_4, T_5], y is defined as below in Eq. 4.22 derived from Eq. 4.18, which is the net TB contribution of each lunar soil layer excluding the contribution of dust and rock layer to TB. The dust and rock layer are excluded due to the fact that values of T_1

(Diviner data) and T_6 are known (250 K, Apollo measurement (*Lunar Sourcebook, 1991*), making the contribution from these two layers calculable.

$$y=\begin{bmatrix} TB_1-CTB_{3GHz} \\ TB_2-CTB_{7.8GHz} \\ TB_3-CTB_{19GHz} \\ TB_4-CTB_{37GHz} \end{bmatrix}=\begin{bmatrix} TB_1-(\frac{k_0\varepsilon_1^{''}}{2\varepsilon_0 k_1^{''}}\left|Q_{01}\right|^2(1-e^{-2k_1^{''}d_1})(1+\left|R_{12}\right|^2e^{-2k_1^{''}d_1})T_1 \\ -\frac{k_0\varepsilon_6^{''}}{2\varepsilon_0 k_6^{''}}\left|Q_{01}Q_{12}Q_{23}Q_{34}Q_{45}Q_{56}\right|^2e^{-2k_1^{''}d_1}e^{-2k_2^{''}d_2}e^{-2k_3^{''}d_3}e^{-2k_4^{''}d_4}e^{-2k_5^{''}d_5}T_6)_{3.0GHz} \\ TB_2-(\frac{k_0\varepsilon_1^{''}}{2\varepsilon_0 k_1^{''}}\left|Q_{01}\right|^2(1-e^{-2k_1^{''}d_1})(1+\left|R_{12}\right|^2e^{-2k_1^{''}d_1})T_1 \\ -\frac{k_0\varepsilon_6^{''}}{2\varepsilon_0 k_6^{''}}\left|Q_{01}Q_{12}Q_{23}Q_{34}Q_{45}Q_{56}\right|^2e^{-2k_1^{''}d_1}e^{-2k_2^{''}d_2}e^{-2k_3^{''}d_3}e^{-2k_4^{''}d_4}e^{-2k_5^{''}d_5}T_6)_{7.8GHz} \\ TB_3-(\frac{k_0\varepsilon_1^{''}}{2\varepsilon_0 k_1^{''}}\left|Q_{01}\right|^2(1-e^{-2k_1^{''}d_1})(1+\left|R_{12}\right|^2e^{-2k_1^{''}d_1})T_1 \\ -\frac{k_0\varepsilon_6^{''}}{2\varepsilon_0 k_6^{''}}\left|Q_{01}Q_{12}Q_{23}Q_{34}Q_{45}Q_{56}\right|^2e^{-2k_1^{''}d_1}e^{-2k_2^{''}d_2}e^{-2k_3^{''}d_3}e^{-2k_4^{''}d_4}e^{-2k_5^{''}d_5}T_6)_{19.0GHz} \\ TB_4-(\frac{k_0\varepsilon_1^{''}}{2\varepsilon_0 k_1^{''}}\left|Q_{01}\right|^2(1-e^{-2k_1^{''}d_1})(1+\left|R_{12}\right|^2e^{-2k_1^{''}d_1})T_1 \\ -\frac{k_0\varepsilon_6^{''}}{2\varepsilon_0 k_6^{''}}\left|Q_{01}Q_{12}Q_{23}Q_{34}Q_{45}Q_{56}\right|^2e^{-2k_1^{''}d_1}e^{-2k_2^{''}d_2}e^{-2k_3^{''}d_3}e^{-2k_4^{''}d_4}e^{-2k_5^{''}d_5}T_6)_{37.0GHz} \end{bmatrix}$$

(Eq.4.22)

Where CTB is the contribution of dust and rock layer to the TB measured by the MRM instrument. Note that the CTB is a known quantity as it is set by Diviner and Apollo measurements. Q is the transmission coefficient (Eq 4.16) and R is the reflection coefficient (Eq 4.17).

According to the temperature uncertainty of the MRM instrument (±0.5 K) given in Table 2.1, the measurement uncertainty covariance matrix is then:

$$S_\varepsilon = \begin{bmatrix} 0.25 & 0 & 0 & 0 \\ 0 & 0.25 & 0 & 0 \\ 0 & 0 & 0.25 & 0 \\ 0 & 0 & 0 & 0.25 \end{bmatrix} \qquad \text{(Eq.4.23)}$$

Where the diagonal elements are given as the square of the error of the MRM instrument. And according to Eq. 4.18, the weighting function matrix is

$$K = \begin{bmatrix} C^{Second}_{3.0\times10^9 GHz} & C^{Third}_{3.0\times10^9 GHz} & C^{Forth}_{3.0\times10^9 GHz} & C^{Fifth}_{3.0\times10^9 GHz} \\ C^{Second}_{7.8\times10^9 GHz} & C^{Third}_{7.8\times10^9 GHz} & C^{Forth}_{7.8\times10^9 GHz} & C^{Fifth}_{7.8\times10^9 GHz} \\ C^{Second}_{19.0\times10^9 GHz} & C^{Third}_{19.0\times10^9 GHz} & C^{Forth}_{19.0\times10^9 GHz} & C^{Fifth}_{19.0\times10^9 GHz} \\ C^{Second}_{37.0\times10^9 GHz} & C^{Third}_{37.0\times10^9 GHz} & C^{Forth}_{37.0\times10^9 GHz} & C^{Fifth}_{37.0\times10^9 GHz} \end{bmatrix} \qquad \text{(Eq.4.24)}$$

Where $C^{Second} = \frac{k_0 \varepsilon_2''}{2\varepsilon_0 k_2''} \left|Q_{01}Q_{12}\right|^2 (1-e^{-2k_2''d_2})(1+\left|R_{23}\right|^2 e^{-2k_2''d_2})e^{-2k_1''d_1}$ （Eq.4.25）

$$C^{Third} = \frac{k_0 \varepsilon_3''}{2\varepsilon_0 k_3''} \left|Q_{01}Q_{12}Q_{23}\right|^2 (1-e^{-2k_3''d_3})(1+\left|R_{34}\right|^2 e^{-2k_3''d_3})e^{-2k_1''d_1}e^{-2k_2''d_2} \quad \text{（Eq.4.26）}$$

$$C^{Forth} = \frac{k_0 \varepsilon_4''}{2\varepsilon_0 k_4''} \left|Q_{01}Q_{12}Q_{23}Q_{34}\right|^2 (1-e^{-2k_4''d_4})(1+\left|R_{45}\right|^2 e^{-2k_4''d_4})e^{-2k_1''d_1}e^{-2k_2''d_2}e^{-2k_3''d_3} \qquad \text{（Eq.4.27）}$$

$$C^{Fifth} = \frac{k_0 \varepsilon_5''}{2\varepsilon_0 k_5''} \left|Q_{01}Q_{12}Q_{23}Q_{34}Q_{45}\right|^2 (1-e^{-2k_5''d_5})(1+\left|R_{56}\right|^2 e^{-2k_5''d_5})e^{-2k_1''d_1}e^{-2k_2''d_2}e^{-2k_3''d_3}e^{-2k_4''d_4}$$

（Eq.4.28）

According to the inverse theory *(Rodgers et al., 2000)*,

$$x = (K^T S_\varepsilon^{-1} K)^{-1} K^T S_\varepsilon^{-1} y \qquad \text{（Eq.4.29）}$$

And expression for the error covariance of the state *x* vector is,

$$S_x = (K^T S_\varepsilon^{-1} K)^{-1} \qquad \text{（Eq.4.30）}$$

The vector of unknowns (x) and its associated error covariance (S_x) can therefore be estimated. However, this S_x is the model calculation error, without the parameter

modelling error included. In chapter 6 an a priori covariance matrix (S_a) will be added to include these significant modelling uncertainties.

A simple test of Eq 4.29 was done to generate a vertical temperature profile for the lunar equator. When assuming a value of S=15 (typical for the lunar equatorial region - according to (*Lunar Sourcebook, 1991*)), a rough average subsurface temperature curve for the Moon's equatorial region can be generated using the radiative transfer model and inverting the equatorial MRM data (Figure 4.6). The surface temperature points are constrained by Diviner measurements (*(Paige et al., 2010)*. The stated error of the Diviner data is within ±2 K *(Paige et al., 2010)*). The bedrock temperature is taken from the Apollo experiment with ±10 K error *(Lunar Sourcebook, 1991)* and the other points have been derived from the Chang'E MRM measurements. Error is within ±6 K. The model shows that the lunar soil temperature changes significantly within the top 2 cm, and becomes stable below 20 cm. Comparing it with the theoretical thermal simulations in chapter 3, section 3.7, we notice that they agree to within the stated uncertainties. The data used for this forward model calculation is summarized in Table 4.1.

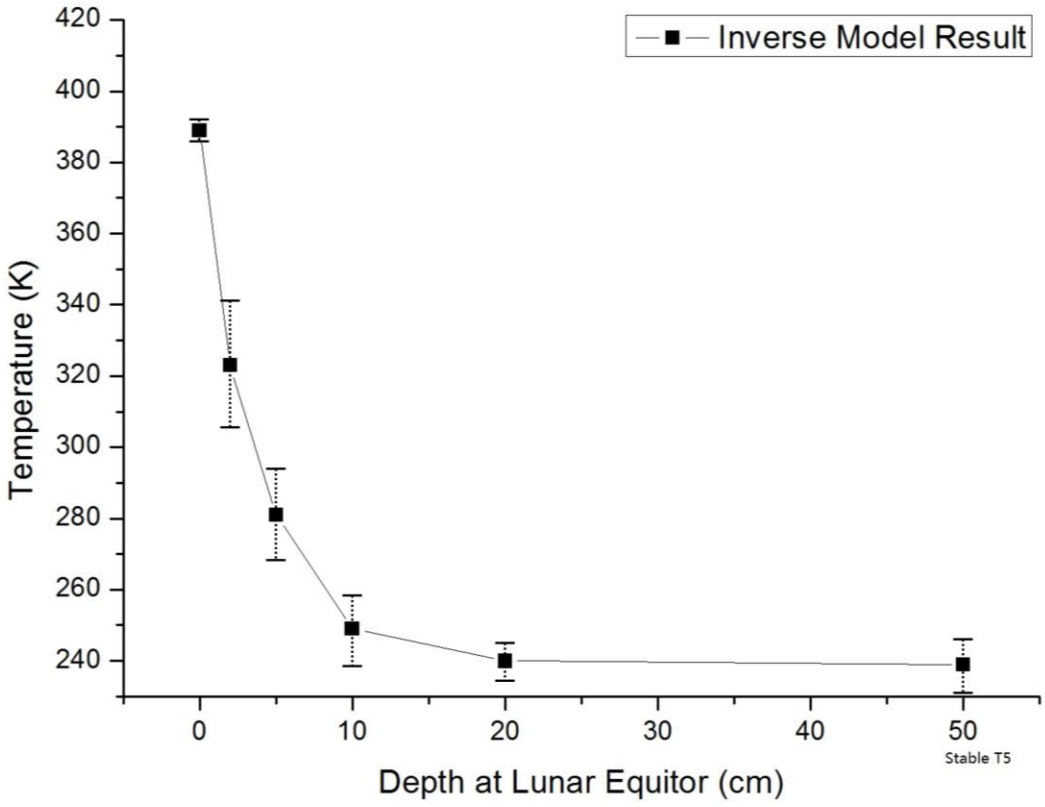

Figure 4.6. Based on ChangE-1 MRM data and my radiative transfer model, the "measured" mean vertical temperature profile beneath the lunar equatorial surface, at the lunar midday, was inverted.

Table 4.1. Data used in forward model calculation is an average of CE-1 and CE-2, details are given in this table.

	CE-1 Microwave Brightness Temperature Dataset	CE-2 Microwave Brightness Temperature Dataset
Size details	346MB	992MB
Time Span	2007.11.27 - 2008.06.30	2010.10.15 - 2011.05.20
Space Resolution	3 GHz channel space resolution is 50 km. All other channels had a spatial resolution of ~35 km	3 GHz channel space resolution is 25 km. All other channels had a spatial resolution of ~17.5 km

Both the thermal simulation (section 3.7) and the MRM data (Figure 4.6) show that the surface temperature at the lunar equator at noon is ~390 K and drops significantly within 20 cm, then is almost stable at ~240 K at depths below 20 cm to 50 cm. This is also as described in the lunar source book (220 < T < 255 K *(Lunar Sourcebook, 1991)*).

In the model covariance matrix, it was noticed that the first three off-diagonal elements are quite large (e.g. +/- 20 K), but the fourth off-diagonal element (T_5 error) was below 2-10 K. This is because as shown in Figure 4.2 the MRM signal mainly comes from the lunar soil at a depth of >50 cm.

Before attempting to derive a global subsurface temperature map, it is important to understand the effect of additional a-prior information that will be used for constraining the inputs to the forward model in chapter 6. The next section describes the influence of each input parameter on the output of the model.

4.5. Forward Radiative Transfer Model Error and Sensitivity Studies

To understand the sources of error in the model caused by the assumptions, this section tries to determine the effect of error in the prior sources of knowledge on the final inversion results. This is done via both traditional (e.g. *Rodgers 2000*) analysis and a Monte Carlo analysis. The nominal parameters of lunar regolith used are the same as the equatorial case in section 4.4.

A traditional error analysis will be provided in 4.5.1, in which an analytical method is used to calculate each parameter's effect on the MRM TB. In addition, given that only two *in*-situ measurements of the sub-surface temperature structure of the Moon have been made *(Lunar Sourcebook, 1991)*, the microwave radiative transfer forward model requires a wider sensitivity study (section 4.5.2). This sensitivity study will use Monte Carlo analysis to investigate which parameters have the biggest influence on the sub-surface temperature of the Moon as derived from MRM data. These parameters can then be investigated further to identify where additional sources of a priori information are required to strengthen the inverse result.

4.5.1 Error and contribution analysis to multi-layer transmission of microwave radiation

The factors that affect the TB calculated by the forward model and their influence on the temperatures derived from the inversion result need to be determined.

4.5.1.1. Potential effect of lunar dust layer temperature (T_1) on TB

From the forward model (Section 4.2), we can re-write Eq. 4.18 as:

$$T_B = A_1T_1 + B_1T_2 + C_1T_3 + D_1T_4 + E_1T_5 + F_1T_6 \qquad \text{(Eq. 4.31)}$$

where T_1 to T_6 are the layer temperatures, A_1 to F_1 are listed below:

$$A_1 = \frac{k_0 \varepsilon_1''}{2\varepsilon_0 k_1''} \left|Q_{01}\right|^2 (1 - e^{-2k_1'' d_1})(1 + \left|R_{12}\right|^2 e^{-2k_1'' d_1}) \qquad \text{(Eq. 4.32)}$$

$$B_1 = \frac{k_0 \varepsilon_2''}{2\varepsilon_0 k_2''} \left|Q_{01}Q_{12}\right|^2 (1 - e^{-2k_2'' d_2})(1 + \left|R_{23}\right|^2 e^{-2k_2'' d_2}) e^{-2k_1'' d_1} \qquad \text{(Eq. 4.33)}$$

$$C_1 = \frac{k_0 \varepsilon_3''}{2\varepsilon_0 k_3''} \left|Q_{01}Q_{12}Q_{23}\right|^2 (1 - e^{-2k_3'' d_3})(1 + \left|R_{34}\right|^2 e^{-2k_3'' d_3}) e^{-2k_1'' d_1} e^{-2k_2'' d_2} \text{ (Eq. 4.34)}$$

$$D_1 = \frac{k_0 \varepsilon_4''}{2\varepsilon_0 k_4''} \left|Q_{01}Q_{12}Q_{23}Q_{34}\right|^2 (1 - e^{-2k_4'' d_4})(1 + \left|R_{45}\right|^2 e^{-2k_4'' d_4}) e^{-2k_1'' d_1} e^{-2k_2'' d_2} e^{-2k_3'' d_3} \quad \text{(Eq. 4.35)}$$

$$E_1 = \frac{k_0 \varepsilon_5''}{2\varepsilon_0 k_5''} \left|Q_{01}Q_{12}Q_{23}Q_{34}Q_{45}\right|^2 (1 - e^{-2k_5'' d_5})(1 + \left|R_{56}\right|^2 e^{-2k_5'' d_5}) e^{-2k_1'' d_1} e^{-2k_2'' d_2} e^{-2k_3'' d_3} e^{-2k_4'' d_4}$$

(Eq. 4.36)

$$F_1 = \frac{k_0 \varepsilon_6''}{2\varepsilon_0 k_6''} \left|Q_{01}Q_{12}Q_{23}Q_{34}Q_{45}Q_{56}\right|^2 e^{-2k_1'' d_1} e^{-2k_2'' d_2} e^{-2k_3'' d_3} e^{-2k_4'' d_4} e^{-2k_5'' d_5} \qquad \text{(Eq. 4.37)}$$

Hence, the potential effect of variations in the lunar dust layer temperature on the forward model calculation can be estimated by plotting the relationship between TB and T_1:

$$\frac{\partial T_B}{\partial T_1} = A_1 = \frac{k_0 \varepsilon_1''}{2\varepsilon_0 k_1''} \left|Q_{01}\right|^2 (1 - e^{-2k_1'' d_1})(1 + \left|R_{12}\right|^2 e^{-2k_1'' d_1}) \quad \text{(Eq. 4.38)}$$

This is dependent on the lunar dust layer depth (d_1) and mineral content (S, as ε is a function of S), Figure 4.7:

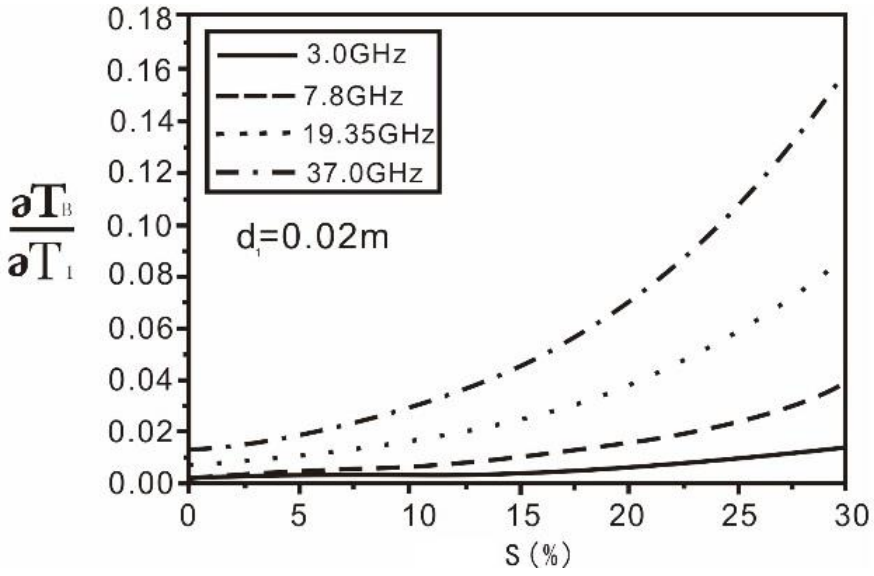

Figure 4.7. Response of TB to lunar dust layer temperature changes. The y axis is the partial derivative of T_B to T_1, while the x axis is the mineral content value S in percentage. Each channel has its own variation curve as shown in the figure. Clearly, the 37 GHz channel is the most sensitive to T_1.

When S is in a normal range (0 < S < 20), the lunar dust temperature T_1 does not affect significantly TB in all four channels ($\frac{\partial T_B}{\partial T_1} < 0.05$, which means a change of 1 K in dT_1 will usually result in < 0.05 K dT_B). However, if the S value is extremely high (S > 25), then in the high-frequency channels, such as at 37 GHz channel, TB will be slightly affected by the dust layer temperature ($\frac{\partial T_B}{\partial T_1} \sim 0.10$).

4.5.1.2. Potential effect of lunar soil layer temperature (T_5) on TB

From Eq 4.33, the effect of small changes in T_5 (lowest soil layer) on TB can be calculated as:

$$\frac{\partial T_B}{\partial T_5} = E_1 = \frac{k_0 \varepsilon_5^{"}}{2\varepsilon_0 k_5^{"}} \left| Q_{01} Q_{12} Q_{23} Q_{34} Q_{45} \right|^2 (1 - e^{-2k_5^{"} d_5})(1 + \left| R_{56} \right|^2 e^{-2k_5^{"} d_5}) e^{-2k_1^{"} d_1} e^{-2k_2^{"} d_2} e^{-2k_3^{"} d_3} e^{-2k_4^{"} d_4}$$

(Eq. 4.39)

And is plotted in Figure 4.8 below:

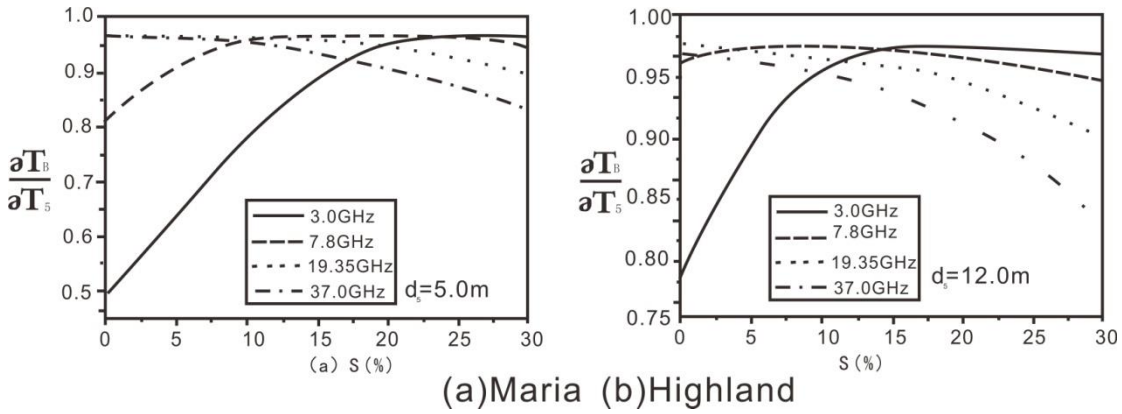

Figure. 4.8. Response of TB to a lunar soil layer temperature change of 1 K.

As seen in Figure 4.8 changes in T_5 (lowest soil layer) temperature have a large effect on the forward model simulated TB. For example, in Figure 4.8a the 3 GHz channel, in the Maria regions (S = 10~15) shows a 1.25 K variation of T_5 causes a 1 K change in the measured TB. The simulated TB is more sensitive to the T_5 (lowest soil layer) temperature compared to the T_1 (lunar dust layer) because this is the source of the majority of the radiance observed by the MRM, especially at longer wavelengths.

We can also estimate the maximum variance of T_5. From the MRM instrument specification in Table 2.1 the MRM TB error is normally within ±0.5 K (*Wang et al., 2010*). Hence, according to the model and using a similar derivation, T_5 could exhibit a maximum 0.6 K error corresponding to the TB error (*Wang et al., 2010*).

4.5.1.3. Potential effect of lunar bedrock layer temperature (T_6) on TB

From Eq 4.33, the effect of small changes in T_6 (bedrock layer) on the forward model simulated TB can be calculated as:

$$\frac{\partial T_B}{\partial T_6} = F_1 = \frac{k_0 \varepsilon_6^{''}}{2\varepsilon_0 k_6^{''}} \left| Q_{01} Q_{12} Q_{23} Q_{34} Q_{45} Q_{56} \right|^2 e^{-2k_1^{''} d_1} e^{-2k_2^{''} d_2} e^{-2k_3^{''} d_3} e^{-2k_4^{''} d_4} e^{-2k_5^{''} d_5} \qquad \text{(Eq. 4.40)}$$

The curves are plotted in Figure 4.9. When lunar soil depth d_5 is small or FeO and TiO_2 content S is low, T_6 exerts a noticeable influence on TB.

However, when the lunar soil depth is large (typical highland region) or S content is high (typical Maria region), microwave radiation cannot penetrate the lunar soil layer. Therefore, the bottom rock layer only exerts a minimal effect on TB (Figure 4.9).

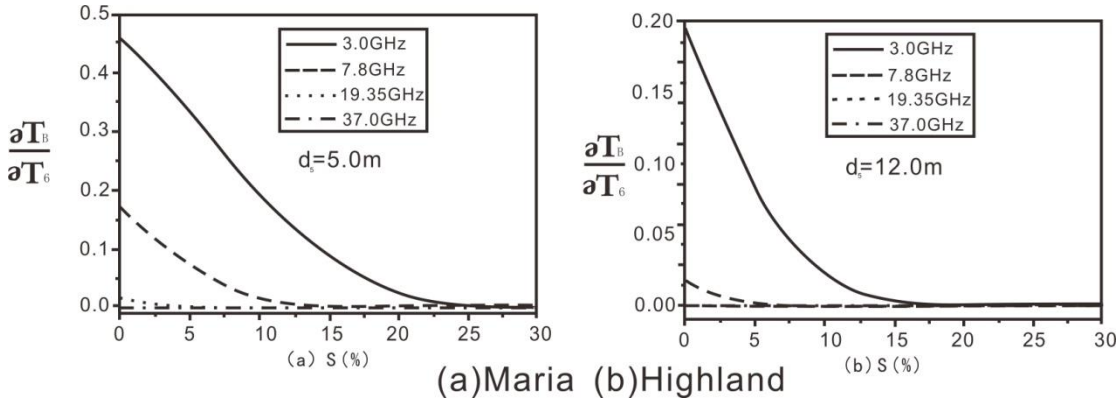

Figure. 4.9. Response of TB to lunar rock layer temperature changes.

4.5.1.4. Potential effect of lunar dust layer depth (d_1) on TB

In addition to temperature, layer depths also affect the measured brightness temperature. This effect of variations in the lunar dust layer depth is investigated by calculating the partial derivative of TB to d_1:

$$\frac{\partial T_B}{\partial d_1} = k_1^{"}\left(\frac{k_0\varepsilon_2^{"}}{2\varepsilon_0 k_2^{"}}\left|Q_{01}Q_{12}\right|^2\cdot e^{-2k_1^{"}d_1} + 2\frac{k_0\varepsilon_1^{"}}{2\varepsilon_0 k_1^{"}}\left|Q_{01}\right|^2\cdot\left|R_{12}\right|^2\cdot e^{-4k_1^{"}d_1}\right)T_1$$

$$-k_1^{"}B_1T_2 - k_1^{"}C_1T_3 - k_1^{"}D_1T_4 - k_1^{"}E_1T_5 - k_1^{"}F_1T_6 \qquad \text{(Eq. 4.41)}$$

The dependency of $\frac{\partial T_B}{\partial d_1}$ value on the lunar mineral content S is plotted in the Figure 4.10 below (TB unit: K, d_1 unit: cm).

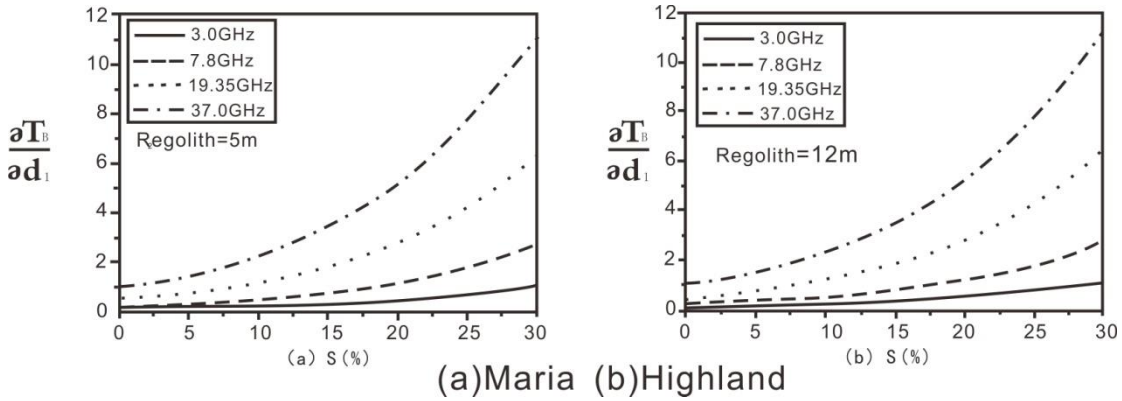

Figure. 4.10. Response of TB to a lunar dust layer thickness change of 1 cm.

A lunar dust layer thickness d_1 of 2 cm is suggested in the proposed model, this can be applied to most of the Moon (*Lunar Sourcebook, 1991*). However, based on the curves in Figure 4.10, when *S* is extremely large (> 25), $\frac{\partial T_B}{\partial d_1}$ could be as high as 3–4 K/cm.

4.5.1.5. The Potential effects of lunar soil layer thicknesses (d_2, d_3, d_4, d_5) on TB

Similarly, the relationship between other layer thicknesses and TB are derived as:

$$\frac{\partial T_B}{\partial d_2} = 2k_2^{''}\left(\frac{k_0\varepsilon_3^{''}}{2\varepsilon_0 k_3^{''}}\left|Q_{01}Q_{12}Q_{23}\right|^2 \cdot e^{-2k_2^{''}d_2} + 2\frac{k_0\varepsilon_2^{''}}{2\varepsilon_0 k_2^{''}}\left|Q_{01}Q_{12}\right|^2\left|R_{23}\right|^2 e^{-4k_2^{''}d_2}\right)e^{-2k_1^{''}d_1}\cdot T_2$$
$$-2k_2^{''}C_1T_3 - 2k_2^{''}D_1T_4 - 2k_2^{''}E_1T_5 - 2k_2^{''}F_1T_6$$

(Eq. 4.42)

$$\frac{\partial T_B}{\partial d_3} = 2k_3^{''}\left(\frac{k_0\varepsilon_4^{''}}{2\varepsilon_0 k_4^{''}}\left|Q_{01}Q_{12}Q_{23}Q_{34}\right|^2 \cdot e^{-2k_3^{''}d_3} + 2\frac{k_0\varepsilon_3^{''}}{2\varepsilon_0 k_3^{''}}\left|Q_{01}Q_{12}Q_{23}\right|^2 \left|R_{34}\right|^2 e^{-4k_3^{''}d_3} \right) e^{-2k_1^{''}d_1} \cdot e^{-2k_2^{''}d_2} \cdot T_3$$
$$-2k_3^{''}D_1T_4 - 2k_3^{''}E_1T_5 - 2k_3^{''}F_1T_6$$

(Eq. 4.43)

$$\frac{\partial T_B}{\partial d_4} = 2k_4^{''}\left(\frac{k_0\varepsilon_5^{''}}{2\varepsilon_0 k_5^{''}}\left|Q_{01}Q_{12}Q_{23}Q_{34}Q_{45}\right|^2 \cdot e^{-2k_4^{''}d_4} + 2\frac{k_0\varepsilon_4^{''}}{2\varepsilon_0 k_4^{''}}\left|Q_{01}Q_{12}Q_{23}Q_{34}\right|^2 \left|R_{45}\right|^2 e^{-4k_4^{''}d_4} \right) e^{-2k_1^{''}d_1} \cdot e^{-2k_2^{''}d_2} \cdot e^{-2k_3^{''}d_3} \cdot T_4$$
$$-2k_4^{''}E_1T_5 - 2k_4^{''}F_1T_6$$

(Eq. 4.44)

$$\frac{\partial T_B}{\partial d_5} = 2k_5^{''}\left(\frac{k_0\varepsilon_6^{''}}{2\varepsilon_0 k_6^{''}}\left|Q_{01}Q_{12}Q_{23}Q_{34}Q_{45}Q_{56}\right|^2 \cdot e^{-2k_5^{''}d_5} + 2\frac{k_0\varepsilon_5^{''}}{2\varepsilon_0 k_5^{''}}\left|Q_{01}Q_{12}Q_{23}Q_{34}Q_{45}\right|^2 \left|R_{56}\right|^2 e^{-4k_5^{''}d_5} \right)$$
$$\cdot e^{-2k_1^{''}d_1} \cdot e^{-2k_2^{''}d_2} \cdot e^{-2k_3^{''}d_3} \cdot e^{-2k_4^{''}d_4} \cdot T_5 - 2k_5^{''}F_1T_6$$

(Eq. 4.45)

d_5 is selected for exploring this effect because it is the largest layer (4.8 m). $\frac{\partial T_B}{\partial d_5}$ also depends on the S value. However, unlike $\frac{\partial T_B}{\partial d_1}$, $\frac{\partial T_B}{\partial d_5}$ decreases as the S value increases. By plotting the curves in Figure 4.11 we can understand the relationships better.

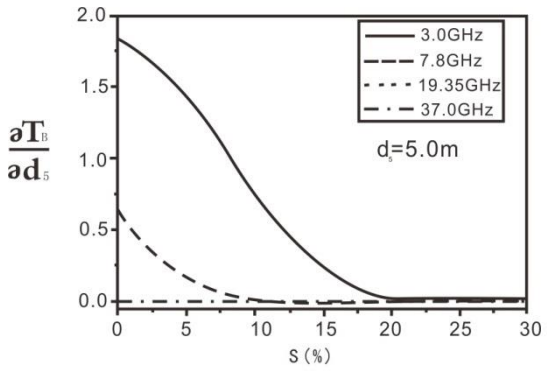

Figure. 4.11. Response of TB to lunar soil layer depth d_5 changes under different S values.

Based on Figure 4.11, when the S value is low (S < 10, e.g. most highland regions), the variation in d_5 has a slight influence on TB (0.9-1.7 K/m). However, when the S value becomes higher, the TB will no longer be sensitive to changes in d_5 because it is below the nominal penetration depth of the MRM instrument.

A summary of the main error sources from above sensitivity analysis (section 4.5.1.1-4.1.5.5) is presented in Table 4.2.

Table 4.2. Summary of main error source from initial sensitivity analysis

Error Source	Input Deviation	Uncertainty in inverted 2 m temperature
Lunar Soil Depth	±1 m	±0.9 K (suggesting S=10)
Lunar Dust Thickness	±1 cm	±0.8 K
Lunar Dust Temperature	±1 K	±0.05 K
TB channels error	±1 K (±0. 5 K normally*)	±1.25 K (±0.6 K normally)

*According to CE MRM calibration document, MRM TB error should be within ±0.5 K (*Wang et al., 2010*).

4.5.2 Monte Carlo Analysis

After the initial sensitivity analysis in 4.5.1, a Monte Carlo analysis was also carried out. Due to the fact that for many of the model parameters (e.g. Fe/Ti and density) the uncertainties are not well-quantified (*Vasavada et al., 1999; Fa et al., 2006; Fa et al., 2007*), an approach that considers a wide range of possible values in these parameters was used to derive a broader estimate of model sensitivity.

One such approach is a Monte Carlo analysis. Monte Carlo methods belong to a class of computational algorithms that relies on repeated random sampling to produce results (*Umrigar et al., 2009*). In section 4.5.2, the effect of the trade-off of different input parameters against each other on the modelled temperature is explored using a Monte Carlo approach.

4.5.2.1. Monte Carlo Analysis on Brightness Temperature Perturbations

First, this work tested how the error in each of the MRM channel brightness temperatures would affect the model output. The other parameters were kept constant while the errors in the brightness temperatures varied within the error limit of ±0.5 K, which was derived from the instrument performance *(Wang et al., 2010)*. This allows the variation in the inverted temperature T_5 in response to the TB error to be calculated, see Figure 4.12:

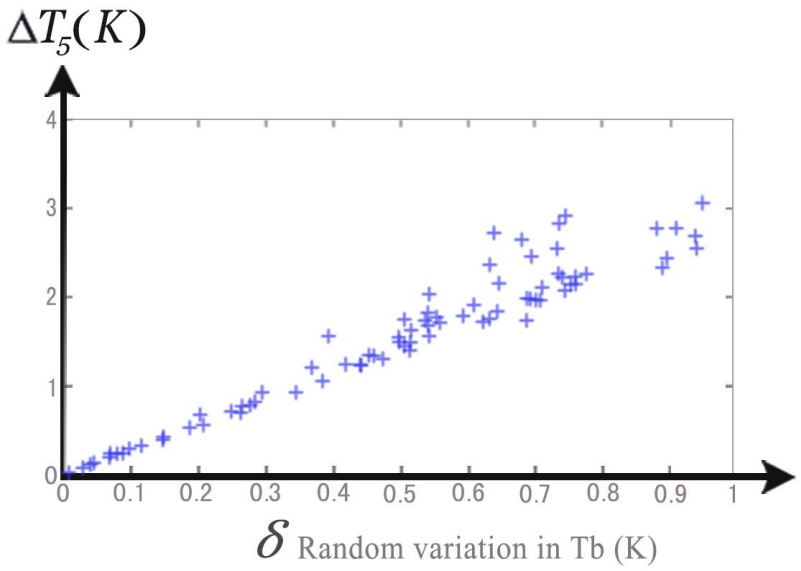

Figure 4.12. The response of the inverted 2 m subsurface temperature (T_5) to the 37 GHz TB error. (Unit: K).

Figure 4.12 seems to be a linear regression: the increase of brightness temperature (or error) would lead to the proportional increase of the modelled 1 metre subsurface temperature, of which the gradient is approximately 3. This is smaller than mineralogy or density effects which will be discussed in the next sections, because the TB error is ±0.5 K (Table 2.1) which means T_5 uncertainly due to 37 GHz TB error would be less than ±1.5 K.

This is then repeated for each of the four channels to test their effects on the derived temperature. Therefore, an additional check is required for the other three channels. These calculations show that the low frequency channels have much smaller

influences than the high frequency channels. For instance, the 7.8 GHz channel only has 1/6 of the effect of the 37 GHz channel (Figure 4.13). The T_5 uncertainly due to the 7.8 GHz TB error would be less than ±0.25 K. Therefore, the effect on the 2 m depth derived temperature due to errors in the other three channels is expected to be even smaller. TB is not a main error source because both CE-1 and CE-2 have calibrated TBs and the error of the instrument performance is smaller than 0.5 K (*Wang et al., 2010*).

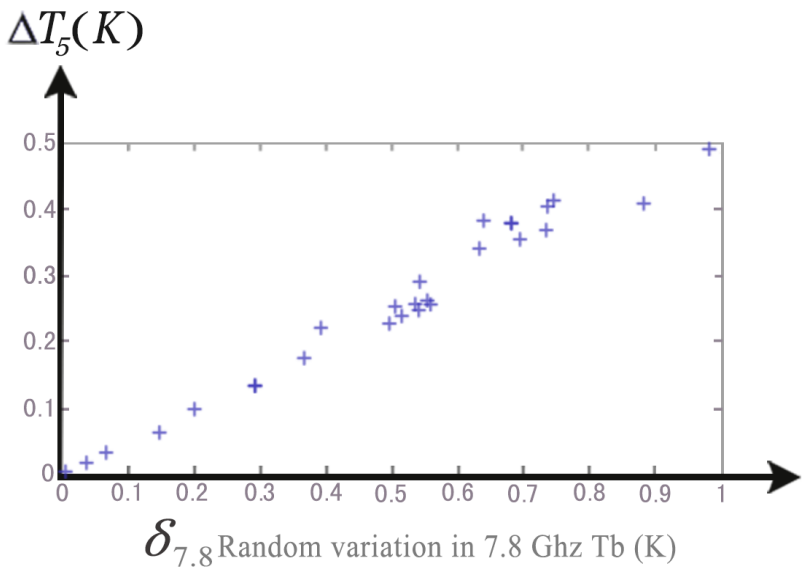

Figure 4.13. Response of the inverted 2 m subsurface temperature to the 7.8 GHz channel, which only has a 1/10 effect of 37 GHz channel and is at the same magnitude of error source, that is, < 0.25 K.

4.5.2.2 Monte Carlo Analysis on Density Perturbations

After analysing the error sources from the MRM instrument itself, the influence of the lunar dust layer / lunar soil layer densities to derived 2 m temperature is studied (Figure 4.14 – 4.15).

The lunar surface is covered by a thin layer of dust caused by a myriad of meteorite impacts. As suggested by *Lunar Sourcebook (1991)*, the density of the lunar dust layer is estimated as 1.3 g/cm^3. (Note: The lunar dust layer bulk density is not the lunar dust particle density because the layer structure is porous *(Li et al., 2009)*). Monte Carlo results in Figure 4.14 indicate that the tolerance is about ±0.3 g/cm^3. Any decrease or increase within 0.3 g/cm^3 will not significantly (e.g. +/-20 K) alter the derived temperature at 2 m depth.

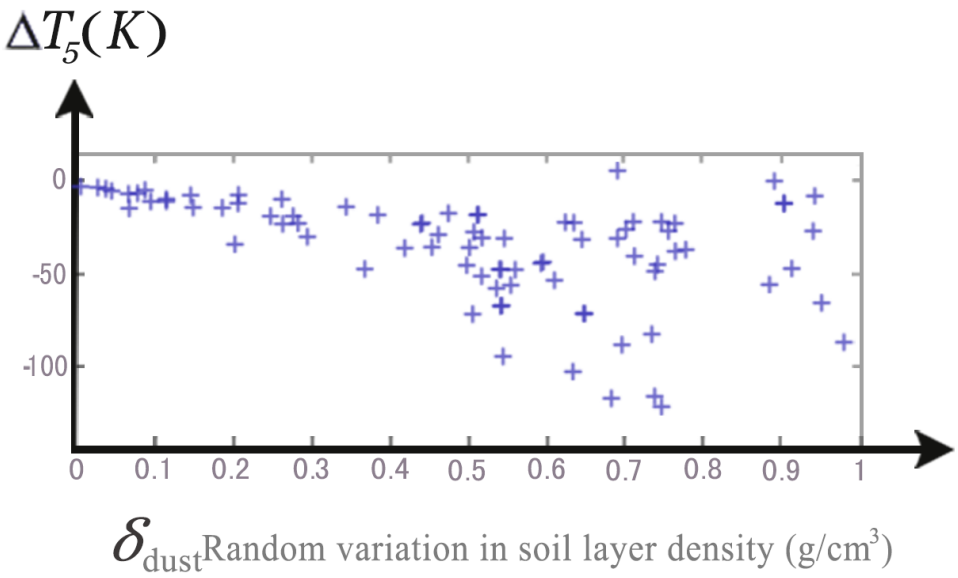

Figure 4.14. (Left) The response of the inverted 2 m subsurface temperature to the decrease of lunar dust density; (Right) The response of the inverted 2 m subsurface temperature to the increase of lunar dust density.

Unless the lunar dust layer density falls to 0.8 g/cm^3 or jumps to 1.6 g/cm^3, then the error needs to be treated with caution, otherwise the generally accepted value of 1.3 g/cm^3 is almost constant over the large scale lunar surface (*Lunar Sourcebook, 1991*).

Similar situations apply to variations in the bottom layer lunar soil density (Figure 4.15), in which an allowed perturbation is ±0.4 g/cm^3:

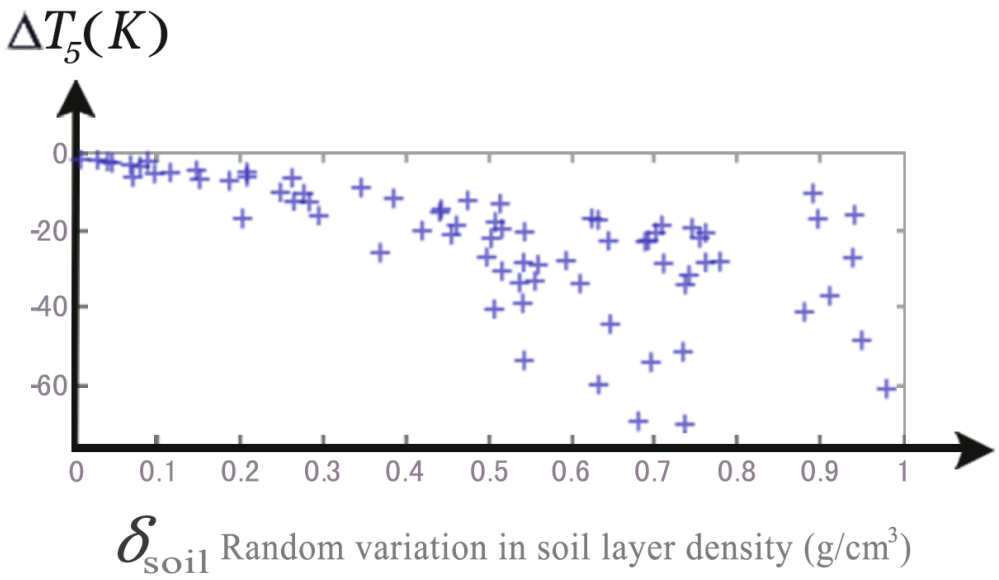

Figure 4.15**.** (Left) The response of the inverted 2 m subsurface temperature to the decrease of lunar soil bottom layer density; (Right) The response of the inverted 2 m subsurface temperature to the increase of lunar soil bottom layer density. This layer's density is calculated by Eq. 3.1.

However, a higher density (5%–10%) than the average may occur in the Maria regions (*Lunar Sourcebook, 1991*), with changes in density that could be higher than

0.4 g/cm^3. Therefore, density variations will be included in the model to account for this possible source of increased uncertainty (in chapter 5).

4.5.2.3 Monte Carlo Analysis on Mineralogy Perturbations

Mineralogy will significantly affect the model as it will change the penetration depth of the microwave radiation at the frequencies measured by the MRM. Variations in composition across the lunar surface are described by difference in the value the S parameter. As a starting point for this analysis, a typical highland S value of 4% is first suggested, and then the effect of variations around this value is studied.

Variation of S within ±1% was shown in Figure 4.16:

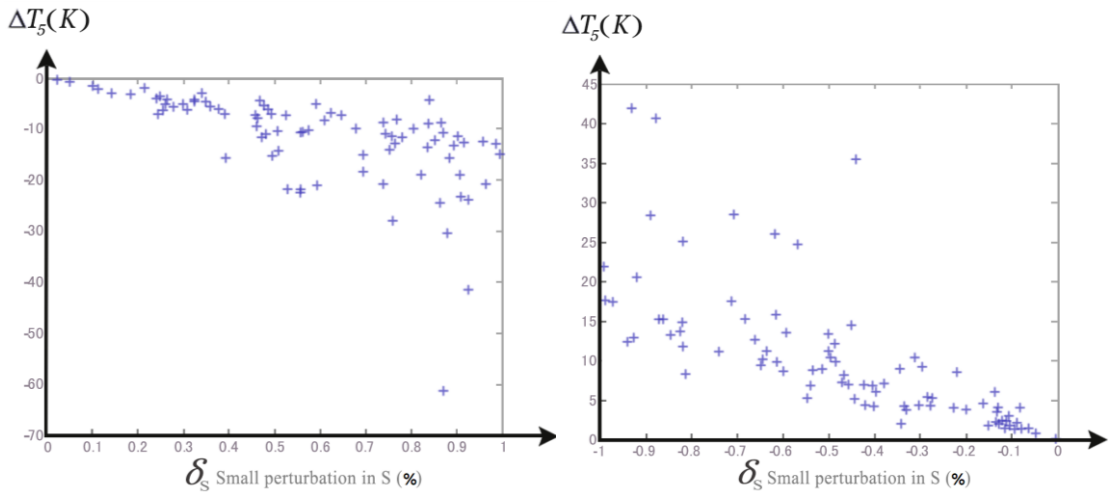

Figure 4.16. Response of the inverted 2-m subsurface temperature to the decrease or increase of S, suggesting the real value of S is 4%.

Based on Figure 4.17, variations in S will affect the inversion result significantly. A ±25% error in S values could cause a ±20 K error in the temperature inversion result

for 2 m depth. Similar tests on Maria high S regions (S > 8%) indicate that this effect may be less significant on Maria regions, but a ±12.5% error in S could still yield a ±5 K error in the temperature inversion result at 2 m depth.

A summary of all the error sources from the Monte-Carlo analysis is presented in Table 4.3.Quantifications of the Fe/Ti elemental abundance and density variation are included in the next chapter.

Table 4.3. Summary of main Error Source from Monte-Carlo Analysis

Error Source	Input Deviation	Output Error	Possible Solution to reduce Error
37 GHz Channels TB	±1 K (±0.5 K*)	±3 K (±1.5 K*)	N/A
7.8 GHz Channels TB	±1 K (±0.5 K*)	±0.4 K (±0.2 K*)	N/A
Lunar Dust Density	±0.1 g/cm^3	±10 K	Density Mapping (Section 5.3)
Lunar Bedrock Density	±0.1 g/cm^3	±5 K	Density Mapping
High S region (S>8)	±1	±5 K	S Mapping (Section 5.2)
Low S region (S<4)	±0.25	±5 K	S Mapping

*According to CE MRM calibration document, MRM TB error should be within ±0.25 K (*Wang et al., 2010*).

Comparing Table 4.2 with Table 4.3, we can see that TB's influence derived by two different methods nearly agree (Table 4.2 gives ±1.6 K, while Table 4.3 gives ±1.5 K), however mineralogy and density have much bigger weights than other parameters in error sources. This is the reason for a complete lunar mineralogy and density study in the next chapter.

Chapter Summary:

This chapter discusses the microwave radiative transfer forward model. A description of the microwave radiative transfer model, which is a multilayer model containing six unequal layers is provided. Deductions from the coherent method and fluctuation dissipation theorem are presented. The forward model calculation results include the following: the expected contribution of each layer in the CE-1 and CE-2 MRM brightness temperature measurements and predicted brightness temperatures (when S = 10%, 25%); a rough average of the equatorial vertical subsurface temperature curve generated using average S = 10% (*Lunar Sourcebook, 1991*); a comparison of the forward model results and the lunar thermal environment measured by the Diviner. Diviner results are also used as boundary conditions in the inverse part.

Our inputs in the radiative transfer model include the following: (1) density depth profile, (2) surface and bottom layer temperature, and (3) mineralogical information (dielectric permittivity), including TiO_2 and FeO contents (%). Subsequently, an error is attributed to these parameters in the inversion. Such error is estimated based on each parameter's uncertainty and its differential relationship with the TB and subsurface temperature.

Monte Carlo methods (or Monte Carlo experiments) are a broad class of computational algorithms, which rely on repeated random sampling to obtain numerical results. The effect of the trade-off of the different input parameters against each other on the modelled temperature is explored using the Monte Carlo approach. This technique is important in showing how the different elements of the model affect retrieval.

Chapter 5. Data sources for inclusion in the improved Forward Model

5.1. Chapter Introduction

Mineralogy can significantly change the penetration depth of microwave signals. The sensitivity analysis in the previous chapter indicates that knowledge of the Fe/Ti abundance (particularly Ti) and bulk density are particularly important to the proposed forward model (chapter 4). Moreover, a variation in the bulk Maria and highlands mineralogy is evident in the TB from the MRM data, as the difference in composition modifies the effective microwave emission depth (Figure 5.1). Smaller penetration depth occurs in the Maria regions as they typically have a higher FeO and TiO_2 content than the highland regions (*Lunar Sourcebook, 1991*).

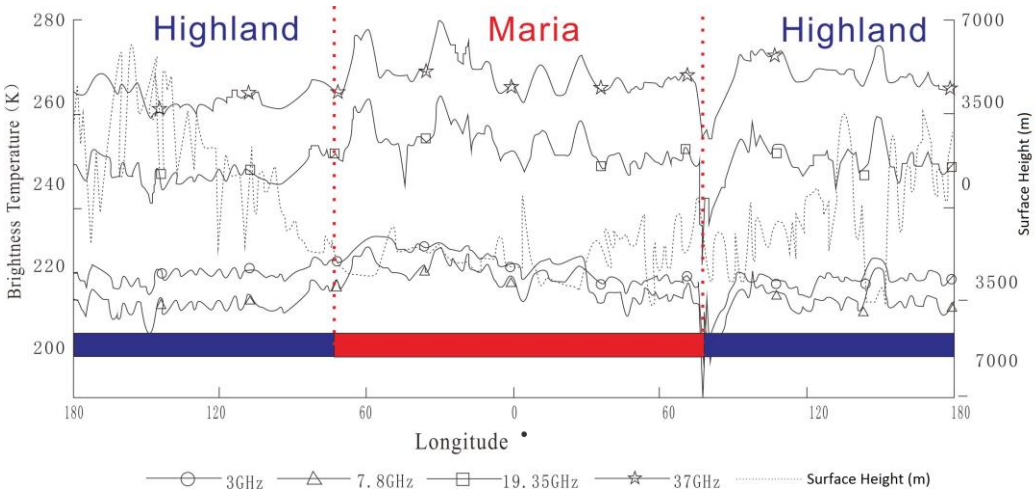

Figure 5.1. MRM TBs of the equatorial region at different longitudes and surface heights at lunar midday. In Maria regions (red highlight), TBs are significantly higher during the daytime than in the highland region (blue highlight) due to the difference in mineralogy changing the penetration depth of the microwave emission.

In this chapter, mineralogical and bulk density information are added to the thermal transfer model, including the effects of varying Fe/Ti composition and varying density profiles across the Moon. To allow the inclusion of Fe/Ti composition a global map is required. The first part of this chapter is therefore concerned with the development of a method for deriving FeO and TiO_2 content from the data measured by the Moon Mineralogy Mapper (M^3) instrument (Figure 5.2) on the Chandrayaan-1 mission.

The FeO and TiO_2 spatial distribution across the lunar surface was originally mapped by the Clementine ultraviolet–visible/near-infrared (UV/VIS/NIR) spectrometer (*Nozette et al. 1994*) and in this chapter it will be further mapped by the M^3 instrument.

Data from M^3 (instrument details are listed in Table 5.1) contains a wider spectral range (more compositional information), higher spatial (70 m/pixel target mode, 140 m/pixel global mode, while the Clementine is 1 km/ pixel) and spectral resolution (256 channels target mode, 85 channels global mode, while Clementine only has 5 channels) (*Pieters et al., 2009*) and has a more well defined calibration scheme than the Clementine data (*Clark et al., 2010*). Therefore, it has significant potential advantage when compared with previous products derived from the Clementine mission and ground-based observations. These advantages of the M^3 data provide an opportunity to improve the accuracy of previous global elemental abundance maps

derived from Clementine (which had large uncertainties) and also provide an important test of different reduction approaches (*Lucey et al., 1995, 1996, 1998, 2000; Blewett et al., 1997; Shkuratov et al., 1999; Pinet et al., 1997*). This research tests the validity of the Clementine-derived maps and Ti/Fe composition models.

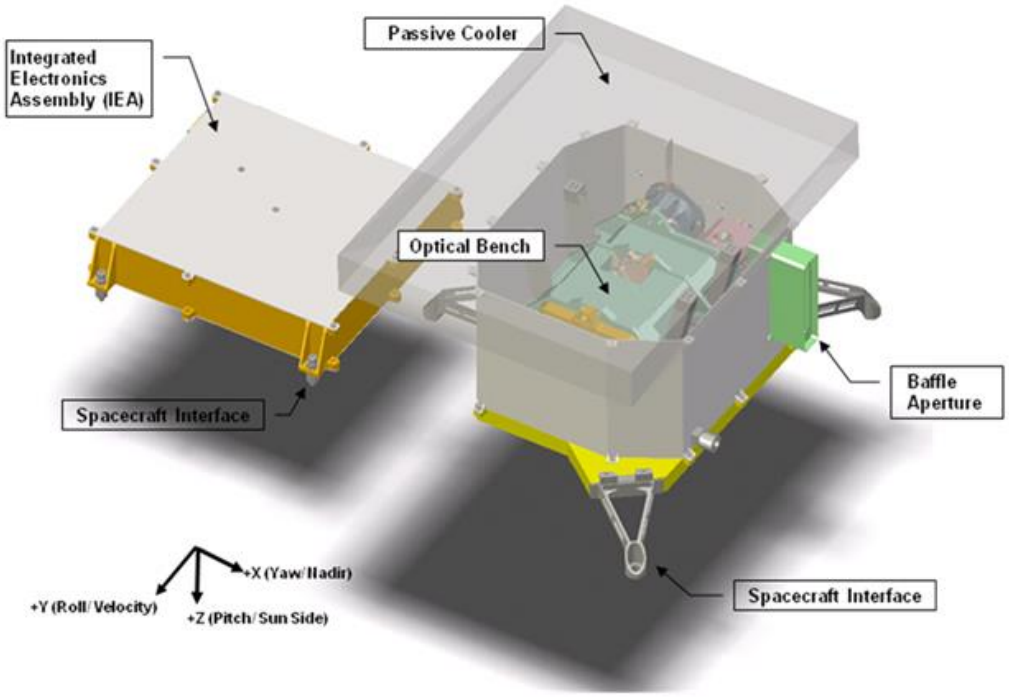

Figure 5.2. M^3 that flew on board on India's Chandrayaan-1 Mission from October 2008 through August 2009 (*Boardman et al., 2011*). Compared with Clementine, M^3 contains a wider spectral range (*Boardman et al., 2011; Green et al., 2011*). The size of M^3 instrument main body is 40 cm ×30 cm.

Table 5.1. M^3 scientific data acquisition sheet and basic performance index.

Name	Index
Wavelength range	~430 to 3000 nm
Global Mode Spatial Resolution	140 to 280 m/pixel
Global Mode spectral capability	85 spectral bands
Target Mode Resolution	~70 m/pixel
Target Mode spectral capability	256 spectral bands
Mission Start Date	October 2008
Mission End Date	late August 2009
Coverage	95% of the Moon in its global mode (*Boardman et al., 2011*). Shown in Figure 5.3 below.

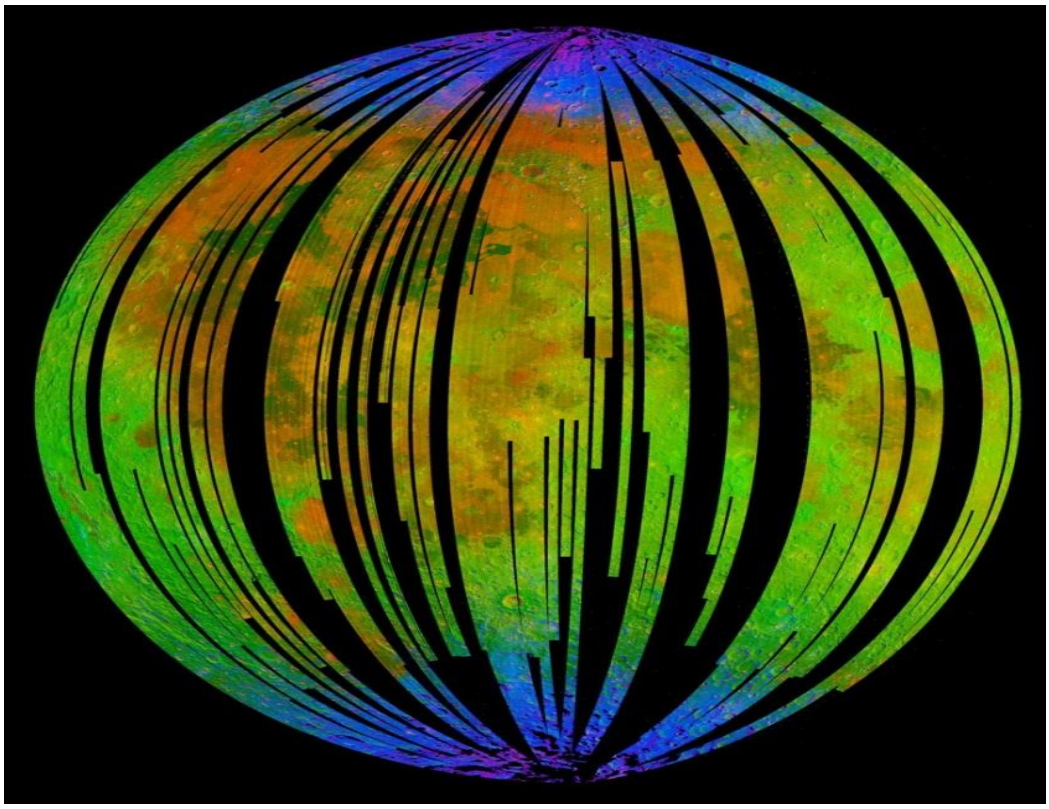

Figure 5.3. Coverage of M^3 dataset in global mode, containing all available optical periods. Blue indicates the signature of water, green shows the brightness of the surface, and red indicates iron-bearing minerals.

Despite the potential for improvement over the Clementine dataset there are factors complicating the data reduction process that need to be discussed. First, the M^3 dataset is large (3.63 TB), requiring a long time for the completion of data reduction, in particular reformatting the data requires about 1 month on a typical desktop computer. Secondly, the M^3 dataset contains several known anomalies. The Chandrayaan-1 spacecraft experienced a diverse range of non-nominal thermal and field-of-view (largely pointing) conditions while acquiring the M^3 data (*Boardman et*

al., 2011). Solar illumination of the lunar surface affected the measured signal level, strongly affecting the spacecraft environment and operations, and consequently affected the temperature of the M^3 detector. Several data correction programs were developed to address such limitations by removing noise sources, repairing banded anomalous data tracks, and cleaning up the data (*Kim et al., 2016*).

Additional details of the operation aspects of the M^3 instrument during lunar mapping are given by Boardman et al. (*2011*), and details of the M^3 instrument design and capabilities are presented by Green et al. (*2011*). Calibrated M^3 data can be downloaded from the NASA PDS node: http://pds-imaging.jpl.nasa.gov/volumes/m3.html.

5.2. Lunar Surface Mineralogy Retrieval

5.2.1. Overview of Previous Ti and Fe Retrieval Methods

The abundance and spatial distribution of both Ti and Fe is important in understanding the petrogenesis of lunar rocks and thus, the nature and origin of the Moon (*Lucey et al. 1998*).

The VIS–NIR reflectance characteristics of the Moon are sensitive to chemical, mineralogical, and physical properties of lunar regolith and have been widely used in

lunar geological explorations (*Lucey et al., 2006*). Many models have been suggested to quantify Fe and/or Ti abundances from Clementine's UV/VIS images (*Lucey et al., 1995; Lucey et al., 1998; Lucey et al., 2000; Blewett et al., 1997; Lawrence et al., 2002; Gillis et al., 2004;*). None of the authors provided content retrieval errors of Clementine FeO or TiO_2 abundances in their papers (*Lucey et al., 1995; Lucey et al., 1996; Lucey et al., 1998; Lucey et al., 2000; Blewett et al., 1997; Shkuratov et al., 1999*). Among these models, Lucey's model (*Lucey et al., 1995, 1996, 1998, 2000*) has been one of the most popular and has undergone a series of refinements. As more mission datasets become available (e.g., Kaguya from Japan, Chang'E-1 from China, Chandrayaan-1 from India, and Lunar Reconnaissance Orbiter from United States) (*Pieters et al., 2008*), a comparison of the results from these datasets as well as the refinement of FeO mapping algorithms will continue to improve global map estimates of Fe/Ti abundances. Previous efforts by other authors to derive compositional information on lunar FeO and TiO_2 abundance from spectrometry were briefly reviewed by *Lucey et al. (1995, 1998)* and are summarized here.

Lucey et al. (1995) introduced a method to determine the Fe content of the lunar surface using the Clementine reflectance data at 750 nm and the ratio of reflectance at 950 nm (NIR) and 750 nm (VIS). *Lucey et al. (1995)* noted a trend with Fe content and maturity in the NIR/VIS ratio versus the VIS reflectance for returned lunar samples (Figure 5.4). *Lucey et al. (1995)* placed an origin near the intersection of

these maturity trends, and a characteristic spectral angular parameter was used to estimate composition information. Such an angular parameter was defined for the location of a sample in the ratio–reflectance plot as the angle between a horizontal line through the origin and a line defined by the origin and the location of each point on the plot (Figure 5.4). The relationship between the Fe content and the angular parameter of the samples was used to provide the composition. *Lucey et al. (1995)* produced a global image of lunar Fe abundance by applying these relationships to early Clementine UV/VIS multispectral data.

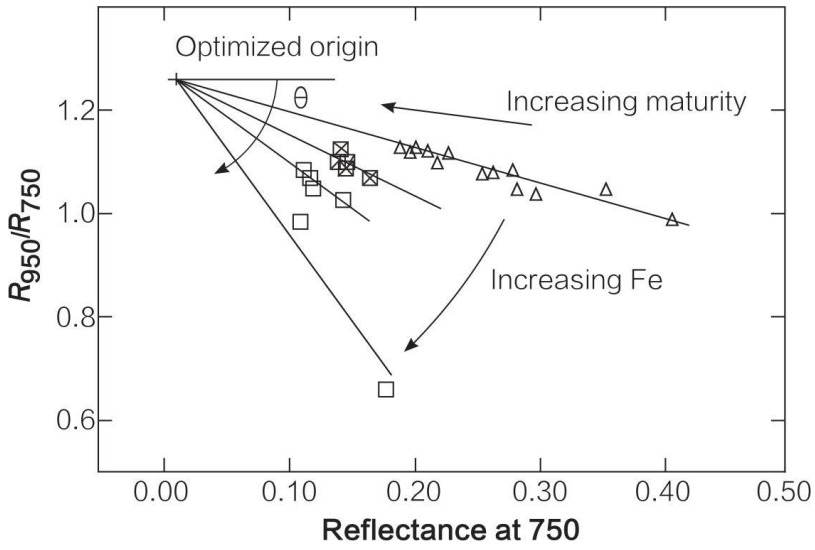

Figure 5.4. Triangles are Apollo 16 soils; boxes are Apollo 15 soils. The contrasting spectral behavior of maturity and total Fe is clearly illustrated. The Lucey method is based on following facts: (1) an absorption band of 750 nm – the 750 nm reflectance decreases with the increase of lunar soil maturity; (2) the ratio of reflected 950 nm / 750 nm increases with lunar soil maturity; (3) both the overall reflectance of 750 nm and the ratio of R950/R750 decrease as Fe increase; and (4) the position of the origin depicted was optimized to maximize the linear correlation between the characteristic angle parameter and bulk iron content, hence is named as the ‘optimized origin’.

Current research on determining the Ti abundance of the lunar surface using M^3 data is limited (*Dhingra et al., 2010*). As M^3 does not have the 415nm channel which was used by *Lucey et al (1998)* to retrieve Ti, I examined two different approaches to derive the abundance and distribution of lunar Ti in this chapter: 1) using the methods of *Shkuratov (1999)* and 2) revising *Lucey* (1998) by adapting the method to the M^3 spectral channels. The first approach was validated within *Shkuratov* (1999). The second approach was validated using ground truth from both Apollo data and samples from various Apollo landing sites. After adding this a priori elemental information to the radiative transfer model, the results were used to calculate spatial variations in the density of the lunar soil bedrock in section 5.3.

5.2.2 Iron Content Retrieval

To recap, using the data from the Clementine instrument, *Lucey et al. (1995)* applied the spectral characteristic angle method which is based on the following phenomena: (1) an absorption band of 750 nm – the 750 nm reflectance decreases with the increase of lunar soil maturity; (2) the ratio of reflected 950 nm / 750 nm, which increases with lunar soil maturity; (3) both the overall reflectance of 750 nm and the ratio of R950/R750 (Figure 5.4) decrease as Fe increase; and (4) the position of the

origin depicted (at 1% reflectance and a ratio of 1.26 in Figure 5.4) was optimized to maximize the linear correlation between the characteristic angle parameter and bulk iron content, hence is named as the 'optimized origin' or 'apparent origin'. Lucey summarized these effects on the spectral slope by developing plots that are similar to those shown in Figure 5.4 and 5.5, which were cited from *Lucey's 1995* paper. Based on the above characteristics, Lucey et al. (*Lucey et al., 1995; Blewett et al., 1997*) developed the spectral characteristic angle method for FeO content retrieval while mapping Clementine UV/VIS data.

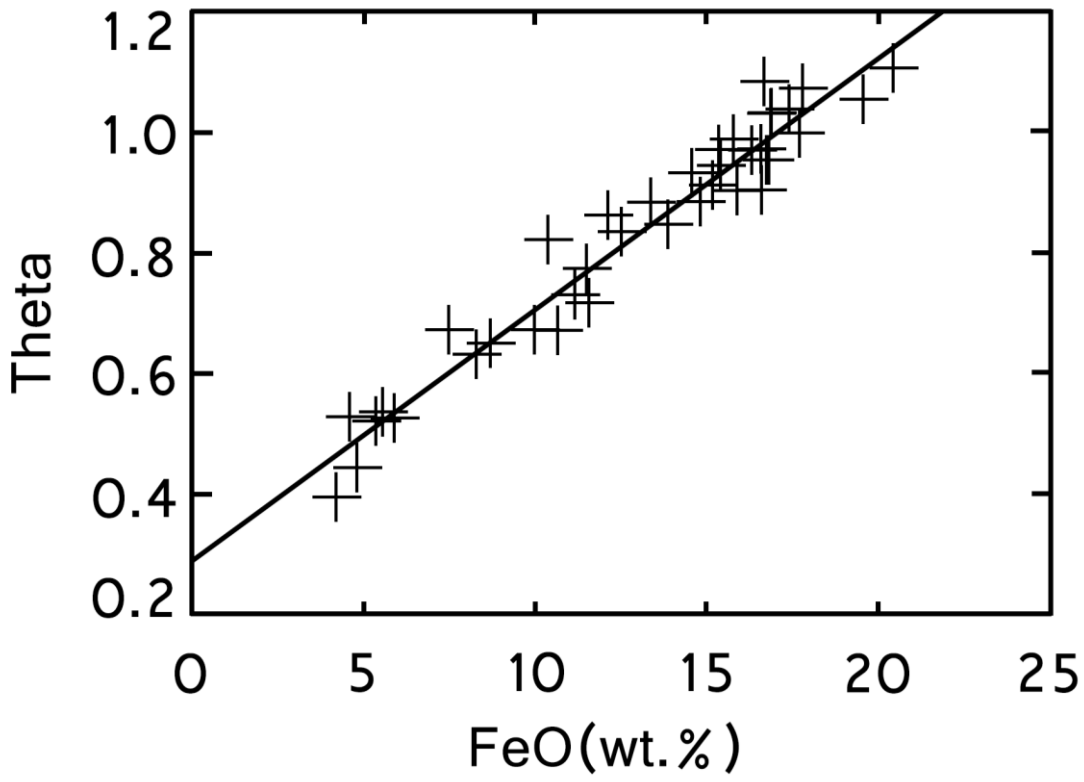

Figure 5.5. Plot of the Fe spectral characteristic angle parameter (θ_{Fe}) computed from Clementine spectral data of sampling sites and stations versus the average FeO content of soils returned from each site or station, taken from *Blewett et al. (1997)*.

The formula to calculate FeO content is provided as follows (*Lucey et al., 1995*):

$$\theta_{Fe} = -\arctan\left(\frac{R_{950}/R_{750} - 1.26}{R_{750} - 0.01}\right) \quad \text{(Eq. 5.1)}$$

$$FeO\% = 17.83 \times \theta_{Fe} - 6.82 \quad \text{(Eq. 5.2).}$$

All data in Eqns. 5.1 and 5.2 are available and can be extracted from M^3 data. However, M^3 data were resampled to fit the Clementine instrument's spectral grid for better precision using Matlab's interpolation function. The difference is smaller than 1% (Figure 5.6). Hence, applying Lucey's model, which was originally derived for Clementine data, for use with the M^3 dataset is reasonable.

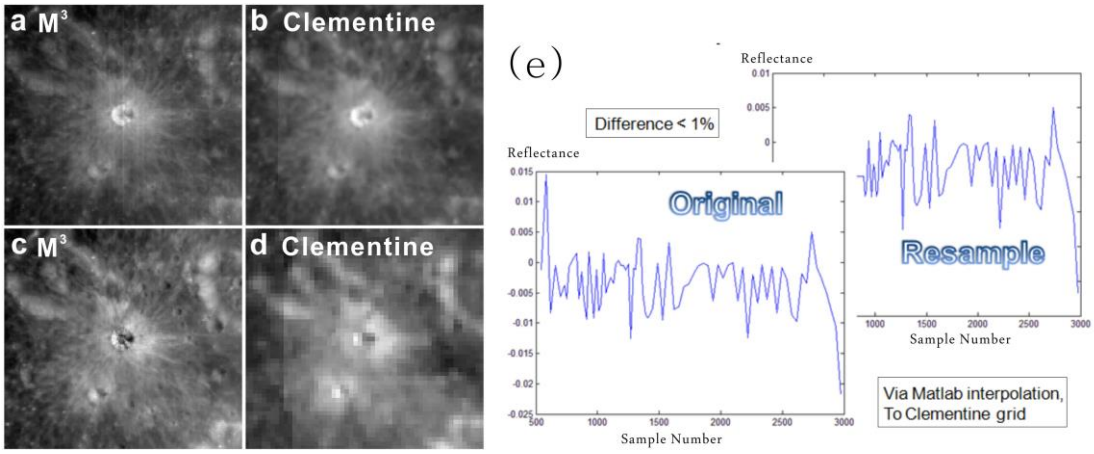

Figure 5.6. Zoom of small crater located at ~3.5 ºS and 35.5 ºE. Each frame is 6.8 km across. Selected to compare spatial resolutions of (a) M^3 at 750 nm reflectance and (b) Clementine's UV‐VIS camera at 750 nm reflectance, (c) M^3 at 2020 nm, and (d) Clementine's NIR camera at 2000 nm; (a –d are cited from *Kramer et al., 2011*) (e) Resampling of M^3 data to Clementine grid. Comparison with original data shows that the difference is within 1%. Hence, Eqns. 5.1–5.2 can be used with M^3. A random selection of 10 different spectra is used for demonstration.

I analyzed the FeO content based on M^3 data according to Eqns. 5.1–5.2. Lunar FeO content varies from 0 wt.% to 20 wt.% (Figure 5.7). However, the upper limit of 20% is a limitation of the model from *Lucey et al.(1995, 1998*) related to band-depth saturation of laboratory spectra of terrestrial mineral samples. The new result has been compared to the Clementine Fe retrieval map to validate these methods and show the datasets are consistent (Figure 5.7). From Figure 5.7 it is possible to see visually that the two sets are in general agreement. There are some artifacts in the derived FeO distribution from the M^3 data set due to the different optical periods used and the lack of complete global coverage. However, further comparative analysis is not possible as *Lucey et al.(1995, 1998*) did not provide any error estimations for their retrievals.

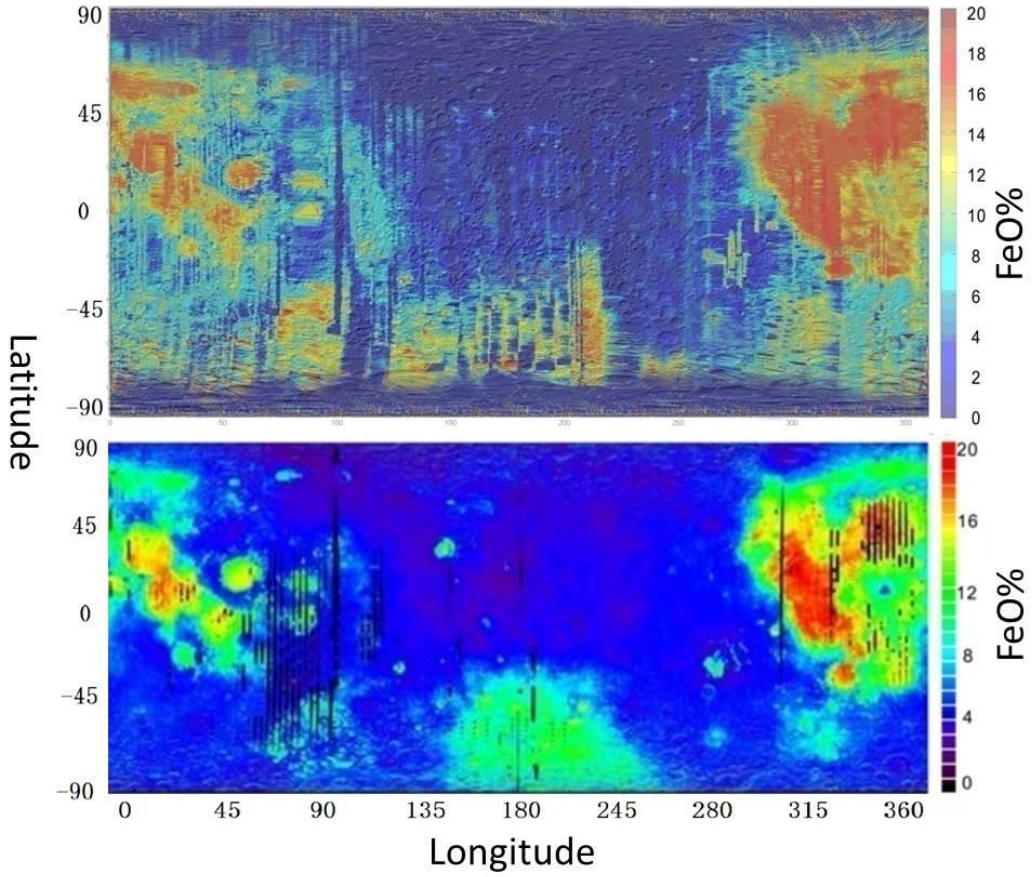

Figure 5.7. (Top) Retrieved FeO content from M^3 over plotted on a Clementine base map. Fe content is between 0%–20% in this map. Several artifacts remain in this plot; they come from the M^3 optical period. (Bottom) Clementine FeO map.

The derived Fe distribution from the M^3 data has also been compared with the Lunar Prospector Fe mapping results in Figure 5.8. The Lunar Prospector dataset, which contains the first global measurements of gamma-ray spectra from the lunar surface, is the first direct measurement of the chemical composition of the entire lunar surface (*Lawrence et al., 2007, 2002*). Hence, it differs from other remote sensing methods and is a good standard against which to check both the Clementine and M^3 retrievals.

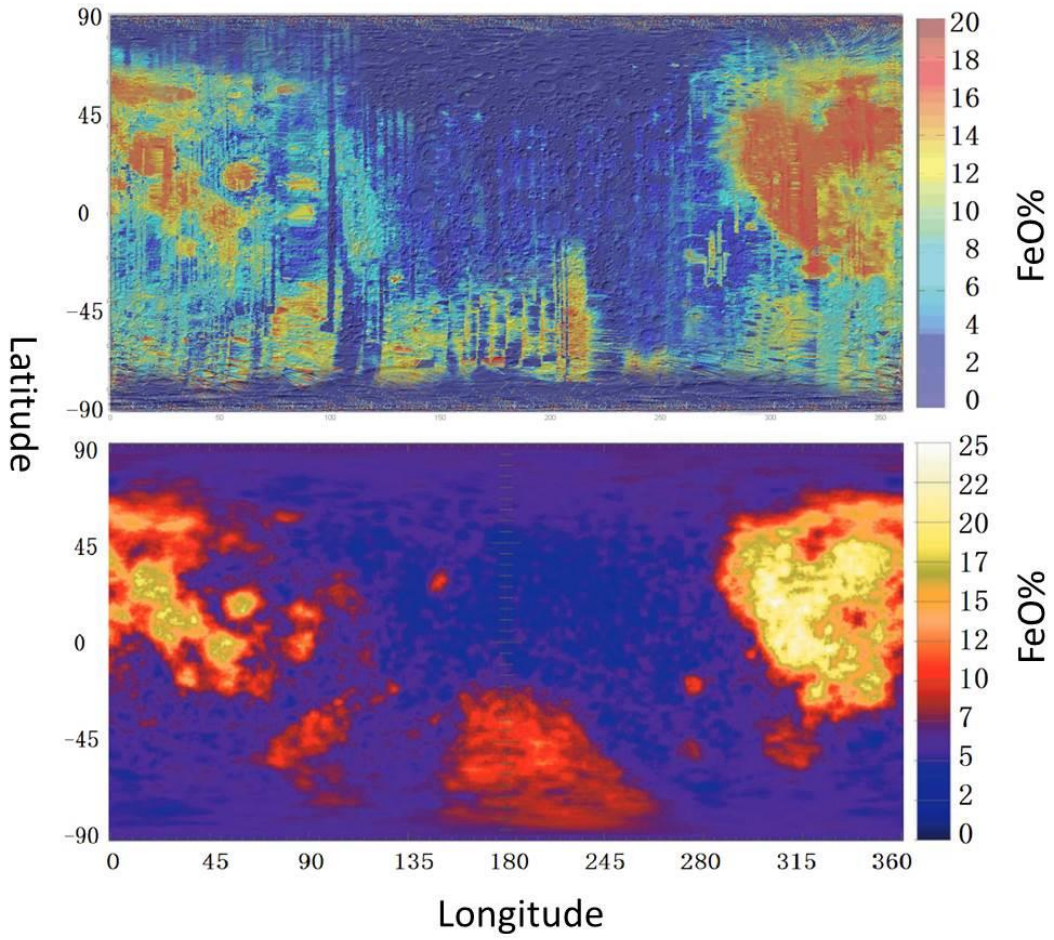

Figure 5.8. Comparison of retrieval result of FeO content from the M^3 (top, over plotted on a Clementine base map) with Lunar Prospector Fe map (below) (*Lawrence* et al., 2002). (Labels of scale bar: Fe%).).

The *Lucey et al., (1995, 1998*) model has been compared with the Lunar Prospector FeO abundance map and they have been found to agree within ±6% (*Lawrence et al., 2002a*). Using this as a crude error analysis, the retrievals of the M^3 and Clementine/Lunar Prospector are also consistent (within ±6%). Such consistency validates the methods used. Several small features that are noticeable on the M^3 are

not seen on the Clementine or Lunar Prospector results, as the M^3 has a much higher spatial resolution than the other two datasets. Furthermore, the M^3 and Clementine results seem to have more artifacts than the Lunar Prospector, as the Lunar Prospector results are a more direct measurement (*Lawrence et al., 2002a*), appearing smoother due to a lower resolution.

5.2.3 Titanium Content Retrieval and Methods

For the TiO_2 content retrieval, Lucey's method (*1998*) also introduces a simple relation between the UV/VIS ratio (415 nm/750 nm) and TiO_2 content. However, an alternative method is required because the M^3 does not include a 415 nm band. The 256 channels that are available in the M^3 data allowed for investigation of other approaches that were inaccessible from the Clementine data, which were more spectrally limited. Two different TiO_2 analysis techniques were applied to the data and are described below.

5.2.3.1. First Approach: Shkuratov model

Using a correlation diagram of FeO–TiO_2 for the lunar nearside, Shkuratov et al. (*1999*) studied the relationship between FeO and TiO_2 abundance. FeO% and log(TiO_2%) have a high correlation coefficient of 0.81. The regression equation is as follows:

$$\log(TiO_2\%) = 0.06(FeO\%) - 0.54 \quad \text{(Eq. 5.3)}$$

The content of surface TiO_2 based on M^3 data according to Eq 5.3 was plotted in Figure 5.10. A comparison with the Clementine result is also provided in Figure 5.9.

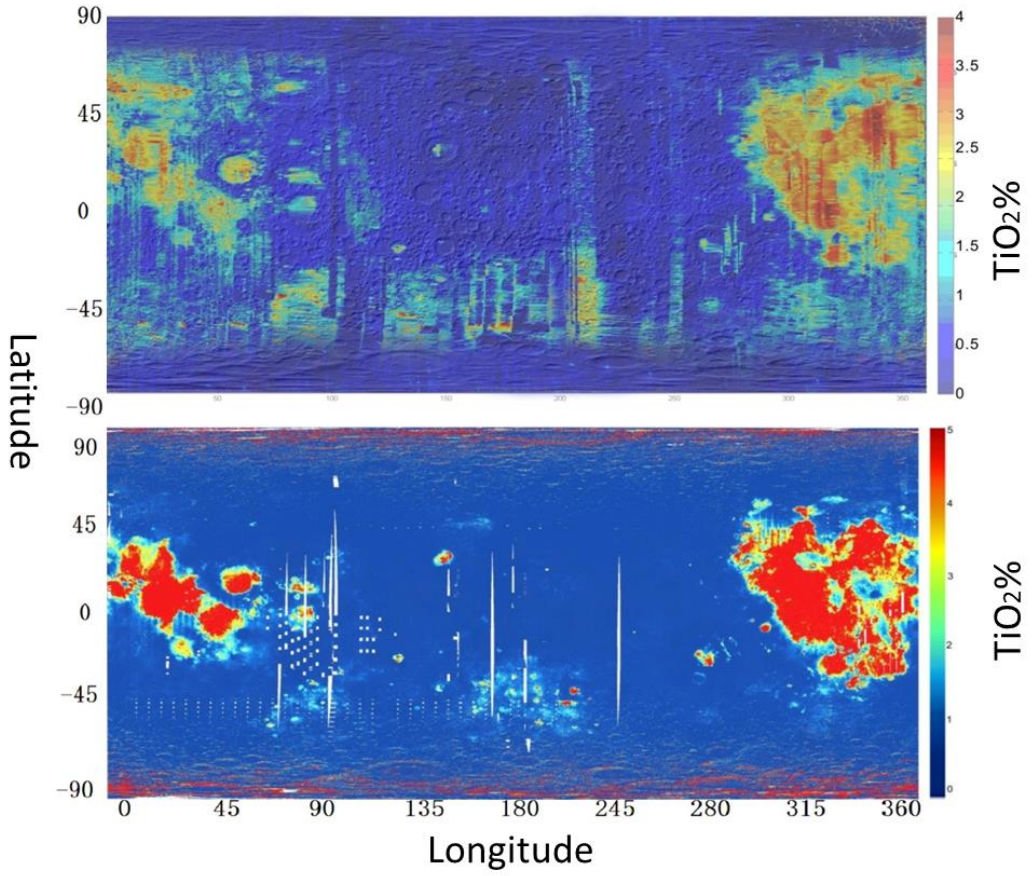

Figure 5.9. (Top) Retrieval result of TiO_2 content derived using the Shkuratov model from the M^3 FeO map shown in Figure 5.7, over plotted on a Clementine base map; (Bottom) Clementine titanium map (*Korokhin et al, 2008*).

The Shkuratov method is a mathematical regression and has been validated by FeO and TiO_2 measurements from telescopic spectra and laboratory chemical data for the Apollo landing sites (Figure 5.10) *(Shkuratov et al., 1999)*.

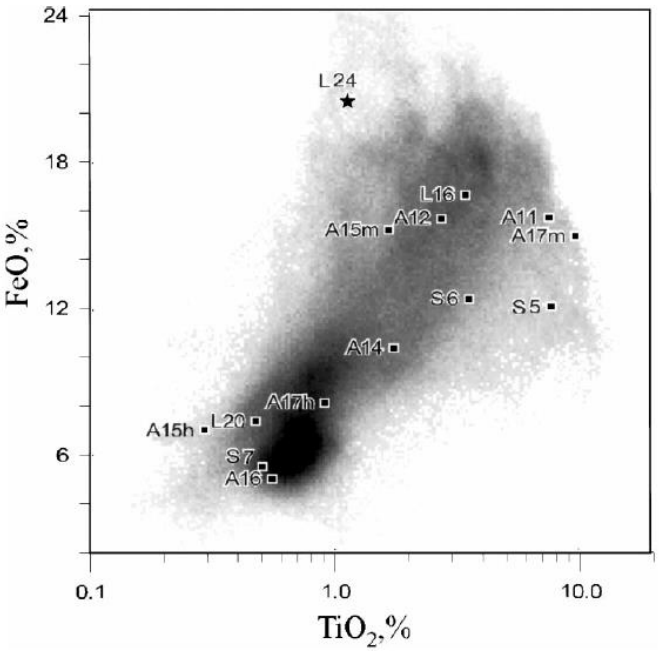

Figure 5.10. Correlation diagram of FeO% and log(TiO_2%) of the lunar nearside. Data points for the Surveyor, Luna, and Apollo landing sites are labeled (*Shkuratov et al., 1999*). Telescope data points are shown as black dots.

The Shkuratov relationship *(Shkuratov et al., 1999)* can be explained for the lunar surface as ilmenite is the main TiO_2 bearing mineral and also contains FeO. *Bhatt et al. (2011*) also correlated FeO abundance to TiO_2 content (both in %) and absorption band parameters using data from an infrared spectrometer (SIR-2) on Chandrayaan-1:

$$FeO\% = 63.94 \times (B + 0.518 \times S) - 5.24 + 0.92\,TiO_2\,\%, \quad \text{(Eq. 5.4)}$$

where B is absorption band depth, and *S* is the continuum slope. The correlation factors are 0.90 and 0.96 for 2 μm and 1 μm absorption bands, respectively. Such correlations may be related to early lunar geology, which has yet to be studied thoroughly.

5.2.3.2. Second Approach: Characteristic angle approach.

A new preliminary model was developed in this research based on ground truths using the samples from Apollo and Luna sites. This model allowed for the production of a Ti abundance map from M^3 images, which analyzes data by using a characteristic angle approach similar to that of Lucey et al. (*1995*). The principles of Lucey et al. *(1995, 1998)* were utilized, but were applied to M^3 spectral bands, so the 540 nm channel was used instead of the 415 nm channel, which the M^3 does not have.

Lunar Ti occurs mainly in the opaque mineral ilmenite ($FeTiO_3$) (*Lunar Sourcebook 1991*). Ilmenite has distinctive reflectance characteristic in the UV/VIS spectrum. As seen in Figure 5.11, ilmenite has two main absorption bands at 500 nm and 1500 nm. The 540 nm M^3 spectral channel is close to the absorption center of the first band and the 750 nm M^3 spectral channel is found near a reflectance maxima between two bands. The 500 nm band is principally due to the Ti^{3+} ion that is octahedrally coordinated to oxygen and is predicted to produce crystal-filed bands in the visible region (*Cloutis et al., 2008)*. This 540 nm position is also observed in lunar ilmenite sample 74220 (*Vaughan and Burns, 1973*) and was attributed to Ti^{3+} (*Vaughan and Burns, 1973)*. Thus, using the nearby spectral channel (540 nm) of the M^3 to predict the Ti content of the lunar surface is reasonable. The new model uses the M^3 540 nm (red line in Figure 5.11) channel as a replacement for the 415 nm channel used in the

clementine retrieval. Both Clementine and M^3 have a 750 nm channel (blue line in Figure 5.11), so the wavelength used in the two techniques is the same.

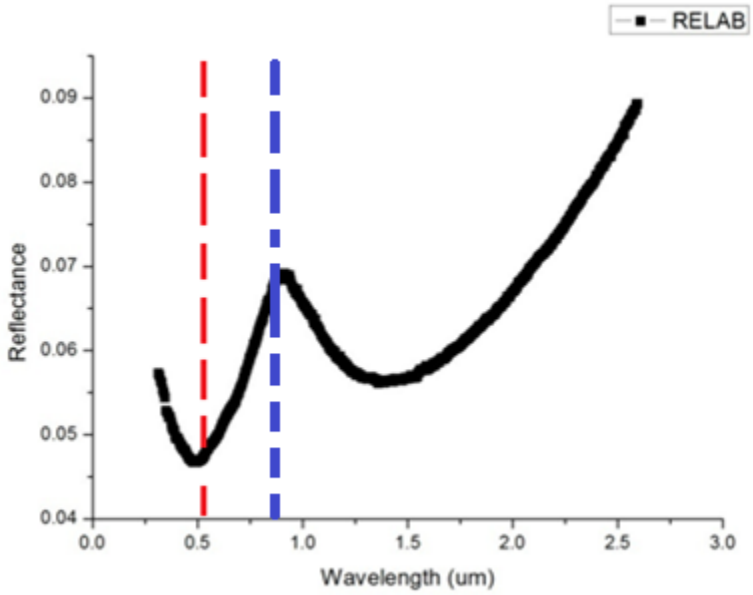

Figure 5.11. UV/VIS/NIR spectrum of ilmenite from Brown University's RELAB (sample number: PI-CMP-006/C1PI06). Available at: www.planetary.brown.edu/relabdata/data/cmp/pi/c1pi06.txt This sample is representative of other samples in the RELAB ilmenite catalogue, and the observation geometry for the sample is the same as that of the M^3 PDS data. The spectral range of M^3 is 415 nm to 2,976 nm (0.4 μm to 3.0 μm). The red dashed line corresponds to the M^3 540 nm channel, and the blue dashed line corresponds to the M^3 750 nm channel.

Using the 540 nm and 740 nm M^3 channels, a similar characteristic angle to *Lucey (1998)* was calculated. The chemical contents of the lunar soil samples returned by the Apollo and Luna missions were then used as ground truths. This approach attempts to correlate the laboratory TiO_2 contents of typical lunar returned soils with

the remotely sensed multispectral images using a technique based on Lucey et al. (*1995, 1998, 2000*). The criteria used to select the M^3 data is outlined in Table 5.2.

Table 5.2. Selection criteria and reasoning of the M^3 data used in the TiO_2 abundance analysis.

	Criteria	**Reason**
Step 1	Search for regions near Apollo and Luna lunar landing sites with the widest spread of TiO_2 content. Apollo and Lunar landing sites with no TiO_2 content are ignored.	The largest range of TiO_2% is used to reduce error.
Step 2	Within the selected regions of Step 1, search for craters with a relatively small diameter (<10 km) and high albedo (>50%).	Small craters with high albedos are generally fresher and as a result are less likely to be contaminated by ejector blankets from other impacts.
Step 3	Within results of Step 2, find the craters that have distinct rays.	Distinct rays in the crater ejecta also indicate relatively new craters. From the center outward along the radiation pattern, TiO_2 content remains equal, whereas maturity increases.
Step 4	Within results of Step 3, find M^3 data points measured at 750 nm and 540 nm.	Plotting the M^3 data using the same technique as *Lucey (1998)* (Figure 5.14) allows the characteristic spectral angular parameter to be calculated.

All the available returned samples from the Apollo and Lunar missions whose landing sites were selected in step one (Table 5.2) were used in the data analysis. This was a total of 91 samples including 68 from the Apollo missions and 23 from the Luna missions. Due to the limited number of available returned samples no selection criteria was used to select the Apollo or Luna samples. This could potentially introduce bias into the analysis as in steps 2 and 3 the M^3 data used was not selected randomly compared to the returned samples which are assumed to have been chosen at random. However, steps 2 and 3 are required to insure the region of interest has not been contaminated by ejector blankets from other impacts, therefore this potential bias is unavoidable in these techniques.

There is further bias in the returned Apollo samples as they generally contain low TiO_2 (this is discussed further in section 5.2.4 – only 4 samples contain >8% TiO_2). Unfortunately due to the limited number of the returned samples it is not possible to remove this bias.

After selecting the M^3 data and the Apollo/Luna returned samples, the reflectance in the 750 nm channel and the ratio of the reflectance in the 540 nm / 750 nm channel was plotted (Figure 5.12). It is clear from the scatter plot in Figure 5.12 that the selected data at different landing sites converge in an optimized origin in a similar way to the previously discussed FeO/TiO_2 abundance analysis by *Lucey et al.* (*1995,1998*) using the Clementine data (Figure 5.4). Based on Figure 5.12, the coordinate of the optimized origin is calculated: X0 = 0.163, Y0 = 0.57.

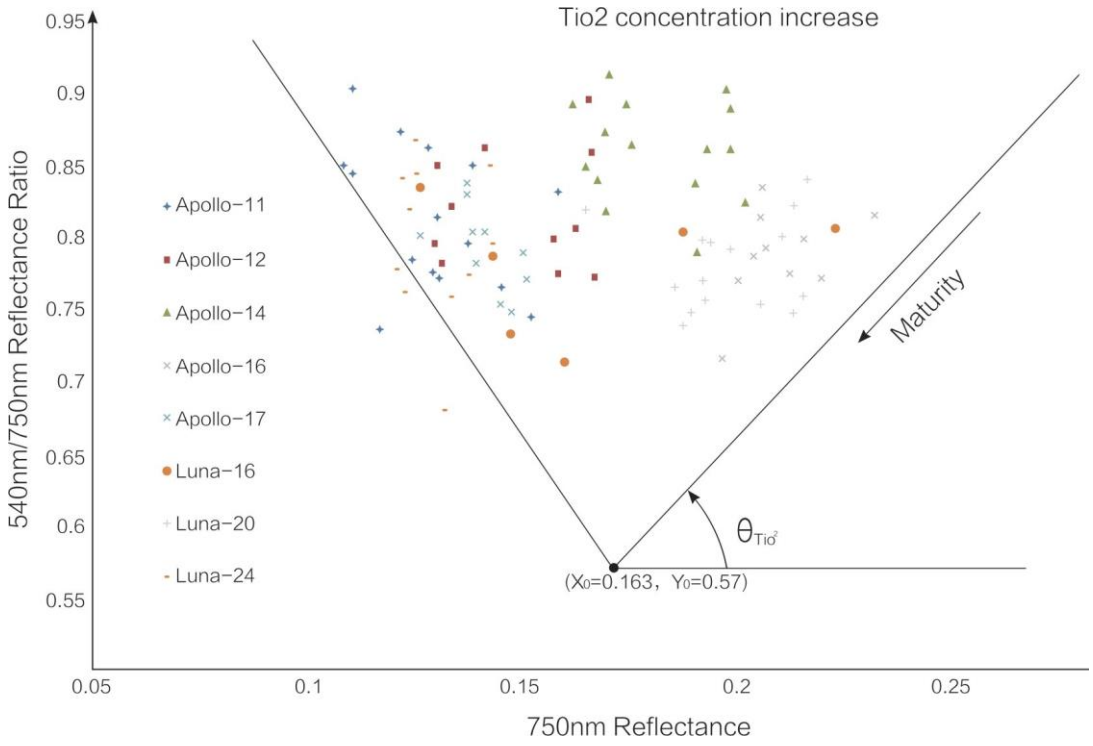

Figure 5.12. Scatter plot of the spectral reflectance ratio (540 nm/750 nm) vs reflectance (750 nm) from micro-craters around Apollo sampling points.

When the reflectance at 750 nm is greater than 0.163, the TiO_2 angle calculation formula is written as follows:

$$\theta_{TiO_2} = \arctan\left(\frac{\frac{R_{540nm}}{R_{750nm}} - 0.57}{R_{750nm} - 0.163}\right). \quad \text{(Eq. 5.5)}$$

When the reflectance at 750 nm is less than 0.163, the TiO_2 angle calculation formula is written as follows:

$$\theta_{TiO_2} = \pi - \arctan\left(\frac{\frac{R_{540nm}}{R_{750nm}} - 0.57}{0.163 - R_{750nm}}\right). \quad \text{(Eq. 5.6)}$$

When the reflectance at 750 nm=0.163, the TiO_2 angle is $\theta_{TiO_2} = 1.57$.

Following the method of *Lucey et al (1995,1998,2000)*, a statistical relationship was built between the TiO_2 angle and the TiO_2 content of the Apollo/Luna returned samples measured in the laboratory by chemical analysis. The statistical relationship was derived using a least squares fitting algorithm (Figure 5.13) and found to be:

$$TiO_2\% = 0.1089 \times \theta_{TiO_2}^{6.6535} \quad \text{(Eq. 5.7)}$$

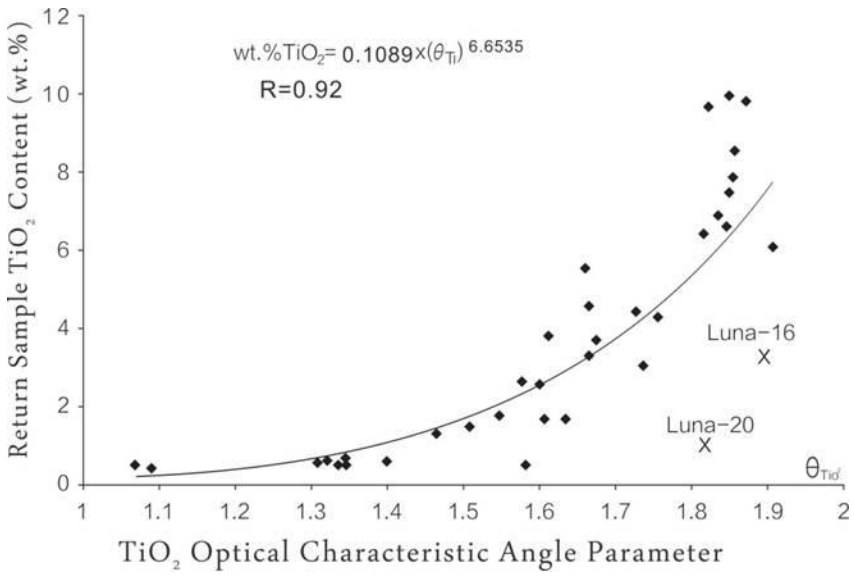

Figure 5.13.Fitting of TiO_2 content against the TiO_2 characteristic angle parameter. Errors of the plotted data are evenly distributed and will not affect the fitting.

Compared with the actual value of the points used to generate the fit, the derived relationship has a high correlation coefficient of 0.92. Using Eq. 5.7, analysis of the TiO_2 content from M^3 data was made and Figure 5.14 shows a comparison of the retrieved TiO_2 content using the two different methods discussed in this chapter, e.g.

the adapted *Lucey et al.,* (*1995,1998)* method and the *Shkuratov et al., (1999)* method.

From Figure 5.14 it can be seen that the *Shkuratov et al., (1999)* method produces much lower TiO_2 abundances than the *Lucey et al., (1995,1998)* method. This is a systematic deviation that can also be observed from *Shkuratov et al., (1999)* and the *Lucey et al., (1995,1998)* papers as the former method presented much lower Ti abundance (0 – 9%) than the latter (0 – 18%). As the returned Apollo and Luna samples generally have very low TiO_2 abundances (only 4 returned samples have $TiO_2 > 8\%$, most samples contain 1-3% TiO_2), the *Shkuratov et al., (1999)* method is preferred. Also given that the *Lucey et al., (1995, 1998)* method operates only with two reflectance's, the *Shkuratov et al., (1999)* method is preferred as it uses more reflectance data including telescopic data.

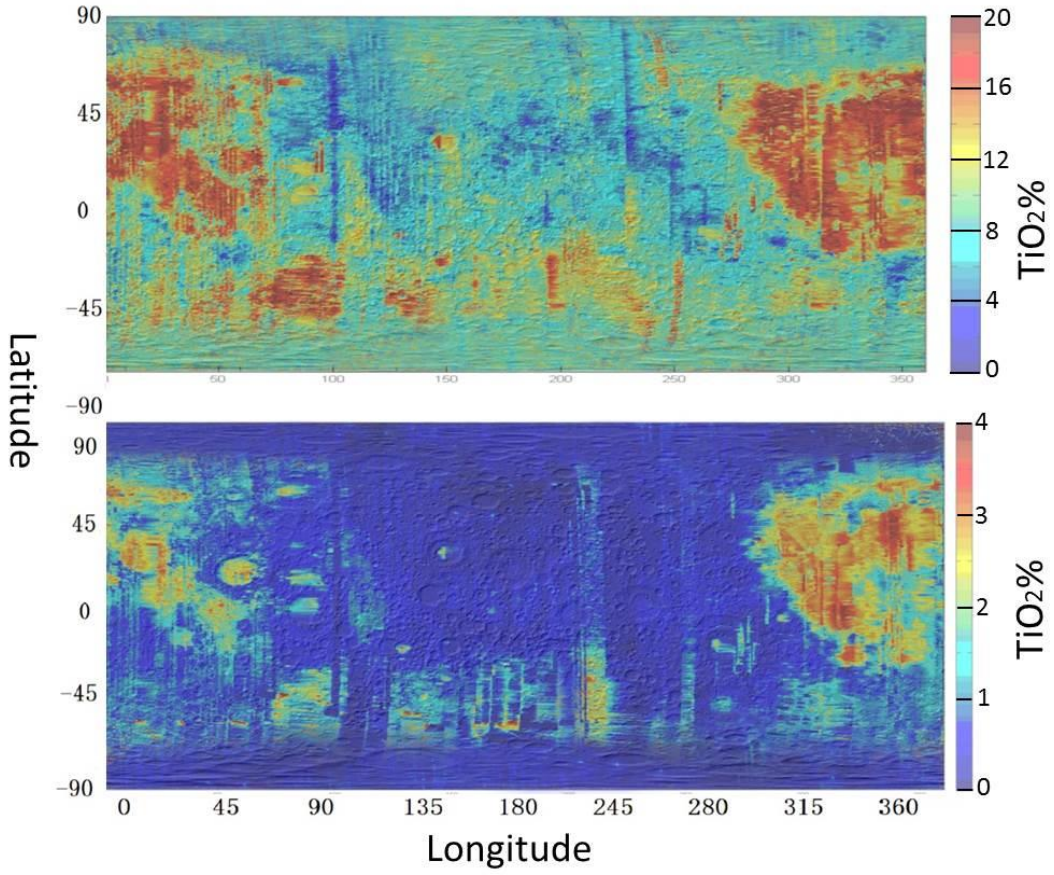

Figure 5.14. Comparison of retrieved TiO_2 content derived from M^3 by the author using two different approaches, where (a) is the result of the Lucey-like approach (second approach, Section 5.2.3.2) and (b) is the result of the Shkuratov approach (first approach, Section 5.2.3.1). Both maps are over plotted on a Clementine base map.

5.2.4. Using a comparison with returned lunar soil samples from Apollo, Luna, and Surveyor landing sites to estimate error

Comparison of the M^3 derived FeO and TiO_2 abundances with values measured from the returned samples of various landing sites is possible (*Shkuratov et al., 1999*; Table 5.3). Table 5.3 compares the FeO and TiO_2 abundances of returned Apollo/Luna

samples with the derived M^3 TiO_2 and FeO abundances calculated in this chapter and with the previously derived values from the Clementine data. Except for the TiO_2 abundance from two extremely high abundance samples (Surveyor 5 and Apollo 11 – 7.6% and 7.4%), the M^3 data matches the returned sample data at all other landing sites with a deviation of less than ±2.8%, based on which we can estimate the error in this approach. The discrepancy in the high TiO_2 regions is likely due to, too few high TiO_2 samples (only four samples) which limits the accuracy of the extrapolation. It is hard to compare the new approach developed in this chapter to the *Lucey et al. (1995, 1998, 2000)* Clementine derived abundances since they do not quote an uncertainty, however, the results are provide in Table 5.3 for the readers interest.

Table 5.3. Comparison with samples returned from the Apollo, Luna, and Surveyor landing sites as well as the Clementine retrieved values. Values given in bold have been calculated by the author as part of this work, all other values have been taken from *Shkuratov et al., (1999*).

Landing site	Sample TiO_2 (%)	M^3 TiO_2 (%)	*Clementine TiO_2 (%)	Sample FeO (%)	M^3 FeO (%)	*Clementine FeO (%)	References
Apollo 11	7.40	**2.23**	11.7±0.7	15.8	**14.8**	13	(*Florensky et al., 1981; Lunar Sourcebook, 1991; King E., 1976;Nawa et al., 1979*)
Apollo 12	2.68	**2.65**	6.4±0.5	15.7	**16.0**	13.5	
Apollo 14	1.72	**1.70**	1.8±0.3	10.4	**12.8**	8.6	
Apollo 15	1.64	**2.32**	1.7±0.6	15.2	**15.1**	12.9	
Apollo 16	0.55	**0.88**	0.8±0.1	5.0	**7.8**	4.0	
Apollo 17(highland)	0.90	**0.95**	3.7±1.8	8.1	**8.6**	6.9	*(LSPET, 1973)*
Luna 16	3.36	**2.71**	6.4±0.6	16.7	**14.8**	13.0	*(Florensky et al., 1981; Lunar Sourcebook, 1991)*
Luna 20	0.47	**0.74**	1.3±0.1	7.4	**6.9**	5.8	
Surveyor 5	7.60	**2.01**	N/A	12.1	**13.8**	N/A	*(Mason et al., 1970)*
Surveyor 6	3.50	**2.41**	N/A	12.4	**13.2**	N/A	
Surveyor 7	0.50	**0.75**	N/A	5.5	**6.9**	N/A	
Luna 24	1.15	**2.52**	5.0±0.5	20.6	**17.8**	15.1	*(Florensky et al., 1981), (Lunar Sourcebook, 1991)*

*Clementine TiO_2 content values and errors were obtained from *Korokhin et al.* (*2008*), and Clementine FeO content values were obtained from *Pinet et al.* (*1997*). None of the authors provided content retrieval errors of Clementine FeO in their

papers (*Hapke et al., 1991; Lucey et al., 1995; Lucey et al., 1996; Lucey et al., 1998; Lucey et al., 2000; Blewett et al., 1997; Shkuratov et al., 1999*). The error range of Clementine and M^3 should be of the same magnitude.

Table 5.3 compares the abundances of FeO and TiO_2 in the returned samples to the values derived from M^3. However, the returned samples used in this table were also used in the technique to the derived the abundance levels from the M^3 data. It would therefore be more appropriate to compare the derived M^3 abundances to returned samples that were not used in the derivation process. This is done in Table 5.4 which extracts from Table 5.3 the five samples that were not used in the derivation process.

Table 5.4. Comparison with unused soil data from the "Apollo" and "Surveyor" Landing Sites. Values given in bold have been calculated by the author as part of this work, all other values have been taken from (*Shkuratov et al., 1999*).

Landing site	Sample TiO_2 (%)	M^3 TiO_2 (%)	*Clementine TiO_2 (%)	SampleFeO (%)	M^3 FeO (%)	*Clementine FeO (%)	References
Apollo 15 (Maria)	1.64	**2.32**	1.7±0.6	15.2	**15.1**	12.9	*(Nawa et al., 1979)*
Apollo 17(highland)	0.90	**0.95**	3.7±1.8	8.1	**8.6**	6.9	*(LSPET, 1973)*
Surveyor 5	7.60	**2.01**	N/A	12.1	**13.8**	N/A	*(Mason et al., 1970)*
Surveyor 6	3.50	**2.41**	N/A	12.4	**13.2**	N/A	
Surveyor 7	0.50	**0.75**	N/A	5.5	**6.9**	N/A	

From Table 5.3 and Table 5.4, it is noticed that the Clementine derived FeO content was systematically 1-2% lower in all the returned samples than the laboratory measurements. The M^3 derived content compared better with the returned Apollo samples and was within ±2.8% of the laboratory measurements, without systematic biases. The Clementine derived TiO_2 abundance was systematically 0.1-4% higher than the laboratory measurements of the returned samples. The M^3 derived TiO_2 compared well (±0.6%) with the laboratory measurements of the returned samples except for samples with high TiO_2 content. Again this discrepancy in the high TiO_2 regions can be improved if more high TiO_2 samples can be provided in the future.

5.3. Lunar Regolith Density Information

The sensitivity analysis showed that the bulk density of the lunar soil is another major cause of uncertainty for MRM modelling. There has been considerable effort expended over the years to estimate the spatial distribution of the bulk density of the lunar soil (*Carrier et al., 1991; Pinet et al., 2012*). However, lunar soil bulk density is yet to be globally measured by instrumentation (the depth of GRAIL data at 40 km is too deep for this research; this research studied only the top 2 m; *Zuber et al., 2013*). The universally accepted estimated depth density profile was shown in section 3.2, Figure 3.2. Using this profile for the global lunar surface may introduce error into the

microwave data inversion (chapter 6), as the Moon's density varies between the highland and the Maria (*Carrier et al., 1991; Pinet et al., 2012*).

The Apollo missions provided the only direct measurements of the lunar soil bulk density; however, they only provide data at discrete points and do not provide global coverage. Core tube samples of the upper lunar regolith were returned from all Apollo sites; however, the landing sites of the Apollo missions were limited to the near side of the lunar surface and equatorial regions. Only one mission (Apollo 16) landed in a typical highland region. Therefore, the lunar soil bulk density measurements made by the Apollo missions may not fairly represent the global bulk density of the lunar surface (Figure 5.15) (*Carrier et al., 1991*).

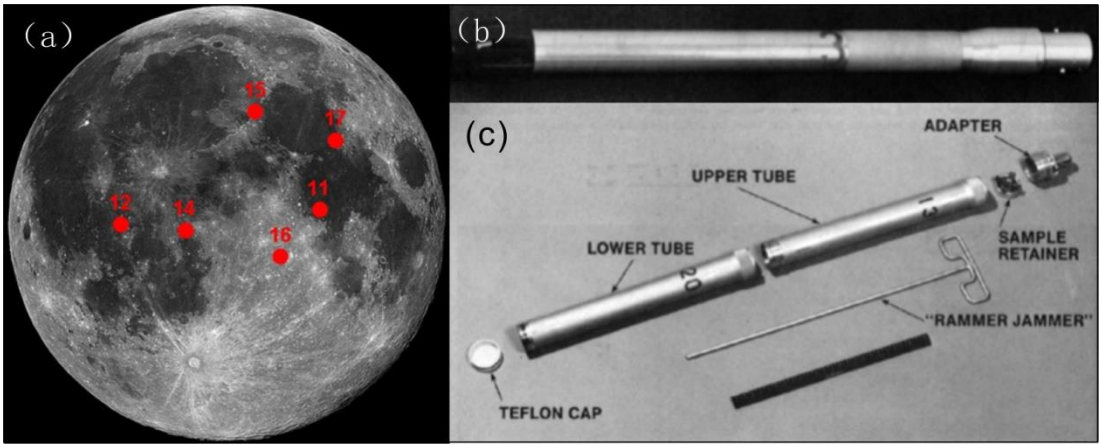

Figure 5.15. (a) Locations of Apollo missions. (b)Core tube sampler used to obtain cores of lunar soil during the Apollo 11 mission. Separate tubes, each 2.8 cm in diameter (outside diameter) and 39.9 cm long, could be connected into a single tube that was progressively hammered into the lunar surface by an astronaut. (NASA Photo S69-31856.); (c)Photograph of the core tube sampler used on the Apollo 15-17 missions. The unit consists of two single tubes, each 4 cm in (inside) diameter and 42 cm long, that can be connected to form a double tube. The "rammer jammer" was used to insert and seat the sample retainer before the core was pulled from the ground. Cited from (*Lunar Sourcebook, 1991*).

The density measurements from the drill samples from all the Apollo landing sites are summarized below in Table 5.5. From Table 5.5 it can be seen that density increases with depth and that the highland regions have a lower density than the Maria regions. Highland samples (Apollo 16) are about 0.2 g/cm^3 lower than Maria samples (Apollo 11, 12 and 17). Apollo 14 and 15 were on a border between the highland and Maria regions. An interpolated density profile based on the values in Table 5.5 is shown in Figure 5.16.

Table 5.5. Summary of the Apollo core density samples (*Carrier et al. 1991*)

Mission	Sample No.	Sample Weight(g)	Length of Sample Used (cm)	Density (g/cm^3)	Depth of Sample (cm)
Apollo 11	10005	52	10	1.71	>25
	10004	65.1	13.5	1.59	<32
Apollo 12	12027	N/A	17.4	N/A	37
	12025	56.1	9.3	1.98	69
	12028	189.6	31.8	1.96	69
	12026	102.9	19.4	1.74	37
Apollo 14	14211	39.5	7.5	1.73	64
	14210	169.7	31.9	1.75	N/A
	14220	80.7	16.5	1.6	<36
	14230	76	12.5	N/A	23/45
Apollo 15	15008	510.1	28	1.36	70.1
	15007	768.7	33.9	1.69	70.1
	15009	622	36.2	1.3	34.6
	15011	660.7	29.2	1.69	67.6
	15010	740.4	32.9	1.91	67.6

Apollo 16	64002	584.1	31.7	1.4	65
	64001	752.3	33.9	1.66	65
	68002	583.5	27.4	1.59	68.6
	68001	840.7	34.9	1.8	68.6
	69001	558.4	N/A	N/A	27.5
	60010	635.3	32.3	1.47	71
	60009	759.8	33.1	1.72	71
	60014	570.3	28.8	1.48	70.5
	60013	757.2	34.7	1.63	70.5
Apollo 17	73002	429	21.8	1.60	70.6
	73001	809	34.9	1.73	70.6
	74002	910	33.3	2.04	71
	74001	1071.4	34.9	2.29	71
	76001	711.6	34.5	1.57	37.1
	79002	409.4	19.4	1.67	71
	79001	743.3	31.9	1.74	71
	70012	434.8	18.4	1.77	28

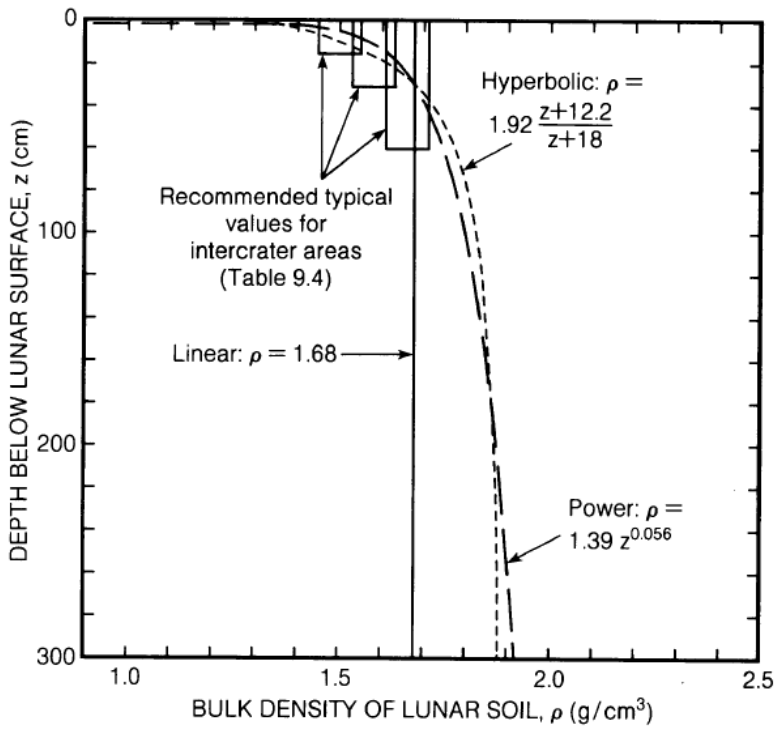

Figure 5.16. Calculated in situ bulk density in the lunar soil layer as a function of depth below the surface, derived from data shown in Fig. 9.15 of Lunar Source Book (1991). Three calculated density-depth relations are presented: linear (solid line), power-law (heavy dashed line), and hyperbolic (light dashed line).

Using the interpolated data displayed in Figure 5.16 the soil layer density profile can be estimated if the bedrock densities (500 cm or below) are known. As the Moon's density varies between the highland and the Maria (*Carrier et al., 1991; Pinet et al., 2012*), the bedrock density is allowed to vary between the Maria and highlands and is assumed to be proportional to the upper crust density at the same location. The latter can be estimated using the empirical correlation of Huang and Wieczorek *(2012)*:

$$\rho = 0.0273FeO + 0.011TiO_2 + 2.773 \qquad \text{(Eq. 5.8)}$$

This relation is based on the estimated mineralogical norms and densities of the lunar samples and has a quoted uncertainty of less than 0.05 g/cm^3 (*Fa et al., 2012*). Because the Maria regions usually have higher FeO and TiO_2 abundances than highland regions, Eq. 5.8 indicates higher density values for Maria regions, which qualitatively agrees with previous research (*Carrier et al., 1991; Pinet et al., 2012*).

This then allows for a different profile to be estimated for the Maria and highland regions. Although this is a rough estimate based on a poorly constrained assumption, it is better than using a uniform profile for the Maria and highland regions.

Based on the mineralogy information derived in the previous section and the regression Eq. 5.8, I derived the spatial distribution of 5 m depth lunar soil regolith density. From this value the layer average bulk lunar soil density for each layer in the inverse model can then be calculated and used in the inverse scheme, described in chapter 6.

Chapter Summary:

In this chapter, VIS to NIR reflectance data acquired by the M^3 instrument was used to investigate the mineralogy of the lunar surface. The FeO content based on M^3 data was analysed with the use of Lucey's model and compared to previous estimates. The derived FeO content also compared well with the measured FeO content of returned Apollo samples (deviation $<\pm 2.8\%$). The TiO_2 content based in the M^3 was also analysed using Lucey's approach and compared to previous estimates derived from

the Clementine data. Although the M^3 derived TiO_2 content compared well with the Clementine data, neither compared well with the measured TiO_2 content of returned Apollo samples (Lucey's method calculates TiO_2 content an order of magnitude higher than the Apollo samples). A second approach, the Shkuratov method, was used to derive the TiO_2 content from the M^3 data and this method compared well with the returned Apollo sample measurements (deviation $< \pm 2.8\%$, except for high TiO_2 regions –greater than 7%). Thus, the Shkuratov derived TiO_2 will be used in the inverse scheme. The Shkuratov method is an empirical fit and more data and laboratory experiments are required to further constrain the empirical fit.

There are two main issues with the methods used to derive the FeO and TiO_2 content:

1. The calculated concentration levels only provide information about minerals found on the lunar surface. However, the inverse scheme requires mineralogical information at depths of up to 2 m. The surface concentration levels are therefore used as a proxy for the concentration levels found at depth.
2. The lack of high TiO_2 region data leads to a lower estimate for the high TiO_2 regions, as the calculation was made using low TiO_2 samples.

Lunar regolith density is another important parameter for our inverse model. The density profile of the lunar between depths of 2 cm – 500 cm can be estimated using

an empirical relationship from the mineralogical concentrations. The next chapter discusses the inversion and result/error range.

Chapter 6. Preliminary Subsurface Temperature Maps from the MRM data Modelling Results

6.1 Chapter Introduction

The results from the previous microwave radiative transfer forward model (chapter 4) are combined with the Fe/Ti and bulk density distributions derived from the M^3 remote sensing surface measurements (chapter 5). This is then used in this chapter to model spatial variations in lunar subsurface temperatures.

I conduct two procedures before the inversion. First, abnormal MRM data is eliminated. Even in the gridded level 2C microwave radiometer data used in this research, problematic measurements still exists, such as negative and unphysically large values. To remove them, I set threshold values for the brightness temperature in the equatorial region (14^oS -14^oN) at local noon time. A brightness temperature greater than 360 K or less than 40 K are judged as abnormal and are excluded in the inversion.

Second, as I am retrieving the base regolith temperature value, the depth value for this inverted temperature need to be determined. The lunar regolith was divided into six

layers (i.e., lunar dust layer, lunar soil layer 1, lunar soil layer 2, lunar soil layer 3, lunar soil layer 4, and lunar rock layer, see Figure 3.10) in Chapter 3. The temperature (T_5, Note that in this scheme the lunar dust layer is layer 1, therefore, lunar soil layer 4 is actually the fifth layer) of the lowest soil layer during lunar mid-day (representing a depth of 0.2–5 m), is derived because it represents a stable temperature that does not vary with insolation. In addition, according to error analysis in section 4.4, the error covariance suggests that the inverse error of T_5 is the smallest among T_2 - T_5. Due to above reasons, this chapter will solely focus on T_5, 0.2 to 5 m temperature inversion.

In addition, temperature T_5 should be interpreted as a temperature value at the median depth of the fifth layer rather than a temperature for all soils ranging from 0.2 to 5 m. Although the temperature is almost stable below 20 cm, it still slightly increases with depth (Figure 6.1). The representative depth of this inversion result can be estimated by the following method: within the fifth layer (ranging from 0.2 to 5 m), the stable temperature slightly increases with depth, but the temperature gradient becomes shallower after 2 m (Figure 6.1), probably due to more compact soils which could conduct heat easier; hence, as we can notice from the Figure 6.1, 2 m is an approximate median value of the 5th layer (0.2 – 5 m), here I use a depth of 2 m to interpret the inverted temperature T_5.

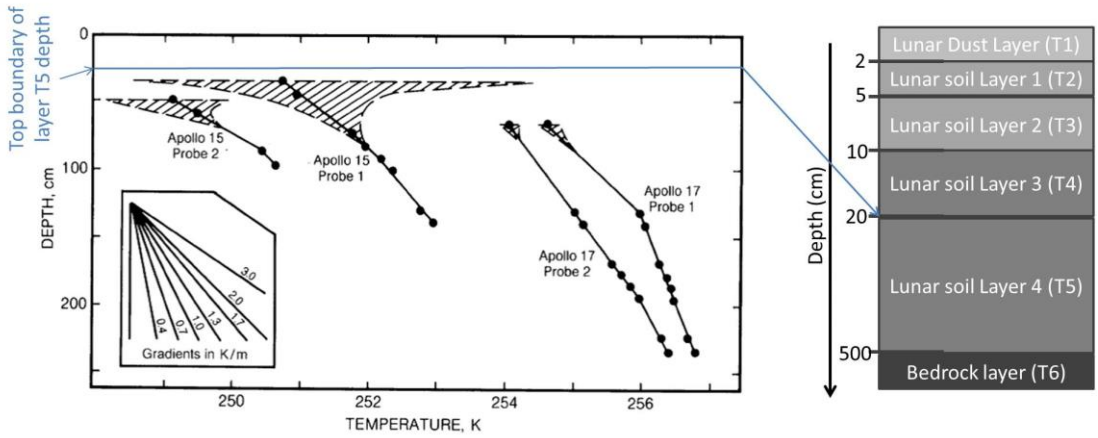

Figure 6.1. (Left) Temperature fluctuations in the lunar regolith as a function of depth (From *Langseth and Keihm, 1997*). Note that the small temperature scale at the bottom of the diagram does not permit the extreme temperature fluctuation at depths less than ~30 cm to be plotted; this region is left blank. Hatched areas show day-night temperature fluctuations below ~30 to 70 cm. Below the blue line is the T_5 layer. (Right) Layer stratification used in the microwave radiative transfer forward model described in chapter 4.

6.2 Inversion Result

I selected midday local observation times ($0\,^\circ <$ solar angle $< 14\,^\circ$), and I inverted the MRM data to reveal the 2 m depth temperature (T_5) from $0\,^\circ$ to $\pm 14\,^\circ$N for the lunar nearside (Figure 6.3).

This research did not invert data from the lunar farside because the farside region has added complications:

1) The parameter quantification modelling is based on the returned samples from the Luna and Apollo mission, which were all found on the lunar nearside. i.e. there have been no ground truth measurements on the farside.

2) The estimated lunar soil dielectric constant and density depth profiles used in the model are only valid for the nearside and may not be applicable to lunar farside regions *(Fa and Jin, 2007; Fa and Wieczorek, 2012)*. The topography of the lunar farside is distinct from that of the nearside, as it has much more highland terrain relative to Mare and the lunar farside highlands have the highest topographic elevations on the Moon. This topographic difference may have been caused by the tidal forces acting early in the Moon's history when its solid outer crust floated on an ocean of liquid rock *(Garrickbethell et al., 2014).*

For these reasons, our inversion is restricted to the lunar nearside. By putting the lunar regolith (chapter 3) mineralogy S-parameter and density values (both chapter 5) into the forward model (chapter 4) equations Eq. 4.22 and Eq. 4.31, it is possible to get an estimate of the fifth layer's temperature (T_5) at mid-day. However, the addition of extra a priori information and the quantification of its associated error into the inversion modifies the approach in chapter 4 so Eq. 4.31 (see p.84) will be replaced as described below.

First, I calculated T_5 without a priori for a small sample region shown in Figure 6.2a. I improved the density profile with geographical information from Chapter 5 (e.g. highland, maria…etc). I then calculated T_5 again with a priori error covariance included to account for the forward model uncertainty. Then, with a priori, Eq. 4.29 (see p.79) becomes Eq.6.1,

$$x_{improved} = (K^T S_\varepsilon{}^{-1} K + S_a^{-1})^{-1}(K^T S_\varepsilon^{-1} y + S_a^{-1} X_a) \qquad \text{(Eq. 6.1)}$$

Where the newly added S_a, is the error covariance matrix of my a priori guess.

The a priori information contains:

1. A rough estimate of equatorial temperature from the Lunar Sourcebook (1991)
2. Diviner measurements of surface bolometric temperature (Paige et al., 2010)
3. Keihm's model (1973, 1975, 1984) of lunar sub-surface temperatures.
4. Modelled 10-20 cm depth temperatures (Vasavada et al., 1999)

Their error ranges are shown in Table 6.1, and S_a is shown in Eq. 6.2.

$$S_a = \begin{bmatrix} 2^2 & 0 & 0 & 0 \\ 0 & 10^2 & 0 & 0 \\ 0 & 0 & 7^2 & 0 \\ 0 & 0 & 0 & 3^2 \end{bmatrix} + S_m \qquad \text{(Eq. 6.2)}$$

Table 6.1. Summary of error information in the error covariance of a priori (S_a).

A priori Source	A priori Value	A priori Error	Position in the error covariance matrix of a priori (S_a)
Diviner surface temperatures (Paige et al., 2010)	Varies depending on exact location (370 – 390 K)	±2 K	T_2
Modelled 10 - 20 cm depth temperature (Vasavada et al., 1999)	280 K	±10 K	T_3
Modelled 1-m subsurface temperature based on Apollo measurements (Keihm, 1973, 1984)	250 K	±7 K	T_4
Apollo temperature measurements (Lunar Sourcebook, 1991)	251 K for Apollo 15, and 255 K for Apollo 17	±3 K	T_5

Comparing with the result derived without an a priori covariance matrix (range from 220-280 K), we can see that the variation of sub-surface temperatures derived with a priori information become smaller (mainly range from 230-270 K).

Inverting Eq. 6.1, I get results for the sample region shown in Figure 6.2b. I calculated both the error covariance and averaging kernel. Error covariance of sample results are represented in Figure 6.2 c. By inspecting Figure 6.2 c, we can see that low temperature regions tend to have higher error.

Hence low temperature regions tend to have a lower averaging kernel as plotted in Figure 6.2 d. In other words, for low temperature regions, more information comes from the a priori information (~30%).

According to the definition of the averaging kernel in Eq.6.3, the averaging kernel is showing the weight/balance between the a priori and measurements in the final retrieved values. In my calculations, the value of averaging kernel ranges from 60% to 80%, indicating that the result is mainly from the MRM measurements.

$$\hat{x} = Ax + (I - A)x_a \qquad \text{(Eq. 6.3)}$$

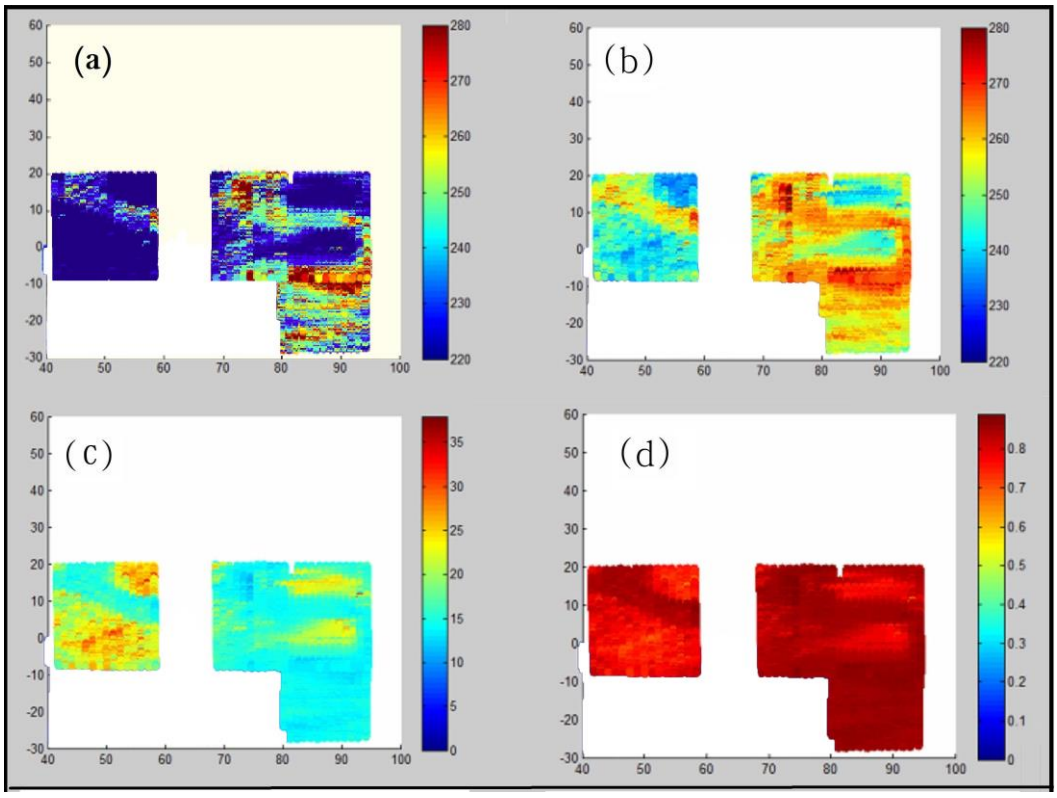

Figure 6.2. An a priori test on a small sample region whose latitude and longitude are shown on X and Y scales. (a) T_5 inversion without a priori, in which unit of color bar is K; (b) T_5 calculation with a priori, in which the unit of the color bar is K; (c) error covariance, in which the unit of the color bar is K^2; (d) averaging kernel, of which the value is shown in the color bar.

By combining the a priori information with the lunar regolith parameters derived in chapter 3 (dielectric constant, specific heat and thermal conductivity) and chapter 5

(mineralogy and bulk density) with the model outlined in chapter 4 (Eq. 4.22 and Eq. 6.1), I can get an inversion result for the lunar soil layer 5 temperature at mid-day as shown in Figure 6.3b. The inversion result (b) is shown with (a) a geographic map, (c) a uranium distribution map and (d) a thorium distribution map for comparison.

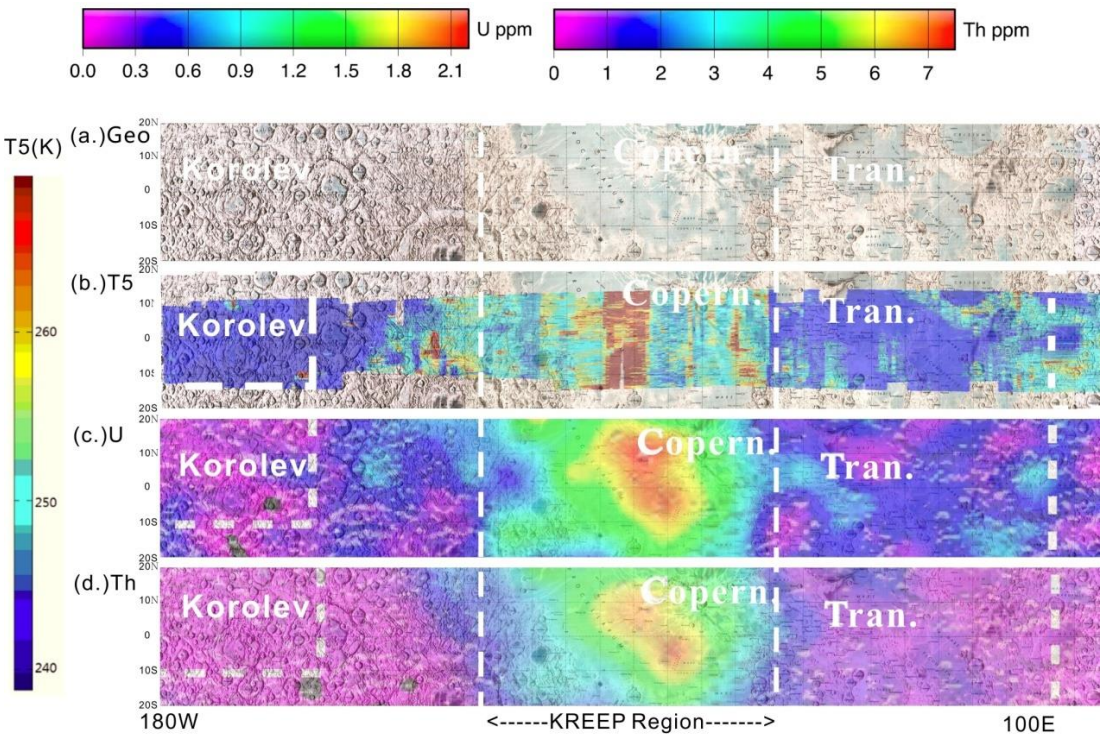

Figure 6.3. Map of the inversion result of the 2-m subsurface temperature (layer 5) (b) with relevant lunar surface properties (a), (c), (d) for comparison. (a) Shaded relief map of the corresponding area; (b) T_5: subsurface temperature at a 2-m depth from the inverted CE MRM data. This figure is the direct output of our work. T_5 is the median temperature of the fifth layer (2 m). "Stripy" Artifacts can be seen in the T_5 map because it is derived from the FeO/TiO_2 maps from M^3 data; (c) Lunar uranium (U) concentration levels on the lunar surface as measured by the Kaguya mission (Adapted from *Yamashita et al., 2010)*; (d) Lunar thorium (Th) distribution. Adapted from *Yamashita et al., 2010*. Abbreviations: Copern, is short for Copernicus crater; Korolev, for Korolev Crater; and Tran, for Mare Tranquillitatis.

The above results indicate a strong connection between the subsurface temperature and the U/Th distribution. U and Th are both radioactive elements that produce heat in the lunar mantle (*Hagerty et al., 2010*). Both elements are found in the KREEP regions and the KREEP regions have the highest subsurface temperature across the Moon (average temperature across the KREEP region is ~260 ± 6 K). The regions with the lowest U/Th distribution, such as Mare Tranquillitatis (and all purple regions on map c), have the lowest 2 m subsurface temperature (~240 ± 4 K), which agrees with *Keihm et al.'s (1973, 1984)* model. Outside the KREEP region the average 2-m subsurface temperature is 246 ± 4 K, so there is in a significant elevated subsurface temperature of 14 ± 10 K inside the KREEP region.

It is possible that the elevated temperature in the KREEP region is caused by factors other than the heating from radiogenic elements. Two other possible factors are geographic, i.e. differences between the highland and Maria regions and differences between the input mineralogy parameter, S. Geographic factors were excluded because in our inversion result Maria regions show both very high subsurface temperature (KREEP region – 260 K) and very low subsurface temperatures (Maria outside of KREEP region – 240 K).

The influence of the input mineralogy parameter can also be excluded. The two Maria regions, namely, the West (Oceanus Procellarum) and East parts (Mare Tranquillitatis, Mare Serenitatis, Mare Nectarius, and Mare Crisium), exhibited extremely different subsurface temperatures although they have highly similar FeO and TiO2 distributions (*Shkuratov et al., 1999; Korokhin et al., 2008*). Overall, no obvious connections are evident in the derived temperature at 2 m depth when it is compared with the Fe or Ti distribution map (Figures 6.4 [c] and [d]).

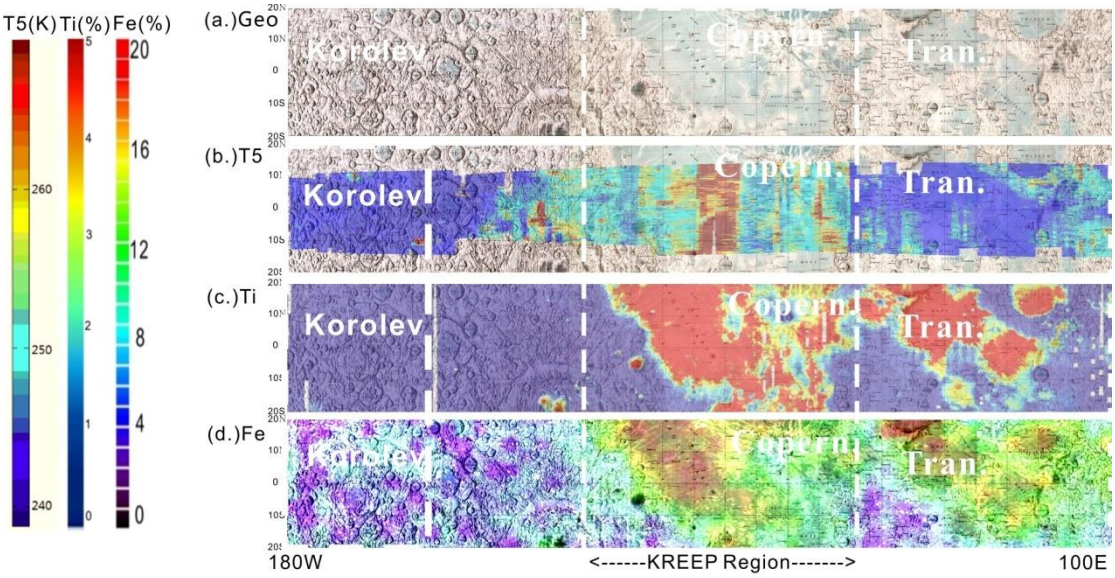

Figure 6.4. (a) Corresponding area's shaded relief map; (b) T_5--Subsurface temperature inverted at 2 m depth from CE MRM data; (c) Lunar titanium distribution from the Clementine data *(Korokhin et al., 2008)*; (d) Lunar iron distribution from the Lunar Prospector data *(Lawrence et al., 2002a).*

Based on Figures 6.3 and 6.4, the KREEP region has a considerably higher subsurface temperature than other mare regions, indicating an additional source of

heat. The 1 sigma error in the inversion is ± 6 K inside the equatorial KREEP region and is ± 4 K across the global lunar subsurface. This error is based on the derived temperature error covariance and the Monte Carlo analysis (Section 4.5.2). Therefore the elevated temperature inside the KREEP region is statistically significant as the temperature difference is greater than the error to 1σ. The KREEP basalt has approximately 300 times more uranium and thorium than non-KREEP Maria regions, implying that a large portion of the Moon's heat-producing elements are located within this single crustal area *(Wieczorek et al., 2000)*. This elevated temperature is further explored in chapter 7.

6.3 Comparison of the 2 m Derived Temperature Result with Earlier Theoretical Models

For the non-KREEP regions, our result agrees with the *Keihm et al., (1973, 1984)* model. *Keihm et al. (1973, 1984)* predicted the central lunar equatorial subsurface temperature at a 2 m depth to be 250 ± 7 K assuming the only heating source was solar radiation. Our derived temperature is in agreement with Keihm's model, providing a non KREEP average result of 246 ± 4 K.

Little et al. (2003) also used a neutron spectrometer onboard the Lunar Prospector to measure emitted thermal neutrons excited by cosmic ray energy from the lunar

surface. The number of emitted neutrons depends on the lunar subsurface temperature at depths of 1 m. *Little et al. (2003)* derived the subsurface temperature around the lunar equator using measurements from the Lunar Prospector's neutron spectrometer. A calculated 1 m subsurface temperature of 250 K around the lunar equator was derived, which is in good agreement with the 251 ± 4 K global mean 2 m subsurface temperature from the MRM inversion result.

Chapter Summary:

This chapter derived the lunar subsurface temperature distribution at a depth of 2 m based on a MRM inversion calculation. Comparisons with previous models (e.g. Keihm et al., 1973, 1975; Little et al., 2003) showed agreement of the general equatorial region subsurface temperature. However, the KREEP region shows a 10 K higher subsurface temperature, indicating additional heat flow, which could be due to radiogenic heat flow from uranium and thorium. The question whether the radiogenic heat production (RHP) can generate a 10 K elevated temperature difference at a depth of 2 m will be carefully examined in the next chapter, chapter 7.

Chapter 7. Inversion of Lunar Heat flow

7.1 Introduction and Background to the Heat Sources of the Moon

Lunar heat flow is defined as the heat released from the lunar interior per unit area per unit time. Through an evolution spanning 4.6 billion years, most of the internal heat of the Moon has been dissipated; however, residual heat of formation is still present, thereby providing information on the origin and evolution of the Moon.

Lunar heat flow contains two endogenic sources, radiogenic heat flow and lunar mantle cooling heat flow. Neither the tenuous (10^{-14} atm) lunar atmosphere or the static lithosphere contribute to heat redistribution. Consequently, the Moon is in a steady state, and the internal lunar heat flow should be approximately equal to the sum of heat produced by radioactive elements, mainly uranium (U), thorium (Th), and potassium (K), as well as lunar mantle heat flow, which comes from the long term cooling process of the interior (*Korotev, 1998*).

According to *Langseth et al.* (*1976*), the heat flow of the long-cooling process is approximately 4 mW/m^2. The ratio of lunar interior cooling heat to overall heat is

called the Urey coefficient. *Spohn and Breuer (2002)* reported that about 50% of Moon's heat comes from the decay of radioactive elements, and the remaining 50% is caused by the cooling process inside the Moon, which corresponds to a Urey coefficient of 0.5. A Urey coefficient of 0.5 can be applied to the Earth and Earth-like planets. A coefficient of 0.5 is consistent with the estimate based on geochemical data measured for the Earth. The Earth's bulk heat flow is 44.2 $\pm$ 1.0 TW in total and 24.0 $\pm$ 8.8 TW is estimated to be contributed by the radiogenic heat production (*The KamLAND Collaboration, 2011*). Unlike heat released by cooling from the interior, radiogenic heat production varies as a result of local geology.

On the lunar surface, the distribution of radioactive elements, including uranium, thorium, and potassium, is concentrated in the Procellarum KREEP Terrane (PKT) (Figure 1.1). The PKT is the distinct geochemical crustal province formed by the Procellarum and Imbrium regions. According to geochemical studies (*Spudis and Schultz, 1985*), a large portion of the lunar crust in this locale consists of a material that is similar in composition to Apollo 15 KREEP basalt. KREEP basalt consists of about 300-fold more uranium and thorium than highland material, implying that a large portion of the heat-producing elements of the Moon are located within this single crustal province.

To date the only lunar surface heat flow experiments were conducted at the Apollo 15 and 17 landing sites. Drilling experiments measured the thermal conductivity and heat flow. After correcting for the influence of the astronauts on modifying the top layers of regolith, *Langseth et al., (1973)* found heat flow of 21 mW/m^2 and 14 mW/m^2 for the Apollo 15 and 17 sites respectively.

Despite a lack of other in-situ measurements, some studies have made early attempts to model the average lunar heat flow. For example, *Krotikov and Troitskii (1964)* used ground based radio astronomy observations and estimated the average heat flow value to be 54.4 mW/m^2; however, this value is higher than the Apollo measurements (*Langseth et al., 1973*). According to ground observations of microwave brightness temperature and reanalysis of Apollo 17 data, *Langseth et al. (1976)* this value was later reduced to give an estimate of the approximate average heat flow of the nearside of 30 mW/m^2.

This chapter will derive and compare two different lunar heat flow maps in order to determine whether the MRM derived results yields a reasonable estimate of lunar heat flow. One map is based on CE-MRM inversion results, and the other is based on a lunar radioactive heat source calculations.

7.2. Heat Flow based on CE MRM Derived Temperature Results

Lunar heat flow may be calculated using the subsurface temperatures from the CE MRM data, as derived in chapter 6. By definition, lunar heat flow can be represented as the product of conductivity and temperature gradient given by

$$Q = -k\frac{dT}{dz} \qquad \text{(Eq. 7.1)}$$

where Q is the heat flow, T is the temperature, z is the depth and k is the thermal conductivity.

To calculate thermal conductivity this work uses an earlier model (*Mitchell and Pater, 1994*), as described previously in section 3.4, from which k is expressed as

$$k = k_c[1+\chi(\frac{T}{T_{350}})^3], \qquad \text{(Eq. 7.2)}$$

Where χ is the ratio of "radiative conductivity" to phonon conductivity at 350 K, k_c is the phonon conductivity given by χ=0.073, T is subsurface temperature in kelvin, and T_{350} is 350 K.

Using the previously derived 2 m subsurface temperature, Eq. 7.2 is used to obtain the thermal conductivity *k* values. The derived *k* value and temperature gradient are then substituted into Eq. 7.1, to calculate the heat flow.

Before applying this method to all the data, it may be tested by comparison with the in-situ measurements made at the Apollo 15 and 17 landing sites. The subsurface temperatures of the Apollo 15 and 17 sites are not directly obtained, because they are on the edge of the MRM derived temperature map (Figure 6.3). Therefore, their derived subsurface temperatures are derived by elongation interpolation. The interpolated values for the Apollo 15 and 17 landing sites are 255 and 256 K respectively. The surface temperature at the Apollo 15 and 17 landing sites was obtained from the Diviner measurements and is 250 and 253 K respectively.

Thus, the derived heat flow at the Apollo 15 site (HF_{A15}) by this thesis is given by:

$$HF_{A15} = -k\frac{dT}{dz} = -K_c[1+\chi(\frac{T}{T_{350}})^3]\cdot\frac{dT}{dz}$$

$$= -9.3\times10^{-3}\times(1+0.073\times(255/350)^3)\times((250-255)/2)\times1000$$

$$=23.90\pm1.8\ \times10^{-3}\ \mathrm{W/m^2}$$

$$=23.90\pm1.8\ \mathrm{mW/m^2}. \qquad \text{(Eq. 7.3)}$$

Similarly, the heat flow at the Apollo 17 landing site (HF_{A17}) is estimated as

$$HF_{A17} = -k\frac{dT}{dz} = -K_c[1+\chi(\frac{T}{T_{350}})^3]\cdot\frac{dT}{dz}$$

$$= -9.3\times10^{-3}\times(1+0.073\times(256/350)^3)\times((253-256)/2)\times1000$$

$$=14.34\pm1.1\times10^{-3}\,\mathrm{W/m^2}$$

$$=14.34\pm1.1\ \mathrm{mW/m^2}. \qquad \text{(Eq. 7.4)}$$

The calculated heat flow at the Apollo 15 site is 23.9 ± 1.8 mW/m^2, the heat flow at the Apollo 17 landing site is 14.3 ± 1.1 mW/m^2. These estimates of the heat flow are based on the derived subsurface temperature and temperature gradients from Chang-E, M^3 and Diviner measurements.

Figure 7.1 shows a the theoretical model by *Wieczorek et al., (2000*) of the lunar heat flow in the KREEP terrane compared with direct measurements from the Apollo heat flow experiments. The heat flow model by Wieczorek (*Wieczorek et al., 2000*) indicates that KREEP regions have a significantly higher heat flux (34 mW/m^2) than non-KREEP regions (11 mW/m^2) in the Moon. As seen in Figure 7.1, the calculated heat flow at the Apollo 15 and 17 landing sites estimated in this thesis agree with the previous model by *Wieczorek et al., (2000*) and with the Apollo measurements.

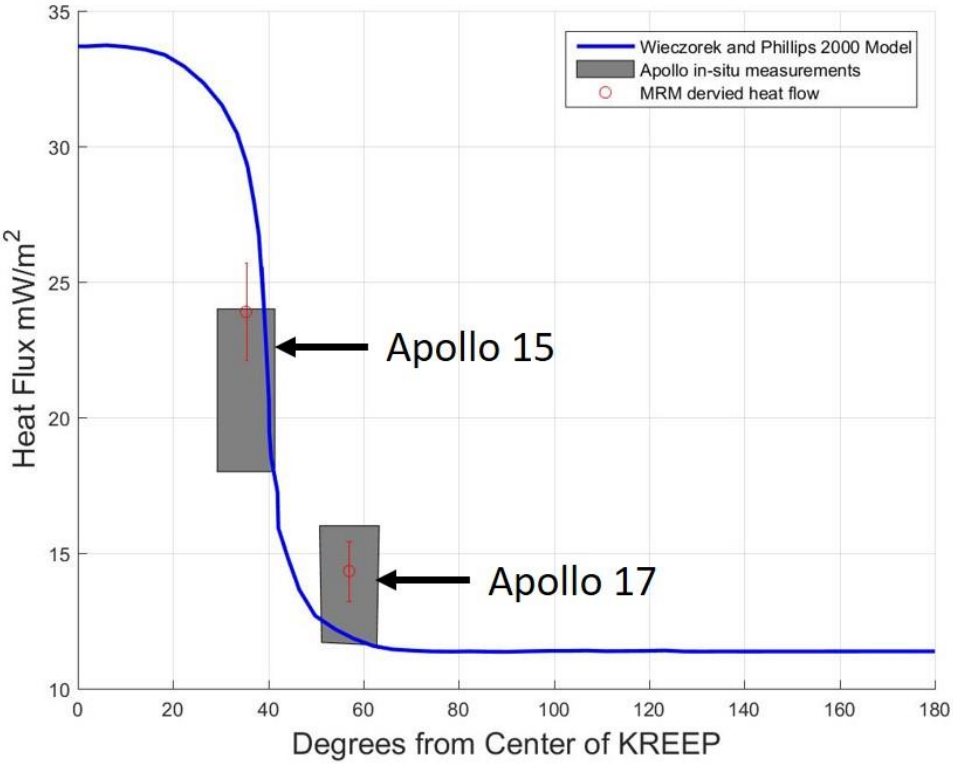

Figure 7.1. Plot of the modelled present-day surface heat flow as a function of distance from the approximate center of the Procellarum KREEP terrane (solid line). Also shown are the Apollo heat flow measurements, grey boxes show the measurements after correction by *Langseth et al., (1973)*, whilst the dashed line boxes are after correction for any enhancement due to their location at a mare/highlands boundary (*Warren and Rasmussen, 1987).* Figure cited from *Wieczorek and Phillips, (2000).*

After performing the validation using the Apollo 15 and 17 site data, this method can be applied to the rest of the Moon. However, the far-side value of *dz* (T_5 depth) in Eq. 7.1 cannot be estimated; hence, I only calculated the nearside heat flow. A heat flow map of the nearside (Latitude 14^o S to 14^o N) from the CE data and using M^3

measurements for mineralogy is overlaid on the Clementine shaded relief map, in Figure 7.2.

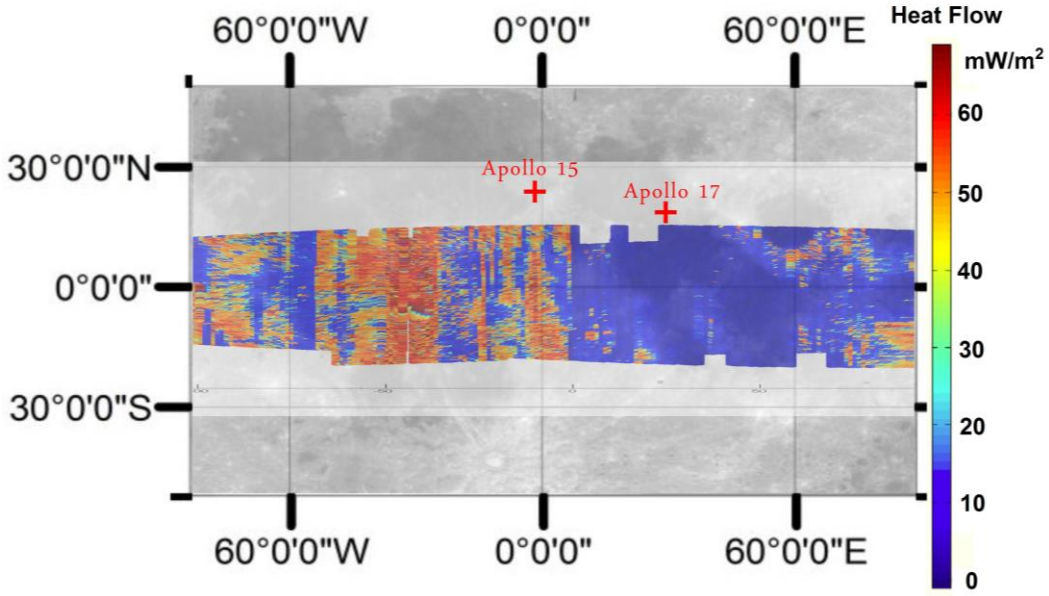

Figure 7.2.CE and M^3 measurement heat flow map of the lunar nearside overlaid on Clementine shaded relief map.

The inverted 2 m lunar subsurface heat flow ranges from 2 mW/m^2 to 68 mW/m^2, which is in the same order of magnitude as earlier ground-based remote sensing measurements, as well as the estimates based on radioactive elements *(Little et al., 2003)*. This also compares well in non KREEP regions with the model by *Wieczorek and Philips., (2000*) which predicts a heat flow of 11 mW/m^2, compared with this thesis which predicts a heat flow of 11 ±4 mW/m^2. However, in the KREEP region this work predicts a heat flow of 45 ±6 mW/m^2 compared to the *Wieczorek and Philips., (2000*) prediction of 34 mW/m^2. Although there is a slight difference in the

two values, this difference is small and can be explained by a small error (± 5 mW/m^2) in *Wieczorek and Philips., (2000*) model. Unfortunately no error analysis was provided (*Wieczorek and Philips., 2000*).

7.3 Heat Flow based on Radiogenic Heat Modelling

The main radioactive elements present on the Moon are uranium, thorium, and potassium. In the decay process, these elements continuously release heat. As mentioned in Section 7.1, additional heat flow comes from long-term cooling of the lunar interior (*Langseth et al., 1976*), the ratio of which to the overall heat can be represented by a Urey coefficient of 0.5.

When discussing the distribution of the lunar heat flow, we assume that mantle heat flow of the Moon is approximately constant and that it is mainly the crustal component that produces local heat flow variations. The radiogenic heat will be calculated first, then the crustal heat flow result will be used to compare with Apollo 15 and 17 measurements to determine the additional constant mantle heat flow.

Distributions of radioactive elements, such as uranium, thorium and potassium, show clear correlation with each other because the elements are all mainly in the PKT region. All the three (K, U, Th) distribution maps are plotted over a base map to show the correlations, as shown in Figure 7.3-7.5.

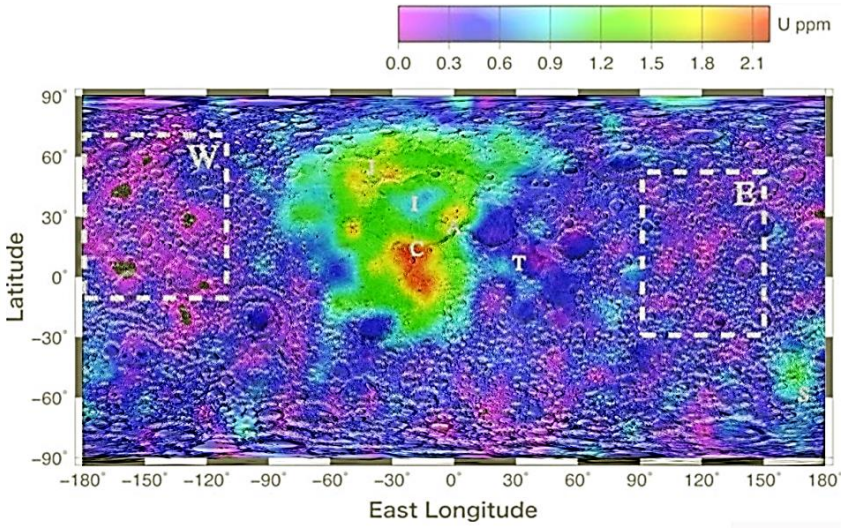

Figure 7.3. A map of uranium (U) distribution on the lunar surface, as measured by the Kaguya mission, overlapped onto a Clementine map. The highest level is at 2.1 parts per million (ppm) at Copernicus crater (C). E and W mark the east and west highland regions on the far side of the Moon; A, the Apennine Bench; I, Mare Imbrium; J, Montes Jura; S, South Pole — Aitken Terrane; and T, Mare Tranquillitatis. *CREDIT: N. Yamashita et al., Geophysical Research Letters, 2010*

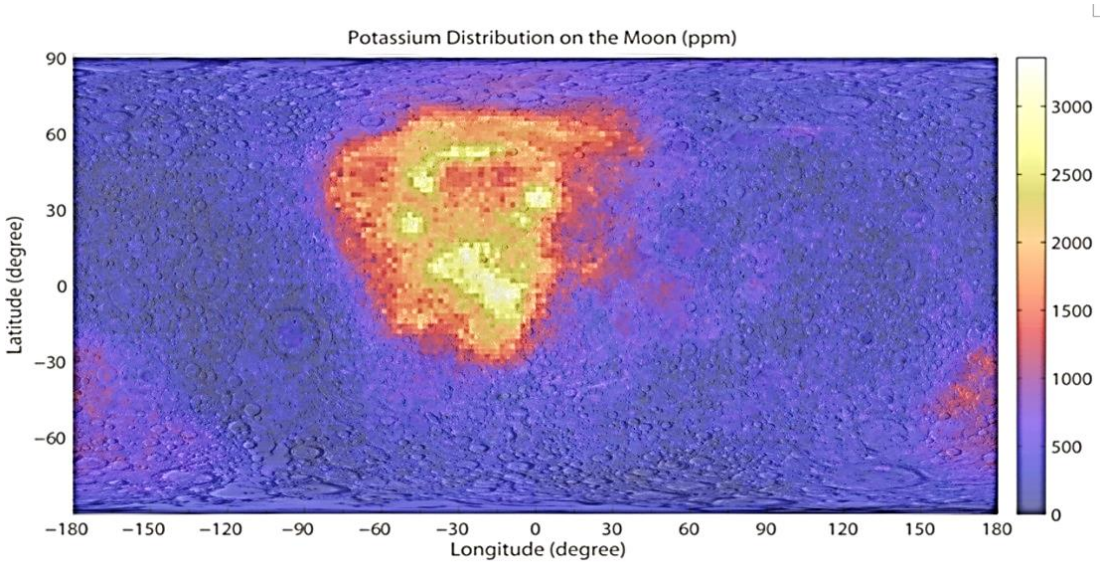

Figure 7.4. Global potassium (K) abundance of the Moon from CE-2 GRS 178-days measurements, overlapped onto a Clementine map. All the data are binned into quasi-equals 2 ° × 2 ° pixels in the equator and displayed in a cylindrical projection.（*Zhu, Meng-Hua, et al. (2013).*）

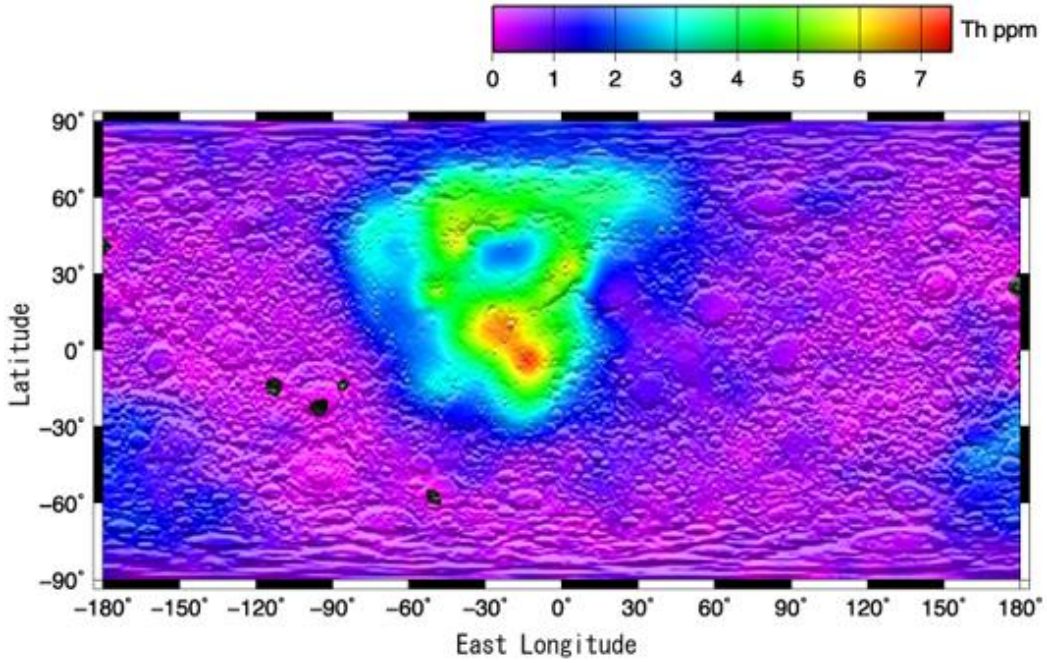

Figure 7.5. Distribution of the thorium abundances of global lunar surface (from Kaguya results) (*Yamashita, 2010*) and is in agreement with Lunar Prospector data (http://www.classe.cornell.edu/~seb/celestia/gallery-003.html) .

The total heat flow produced by lunar radioactive elements depends on the heat generation rates of those radioactive elements. A large amount of research, mainly on Earth's radioactive processes, has been performed to measure heat generation rates (*Jaupart, 1983; Vasseur and Singh, 1986*). Previous lunar studies have assumed that the relationship between the abundance of radioactive elements and radiogenic lunar heat flow can be determined, if the radioactive decay process on Earth is similar to that of the Moon (despite different heat losses). Considering the heating effect of each radioactive element, the lunar radioactive heat rate can be described (*Rybach, 1988*):

$$P_t = 10^{-11}\rho(9.52\,C_U + 2.56C_{Th} + 3.48C_K)\,, \qquad \text{(Eq. 7.5)}$$

where P_t is the radiogenic heat generation rate (W/m^3), ρ is the lunar rock density (g/cm^3) and C_U, C_{Th} and C_K are the abundance of the radiative elements, uranium, thorium, and potassium respectively, in ppm.

In the abundance maps from the Lunar Prospector and Kaguya nuclear detection experiments (*Lawrence et al., 2002a; Yamashita, 2010*), the resolutions of C_U and C_K are smaller than that of C_{Th}. For a high-resolution map of radiative heat generation, the correlations between C_U, C_{Th} and C_K, should be determined. This will allow the higher spatial resolution available from the C_{Th} abundances maps to derive the amounts due to the other radioactive elements.

The spatial correlation in these radioactive elements may be a product of the Lunar Magma Ocean early in the Moon's formation (*Taylor, 2009*). Further discussion is beyond the scope of this thesis but lunar soil and rock samples show a high correlation with the abundances of the three radioactive elements (*Korotev 1998; Zhang 2014*). The cause of the correlation can be attributed to large impacts (*Shervais and Taylor 1986).* After the lunar formation KREEP terrain is predicted to be buried in the lunar deep subsurface (100 km). A large impact can lead to the excavation of this material, inducing the upwelling of the deep KREEP material leading to the observed spatial correlation.

Such correlation in the distributions can also be observed in the Lunar Prospector data (Figure 7.6). The abundance of uranium and potassium in Eq. 7.5 can be interpolated and replaced by thorium to make use of the high resolution of thorium data.

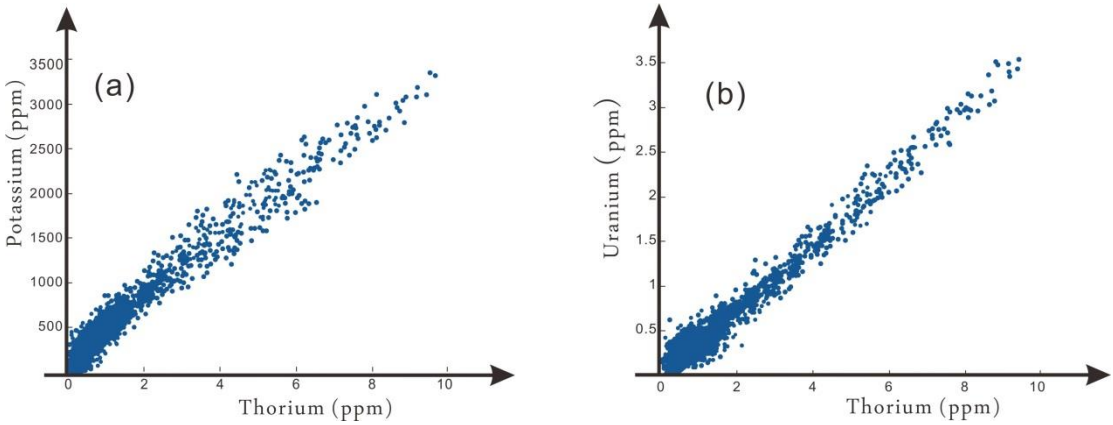

Figure 7.6. Correlation among potassium, uranium and thorium abundances.

The fitted potassium/thorium correlation in Figure 7.6a is provided in Eqns. 7.6–7.7 and the uranium/thorium correlation in Figure 7.6b is provided in Eqns 7.8-7.9

$$C_K = 0.034 C_{Th} + 0.013, \quad \text{(Eq. 7.6)}$$

$$R_{K,Th} = 0.96, \quad \text{(Eq. 7.7)}$$

$$C_U = 0.362 C_{Th} + 0.010, \quad \text{(Eq. 7.8)}$$

$$R_{U,Th} = 0.97. \quad \text{(Eq. 7.9)}$$

The above correlations show that potassium/thorium, and uranium/thorium, both exhibit a linear correlation.

Using the two correlations, Eq 7.5 can be simplified as

$$P_t = 10^{-11}\rho(6.15C_{Th} + 0.14)\,. \qquad \text{(Eq. 7.10)}$$

The vertical distribution of lunar radioactive elements has not been measured; thus, the most suitable option is to assume that the vertical distribution of radioactive elements on the Moon is similar to the vertical distribution of radioactive elements on Earth, i.e., decreasing with depth exponentially *(Korotev 1998)*. Consequently, the abundance of radioactive elements on the Moon by depth is represented as

$$P_t(z) = P_t \cdot e^{-\frac{z}{h_r}}, \qquad \text{(Eq. 7.11)}$$

where *z* is the depth, *Pt (z)* represents the thermal generation rate at such depth and *Pt* represents the surface heat generation rate. In addition, h_r is the characteristic length, which is defined as the depth where heat generation rate has decayed to l/e on the surface (*Sandiford et al 2002)*.

The heat flow from radiative elements in the crust, $q_{crust,}$ may be calculated by integrating the heat generation per unit volume, $P_t(z)$, from the surface to a depth equal to the crustal thickness, *H*,

$$q_{crust} = \int_0^H P_t(z)\,\mathrm{dz} = \int_0^H P_t \cdot e^{-\frac{z}{h_r}}\,\mathrm{dz} \qquad \text{(Eq. 7.12)}$$

Substituting Eq. 7.11 into the equation above, we can obtain

$$q_{crust} = 10^{-11} \rho \cdot h_r \cdot (6.15 C_{Th} + 0.14) \cdot \left(1 - e^{-\frac{H}{h_r}} \right) \qquad \text{(Eq. 7.13)}$$

Where ρ is the average lunar rock density which is 2.8 g/cm^3. Considering that the interior heat of the Moon is generated by long-term cooling, the total subsurface heat flow can be expressed as

$$Q_s = 10^{-11} \rho \cdot h_r \cdot (6.15 C_{Th} + 0.14) \cdot \left(1 - e^{-\frac{H}{h_r}} \right) + Q_{mantle}, \qquad \text{(Eq. 7.14)}$$

where Q_s is the lunar heat flow, and Q_{mantle} is heat generated by the internal long-term cooling of the Moon.

As mentioned at the beginning of this section, when radiogenic heat is calculated first, then the crustal heat flow result can be compared with Apollo 15 and 17 measurements to determine the additional constant mantle heat flow Q_{mantle}.

Lunar crustal thickness (H) has been calculated by *Wieczorek et al. (2006)* and global maps are maintained in an online archive, updated in 2012. The archive includes three similar crustal models, of which the "traditional" Model 1 is used as a single layer crustal thickness model in which the gravitational field is assumed to be a result of surface and Moho relief, and mare basalt fill. The archive is available at http://www.ipgp.fr/~wieczor/CrustalThicknessArchive/CrustalThickness.html

The characteristic length h_r (as defined below Eq. 7.11) can be derived by using the thickness of the lunar crust and the abundance of radioactive elements at the Apollo 15 and 17 landing sites. Then according to Eq. 7.14, h_r can be obtained using the equation

$$\frac{1-e^{-\frac{H_1}{h_r}}}{1-e^{-\frac{H_2}{h_r}}} = \frac{q_{crust\_15} \times (6.15 C_{Th\_17} + 0.14)}{q_{crust\_17} \times (6.15 C_{Th\_15} + 0.14)}, \qquad \text{(Eq. 7.15)}$$

where H_1 and H_2 are the lunar crust thicknesses at Apollo 15 and 17 areas, respectively. In addition, q_{crust_15} and q_{crust_17} are the heat flows generated by radiative elements, which are assumed to be half of the measured total heat flow (Urey number = 0.5). The measured total heat of Apollo 15 is 21 mW/m^2, and that of Apollo 17 is 14 mW/m^2; therefore, q_{crust_15} = 10.5 mW/m^2 and q_{crust_17} = 7 mW/m^2. All the parameters that were be used in calculating the h_r value are listed in Table 7.1.

Table 7.1. Apollo 15 and 17 landing site information (*Warren and Rasmussen, 1987*).

	Measured heat flow (mW/m^2)	Heat flow generated by radiative elements (mW/m^2)	Thorium (ppm)	Lunar Crust Thickness (km)
Apollo15	21	10.5(q_{crust_15})	5.05(C_{Th_15})	31.85(H_1)
Apollo17	14	7(q_{crust_17})	2.64(C_{Th_17})	49.25(H_2)

Using the above parameter values, an h_r value of 35.72 km was derived by solving the Eq. 7.15. The values of the characteristic length h_r, lunar crust density ρ, lunar thorium abundance $C_{Th,}$ and thickness of the lunar crust H, were then substituted into Eq. 7.14 and the distribution of the heat flow generated by the radioactive element was obtained.

Summary of input model assumptions:

1. **We assume that mantle heat flow of the Moon is approximately constant and that it is mainly the crustal component produces local heat flow variations.**
2. **The crust thickness data was taken from the *Wieczorek et al. (2006)* Model**
   This model is currently the most widely used crustal thickness model in the lunar community (*Ishihara et al., 2009*). The model contains inputs from a large number of data sets including grail gravitational measurements and clementine topographical measurements. However, improvements to this model could change the calculated heat flows.
3. **The distribution of thorium is based on the Lunar Prospector high resolution data.**
4. **The distribution of uranium and potassium are calculated using a correlation expression on the distribution of thorium.** Such a correlation is empirical, but is required to make use of the high resolution of the thorium abundance map.

These poorly constrained assumptions mean that the result of the radiogenic heat flow model in this section can only be regarded as a qualitative analysis. The model here is only a framework at this point, and future work is needed to improve key parameters e.g. Urey coefficient, lunar crustal thickness distribution etc.

7.4. Results and Discussion of lunar heat flow maps and models

The heat flow caused by radiogenic heat sources (shown in Figure 7.7) is obtained by substituting the characteristic length parameter h_r, lunar crust density distribution ρ, thorium abundance and lunar crust thickness values into Eq 7.13.

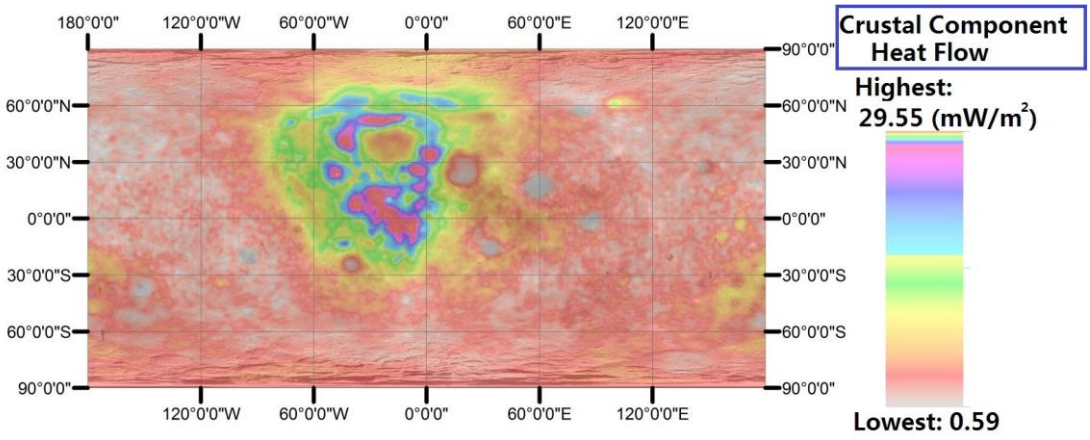

Figure 7.7. Distribution of lunar heat flow contributed by crustal component. Heat flow value caused by radioactive elements ranges from 0.59 mW/m^2 to 29.55 mW/m^2. From this figure we can notice that Apollo 15 landing site falls on a blue rim, while Apollo 17 landing site falls on a yellow-brown area, and the difference of heat flow caused by crustal components is about 7 ±4 mW/m^2.

According to Figure 7.7, the heat flow value of Apollo 15 landing site caused by crustal components is 17 ±4 mW/m^2, while the measured value by Apollo 15 mission is 21 mW/m^2 (*Wieczorek et al., 2000*). And the heat flow value of Apollo 17 landing site caused by crustal components is 10 ±4 mW/m^2, while the measured value by Apollo 17 mission is 14 mW/m^2 (*Wieczorek et al., 2000*). Therefore, if mantle heat flow Q_{mantle} is approximately constant as assumed, then it is reasonable to say that this value is 4 mW/m^2. As a result, according to Eq. 7.15, the total heat flow would be the crustal heat flow (shown in Figure 7.7) plus the mantle heat flow (4 mW/m^2). Therefore the total heat flow ranges from 5 ±4 mW/m^2 to 34 ±6 mW/m^2.

The lunar heat flow spatial distribution in Figure 7.7 is similar to the spatial distribution of radioactive elements (Figures 7.3-7.5). However, some differences are can be observed because the model also contains density information and lunar crust thickness information. The derived lunar heat flow indicates that the average heat flow for non KREEP terrain is 8 ±4 mW/m^2 which is in agreement with CE MRM derived temperature result in Figure 7.2 which gives 11 ±4 mW/m^2 for non KREEP terrain, while the heat flow for KREEP terrain can reach 34 ±6 mW/m^2. In both maps the areas with the highest amount of heat flow are concentrated on the KREEP terrain. The derived heat flow measurement in Figure 7.7 is also in agreement with the Apollo in-situ measurements. From this figure we can notice that Apollo 15 landing site falls on a blue rim, while Apollo 17 landing site falls on a yellow-brown area, and

the difference of heat flow caused by crustal components is about 7 ± 4 mW/m^2. This is in accordance with the measurements (*Langseth et al., 1976*).

Results of this chapter provide clues to the lunar geologic history. First, based on Figure 7.2 MRM showing the inverse sub-surface heat flow result, we can see that although there is large error range of ± 6 mW/m^2, it is still clear that the KREEP regions, especially the Oceanus Procellarum region, have particularly high subsurface heat flow (45 ± 6 mW/m^2), while for the non-KREEP terrain the average is only 11 ± 4 mW/m^2. Even in KREEP regions, the subsurface heat flow seems to rise as towards the centre of the region. For instance, the Apollo 15 site, which is closer to KREEP centre areas, has a subsurface heat flow of 24 ± 1.8 mW/m^2, while the Apollo 17 site, further from the centre of the KREEP region, has a lower subsurface heat flow of 14.34 ± 1.1 mW/m^2. These values are in accordance with the Apollo in-situ measurements, which suggest 22 mW/m^2 for Apollo 17 and 14 mW/m^2 for Apollo 15. Such findings are also supported by the endogenic heat production model in section 7.3, which suggests the radioactive elements in the lunar crust is the main source that is responsible for producing these heat flow variations.

This result is important to our understanding of the KREEP terrain. Because if the centre of KREEP has higher subsurface heat flow than neighbouring KREEP regions around it, and the entire KREEP terrain as a whole has a much higher average

subsurface heat flow than other non-KREEP lunar regions, then this would imply that the potential origin of the PKT is a large scale volcanic event, such as a mantle plume (*Campbell, 2005*). Mantle plumes are believed to start at the core-mantle boundary and rise through the lunar mantle, pushing KREEP materials upwards, and forming the distinct region of KREEP terrain that we observe on the Moon today.

Evidence for a volcanic rather impact driven process to form the PKT can be found in deep surface gravity anomalies measured by recent the GRAIL gravity gradient mapping mission. GRAIL also found a polygon-like formation resembling a system of rift valleys surrounding the region beneath the lava plains, suggesting the basin was formed by heating and cooling of the lunar surface by internal processes rather than by an impact, which would have left deep structures more typical of a large impact basin. (*Andrews-Hanna et al., 2014*)

Secondly, another implication of this result is that the Moon may still be geologically active. Based on the CE MRM inverted subsurface heat flow results, average non-KREEP region subsurface temperature is 11 ± 4 mW/m^2. However, if we only consider the cooling process due to a completely geologically inactive, solid core then this value should be ~4 mW/m^2 (*Langseth et al., 1976*). This also explains some recent finding that some parts of the Moon may be warmer than previously thought (*Braden et al., 2014*). Volcano activity at Ina, ended about 33 million years ago, and

at another irregular mare patch, Sosigenes, it stopped only about 18 million years ago (*Braden et al., 2014*).

(Figure 7.7 does not have as many artifacts as Figure 7.2. This is because Figure 7.2 represents inverted MRM measurement which has data tracks and different optical bands, while Figure 7.7 is a theoretical model based on radioactive elements distribution.)

Chapter Summary:

This chapter first calculated lunar heat flow based on the CE derived temperature results obtained from the MRM data in chapter 5. From the CE data, the heat flow at the Apollo 15 landing site is 23.9±4 mW/m^2. Meanwhile, the heat flow at Apollo 17 landing site is 14.3±4 mW/m^2. These values are in agreement with Apollo heat flow measurement results (*Warren and Rasmussen, 1987*).

On the basis of the mineralogical parameter, *S* spatial distribution derived from the M^3 surface measurements and the density distribution in chapter 5, I inverted the 2-m deep lunar subsurface heat flow from CE data. The heat flow was found to range within 2 mW/m^2–68 mW/m^2, which is the same order of magnitude as earlier

estimates *(Krotikov and Troitskii, 1964; Langseth et al., 1973, 1976)*. A spatial correlation was observed in the plotted the 2-m deep lunar subsurface heat flow map with maps showing the distribution of radioactive elements. In section 7.2 the KREEP-rich region Oceanus Procellarum was found to have an elevated 2-m subsurface heat flow of ~34 ±10 mW/m^2 compared to non-KREEP terrain. In section 7.3, a hypothesis was presented, which suggested that the high subsurface temperature may be attributed to high thorium, potassium, and uranium abundance. To investigate this hypothesis a new lunar heat flow model framework was derived in section 7.3 using the distribution of radioactive elements providing radiogenic heating.

The new model of the lunar subsurface heat flow gives a qualitative comparison between the MRM derived heat flow and spatial distribution of radioactive elements. The model predicts a range in heat flow values from 5 ±4 mW/m^2 to 34 ±6 mW/m^2, providing a non-KREEP average flow of 8 ±4 mW/m^2. The new model is in good agreement with the CE MRM result in section 7.2. In both the derived temperature heat flow model and the new radiogenic heat flow model, the highest heat flow values are found inside the KREEP terrain. This finding constrains the possible source of the abnormal 3 GHz TB described in chapter 1 observed in Figure 1.3.

Chapter 8. Conclusion and Future Applications

8.1. Thesis Summary

As discussed in chapter 1, the lunar soil temperature profile and subsurface heat flow are important parameters in lunar exploration. Modelling the heat flow of the Moon is an important part of the diagnostic tests of thermal evolution models. This measurement can also help to constrain the Moon's crustal composition of radioactive elements and gives clues to its differentiation.

The lunar surface temperature has been measured using the Diviner lunar radiometer, however the subsurface temperature had only been measured directly at the Apollo 15 and 17 landing sites before the launch of Chang'E-1 (CE-1). The CE-1 and Chang'E-2 (CE-2) lunar orbiters were each equipped with a four channel Microwave Radiometer (MRM) instrument. The MRM can detect the brightness temperature of the lunar surface to retrieve subsurface lunar regolith temperatures and other related properties. In this thesis, MRM data used to estimate the lunar subsurface heat flow. In order to achieve this, a total of 8 steps were required and. each step is summarized below.

1. Initial MRM validation (chapter 2)

In this thesis, an initial three-dimensional lunar brightness temperature (TB) map was derived from the MRM data of the lunar soil from the near-surface to a nominal 5 m depth. To validate the MRM measurements, the near-surface TB measurements from MRM were compared to the near-surface temperature measurements made by Diviner. From the initial TB map of the CE MRM data, a unique 3 GHz (5 m subsurface depth) TB elevation in the Oceanus Procellarum region was observed. It was hypothesized that this elevation in subsurface temperature could be due to the presence of radioactive KREEP materials. Further analysis of the MRM data was required to investigate this.

2. Lunar soil modelling and vertical temperature profile estimate (chapter 3)

Knowledge of the lunar soil temperature profile depends on the only in-situ measurements from two Apollo sites. However, to simulate the microwave emission from the lunar surface and develop a forward model of the MRM data, a global distribution of the subsurface soil temperature profile is required. A one-dimensional thermal diffusion model was generated to estimate the global temperature distribution in the top 5 m of the lunar regolith. This model was adapted from the *Spencer et al. (1989)* model and was compared with the *Vasavada et al. (1999)* model. Analytical expressions for the thermal physical parameters (e.g. bulk density, heat capacity, dielectric constant and thermal conductivity) required in the one-dimensional thermal

diffusion models were derived from in-situ Lunar and Apollo measurements and laboratory measurements of returned samples.

The Apollo measured temperature profile beneath the lunar surface matched well with the curve provided by the theoretical model simulations. The combination of CE MRM and Diviner data, as well as the theoretical model simulation, shows that the lunar surface temperature profile varies mainly within the top 20 cm, varies slightly within the top 20–50 cm (*Vasavada et al., 1999*), and is almost stable under 2 m depth. These findings are also indicated in the theoretical model.

3. Forward radiative transfer model and TB test (chapter 4)

Using the parameters derived in the previous step for the one-dimensional thermal diffusion model, a microwave radiative transfer model was established to interpret the MRM data according to the coherent approach of microwave transmission theory and fluctuation–dissipation theorem. To test the forward model, the predicted TB's contributions from different depths of the 4 channels were compared with the real MRM received TB data and were shown to be in good agreement.

To further test the forward model, the subsurface variation of the lunar temperature with depth at a single point in the equatorial region was derived, and compared with the theoretical predictions of the one-dimensional thermal diffusion model from the previous step. It was also discovered most of the information from the MRM

measurements comes from the temperature of the model's layer T_5 (depth 20 cm – 500 cm). Hence the error in the inverted temperatures of the other layers is much greater than the error in the derived temperature of T_5. It was therefore decided that only the temperature of the layer T_5 would be derived in the inversion scheme in chapter 6.

4. Forward model error analysis (chapter 4)

As the errors of many model parameters were unknown, both traditional error and Monte Carlo sensitivity analyses were conducted to investigate how the parameter errors affected the forward model's predicted temperature of layer T_5. From this analysis the lunar mineralogy and soil bedrock density were found to be the main sources of uncertainty.

5. Lunar mineralogy and density studies and model improvements (chapter 5)

Methods of deriving FeO and TiO_2 content from Clementine spacecraft data were discussed and our own approach was developed for deriving the content from measurements made by the M^3 instrument on Chandrayaan 1. The density of lunar soil bedrock was then modeled based on the derived FeO and TiO_2 information. The FeO and TiO_2 abundance we derived from the M^3 data was compared to previous results from the Clementine data and was in good agreement. The FeO abundance

data also compared well with the Lunar Prospector data which was used as an independent source.

The previous Clementine and new M^3 derived abundances were compared to the laboratory measured FeO and TiO_2 content in the Apollo and Luna returned samples.

The Clementine derived FeO content was systematically 1-2% lower in all the returned samples than the laboratory measurements. The M^3 derived content compared better with the returned Apollo samples and was within ±2.8% of the laboratory measurements. The Clementine derived TiO_2 abundance was systematically 0.1-4% higher than the laboratory measurements of the returned samples. The M^3 derived TiO_2 compared well (±0.6%) with the laboratory measurements of the returned samples except for samples with high TiO_2 content. However, caution should be used when interpreting these results as the error range needs further study. Unfortunately no error analysis was provided with the previous Clementine derived contents.

6. Inversion of subsurface temperature (chapter 6)

The global subsurface temperature at 2 m depth was derived by inverting the MRM brightness temperatures using the newly developed thermal transfer model with new mineralogy and density inputs from chapter 5. Comparisons of uranium, thorium and potassium abundance maps show that there is spatial correlation between the 2 m

depth subsurface temperature and the distribution of the abundances of these elements. These radioactive elements would provide a local radiogenic heating source that would elevate the temperature at a depth of 2 m. The regions with the lowest heating source (i.e. the lowest abundance of uranium, thorium and potassium), have the lowest 2 m subsurface temperature (approximately 240 ±4 K). This finding is in agreement (to within 3%) with the model used by *Keihm et al. (1973)*, which did not consider radiogenic heating. By contrast, the region with the highest heating source (KREEP), has the highest 2 m subsurface temperature (approximately 260 ±6 K). The KREEP region on the lunar surface contains the greatest abundance of uranium, thorium and potassium. The average 2 m subsurface temperature in non-KREEP regions is 246 ±4 K. The difference between the KREEP region and the non-KREEP is supported by Wieczorek's KREEP heat flow model (*Wieczorek et al., 2000*), which predicts a 10 K difference between the KREEP center and non-KREEP regions.

7. Inversion of lunar heat flow and the radioactive heat calculation (chapter 7)

The lunar heat flow was calculated based on the subsurface temperature result obtained from the MRM data inversion. According to the inversion result, the heat flow at the Apollo 15 landing site was 23.9±4 mW/m^2 and the heat flow at the Apollo 17 landing site was 14.3±4 mW/m^2. Such values are in good agreement (<10% deviation) with Apollo heat flow measurement results (*Warren and Rasmussen, 1987*).

A 2 m deep lunar subsurface heat flow map was also derived from the MRM data. The 2 m subsurface heat flow was found to range from 2 mW/m^2 to 68 mW/m^2, and was found to have a strong correlation with the radioactive elements distribution. To confirm this correlation, a lunar heat flow model based on radiogenic element distribution was then built, whose result is in accordance with the MRM inversion. Areas with modeled high heat flow are generally found in the KREEP terrain. This finally explained the finding in chapter 1, Figure 1.3 that the Oceanus Procellarum (KREEP terrain) region has an increased subsurface temperature compared to the mean lunar subsurface temperature. The increased subsurface temperature is due to higher heat flow in the region from radiogenic heat sources.

8. Scattering effect of rough surface on MRMs (Appendix)

By using the small perturbation method and the shadowing function, results show that, in most cases, large-scale (m – km) lunar surface roughness mainly reduces solar radiation and hence will reduce the temperature of the lunar soil and the MRM measured TB. The effect of small-scale (mm) lunar surface roughness on the MRM measured TB was only explored in the 3 GHz channel because this where most of the information in the inversion scheme comes from. For typical small scale lunar roughness, the effect on the MRM measured TB in the 3 GHz channel was found to be < 0.5 K. This is negligible compared to the 14 ± 10 K measured elevated temperature in the KREEP terrain.

8.2 Possible future MRM Applications, including Martian MRM remote sounding.

8.2.1 Importance and feasibility of Mars microwave sounding

Compared with the Earth's surface, the surfaces of the Moon and Mars lack water and vegetation. Therefore, a microwave sounding instrument, such as the MRM, also has applications on Mars and any other arid surface (e.g. asteroids). In the subsequent section, the use of a multichannel MRM instrument in observing the Martian surface will be discussed. The possibility of water that is locked away in the subsurface of Mars will also be discussed as an MRM instrument could be used for the detection of the water depth.

Mars has an equatorial radius of 3,397.2 km (approximately half of the Earth), a mass of 6.421×10^{23} kg, and an average density of 3.94 cm^3 (which is similar to that of the Earth). Compared to Earth, Mars has a greater orbital and rotational period of 686.98 days and 24.6 hours respectively (*Simon et al., 1994*). The main components of the Martian atmosphere are CO_2 (95.32%), N (2.7%), Ar (1.5%), and H_2O (0.03%). Mars is farther from the Sun than the Earth and hence receives less solar energy. Moreover, the Martian atmosphere is thin and cannot conserve heat, (unless there is a dust storm, in which case the thermal balance shifts a lot) therefore, the surface temperature of

Mars is low, with an average temperature of 210 K, close to that of the Moon's average temperature. The difference between the day and night surface temperatures of Mars is approximately 140 K to 300 K (*Erard, 2001*).

Mars has a dry surface, thin atmosphere, and low-temperature environment. Thus, Mars is a possible MRM target for subsurface temperature sounding or water detection. There is believed to be trapped water in the subsurface of Mars, but this has not been well characterized. Typical science questions that an MRM instrument can help address include the following:

- What are the water reservoirs on Mars?
- Where are the water reservoirs on Mars?
- Is the planet active today?
- What does the global subsurface geologic structure tell us about the evolution of the planet?
- What are the global distributions of near-surface materials and volatiles?

The surface of Mars is composed of distributed basins (e.g., a giant northern basin that covers approximately 40% of Mars' surface, sometimes called the Borealis basin), dry riverbeds, craters (formed by meteorites or small celestial bodies), and sand dunes (piled up by the wind). Typical Martian terrain from the High Resolution Imaging Science Experiment is shown in Figure 8.1.

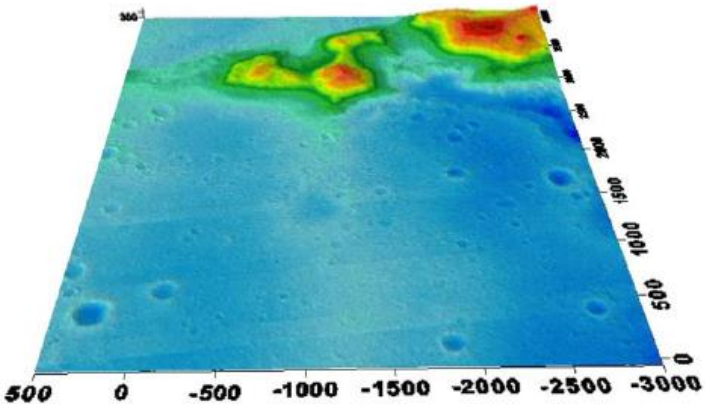

Figure 8.1. Three-dimensional surface maps of the area surrounding the Spirit rover landing site (cited in *Li et al., 2011*). A sample Martian area contains craters, riverbeds, and hills.

At the north and south poles, a large seasonal ice sheet has been formed by the accumulation of dry and water ice. A newly formed low-lying plain is located on the northern hemisphere, which is 30% of the total surface area of Mars (*Mitch, 1976*). By contrast, the southern hemisphere is composed of ancient highlands with many craters (*Mitch, 1976*). Several radar experiments already mapped the Martian subsurface down to several kilometres (*Picardi et al., 2004*) and a search for subsurface liquid water reservoirs has been conducted using different concepts and techniques.

At the Martian poles where the regolith is kilometres deep, radar experiments are suitable for searching for liquid water reservoirs. However in equatorial regions where the regolith is metres thick, radar experiments are not ideal as they penetrate to kilometres of depth and have a low resolution. Microwave sounding instruments

would be much better suited as they have a high resolution and penetrate to depths of several metres (<5 m).

Mars may have water content that can provide important information on the geology, hydrology, and climate evolution of the planet. One of the main objectives of current Martian research is to find water on Mars (*Clifford, 1993*). Given that the surface of Mars has low atmospheric pressure (approximately 6 hPa) and the average temperature is only 210 K, water on Mars' surface is difficult to obtain. From the Martian surface temperature, thermal conductivity, heat flow, and underground water freezing temperature, the theoretical and geophysical models of the Martian surface predicted that water may be present below the Martian surface (*Clifford, 1993*). Mars has a potentially habitable environment because of the possible presence of water and other liquid features observed in the planet. Submillimeter (microwave) spectroscopy is a potential technique for observing water vapor and constraining its concentration and isotopic composition (*Hayneet al., 2014*).

As well as investigating subsurface water ice, an MRM instrument could be used to monitor Martian dust storms. Dust absorbs thermal radiation from the Sun and hence during a dust storm a temperature increase in the Martian atmosphere would be observed. An MRM instrument could be used to detect such an increase in

atmospheric temperature provided channel selection was tailored for a low penetration depth.

A further application of an MRM instrument on Mars would be inverting the subsurface temperatures. The thickness of the Martian surface dust layer is less than 5 m (*Heggy et al., 2001*). Thus, if the temperature difference between the dust layer and the underlying layer is relatively large or if a large contrast in dielectric constant exists between different layers, then the subsurface temperature can be inverted from multichannel microwave emission data. This approach is important in understanding the geological history of Mars. The temperature distribution of the soil in the Martian surface may provide direct evidence for the present state and distribution of water on Mars' surface/subsurface.

8.2.2 Previous detection by radar instruments

ESA's Mars Express deployed the Mars Advanced Radar for Subsurface and Ionosphere Sounding (MARSIS) in 2005. MARSIS is a multiband and low-frequency (0.1 MHz to 5.5 MHz) vertical incidence radar detector which has a detection range of 5 km below Mars' surface (*Picardi et al., 2004*). The purpose of MARSIS is to find water or ice on Mars. The center frequencies of MARSIS at night are 1.8, 3.0,

4.0, and 5.0 MHz, whereas the centre frequencies MARSIS during the daytime are 4.0 and 5.0 MHz.

The main purpose of MARSIS is to probe the presence of water and its distribution. If the velocity of the electromagnetic wave propagation in the Martian subsurface is known by measuring the Martian surface and subsurface radar echo time delays, then the determination of the subsurface thickness will be straightforward. The echo signal strength can be used to estimate the attenuation and reflection properties of the electromagnetic waves in the subsurface of Mars. The basic principle of MARSIS detection has been previously discussed by *Picardi et al. (2004)*, Figure 8.2.

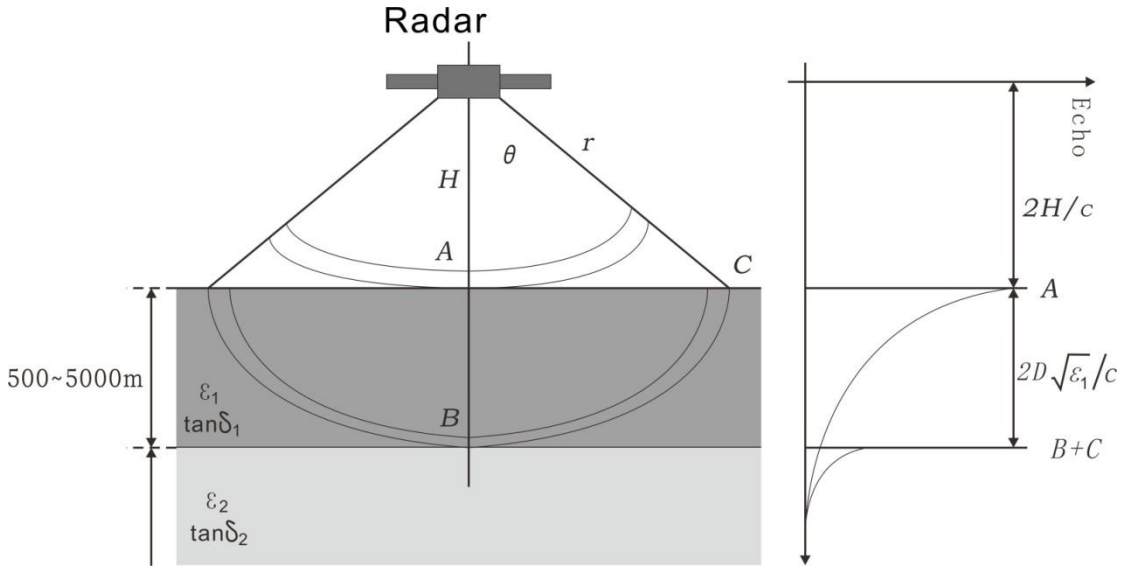

Figure 8.2. Subsurface detection principle of the MARSIS according to *Picardi et al. (2004)*. By calculating the time delay of echo signal, the depth of water layer can be estimated.

However, the MARSIS resolution in the vertical direction in the Martian subsurface soil is approximately 100 m, with an orbit height of less than 1,200 km (*Picardi et al., 2004*). If the water layer thickness is only a few centimeters or even several metres, then it may not be detected.

8.2.3 Methodology of a Mars orbiter MRM

8.2.3.1 Instrument frequency band choice

The electromagnetic scattering properties of the regolith and rocks must be determined to understand the use of an MRM instrument on Mars. From the perspective of a microwave instrument, the Martian topsoil is a blend of silicates, iron, and other metal oxide components. The planet's topsoil is a low-loss dielectric, where the depth of penetration of the electromagnetic wave is written as:

$$d_0 = \frac{\sqrt{\varepsilon_r'}}{\pi \varepsilon_r''} \lambda \quad , \qquad \text{(Eq. 8.1)}$$

where ε' and ε'' are the real and imaginary parts of the relative permittivity of the surface of Martian soil, respectively, and λ is the vacuum wavelength.

Radiometer frequency selection should consider the influence of penetration depth to investigate the subsurface water/ice distribution. Usually, low-frequency channels

have a deeper depth of penetration. However, when the frequency is significantly low, the resolution may also be affected by the diffraction limit of the antenna.

Given that the depth of the top dust layer on Mars, in some places at least, is thicker (2 m) than that of the Moon (2 cm), the MRM channels should have at least one low-frequency channel at 200 MHz to 500 MHz and at least one high-frequency channel at 2 GHz to 5 GHz. If this makes the antenna larger than the current MRMs on CE, we can slightly reduce the spatial resolution as in practice spatial resolution is not a key factor in global mapping.

8.2.3.2. Physical parameters

The main physical parameters of Martian microwave remote sensing are the dielectric constant, structural distribution, subsurface bulk density, geometry, shape, and surface roughness. The actual component of the dielectric constant of the Martian surface dust layer is mainly related to the Martian soil density, where the volume density of the dust layer varies between 1.4 and 2.0 g/cm^3 and the bulk regolith density varies between 2.5 and 3.0 g/cm^3. The loss tangent is then closely related to the hematite and titanium contents in the Martian soil (*Campbell et al., 2004*).

The main compositional components of the Martian surface soil are assumed to be andesite and basalt. The dielectric constants of andesite are ε_r = 3.5, tanδ = 0.005, whereas the dielectric constants of basalt are ε_r = 7.1, tanδ = 0.014 (*Biccari et al., 2001*). Figure 8.3 shows that the calculated (from Eq 8.1) electromagnetic penetration depth of the two different substances on the surface of Mars changes with frequency. If the channels of an MRM instrument are selected between 1 GHz and 5 GHz then depths between a few metres and up to 30 m can be explored on the Martian surface, as shown in Figure 8.3.

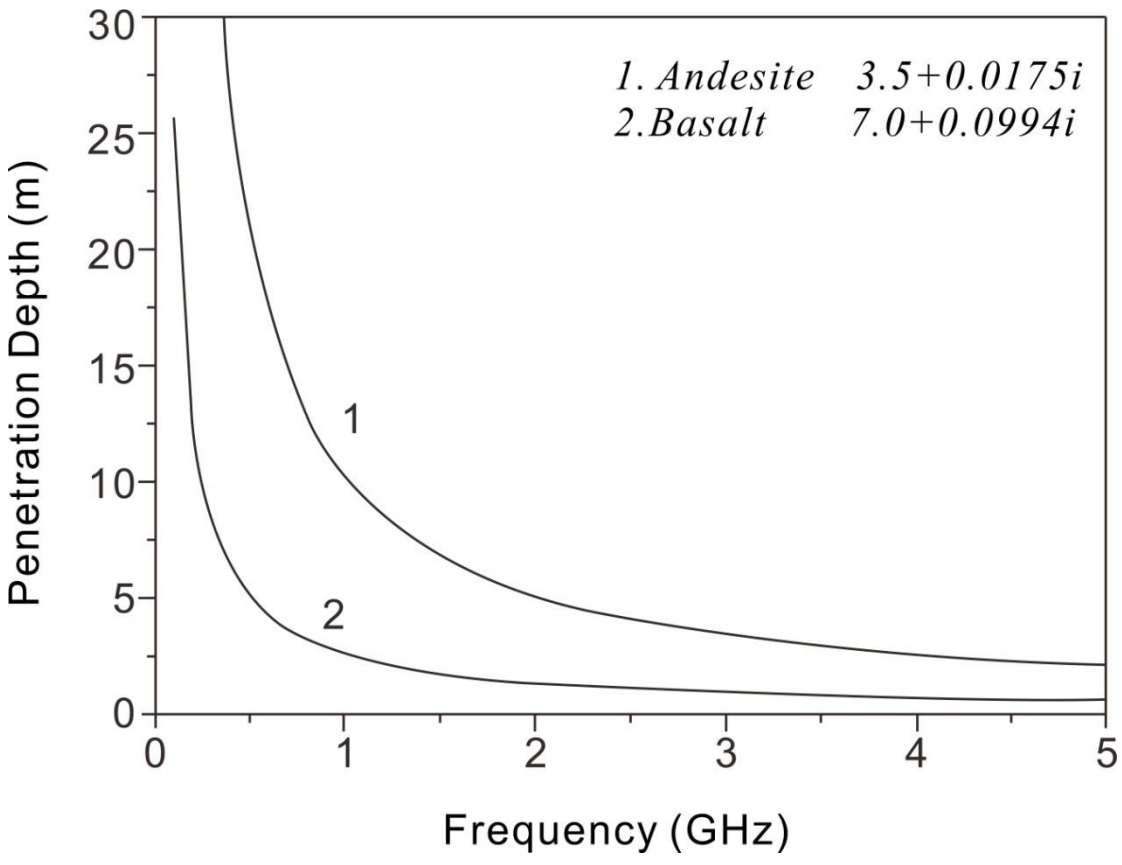

Figure 8.3. Calculated penetration depth of microwave instrument on andesite (1) and basalt (2).

A layer division model for Mars microwave subsurface detection purposes is proposed. Given the presence of weathering and the effect of meteorites and other small objects, most of Mars' surface is covered with a layer of dust, mainly iron oxide that is between 0.1 – 2 m deep. Although globally the dust layer thickness could vary between 1 m to 10 m. Some important geological structures, such as craters and river water, may be covered by a dust layer. Heggy et al. (*2001*) provided a hypothetical shallow structure of Mars, as shown in Figure 8.4.

The distributed dust layer on the surface of Mars has a thickness of approximately 2 m to 10 m, and Mars' altered basalt layer has a thickness of approximately 40 m. Weathered layers and volcanic lava with a thickness of 50 m to 200 m are observed, and approximately 200 m to 400 m of a deposited layer can also be seen (Figure 8.4). Under the deposited layer is a 2.5 km thick layer of permafrost and liquid water may exist below this permafrost layer.

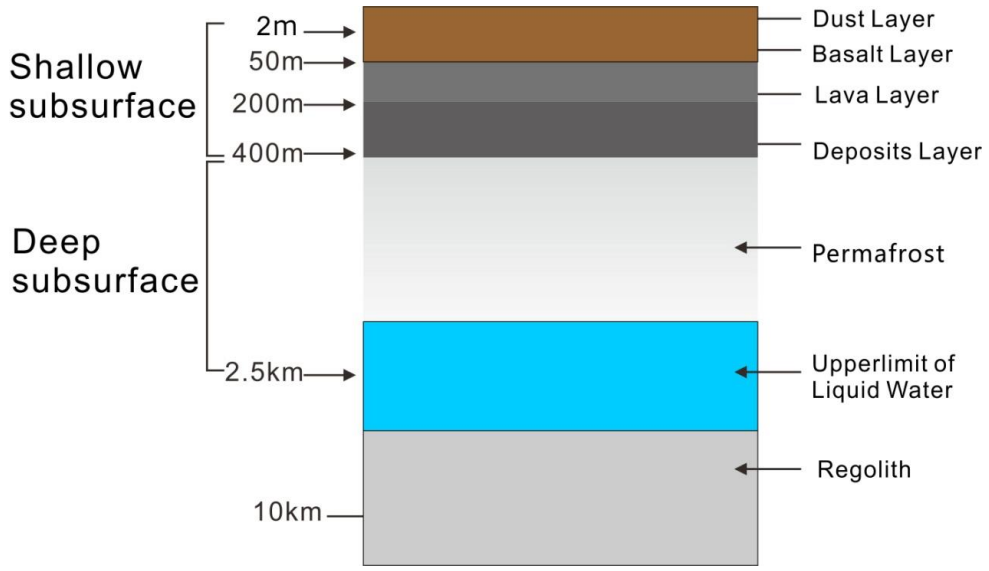

Figure 8.4. Layer division for a possible Martian inversion model.

Microwave remote sensing can play a unique role in the exploration of Mars' geology and evolution history, including probing of subsurface water. According to *Ulaby (1985)*, water and andesite mixtures have a different dielectric constant to normal andesite rock. Thus, these mixtures could be detected by the inversion of the dielectric constant numbers from a MRM instrument.

8.3 Future Improvement of MRM Missions

As discussed in chapter 1, CE MRM comprises four channels that feature frequencies at 3, 7.8, 19, and 37 GHz. Penetration depth and band choice are expressed in Eq. 8.1. This section discusses possible improvements to the MRM instrument to obtain a greater accuracy in the derived subsurface temperatures and avoid some of the degeneracies found in analyzing the data. For example, the current frequency selection is imperfect for subsurface temperature inversion of the Moon. The 3 GHz channel can detect signals from a depth of several metres in the absence of moisture. However, the nominal penetration depths of 19 and 37 GHz are quite close, i.e., 5 and 2 cm, respectively (*Wang et al., 2010*). In addition to frequency selection, the forward model and subsequent measurement inversion work detected other aspects that need attention. These aspects will be discussed in the subsequent sections.

8.3.1 Mineral distribution along the depth through more ground truth studies

Mineral composition along the depth should be determined to assist in the modelling

and inversion process. However, the Apollo lunar soil core samples are limited to individual points, with the maximum depth of 2.8 m below the lunar surface. As such, few studies have reported on the variation of the lunar soil dielectric constant with depth.

Variations in composition with depth implies including different dielectric constant profiles and improving knowledge with constraining the derived subsurface temperatures. Research using microwave remote sensing observations to examine the difference between theoretical prediction and measured values would allow changes in the dielectric constant with the depth of the internal lunar soil layer to be studied. More samples and laboratory measurements should be required. Thus, the change in the FeO and TiO_2 content in the lunar soil with depth should also be determined to derive better dielectric information.

8.3.2 Number and frequency range of radiometer channels

The number of channels in the MRM instrument should ideally be more than the number of parameters to be measured. Channels need to be carefully designed to get the maximum spread in the weighting function. A set of channels that are specifically designed for the Maria (i.e. sound to less depth due to the high TiO_2 concentration) and highlands (sound to greater depths) regions could also be included to further improve the MRM instrument.

From the trade of cost and volume, many frequency bands should be set to ensure a good distribution of penetration depths. The distribution of penetration depths should not be too close; otherwise, the approximate penetration depth will be inapplicable to the subsequent inversion operation.

8.3.3 Integrating microwave remote sensing and other detection techniques

The multicolor photometry of a planet's surface is an important method to determine the metallic material composition of the planet's surface because the optical properties of the soil materials on the surfaces of the Moon, Mars, and other planets are related to the metal element contents (*Jaumann, 1991; Lucey et al., 1995*).

For example, in the case of a Martian MRM a combination of optical remote sensing and microwave remote sensing is preferable. For example, the metal content of Martian surface soil should first be estimated through optical remote sensing. The dielectric constant of the Martian surface can then be calculated from the measured metallic abundance. Assuming the mineralogy at the surface correlates to the subsurface, the subsurface information can be obtained if the surface mineralogy information and dielectric constant are known. The subsurface of Mars could be subsequently investigated through microwave remote sensing, although the higher orbital altitude, due to the presence of an atmosphere will reduce the spatial resolution when compared to the Moon (15 km). This chapter uses Mars as an example, but it can be used as a guide in the exploration of other planets and arid bodies.

Appendix. Effect of surface scattering on MRM Derived Subsurface Temperatures

A.1. Appendix Introduction

In this appendix, the effects of surface roughness at differing scales on the TB measured by the MRM will be studied. Calculations will show that introducing a small-scale (mm) lunar surface roughness can increase the brightness temperature of radiation for the MRM high-frequency channels (19 GHz and 37 GHz). Meanwhile, in most cases, large-scale (m - km) lunar surface roughness reduces solar radiation by the shadowing effects, which obscures solar radiation, thereby decreasing the temperature of the lunar soil for the nadir viewing case considered in this appendix.

Various approaches can be employed to model surface "roughness" scattering and volumetric scattering at microwave wavelengths. Two of the most widely used methods to calculate the small-scale (where the roughness is of the same order of magnitude as the wavelength of light) roughness effect, are the Kirchhoff Approximation (KA) and the small perturbation method (SPM) (*Jin, 1993*). The KA is suitable when the angle of incidence is small and the wavelength of the incident wave is significantly smaller than the mean surface curvature radius. The SPM is suitable for small-scale surface roughness with a small root–mean–square (RMS) height (<4 mm) and shallow slope distribution (gradient <0.5).

This appendix examines the transmission characteristics of small-scale rough surfaces using the SPM to analyze the effect of small-scale roughness on the microwave brightness temperature of the lunar soil. On the basis of Huygens' Principle and the law of light absorption, the next section derives the zero-order, first-order, and second-order transmission fields of a random small-scale rough surface using the SPM, as well as the analytical formulas of the second-order two-way transmission coefficient and second-order transmittance.

A.2 Small-scale Roughness (mm scale)

The Apollo 12 mission included a close-up camera which took stereo-pair images at 50 cm resolution (Figure A.1) to determine the local topography of the landing site (*Helfenstein and Shepard, 1999*). The site is relatively flat, but is characterized by small-scale roughness. Analysis of the stereo-pair images showed that on a 1 mm scale, the surface standard deviation is between 0.9 mm and 3.6 mm and the RMS inclination is between 13.9 ° and 37 ° (*Helfenstein, 1999*). In strict terms, at the MRM frequencies (3 GHz to 37 GHz) this type of rough surface cannot be assumed to be a flat uniform plane, as the wavelength of the radiation (8 mm to 100 mm) is of similar size to the roughness, especially for the higher frequency channels.

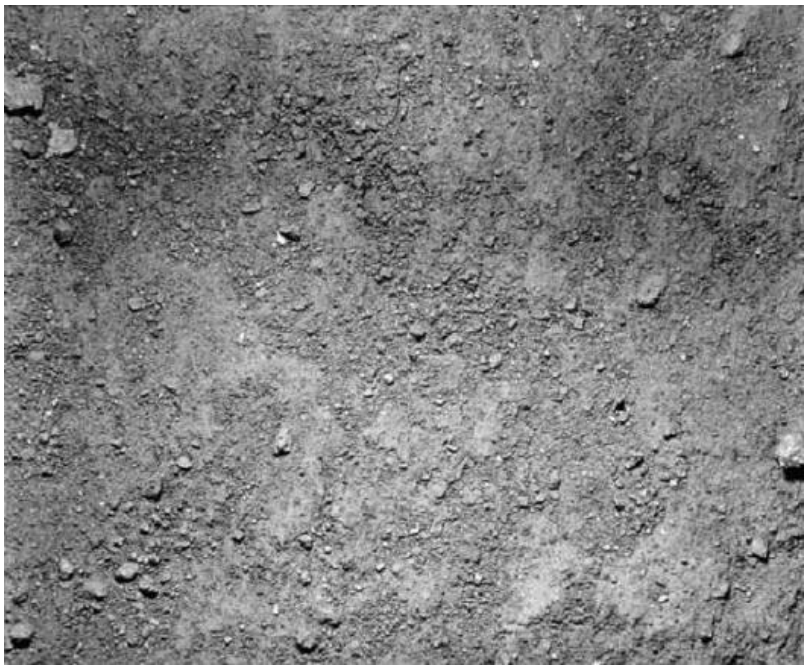

Figure A.1. Apollo 12 site AS12-57-8449 area surface photo (photo length scale is 90 mm). (*Helfenstein and Shepard, 1999*).

In the SPM, the random surface scattering field is expressed as the disturbance sequences of surface heights, whose zero-order scattering field corresponds to the smooth surface scattering field, and the first-order solution is consistent with the lowest-order incoherent scattering field of the rough surface. Meanwhile, the second-order solution was employed to conserve energy (the first-order solution may not conserve energy precisely enough), which is particularly important in calculating the emission rate. The lunar soil microwave transmission was simplified by using a three layer depth model of lunar subsurface as illustrated in Figure A.2.

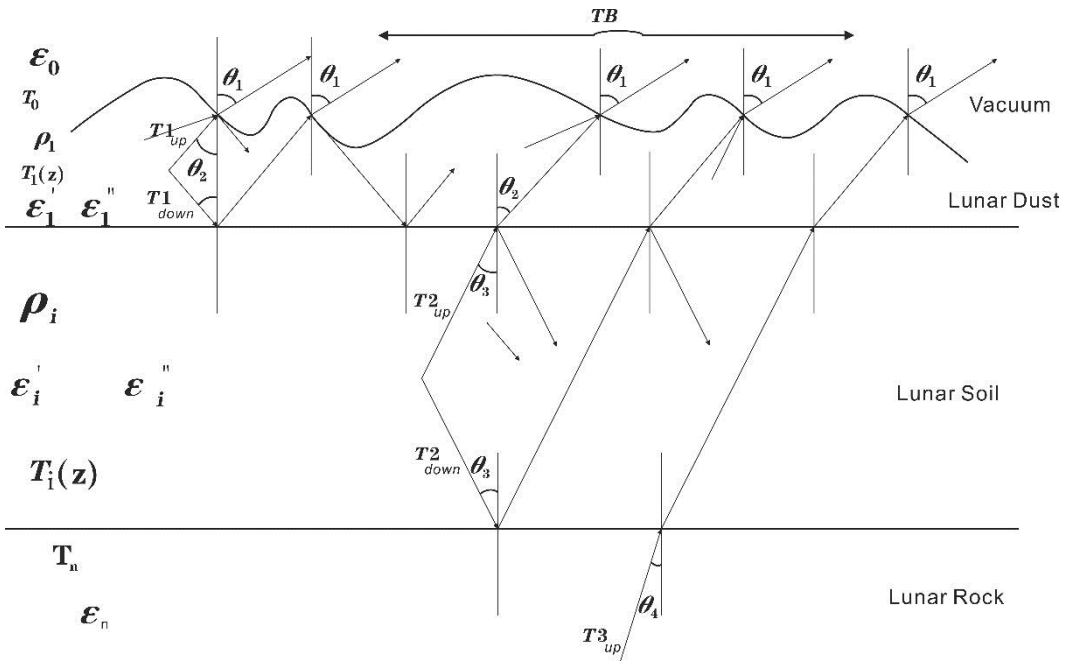

Figure A.2. A simplified three-layer model is introduced to analyze the transmission changes of small-scale roughness. In this figure, the receiver is viewing across a large area and is integrating over emission angle.

In chapter 4, the lunar dust layer, lunar soil layer, and lunar bedrock layer were divided into six layers for the combined thermal diffusion and radiative transfer models. However, in this case, the four lunar soil layers, which have similar densities (in the range of 1.6 g/cm^3 to 1.9 g/cm^3), were combined to simplify the calculations because the physical issue under investigation is the contribution to scattering from the neas-surface layers.. In this chapter, the vacuum is defined as layer 1 and the lunar regolith has been divided into 3 layers. The lunar dust layer is defined as layer 2, the four lunar soil layers are combined into a single layer, layer 3 and the bedrock layer is

defined as layer 4. Figure A.3 shows the diagram of the relationship between the two models.

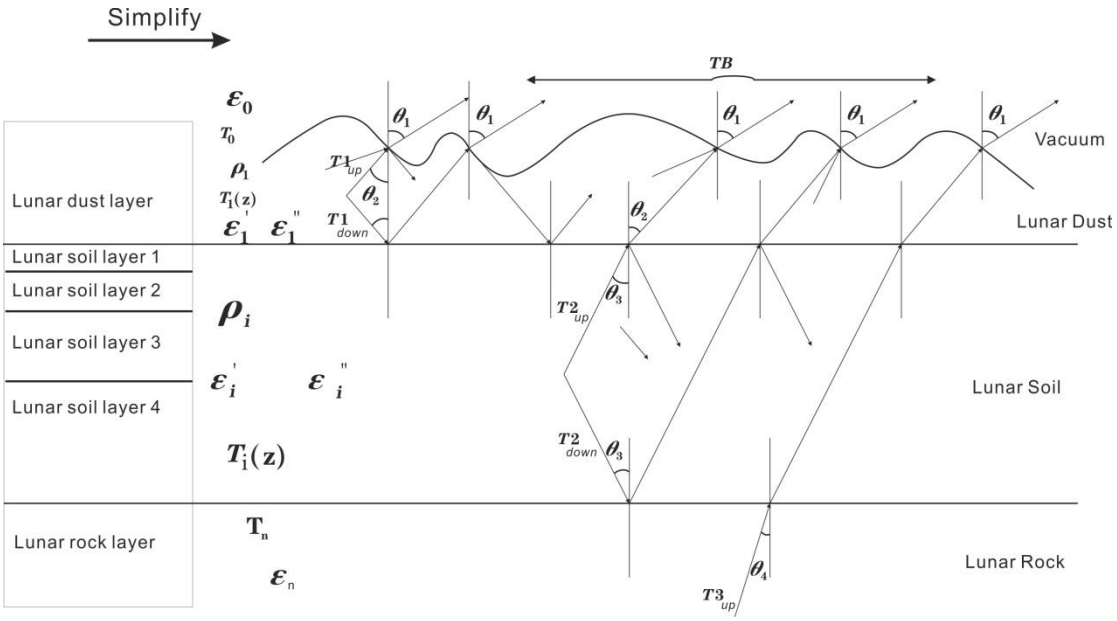

Figure A.3. The relationship between the two models: in the left box is the layer division of TB simulation model, while it simplifies to the three layer roughness model on the right. This is because the roughness effect study mainly focus on the geometric properties, which is similar among lunar soil layers 1-4, hence the four lunar soil layers were combined together here into one lunar soil layer.

In this analysis the lunar bedrock is ignored because it is below the penetration depth of the MRM instrument and does not contribute to the observed signal (see chapter 4 Figure 4.2 and 4.3). Therefore the TB received by a microwave radiometer at a point (θ_1, ϕ_1, as defined in Figure A.4) can be estimated from the contributions from layers 2 and 3 (e.g. dust layer and soil layer). The radiation incident and transmitted from

the two layers is assumed to be unpolarized and contains 50% q-polarization and 50% p-polarization.

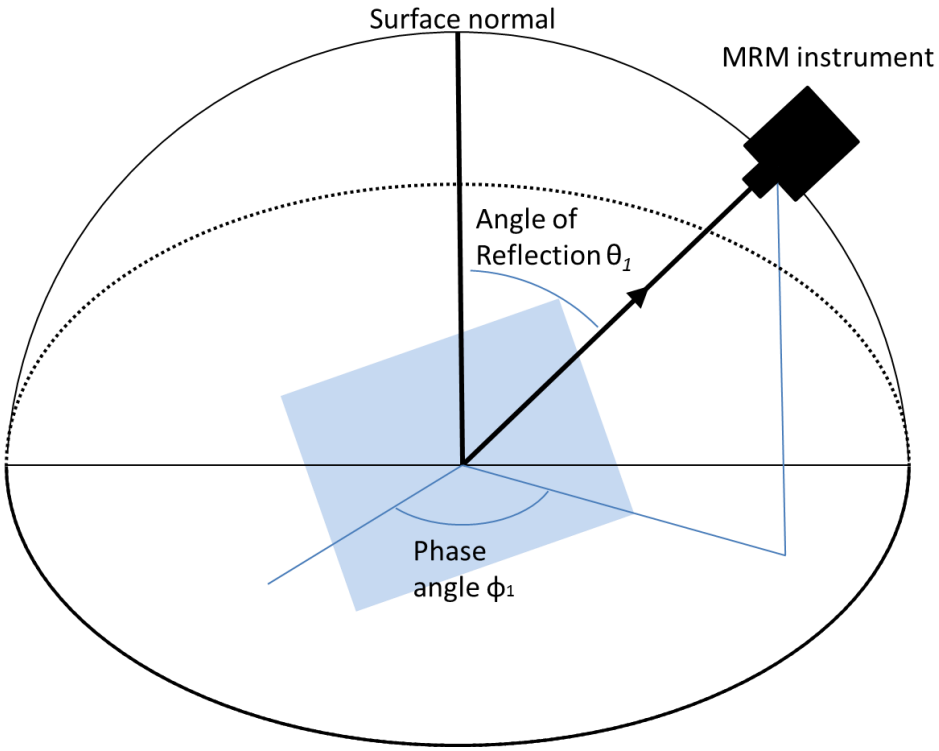

Figure A.4. Defination of scattering angles used in chapter 8 calculation.

The TB that would be measured by a microwave radiometer from only the p-polarization contribution is given below:

$$T_{B,\mathrm{p}}(\theta_1,\phi_1,1^+) = \mathrm{T}_{B3,p}(\theta_1,\phi_1,1^+) + \mathrm{T}_{B2,p}(\theta_1,\phi_1,1^+)\,, \qquad \text{(Eq. A.1)}$$

where the superscript + indicates radiation emitted from the upper boundary of a layer as illustrated in Figure A.3. Analysis is only required in one polarization sense because the p-polarization is equal to q-polarization. Although Eq. A.1 looks simple,

to analytically expand it requires very complex calculations, which fortunately can be built upon from previous work (*Helfenstein and Shepard, 1999; Chen et al., 2011; He, 2013*). This work simplifies these major previous derivations (*Helfenstein and Shepard, 1999; Chen et al., 2011; He, 2013*), by applying the formulas to the lunar surface to simulate the quantitative effect of the 3 GHz MRM TB channel only. Only the 3 GHz channel is studied because most of the information from the inversion model comes from this channel (Chapter 6).

A.2.1. Contribution from layer 3

The contribution from layer 3 using only p-polarization is expressed as *(Chen et al., 2011)*:

$$T_{B3,\mathrm{p}}(\theta_1,\phi_1,\theta_2,\phi_2,1^+)=\frac{T_{B3,\mathrm{p}}(\theta_2,2^+)}{L_2}\cdot t_{pp}^{12}(\theta_1,\phi_1,\theta_2,\phi_2)\cdot\frac{\varepsilon_2}{\varepsilon_1}+\frac{T_{B3,q}(\theta_2,2^+)}{L_2}\cdot t_{pq}^{12}(\theta_1,\phi_1,\theta_2,\phi_2)\cdot\frac{\varepsilon_2}{\varepsilon_1}$$

(Eq. A.2)

where the attenuation factor is defined as $L_2=e^{k_{e2}\cdot d_2\sec\theta_2}$, the absorption coefficient is $k_{e2}\approx \mathrm{Im}(2\omega\sqrt{\mu_0\varepsilon_2})$, (the beams are attenuated by layer 2 in the upward path), and θ_2 and ϕ_2 are the incident and phase angles respectively. $t_{pq}^{12}(\theta_1,\phi_1,\theta_2,\phi_2)$ is the two-way transmission rate from layer 2 to layer 1.

$$t_{pq}^{12}(\theta_1,\phi_1,\theta_2,\phi_2)=\frac{1}{4\pi}\sigma_{pq}^{t12}(\theta_1,\phi_1,\theta_2,\phi_2)\cdot\frac{\cos\theta_2}{\cos\theta_1}$$

(Eq. A.3)

Where $\sigma_{pq}^{t12}(\theta_1,\phi_1,\theta_2,\phi_2)$ is the two-way transmission sigma function from layer 2 to layer 1. Note θ_2 ranges from 0 to π/2, whereas ϕ_2 ranges from 0 to 2π. Integration is required to contain all the different incident angles of θ_2 and ϕ_2.

$$T_{B3,p}(\theta_1,\phi_1,1^+)=\int_0^{2\pi}d\phi_2\int_0^{\pi/2}\sin\theta_2 d\theta_2[T_{B3,p}(\theta_2,2^+)\cdot\frac{1}{L_2}\cdot t_{pq}^{12}(\theta_1,\phi_1,\theta_2,\phi_2)\frac{\varepsilon_2}{\varepsilon_1}]$$

$$+\int_0^{2\pi}d\phi_2\int_0^{\pi/2}\sin\theta_2 d\theta_2[T_{B3,p}(\theta_2,2^+)\cdot\frac{1}{L_2}\cdot t_{pq}^{12}(\theta_1,\phi_1,\theta_2,\phi_2)\frac{\varepsilon_2}{\varepsilon_1}] \quad \text{(Eq. A.4)}$$

According to the small perturbation theory (*Johnson, 1999*),

$$t_{pp}^{12}(\theta_1,\phi_1,\theta_2,\phi_2)=t_{pp}^{(0)12}(\theta_1,\phi_1,\theta_2,\phi_2)+t_{pp}^{(1)12}(\theta_1,\phi_1,\theta_2,\phi_2)+t_{pp}^{(2)12}(\theta_1,\phi_1,\theta_2,\phi_2) \quad \text{(Eq. A.5)}$$

$$t_{pq}^{12}(\theta_1,\phi_1,\theta_2,\phi_2)=t_{pq}^{(0)12}(\theta_1,\phi_1,\theta_2,\phi_2)+t_{pq}^{(1)12}(\theta_1,\phi_1,\theta_2,\phi_2)+t_{pq}^{(2)12}(\theta_1,\phi_1,\theta_2,\phi_2) \quad \text{(Eq. A.6)}$$

As mentioned previously, only the zero-order (flat surface case, height h as h_0), first-order ($h = h_0 + ax$, where x is the coordinate of a horizontal axis), and second-order ($h = h_0 + ax + bx^2$, where x is the coordinate of a horizontal axis) transmission fields are considered.

By substituting Eq A.5 and Eq A.6 into Eq A.4, Eq. A.7 can be obtained:

$$T_{B3,p}(\theta_1,\phi_1,1^+)=\int_0^{2\pi}d\phi_2\int_0^{\pi/2}\sin\theta_2 d\theta_2[T_{B3,p}(\theta_2,2^+)\cdot\frac{1}{L_2}\cdot t_{pp}^{(1)12}(\theta_1,\phi_1,\theta_2,\phi_2)]\cdot\frac{\varepsilon_2}{\varepsilon_1}$$
$$+\int_0^{2\pi}d\phi_2\int_0^{\pi/2}\sin\theta_2 d\theta_2[T_{B3,\mathrm{q}}(\theta_2,2^+)\cdot\frac{1}{L_2}\cdot t_{pq}^{(1)12}(\theta_1,\phi_1,\theta_2,\phi_2)]\cdot\frac{\varepsilon_2}{\varepsilon_1}$$
$$+T_{B3,p}(\theta_{2c},2^+)\cdot\frac{1}{L_2}\cdot t_p^{(0)}(\theta_{2c})+T_{B3,p}(\theta_{2c},2^+)\cdot\frac{1}{L_2}\cdot t_p^{(2)}(\theta_{2c})$$

(Eq. A.7)

where θ_{2c} is the coherent incidence angle of θ_1, which means θ_{2c} is defined in Eq. A.8, i.e., Snell's law, as:

$$\eta_1 \sin\theta_1 = \eta_2 \sin\theta_{2c} \qquad \text{(Eq. A.8)}$$

and the zero-order coherent transmission rate is defined in Eq. A.9, i.e. Fresnel equation, as:

$$t_p^{(0)}(\theta_{2c}) = \frac{\eta_2 \cos\theta_1}{\eta_1 \cos\theta_{2c}} \left| T_p(\theta_{2c}) \right|^2, \qquad \text{(Eq. A.9)}$$

where η is the refractive index.

A.2.2. Contribution from layer 2

The contribution from layer 2 is more complex because it contains both upward and downward portions (the downward part turns upward again once reflected):

$$T_{B2,p}(\theta_1,\phi_1,1^+) = T_{B2\_up,p}(\theta_1,\phi_1,1^+) + T_{B2\_dn,p}(\theta_1,\phi_1,1^+). \qquad \text{(Eq. A.10)}$$

In this case, T_{B2_up} represents the brightness temperature contributions of the upcoming beam. Similar to Eq. A.7, T_{B2_up} can be derived as

$$\begin{aligned} T_{B2\_up,p}(\theta_1,\phi_1,1^+) &= \int_0^{2\pi} d\phi_2 \int_0^{\pi/2} \sin\theta_2 d\theta_2 \cdot T_{B2\_dn,p}(\theta_2,1^-) \cdot t_{pp}^{(1)12}(\theta_1,\phi_1,\theta_2,\phi_2) \cdot \frac{\varepsilon_2}{\varepsilon_1} \\ &+ \int_0^{2\pi} d\phi_2 \int_0^{\pi/2} \sin\theta_2 d\theta_2 \cdot T_{B2\_up,q}(\theta_2,1^-) \cdot t_{pq}^{(1)12}(\theta_1,\phi_1,\theta_2,\phi_2) \cdot \frac{\varepsilon_2}{\varepsilon_1} \\ &+ T_{B2\_up,p}(\theta_{2c},1^-) \cdot t_p^{(0)}(\theta_{2c}) + T_{B2\_up,p}(\theta_{2c},1^-) \cdot t_p^{(2)}(\theta_{2c}) \end{aligned}$$

(Eq. A.11)

where

$$T_{B2\_up,p}(\theta_2,1^-) = T_{B2\_up,q}(\theta_2,1^-) = \mathrm{T}_0(1-\frac{1}{L_2}) + g[\frac{d_2}{L_2} - \frac{1}{\eta_{e2}\sec\theta_2}(1-\frac{1}{L_2})] \quad \text{(Eq. A.12)}$$

and g = 50 K cm^{-1} is the temperature gradient of the lunar dust layer (layer 1) *(Vasavada et al, 1999)*.

In Eq. A.11, the first and second integrals are contributions from the incoherent field, representing the upward brightness temperature generated by layer 2 at the lower boundary of the rough surface ($z = 0^-$) and transmitted through the rough surface. The third and fourth integrals are generated by layer 2 at the lower boundary of layer 1 ($z = 1^-$), which is incident to the rough surface with an incidence angle of θ_{2c}, and transmitted through the rough surface.

The downward brightness temperature generated by layer 2 at boundary 2 is defined as: $T_{B2\_dn,p}(q_2,2^+)$, p-polarization, or $T_{B2\_dn,q}(q_2,2^+)$, q-polarization.

Thus, the TB contribution of layer 2's downward radiation, which is reflected at boundary 2, passed through layer 2 with attenuation, and transmitted to the MRM is expressed as:

$$T_{B2\_dn,p}(\theta_1,\phi_1,1^+)=\int_0^{2\pi}d\phi_2\int_0^{\pi/2}\sin\theta_2 d\theta_2\cdot T_{B2\_dn,p}(\theta_2,2^+)\cdot r_{3,p}(\theta_2,2^+)\cdot\frac{1}{L_2}\cdot t_{pp}^{(1)12}(\theta_1,\phi_1,\theta_2,\phi_2)\cdot\frac{\varepsilon_2}{\varepsilon_1}$$
$$+\int_0^{2\pi}d\phi_2\int_0^{\pi/2}\sin\theta_2 d\theta_2\cdot T_{B2\_dn,\mathrm{q}}(\theta_2,2^+)\cdot r_{3,\mathrm{q}}(\theta_2,2^+)\cdot\frac{1}{L_2}\cdot t_{pq}^{(1)12}(\theta_1,\phi_1,\theta_2,\phi_2)\cdot\frac{\varepsilon_2}{\varepsilon_1}$$
$$+T_{B2\_dn,p}(\theta_{2c},2^+)\cdot r_{3,p}(\theta_2,2^+)\cdot\frac{1}{L_2}\cdot t_p^{(0)}(\theta_{2c})+T_{B2\_dn,p}(\theta_{2c},2^+)\cdot r_{3,p}(\theta_2,2^+)\cdot\frac{1}{L_2}\cdot t_p^{(2)}(\theta_{2c})$$

……(Eq. A.13)

where:

$$T_{B2\_dn,p}(\theta_2,2^+)=T_{B2\_dn,\mathrm{q}}(\theta_2,2^+)=\mathrm{T}_0(1-\frac{1}{L_2})+g[-d_2+\frac{1}{\eta_{e2}\sec\theta_2}(1-\frac{1}{L_2})]\quad\text{(Eq. A.14)}$$

In Eq.A.13, $r_{3,p}(q_2,2^+)$ is the p-polarization equivalent reflectivity of layer 3.

Thus, at θ_1 and ϕ_1, the brightness temperature being observed is the total contribution of layers 2 and 3:

$$T_{B,p}(\theta_1,\phi_1,1^+)=T_{B3,p}(\theta_1,\phi_1,1^+)+T_{B2,p}(\theta_1,\phi_1,1^+)=$$

$$+\int_0^{2\pi}d\phi_2\int_0^{\pi/2}\sin\theta_2 d\theta_2[T_{B3,p}(\theta_2,2^+)\cdot\frac{1}{L_2}\cdot t_{pp}^{(1)12}(\theta_1,\phi_1,\theta_2,\phi_2)]\cdot\frac{\varepsilon_2}{\varepsilon_1}$$
$$+\int_0^{2\pi}d\phi_2\int_0^{\pi/2}\sin\theta_2 d\theta_2[T_{B3,\mathrm{q}}(\theta_2,2^+)\cdot\frac{1}{L_2}\cdot t_{pq}^{(1)12}(\theta_1,\phi_1,\theta_2,\phi_2)]\cdot\frac{\varepsilon_2}{\varepsilon_1}$$
$$+T_{B3,p}(\theta_{2c},2^+)\cdot\frac{1}{L_2}\cdot t_p^{(0)}(\theta_{2c})+T_{B3,p}(\theta_{2c},2^+)\cdot\frac{1}{L_2}\cdot t_p^{(2)}(\theta_{2c})$$

$$+\int_0^{2\pi}d\phi_2\int_0^{\pi/2}\sin\theta_2 d\theta_2\cdot T_{B2\_dn,p}(\theta_2,1^-)\cdot t_{pp}^{(1)12}(\theta_1,\phi_1,\theta_2,\phi_2)\cdot\frac{\varepsilon_2}{\varepsilon_1}$$
$$+\int_0^{2\pi}d\phi_2\int_0^{\pi/2}\sin\theta_2 d\theta_2\cdot T_{B2\_\mathrm{up,q}}(\theta_2,1^-)\cdot t_{pq}^{(1)12}(\theta_1,\phi_1,\theta_2,\phi_2)\cdot\frac{\varepsilon_2}{\varepsilon_1}$$
$$+T_{B2\_\mathrm{up},p}(\theta_{2c},1^-)\cdot t_p^{(0)}(\theta_{2c})+T_{B2\_\mathrm{up},p}(\theta_{2c},1^-)\cdot t_p^{(2)}(\theta_{2c})$$

$$+\int_0^{2\pi} d\phi_2 \int_0^{\pi/2} \sin\theta_2 d\theta_2 \cdot T_{B2\_dn,p}(\theta_2, 2^+) \cdot r_{3,p}(\theta_2, 2^+) \cdot \frac{1}{L_2} \cdot t_{pp}^{(1)12}(\theta_1, \phi_1, \theta_2, \phi_2) \cdot \frac{\varepsilon_2}{\varepsilon_1}$$

$$+\int_0^{2\pi} d\phi_2 \int_0^{\pi/2} \sin\theta_2 d\theta_2 \cdot T_{B2\_dn,\mathrm{q}}(\theta_2, 2^+) \cdot r_{3,\mathrm{q}}(\theta_2, 2^+) \cdot \frac{1}{L_2} \cdot t_{pq}^{(1)12}(\theta_1, \phi_1, \theta_2, \phi_2) \cdot \frac{\varepsilon_2}{\varepsilon_1}$$

$$+T_{B2\_dn,p}(\theta_{2c}, 2^+) \cdot r_{3,p}(\theta_2, 2^+) \cdot \frac{1}{L_2} \cdot t_p^{(0)}(\theta_{2c}) + T_{B2\_dn,p}(\theta_{2c}, 2^+) \cdot r_{3,p}(\theta_2, 2^+) \cdot \frac{1}{L_2} \cdot t_p^{(2)}(\theta_{2c})$$

(Eq. A.15)

Using the derived roughness parameters for the Apollo 12 landing site (*Helfenstien and Shepard., 1999*), the expected 3 GHz TB measurement was calculated and is shown in Figure A.5 with different surface RMS slopes. TB of the 3 GHz channel increased as the small-scale roughness increased. However, the increase starts to plateau for RMS slopes greater than 0.2^o and the total change in TB is less than 0.5 K. The lowest measurement made by the 3 GHz MRM channel in the equatorial region is 220 K, so a change of 0.5 K is negligible. Hence the role of small-scale roughness is negligible for the 3 GHz MRM channel.

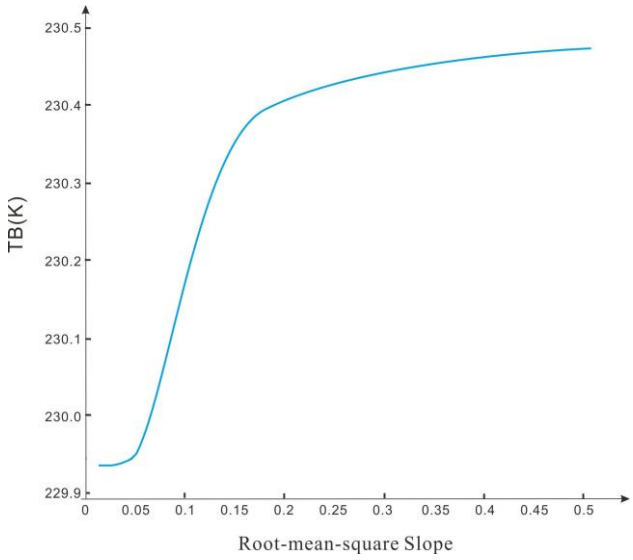

Figure A.5. Simulated 3 GHz TB's variation vs surface RMS slope at the Apollo12 landing site, viewing angle is 0 °and surface standard deviation set as 1.35 mm. (For Apollo12 landing site area the average surface standard deviation ranges 1.35 ±0.64 mm). Therefore, small scale roughness can cause an increase in the measured 3 GHz TB of 0.5 K.

A.3 Large-scale Roughness (m to km scale)

In calculating large-scale lunar surface roughness, *Smith (1967)* proposed that the rough lunar surface topography is composed of many flat Lambertian surface elements with various slopes. Considering the shadowing effect between elements, *Smith (1967)* investigated the effect of the large-scale roughness of the lunar surface on brightness temperature. This area has been developed further recently because we now have better topographic data for the Moon and asteroids *(Bandfield et al. 2015)*. However, both the work of *Smith (1967) and Bandfield et al., (2015)* are for infrared radiation and not strictly for microwave radiation. The development of a microwave

radiation model for the large scale surface roughness would be a very complex task that is beyond the scope of this thesis. Therefore the infrared models of *Smith (1967)* and *Bandfield et al., (2015)* are both discussed and provided qualitative information on the large scale roughness effect.

Smith (1967) states solar radiation controls the diurnal variation of the lunar surface temperature and that the solar radiation is affected by the shadowing effect (Figure A.6). The shadowing effect is due to uneven terrain that shields solar illumination incident upon the surface. Thus, the statistical characteristics of the terrain's roughness are required to evaluate the effective solar irradiance incident upon the surface.

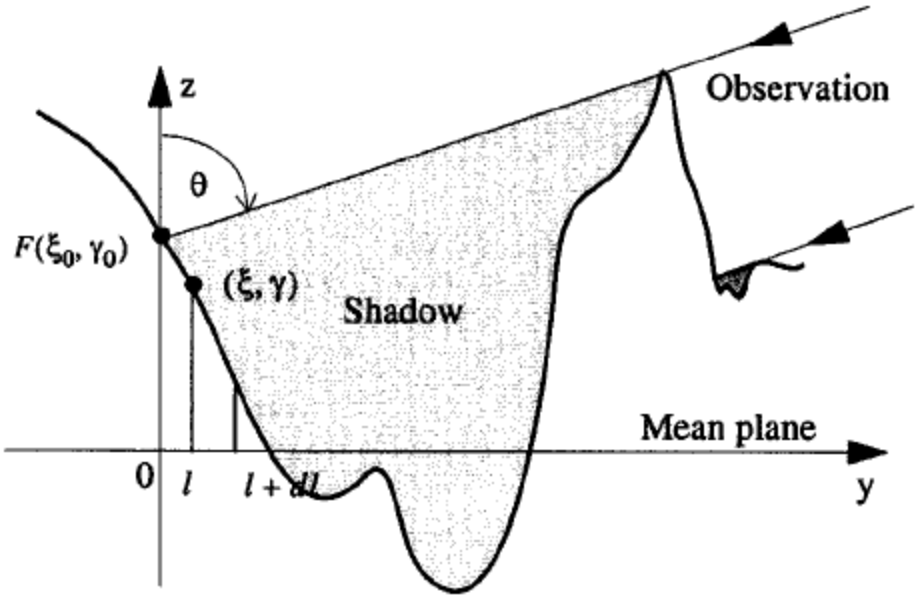

Figure A.6. Illustration of the shadowing function. Cited from *Bourlier et al. (2002)*

According to *Bourlier et al. (2002)*, there are two approaches that can be used to determine the two dimensional statistical shadowing function S: the Wagner approach (S_W) (*Wagner, 1966*) and the Smith approach (S_S) (*Smith et al., 1967*). Both approaches are defined below:

$$S_W = \Lambda' \times \frac{1-\exp(-\Lambda)}{\Lambda}, \quad \text{(Eq. A.16)}$$

$$S_S = \Lambda' \times \frac{1}{\Lambda+1}, \quad \text{(Eq. A.17)}$$

Where Λ is defined as $\Lambda = \frac{1}{\mu}\int_{\mu}^{\infty}(\gamma-\mu)\,p(\gamma)\,\mathrm{d}\gamma$ (Eq. A.18)

$$\Lambda' = \int_{-\infty}^{\mu} p(\gamma)d\gamma \quad \text{(Eq. A.19)}$$

Where $p(\gamma)$ is the surface slope probability density function and γ is the surface slope in radians. Thus, the Wagner and Smith shadowing functions S_w and S_s depend on the surface slope probability density function $p(\gamma)$ and depend on μ, where $\mu = \cot\theta$ is the slope of the incident ray.

The formulas for the two dimensional (2D) shadowing function can be expanded into three dimensions (3D) using an approach outlined in *Bourlier et al. (2002)* and summarized here. Figure A.7 defines the parameters used in the expansion of a 2D slice of a random rough surface into a 3D plane.

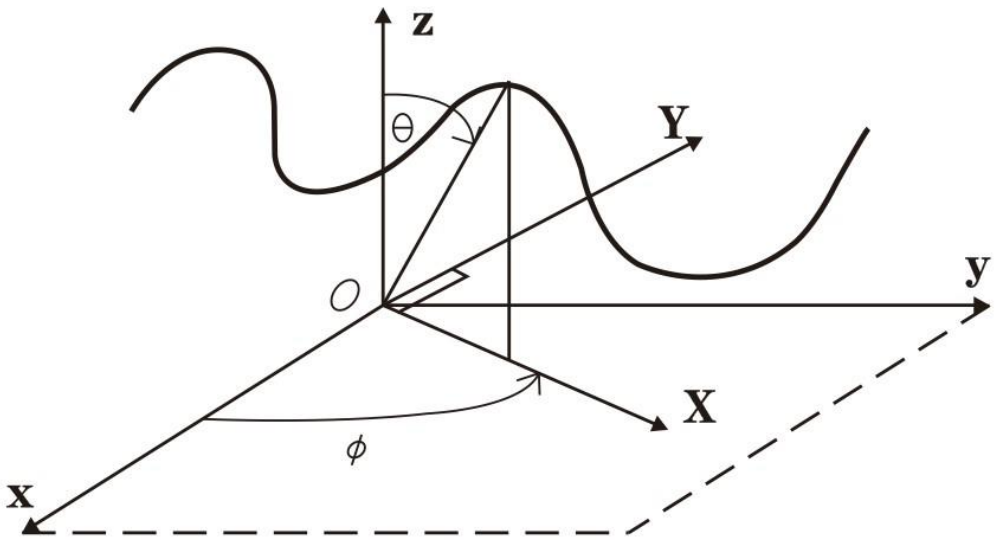

Figure A.7. 3D plane shadowing function.

According to *Bourlier et al. (2002)*, if expanded to 3D, then the 2D result would be expressed as:

$$S(\mathrm{p},\mathrm{q},\theta,\phi)=\gamma(\mu-\mathrm{p}\cdot\cos\phi-q\cdot\sin\phi)\,\mathrm{G}(\mu), \qquad \text{(Eq. A.20)}$$

where the angles θ and ϕ are defined in Figure A.7, $p=\partial \mathrm{z}/\partial x, q=\partial \mathrm{z}/\partial y, \gamma(\mu-\mathrm{p}\cdot\cos\phi-q\cdot\sin\phi)$ is the unit step function,

$$\mu=\cot\theta, \qquad \text{(Eq. A.21)}$$

$$G(\mu)=\frac{1}{[\Lambda(\mu)+1]}, \qquad \text{(Eq. A.22)}$$

$$\Lambda(\mu)=\frac{1}{2}[(\frac{2}{\pi})^{1/2}\frac{w}{\mu}\mathrm{e}^{-\mu^2/2w^2}-\mathrm{erfc}(\frac{\mu}{\sqrt{2}w})], \qquad \text{(Eq. A.23)}$$

and *erfc* is the complementary set of error function (the integral between 0 and *x* of a Gaussian distribution function, whose detailed explanation can be found in *Smith 1967* and *Bourlier et al. 2002*).

Figure A.8 shows solar incident light emitted from a source at S that is not obscured, but is incident on a rough surface at point P, which is the center of unit surface element δA. The normal to the global surface element is displayed as dashed line V, the normal to unit surface element δA is shown as N. The angle between the vertical of the global surface and the vector of the incoming solar radiation is θ.

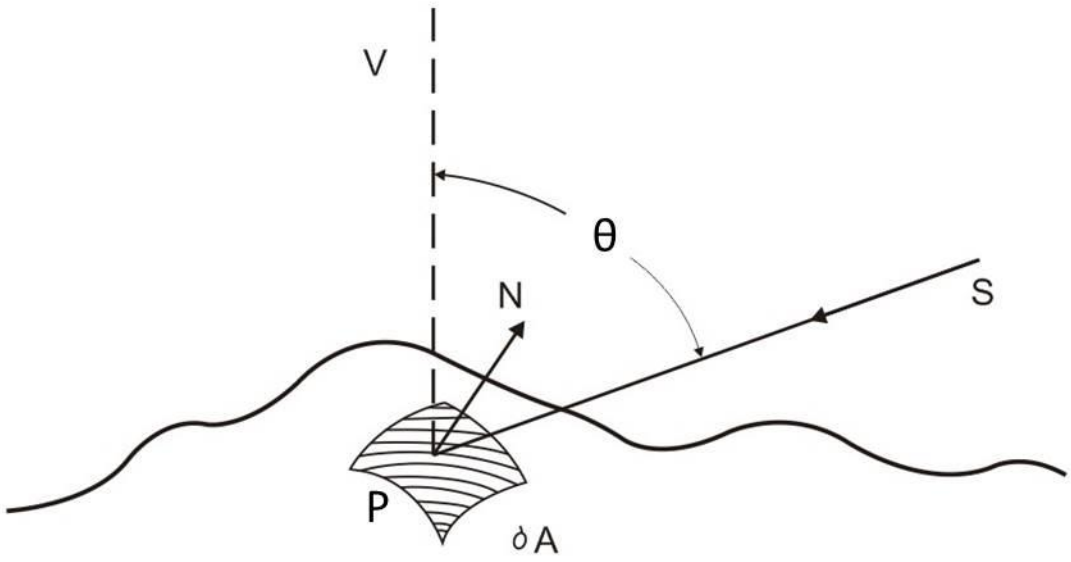

Figure A.8. Solar incident rays on the rough surface

If δA's projection on the bottom plane is plane surface element dxdy, then the relationship can be expressed as:

$$\delta A \cdot \cos(\angle VPN) = dxdy. \quad \text{(Eq. A.24)}$$

where $\angle$VPN is the angle between points V, P and N in Figure A.8. Thus, the total energy R received by δA is proportional to δA·cos($\angle$SPN)·$S\ (p,\ q,\ \theta,\ \phi)$; thus,

$$R \propto \iint_{mean\_plane} \delta A \cdot \cos(\angle SPN) S(p, q, \theta, \phi) = \iint_{mean\_plane} dxdy \frac{\cos(\angle SPN)}{\cos(\angle VPN)} S(p, q, \theta, \phi), \quad \text{(Eq. A.25)}$$

Where $\angle$SPN is the angle between points S, P and N in Figure A.8, $S(p,\ q,\ \theta,\ \phi)$ is the shading function in the direction of travel of the solar ray.

If we compute the average surface integral and divide it by the projected δA, then the energy per unit area projected onto δA can be obtained, which is proportional to:

$$R \propto \iint_{mean\_plane} dpdqP(p)P(q) \frac{\cos(\angle SPN)}{\cos(\angle VPN)} S(p, q, \theta, \phi), \quad \text{(Eq. A.26)}$$

where:

$$\cos(\angle SPN) = \hat{n} \cdot \overrightarrow{PS} = \frac{-p\hat{x} - q\hat{y} + \hat{z}}{\sqrt{1 + p^2 + q^2}} \cdot (\hat{x}\sin\theta\cos\phi + \hat{y}\sin\theta\sin\phi + \hat{z}\cos\theta)$$

$$= \frac{-p\sin\theta\cos\phi - q\sin\theta\sin\phi + \cos\theta}{\sqrt{1 + p^2 + q^2}} \quad \text{(Eq. A.27)}$$

$$\cos(\angle VPN) = \hat{n} \cdot \hat{v} = \frac{-p\hat{x} - q\hat{y} + \hat{z}}{\sqrt{1 + p^2 + q^2}} \cdot \hat{z} = \frac{1}{\sqrt{1 + p^2 + q^2}}. \quad \text{(Eq. A.28)}$$

If the energy of solar radiation incident along SP onto surface element δA is defined as I_0, then the surface effective solar irradiance I_{eff} incident onto the element is expressed as:

$$I_{eff} = I_0 \cdot IN \,, \qquad \text{(Eq. A.29)}$$

where:

$$IN = \iint dpdqP(\mathrm{p})P(\mathrm{q})\mathrm{S}(\mathrm{p},\mathrm{q},\theta,\phi)(\cos\theta - \mathrm{p}\sin\theta\cos\theta - \mathrm{q}\sin\theta\sin\phi) \qquad \text{(Eq. A.30)}$$

IN is defined as the attenuation factor of solar irradiance.

From the assumption that the rough surface is a Gaussian random rough surface, the slope probability density function is expressed as:

$$. \quad P(p) = \frac{1}{\sqrt{2\pi}\omega}\exp(-\frac{p^2}{2\omega^2}) \qquad \text{(Eq. A.31)}$$

Where ω is the RMS slope of the rough surface. Thus,

$$I_{eff} = I_0 \cdot \iint dpdq \frac{1}{2\pi\omega^2}\exp(-\frac{p^2+q^2}{2\omega^2})\mathrm{S}(\mathrm{p},\mathrm{q},\theta,\phi)(\cos\theta - \mathrm{p}\sin\theta\cos\theta - \mathrm{q}\sin\theta\sin\phi) \,. \qquad \text{(Eq. A.32)}$$

The formula represents effective solar irradiance incident on the large-scale rough surface.

From the preceding analysis, the following observations are made:

(a) When the angle of incidence is zero, that is, when the incident is vertical to the surface, then roughness does not affect solar irradiance and the attenuation factor *IN* value is 1.

(b) The larger the incident angle θ, the smaller the attenuation factor *IN*, resulting in a significantly smaller I_{eff}. This is because the probability that light is blocked by rough terrain is significantly higher with larger angles of incidence.

(c) The greater the RMS slope ω, the smaller the attenuation factor *IN*, the smaller the I_{eff} and measured brightness temperature. A high RMS value indicates more undulating (uneven) features of the region because the RMS slope represents terrain roughness. Thus, the probability of blocking incident light should be large.

(d) If the local plane is inclined backward from the rays of the sun, then the local angle of incidence becomes large and decreases the amount of solar irradiance, thereby reducing the surface temperature. For example *Bourlier et al. (2002)* calculated using Eq. A.32 that when ω = 0.6, the brightness temperature would be expected to reduce ~3 K. However, if the local inclined plane is oriented toward solar radiation, then the temperature would be expected to increase.

Based on qualitative interpretation of Eq. A.32, clearly large scale surface roughness will have minimal effect on Maria region, equatorial region and mid-day data.

Using the time of day (mid-day) and latitude range considered that minimizes surface roughness effects described in chapter 6 (0 – 14^{o}N), the effect on the measured 3 GHz MRM measured TB will be within +/- 1 K.

Appendix Summary:

Our results show that, in most cases, large-scale lunar surface roughness mainly reduces solar radiation and therefore reduces the measured MRM TB, whereas small-scale lunar surface roughness mainly increases the measured MRM TB. From the Apollo 12 simulation, small-scale lunar surface roughness only has a trivial effect on the MRM long wavelength channels, such as the 3 GHz channel. Small scale roughness only causes a TB increase of less than 0.5 K in the 3 GHz MRM channel. The forward model in chapter 4 and the inversion model in chapter 6 mainly depend on information from the long wavelength channel (i.e. 3 GHz channel – see chapter 4 Figures 4.2 and 4.3). As the lowest measured TB around the equatorial region in the 3-GHz channel is 220 K, this chapter's discussions indicate that the small surface roughness scattering effect (0.5 K) is negligible in the MRM inversion. Also, by using mid-day MRM data, and choosing latitude range that minimizes large scale surface roughness effects (0 – 14^{o}N), the large scale roughness' effect on the measured 3-GHz MRM measured TB is also minimized and will be within +/- 1 K.

References

Andrews-Hanna J C, Besserer J, Head III J W, et al. Structure and evolution of the lunar Procellarum region as revealed by GRAIL gravity data. Nature, 2014, 514(7520): 68-71.

Bandfield J L, Ghent R R, Vasavada A R, Paige D A, Lawrence S J, and Robinson M S. Lunar surface rock abundance and regolith fines temperatures derived from LRO Diviner Radiometer data. Journal of Geophysical Research, 2011, 116: E00H02.

Bandfield J L, Hayne P O, Williams J, et al. Lunar surface roughness derived from LRO Diviner Radiometer observations. Icarus, 2015: 357-372.

Barth E L, Farrell W M, Rafkin S C R. Electric field generation in Martian dust devils. 2011, 268：1667.

Bhatt M, Mall U, Bugiolacchi R. Iron mapping method based on 2μm absorption parameters using SIR-2 data on-board Chandrayaan-1, EPSC-DPS conference, 2011, 6: 441.

Biccari D, Picardi G, Seu R, et al. Mars surface models and subsurface detection performance in MARSIS. Geoscience and Remote Sensing Symposium, IGARSS'01.IEEE 2001 International. IEEE, 2001, 6: 2560-2562.

Blewett D T, Lucey P G, Hawke B R, et al. Clementine images of the lunar sample-return stations: Refinement of FeO and TiO2 mapping techniques. Journal of Geophysical Research, 1997, 102: 16319–16325.

Boardman J W,Pieters C M, Green R O, et al. Measuring moonlight: An overview of the spatial properties, lunar coverage, seleno location, and related Level 1B products of the Moon Mineralogy Mapper. Journal of Geophysical Research, 2011, 116: E00G14.

Bourlier C, BergincG, Saillard J. One- and Two-Dimensional Shadowing Functions for any Height and Slope Stationary Uncorrelated Surface in the Monostatic and Bistatic Configurations. IEEE transactions on antennas and propagation, 2002, 50(3):312-324.

Burke W J, Schmugge T, Paris J F. Comparison of 2.8- and 21-cm Microwave Radiometer Observations over Soils With Emission Model Calculations, Journal of Geophysical Research, 1979, 84: 287-294.

Burns R. Mineralogical Applications of Crystal Field Theory. Cambridge, UK: Cambridge University Press, 1993.

Braden S E, Stopar J D, Robinson M S, et al. Evidence for basaltic volcanism on the Moon within the past 100 million years. Nature Geoscience, 2014, 7(11): 787.

Campbell B A, Maxwell T A, Freeman A. Mars orbital synthetic aperture radar: Obtaining geologic information from radar polarimetry. Journal of Geophysical Research: Planets, 2004, 109(7):253-258.

Campbell I H. Large igneous provinces and the mantle plume hypothesis. Elements, 2005, 1(5): 265-269.

Carrier W D, Olhoeft G R. Mendell W.Physical Properties of the Lunar Surface. Lunar Sourcebook (G. Heiken, D. Vaniman, and B. M. French, eds.), Cambridge University Press, Cambridge, 1991, 475-594.

Cartier W D III, Mitchell J K, Mahmood A.The nature of lunar soil. Journal of the Soil Mechanics and Foundations Division, 1973, 75:813-832.

Chen, P, Tian Y, Hua L, Song DW, Li Q X, Huang Q L, Gui LQ. Second-order small perturbation method for transmission from dielectric rough surfaces, Waves Random Complex Media, 2011, 21(4): 668–689.

Clark R,Pieters C M, Green R O, et al. Water and hydroxyl on the Moon as seen by the Moon Mineralogy Mapper (M^3). 41st Lunar Planet Science Conference, 2010, 1533: 2302.

Clifford S M. A model for the hydrologic and climatic behavior of water on Mars. Journal of Geophysical Research: Planets, 1993, 98(E6): 10973-11016.

Clifford S M, Parker T J. The evolution of the Martian hydrosphere: Implications for the fate of a primordial ocean and the current state of the northern plains. Icarus, 2001, 154(1): 40-79.

Cloutis E A, Mccormack K A, Iii J F B, et al. Ultraviolet spectral reflectance properties of common planetary minerals. Icarus, 2008, 197, 321-347.

Conel, JE, MortonJB. Interpretation of lunar heat flow data.The Moon.1975, 14: 263–289.

Cui H Y, Wang Z Z, Zhang X H, et al. Analysis on Effect of Space Microwave Emission Environment on In-Orbit Calibration of Chang'e-1 Microwave Sounder. Remote Sensing Technology and Application, 2009, 24: 435-441.

Dhingra D, Pieters C M, Isaacson P, et al. Spectroscopic signature of the high titanium basalts at Mare Tranquillitatis from Moon Mineralogy Mapper (M^3). 41st Lunar Planet Science Conference, 2010, 1533: 2494.

Erard S. A spectro-photometric model of Mars in the near-infrared. Geophysical Research Letters, 2001, 28(7): 1291-1294.

Fa W Z, Jin Y Q. Inversion of lunar regolith layer thickness using optical data and microwave emission simulation (in Chinese), Chinese Journal of Radio Science, 2006, 21 (3): 347-356.

Fa W Z, Jin Y Q. Simulation of brightness temperature from lunar surface and inversion of regolith-layer thickness. Journal of Geophysical Research, 2007, 112: E05003.

Fa W, Wieczorek M A. Regolith thickness over the lunar nearside: Results from Earth-based 70-cm Arecibo radar observations. Icarus, 2012, 218:771–787.

Feldman W. C, Barraclough B. L, Fuller K. R, et al.The Lunar Prospector gamma-ray and neutron spectrometers. Nuclear Instruments and Methods in Physics Research Section A: Accelerators, Spectrometers, Detectors and Associated Equipment, 1999,422(1): 562-566.

Feng J Q, Yan S U, Liu J J, et al. Data Processing and Result Analysis of CE-2 MRM. Earth Science(Journal of China University of Geosciences), 2013, 38(4):898-906.

Florensky K P, et al. Essays of Comparative Planetology (V. L. Barsukov, Ed.). Nauka Press,1981.

Fung A K, Bredow J, Tjuatja A. Emission from Lunar Regolith. Technical Report, 2006.

Garrickbethell I, Perera V J, Nimmo F, et al. The tidal-rotational shape of the Moon and evidence for polar wander. Nature, 2014, 512(7513):181-184.

Gillis J J, Jolliff B L, Korotev R L. Lunar surface geochemistry: Global concentrations of Th, K, and FeO as derived from lunar prospector and Clementine data. Geochimica Et Cosmochimica Acta, 2004, 68: 3791–3805.

Green R O et al. The Moon Mineralogy Mapper (M^3) imaging spectrometer for lunar science: Instrument description, calibration, on-orbit measurements, science data calibration and on-orbit validation. Journal of Geophysical Research Atmospheres, 2011, 116(10):1241-1249.

Hagermann A, Tanaka S. Ejecta deposit thickness, heat flow, and a critical ambiguity on the Moon. Geophysical Research Letters, 2006, 33(19):277-305.

Halliday, A.N. Terrestrial accretion rates and the origin of the Moon.Earth and Planetary Science Letters. 2000, 176 (1): 17–30.

Hapke, B. Bidirectional reflectance spectroscopy: I. Theory. Journal of Geophysical Research, 1981, 86: 3039-3054.

Haskin, L.A.TheImbrium impact event and the thorium distribution at the lunar highlands surface. Journal of Geophysical Research, 1998, 103: 1679–1689.

Hartmann W K, Phillips R J, Taylor G J. Origin of the Moon. Origin of the Moon.1986, 1.

He, Y.C. Effects of small scale roughness on microwave radiative brightness temperature of lunar regolith. Electromagnetic and Microwave Technology (in Chinese), 2013, 2: 23.

Hegde U, Balasubramaniam R, Gokoglu S. Analysis of Water Extraction from Lunar Regolith. Aiaa Aerospace Sciences Meeting Including the New Horizons Forum and Aerospace Exposition, 2000.

Heggy E, Paillou P, Ruffle G, Malezieux J.M.Costard F, Grandjean G. On Water Detection in the Martian Subsurface Using Sounding Radar. Icarus, 2001, 154(2): 244-257.

Heiken G H, Vaniman D T, Bevan M. Lunar Sourcebook. Cambridge University Press, 1991

Helfenstein P, Michael K Shepard. SubmillimeterScale Topography of Lunar Regolith, Icarus, 1999, 141:107-131.

Hiesinger H, Head III J W, Wolf U,Jaumann R, Neukum G. Ages and stratigraphy of mare basalts in OceanusProcellarum, Mare Nubium, Mare Cognitum, and Mare Insularum. Journal of Geophysical Research, 2003, 108 (E7): 5065.

Hiesinger, H. et al. Ages and stratigraphy of lunar mare basalts in Mare Frigoris and other nearside maria based on crater size-frequency distribution measurements. Journal of Geophysical Research, 2010.115, E03003.

Hirth W, Butz M, Fuerst E, et al. The Brightness Distribution over the Moon's Disk at 6 cm Wavelength. The Moon, 1976,15: 317-323.

Horai K, Fujii N. Thermo physical properties of lunar material returned by Apollo missions. Technical Report of Conference on lunar geophysics, 1971.

Huang Q, Wieczorek M A. Density and porosity of the lunar crust from gravity and topography. Journal of Geophysical Research, 2012, 117: E05003.

Ishihara Y, Goossens S, Matsumoto K, Noda H, Araki H, Namiki N, Hanada H, Iwata T, Tazawa S, Sasaki S. Crustal thickness of the Moon: Implications for farside basin structures. Geophysical Research Letters, 2009, 36(19): 82-90.

Jaeger J C. Sub-surface temperatures on the Moon. Nature, 1959,1316-1317.

Jaumann R. Spectralchemical analysis of lunar surface materials. Journal of Geophysical Research: Planets, 1991, 96(E5): 22793-22807.

Jaupart C. Horizontal heat transfer due to radioactivity contrasts: Causes andconsequences of the linear heat flow relation. Geophysical Journal International, 1983, 75(2):411-435.

Jin Y Q. Remote sensing theory of electromagnetic scattering and thermal emission. Science Press, 1998:118-180.

Johnson J T, Third order small perturbation method for scattering from dielectric rough surfaces. Journal of the Optical Society America, 1999, 16:2720-2726.

Jolliff BL,GillisJJ,HaskinLA,KorotevRL, WieczorekMA. Major lunar crustal terranes: surface expressions and crust-mantle origins. Journal of Geophysical Research, 2000, 105: 4197–4216.

Jones W P, Watkins J R, Calvert T A. Temperatures and thermophysical properties of the lunar outmost layer. The Moon, 1975, 13: 475–494.

Keihm S J, Langsth M G. Surface brightness temperatures at the Apollo 17 heat flow site: Thermal conductivity of the upper 15 cm of regolith. Proceeding 4th Lunar Science Conference, 1973, 3: 2503-2513.

Keihm S J, Peters K, Langseth M G. Apollo 15 measurement of lunar surface brightness temperatures thermal conductivity of the upper 1 and 1/2 metres of regolith. Earth and Planetary Science Letters, 1973, 19: 337-351.

Keihm S J. Interpretation of the lunar microwave brightness temperature spectrum: Feasibility of orbital heat flow mapping. Icarus, 1984, 60(3): 568-589.

Kim K J, Wöhler C, Hasebe N, et al. Lunar Silicon Distribution as Observed by the Kaguya Gamma-Ray Spectrometer and Chandrayaan-1 Moon Mineralogy Mapper (M3) Calibration. Lunar and Planetary Science Conference. 2016, 47: 1473.

King E. Space Geology (an Introduction).Wiley, New York, 1976.

Korokhin V V, Kaydash V G, Shkuratov Y G, Stankevich D G, Urs M. Prognosis of TiO2 abundance in lunar soil using a non-linear analysis of Clementine and LSCC data. Planetary and Space Science, 2008, 56: 1063–1078.

Korotev R L. Concentrations of radioactive elements in lunar materials. Journal of Geophysical Research: Planets (1991—2012), 1998, 103(E1): 1691-1701.

Kramer G Y, Besse S, Nettles J, et al. Newer views of the Moon: Comparing spectra from Clementine and the Moon Mineralogy Mapper. Journal of Geophysical Research: Planets, 2011, 116(E6).

Krotikov V D,Troitski UIV S. Radio emission and nature of the Moon. Physics-Uspekhi, 1964, 6(6): 841-871.

Lan A L, Zhang S W. Study on the thickness of Lunar Soil with Microwave Radiometer (in Chinese). Remote Sensing Technology and Application, 2004, 19 (3): 154-158.

Langseth M G Jr, Keihm S J, Chute J L Jr. Heat-flow experiment. Apollo 17 Preliminary Science Report, 1973, NASA SP-330: 9–1, 9–24.

Langseth M G, Keihm S J, Peters K. Revised Lunar Heat Flow Values. Proc. 7th Lunar Science Conference, 1976, 3143–3171.

Lawrence D J, et al. Global elemental maps of the Moon: the Lunar Prospector gamma-ray spectrometer. Science, 1998, 281: 1484–1489.

Lawrence D J, et al. High resolution measurements of absolute thorium abundances on the lunar surface. Geophysical Research Letters, 1999, 26(17): 2681-2684.

Lawrence D J, Feldman W C, Elphic R C, et al. Iron abundances on the lunar surface as measured by the lunar prospector gamma-ray and neutron spectrometers. Journal of Geophysical Research, 2002a, 107: 5130.

Lawrence D J, Elphic R C, Feldman W C, Gasnault O, Genetay I, Maurice S, Prettyman T H. Small-area thorium enhancements on the lunar surface. 33rd Lunar and Planetary Science Conference, 2002b: Abstract no.1970.

Lawrence D J, Puetter R C, Elphic R C, Feldman W C, Hagerty J J, Prettyman T H, and Spudis P D. Global spatial deconvolution of Lunar Prospector Th abundances. Geophysical Research Letters, 2007, 34: L03201.

Li R X, Juwon H, Chen Y H, Di K C. Rigorous Photogrammetric Processing of HiRISE Stereo Imagery for Mars Topographic Mapping. IEEE Transactions on Geoscience and Remote Sensing, 2008, 49(7): 2558-2572.

Li Y, Wang Z Z, Jiang J S. Influence of lunar surface temperature profiles on brightness temperature of CE-1 lunar microwave sounder (in Chinese). Science China Ser D-Earth Sciences, 2009, 39 (8): 1045-1058.

Li Y, Wang Z Z, Jiang J S. Simulations on the influence of lunar surface temperature profiles on CE-1 lunar microwave sounder brightness temperature. Science China Earth Sciences, 2010, 53 (9): 1379–1391.

Linsky J L. Models of the lunar surface including temperature dependent thermal properties. Icarus, 1966, 5: 606–634.

Little R C, Feldman W C, Maurice S, et al. Latitude variation of the subsurface lunar temperature: Lunar Prospector thermal neutrons. Journal of Geophysical Research: Planets (1991-2012), 2003, 108(E5): 8-11.

LSPET (Lunar Sample Preliminary Examination Team). Apollo 17 lunar samples: Chemical and petrographic description. Science, 1973, 183: 659–672.

Lunar Sourcebook. Cambridge University Press. Edit: Grant H Heiken, David T Vaniman, Bevan M. 1991.

Lucey P G, Blewett D T, Hawke B R. Mapping the FeO and TiO2 content of the lunar surface multispectral imagery. Journal of Geophysical Research, 1998, 103: 3679–3699.

Lucey P G, Blewett D T, Johnson J R, Taylor G J, Hawke B R. Lunar titanium content from UV-VIS measurements(abstract). Lunar Planet Science, 1996, 27: 781-782.

Lucey P G, Blewett D T, Jolliff B L. Lunar iron and titanium abundance algorithms based on final processing of Clementine ultraviolet-visible images. Journal of Geophysical Research, 2000, 105: 20297–20305.

Lucey P G, Taylor G J, Malaret E. Abundance and distribution of iron on the Moon. Science, 1995, 268(5214): 1150-1153.

Lucey P, Korotev R L, Gillis J J, et al. Understanding the lunar surface and space-Moon interactions. Reviews in Mineralogy & Geochemistry, 2006, 60: 83–219.

Mason B, Melson W. The Lunar Rocks. Wiley, New York, 1970.

Matsunaga T, Ohtake M, Haruyama J, et al. Discoveries on the lithology of lunar crater central peaks by SELENE spectral profiler. Geophysical Research Letters, 2008, 35: L23201.

Mao H K, Virgo D, Bell P M. Analytical and experimental study of iron and titanium in orange glass from Apollo 17 soil sample 74220. Proc. 4th Lunar Science Conference, Geochim.Cosmochim.Acta, Suppl. London: Pergamon, 1973, 4(1): 397–412.

Meng Z G. Lunar Regolith Parameters Retrieval using Radiative Transfer Simulation and Look-up Technique (in Chinese), Jilin University Ph.D. dissertation, 2008.

Metzger A E, Trombka J I, Reedy R Ct, et al. Element concentrations from lunarorbital gamma-ray measurements. Lunar and Planetary Science Conference, 1974, 5:1067-1078.

Mitchell D L, Pater I D. Microwave imaging of Mercury's thermal emission at wavelengths from 0.3 to 20.5 cm. Icarus, 1994, 110: 2–32.

Moss B E, Haskin L A. Toward systematic estimation of the origins of regolith materials that might be sampled during a lunar highland geologic traverse. Lunar and Planetary Science Conference, 1994, 25.

Mutch T A, Arvidson R E, Head III J W, et al. The geology of Mars. Princeton N.J.Princeton University Press P, 1976, 13(2): 297–301.

Nakagawa T, Tackley P J. Influence of magmatism on mantle cooling, surface heat flow and Urey ratio. Earth and Planetary Science Letters, 2012, 329: 1-10.

Nawa D F, Philpotts J A. A lunar differentiation model in light of new chemical data on Luna 20 and Apollo 16 soils. Regolith from the Highland Region of the Moon (V. L. Barsukov, Ed.), Nauka Press, 1979, 336–344.

Njoku E, Kong J A. Theory for passive microwave remote sensing of near-surface soil moisture. Journal of Geophysical Research, 1977, 82(20): 3108-3118.

Nozette S, Rustan P, Pleasance L P, et al. The Clementine mission to the Moon—Scientific overview. Science, 1994, 266: 1835–1839.

Olhoeft G R, Strangway D W. Dielectric properties of the first 100 metres of the Moon. Earth and Planetary Science Letters, 1975, 24: 394-404.

Paige D A, Foote M C, Greenhagen B T, et al. The Lunar Reconnaissance Orbiter Diviner Lunar Radiometer Experiment. Space Science Reviews, 2010, 150 (1-4): 125-160.

Picardi G, Biccari D, Seu R, et al. MARSIS: Mars advanced radar for subsurface and ionosphere sounding. Mars Express: The Scientific Payload, 2004, 1240: 51-69.

Picardi G, Biccari D, Seu R, et al. Performance and surface scattering models for the Mars Advanced Radar for Subsurface and Ionosphere Sounding (MARSIS). Planetary and Space Science, 2004, 52(1): 149-156.

Pieters C M, Boardman J, Buratti B, et al. The Moon mineralogy mapper (M-3) on Chandrayaan-1. Current Science, 2009, 96: 500–505.

Pieters C M, Goswami J N, Clark R N, et al. Character and spatial distribution of OH/H2O on the surface of the Moon seen by M^3 on Chandrayaan-1. Science, 2009, 326(5952): 568–572.

Pieters C M, Head J W, Isaacson P, et al. Lunar international science coordination/calibration targets (L-ISCT). Advances in Space Research, 2008, 42: 248–258.

Pinet P C, Shevchenko V V, Chevrel S. Reiner gamma formation from Clementine uv-visible spectro-imaging data: the lunar chronology and iron content. 28th Lunar and Planetary Science, 1997: 1431.

Prettyman T H, Feldman W C, Lawrence D J, et al. Library least squaresanalysis of Lunar Prospector gamma-ray spectra. Lunar and Planetary Science Conference, 2002, 33.

Ran Z, Wang Z Z, Li Y. Comparison between Diviner Data and CELMS Data. Chinese Journal of Space Science, 2014, 34(3):249-261.

Rodgers C D. Inverse methods for atmospheric sounding: Theory and Practice. Series on Atmospheric, Oceanic and Planetary Physics World Scientic, 2000.

Rybach L. Determination of heat production rate. Handbook of Terrestrial HeatFlow Density Determination, 1988: 486.

Sandiford M, Mclaren S. Tectonic feedback and the ordering of heatproducing elements within the continental lithosphere. Earth and Planetary Science Letters, 2002,204(1): 133-150.

Shervais J W, Taylor L A. Petrologic constraints on the origin of the Moon. Hartmann W K, Philips R J, Taylor G J. Origin of the Moon. Houston: Lunar Planet Inst, 1986:173-201.

Shkuratov Y G, Kaydash V G, Opanasenko N V. Iron and titanium abundance and maturity degree distribution on lunar nearside. Icarus, 1999, 137, no. 2: 222-234.

Shkuratov Y G, Bondarenko N V. Regolith layer thickness mapping of the Moon by radar and optical data. Icarus, 2001, 149: 329–338.

Simon J L, Bretagnon P, Chapront J, Chapront-Touzé M, Francou G, Laskar J. Numerical expressions for precession formulae and mean elements for the Moon and planets. Astronomy and Astrophysics, 1994, 282 (2): 663–683.

Smith B G. Lunar Surface Roughness: Shadowing and Thermal Emission. Journal of Geophysical Research, 1967, 72(16):4059-4067.

Spencer J R, Lebofskyf L A, Sykes M V. Systematic Biases in Radiometric Diameter Determinations. Icarus, 1989, 78(2):337-354.

Spohn T, Breuer D. Surface Heat Flow, Radiogenic Heating, and The Evolution of The Moon. in: EGS XXVII General Assembly, 2002, abstract 6000.

Spudis P D, Schultz P H. The proposed lunar Procellarum basin: Some geochemical inconsistencies Lunar Planet. Science, 1985, 16: 809– 810.

Spudis P, Carle P. Global and regional data about the Moon. Lunar Sourcebook: A User's Guide to the Moon, 1991, 595-632.

Taylor G J. Ancient lunar crust: Origin,composition, and implications. Elements, 2009, 5(1):17-22.

The Kam LAND Collaboration.Partial radiogenic heat model for Earth revealed by geoneutrino measurements. Nature Geoscience, 2011, 4: 647-651.

Tsang L, Njoku E, Kong J A. Microwave thermal emission from a stratified medium with non uniform temperature distribution. Journal of Applied Physics, 1975, 46(12): 5127-5133.

Ulaby F T, Moore R K, Fung A K. Microwave remote sensing: Active and passive. Norwood, Massachusetts: Addison Wesley Publishing Company, 1981: 37 - 229.

Umrigar C. Monte Carlo Methods. Cornell University Open Lecture Notes, 2009: www.physics.cornell.edu/~cyrus.

Urquhart M L, Jacksky B M. Lunar thermal emission and remote determination of surface properties. Journal of Geophysical Research, 1997, 102: 10959–10969.

Vasavada A R, Paige D A, Wood S E. Near-surface temperatures on Mercury and the Moon and the stability of polar ice desposits. Icarus, 1999, 141: 179—193.

Vasseur G, Singh R N. Effects of random horizontal variations in radiogenic heat source distribution on its relationship with heat flow. Journal of Geophysical Research: Solid Earth (1978-2012), 1986, 91(B10): 10397-10404.

Vaughan D J, Burns R G. Low oxidation states of FeO and TiO2 in the Apollo 17 orange soil. EOS (Trans. A.G.U.), 1973, 54: 618–620.

Wagner R J. Shadowing of randomly rough surfaces. Journal of the Acoustical Society of America, 1966, 41(1): 138–147.

Wang Z Z, Li Y, Jiang J S, et al. Microwave Transfer Models and Brightness Temperature Simulations of MWS for Remote Sensing Lunar Surface on CE-1 Satellite. 2008 International Conference on Microwave and Millimeter Wave Technology, 2008, 21-24.

Wang Z Z, Li Y, Zhang X H, et al. Calibration and brightness temperature algorithm of CE-1 Lunar Microwave Sounder (CELMS). Science China Earth Sciences, 2010, 53: 1392-1406.

Warren P H, Rasmussen K L. Megaregolith insulation, internal temperatures, and bulk uranium content of the Moon. Journal of Geophysical Research: Solid Earth (1978–2012), 1987, 92(B5): 3453-3465.

Whitaker E A. The lunar Procellarum basin.Lunar Planet. Science, 1981, 12A, 105–111.

Wieczorek, M.A, Phillips, R.J. The" Procellarum KREEP Terrane": Implications for mare volcanism and lunar evolution. Journal of Geophysical Research, 2000, 105(E8):20417-20430.

Wieczorek M A, et al. The constitution and structure of the lunar interior. Reviews in Mineralogy & Geochemistry, 2006, 60(1):221-364.

Yamashita N, et al., Uranium on the Moon: Global distribution and U/Th ratio. Geophysical Research Letters, 2010, 37: L10201.

Young E D, Kohl I E, Warren P H, et al. Oxygen isotopic evidence for vigorous mixing during the Moon-forming giant impact. Science, 2016, 351 (6272): 493–496.

Zhang D. Retrieval of Lunar Heat Flow and the Density of Lunar Regolith Based on Remote Sensing Data. Huazhong University of Science & Technology Dissertation, 2014, 5.

Zhang D H, Zhang X H, Wang Z Z, et al. Mechanism of Lunar Soil Depth Sounding and Ground Validation Experiment for the CE-1 Lunar Microwave Sounder. Science China Series D-Earth Science, 2009, 39(8): 1097—1104.

Zhang W J，Zhang X J，Li F. Backscattering from Multilayer Soil and Its Application to Deep Soil Moisture Estimation. Journal of Electronics & Information Technology, 2008, 30 (9): 2107-2110.

Zhang W, Bowles N E. Mapping lunar TiO2 and FeO with M^3 data. European Planetary Science Congress 2013, 2013, 8: EPSC2013-374.

Zheng Y C, Tsang K T, Chan K L, et al. First Microwave Map of the Moon with Chang'E-1 Data: The Role of Local Time in Global Imaging. Icarus, 2012, 219: 194-210.

Zhu M H, et al. Potassium Map from Chang'E-2 Constraints the Impact of Crisium and Orientale Basin on the Moon. Scientific reports, 2013, 3: 1611-1611.

Zuber M T, Smith D E, Lehman D H, et al. Gravity Recovery and Interior Laboratory (GRAIL): Mapping the Lunar Interior from Crust to Core. Space Science Reviews, 2013, 178(1): 3-24.